STRUCTURAL AND ELECTRICAL PROPERTIES OF CONVENTIONAL AND MICROWAVE PROCESSED LEAD FREE KNN BASED CERAMICS

by

PRAKASH KUMAR PALEI

THESIS SUBMITTED IN PARTIAL FULFILLMENT OF THE REQUIREMENTS FOR THE DEGREE OF

DOCTOR OF PHILOSOPHY

DEPARTMENT OF PHYSICS
NATIONAL INSTITUTE OF TECHNOLOGY
ROURKELA, ODISHA, INDIA-769008

APRIL-2012

Dedicated to

My Loving Parents

DECLARATION

I certify that

a. The work contained in the thesis is original and has been done by myself under the general supervision of my supervisor.

b. The work has not been submitted to any other Institute for any degree or diploma.

c. I have confirmed to the norms and guidelines given in the ethical code of conduct of the institute.

d. Whenever I have used materials (data, theoretical analysis, and text) from other sources, I have given due credit to them by citing them in the text of the thesis and giving their details in the references.

Prakash Kumar Palei

Signature of the Student

CERTIFICATE

This is to certify that the thesis entitled "**STRUCTURAL AND ELECTRICAL PROPERTIES OF CONVENTIONAL AND MICROWAVE PROCESSED LEAD FREE KNN BASED CERAMICS**" submitted by **Prakash Kumar Palei** to the National Institute of Technology, Rourkela for the award of the degree of Doctor of Philosophy is a bonafide record of research work carried out by him under my supervision. In my opinion, the work fulfills the requirements for which it is being submitted. The contents of the thesis, in full or in parts, have not been submitted to any other Institute or University for the award of any degree.

(Signature of Supervisor)

Dr. Pawan Kumar, Associate Professor

Department of Physics,

National Institute of Technology, Rourkela-769008

ACKNOWLEDGEMENTS

I would like to express my deep and sincere appreciation to my supervisor, Dr. Pawan Kumar, Department of Physics, NIT Rourkela for giving me the opportunity to work on this research project. He provided me the scope to follow my thoughts and work independently to develop my scientific skills. He was always available for me to give helpful guidance and strong support whenever I was needed. Not only in academics but also in my personal life he had made a great influence on me. I was the most fortunate to have him as my supervisor. Especially, I would like to express my most sincere gratitude to Dr. Mukesh Goel and Sonia Madam who have motivated me through all these years for all the support, advices and inspirations.

My many thanks also go to my DSC committee members, Dr. S. Jena, Dr. D. K. Bisoyi and Dr. K. K. Mohapatra, for their valuable suggestions and encouragement during the course of this work.

I am grateful to all my friends and juniors of Electroceramic Laboratory research group of the Department of Physics, both past and present, for their wonderful help, support and friendship during the course of my work. Especially, I would like to thank Miss Sridevi Swain for her timely help and cooperation.

I also express my gratitude for all the members of the Department of Physics for their great support. Especially, I am thankful to all my friends who made my stay at NIT Rourkela, a memorable one.

Finally, I would like to express my deepest appreciation to my family members, especially my brother, Prasanna, who has never stopped giving me support and hope that held me through all the difficult and demanding times during my personal and academic career.

ABSTRACT

Due to their excellent piezoelectric and ferroelectric properties lead oxide based ceramics, generally represented by lead zirconate titanate [$PbZr_xTi_{1-x}O_3$]/ (PZT), are the most widely used materials for piezoelectric actuators, sensors and transducers applications. Considering lead toxicity, there is an urgent need to develop effective lead-free ferroelectric systems, which are biocompatible and environmental friendly in nature. Several classes of materials are now being reconsidered as potentially attractive alternatives to PZT based systems. The solid solution of potassium niobate and sodium niobate, (1-*x*)$KNbO_3$–*x*$NaNbO_3$, was found to exhibit better piezoelectric properties around the MPB at *x*~0.5, which separates two orthorhombic ferroelectric phases. Therefore, $K_{0.5}Na_{0.5}NbO_3$ (KNN) has been recognized as one of the most promising host materials for new lead-free piezoelectrics. However, the piezoelectric properties of KNN ceramics are not comparable to PZT ceramics. Moreover, the proper densification of KNN ceramics, synthesized by conventional process is very difficult. The presence of volatile alkali elements further makes the sintering of KNN ceramics difficult. In order to solve these problems researchers have tried to make solid solution of KNN system with other systems. $LiSbO_3$ (LS) modification in KNN based ceramics improves the piezoelectric properties as well as the sintering behavior and makes them comparable to lead based systems. The enhanced piezoelectric and ferroelectric properties in KNN-LS ceramics are due to the presence of the orthorhombic to tetragonal (T_{O-T}) polymorphic phase transition (PPT) temperature close to room temperature. The role of PPT in KNN-LS ceramics is similar to the MPB in PZT based systems. However, the MPB in PZT based systems is nearly independent of temperature and exists over a broad temperature range. Whereas in

KNN-LS based system it is dependent on temperature and maximum properties are obtained when the PPT occurs close to RT. Hence, poling temperature will have strong effect on the piezoelectric properties of KNN-LS based ceramics.

In this work, lead-free (1-x)[$K_{0.5}Na_{0.5}NbO_3$]-x[$LiSbO_3$] (x=0, 0.04, 0.05 and 0.06)/(KNN-LS) ceramics were prepared by conventional solid-state reaction (CSSR) route. For dense morphology, pure KNN ceramics were sintered at 1120^oC for 4h, whereas in LS modified KNN ceramics dense morphology was obtained at 1080^oC for 4h. The structural study at room temperature (RT) revealed the transformation of pure orthorhombic to tetragonal structure with the increase in LS content in (1-x)KNN-(x)LS ceramics. Temperature dependent dielectric study confirmed the increase of diffuse phase transition nature with the increase in LS content in KNN-LS ceramics. The presence of orthorhombic to tetragonal (T_{O-T}) polymorphic phase transition temperature (PPT) ~43^oC confirmed the existence of two ferroelectric (orthorhombic and tetragonal) phases in 0.95KNN-0.05LS ceramics at RT. 0.95KNN-0.05LS ceramics showed better ferroelectric and piezoelectric properties i.e., remnant polarization (P_r) ~ 18.7 μC/cm^2, coercive field (E_c) ~ 11.8 kV/cm, piezoelectric coefficient (d_{33}) ~ 215 pC/N, planar mode coupling coefficient (k_p) ~ 0.415 and remnant strain ~0.07% were obtained. These properties are still lower than the PZT based ceramics. In order to further improve the piezoelectric properties the effect of Ag, Ta and V doping in 0.95KNN-0.05LS system has been investigated in detail. It was found that the substitution of Ag^+ ions in place of $(K_{0.5}Na_{0.5})^+$ ions in 0.95[$(K_{0.5}Na_{0.5})_{(1-x)}Ag_xNbO_3$]-0.05$LiSbO_3$ / KNAN-LS system initially decreased the piezoelectric and ferroelectric properties but for *x*=0.06 improvement in the piezoelectric and ferroelectric properties were obtained in comparison to the 0.95KNN-

0.05LS ceramics. The improved properties were discussed in terms of the structural changes occurred in the ceramics. Substitution of Ta^{+5} ions in place of Nb^{+5} ions in $0.95[(K_{0.5}Na_{0.5})Nb_{(1-x)}Ta_xO_3]$-$0.05LiSbO_3$/KNNT-LS ceramics increased the ferroelectric and piezoelectric properties without affecting the crystal structure of the ceramics. The KNNT-LS ceramics with x=0.02 exhibited maximum ferroelectric and piezoelectric properties. Moreover, the piezoelectric properties were found to be nearly independent of temperature up to ~ 200^{o}C, which is a good characteristic requirement for the ceramic to be used in high temperature piezoelectric applications. In order to improve the sintering behavior of the ceramics, V^{+5} has been substituted on the Nb^{+5} site of the $0.95[(K_{0.5}Na_{0.5})Nb_{(1-x)}V_xO_3]$-$0.05LiSbO_3$/KNNV-LS ceramics. The sintering temperature was drastically reduced with the increase in V^{+5} content, whereas the electrical properties also decreased significantly. Among all the V^{+5} doped ceramics, maximum piezoelectric and ferroelectric properties were obtained in case of KNNV-LS ceramics with x=0.06.

It is well known from the previous reports on different piezoelectric ceramics that microwave (MW) processing of ceramics could be an effective way to enhance the densification behavior as well the electrical properties. To further enhance the density and the electrical properties of $0.95[K_{0.5}Na_{0.5}NbO_3]$-$0.05[LiSbO_3]$, $0.95[(K_{0.5}Na_{0.5})_{0.94}Ag_{0.06}NbO_3]$-$0.05LiSbO_3$, $0.95[(K_{0.5}Na_{0.5})Nb_{0.98}Ta_{0.02}O_3]$-$0.05LiSbO_3$, $0.95[(K_{0.5}Na_{0.5})Nb_{0.94}V_{0.06}O_3]$-$0.05LiSbO_3$ ceramics, these ceramics were synthesized by microwave processing technique. It was found that microwave processing of these ceramics not only saved the processing time but also improved the ferroelectric and piezoelectric properties in comparision to the conventionally processed ceramics. Among all the microwave processed ceramics, $0.95[(K_{0.5}Na_{0.5})Nb_{0.98}Ta_{0.02}O_3]$-$0.05LiSbO_3$

ceramic showed maximum ferroelectric and piezoelectric properties i.e., d_{33}~ 257 pC/N, P_r ~ 30.48 μC/cm^2, k_p ~ 0.48 and remnant strain ~ 0.10%.

The present work is reported in the following chapters:

This work is reported in eight chapters. First chapter covers the fundamentals of piezoelectricity, ferroelectricity, and literature reviews on sodium potassium niobate (KNN) based ceramics along with the motivation and objectives of the present work.

Chapter II describes about the detail of synthesis routes used and the investigated parameters.

Chapter III describes about the methodology of sample preparation and characterization techniques used for studying structural, micro-structural, dielectric, ferroelectric, piezoelectric properties and strain induced by electric field behaviors.

Chapter IV discusses about the structural, dielectric, ferroelectric and piezoelectric properties of (1-x)[$K_{0.5}Na_{0.5}NbO_3$]-x[$LiSbO_3$] ceramics.

Chapter V discusses about the structural, microstructural and density studies of Ag, Ta and V modified 0.95KNN-0.05LS ceramics.

Chapter VI discusses about the dielectric, ferroelectric & piezoelectric properties and strain induced by electric field behaviors of Ag, Ta and V modified 0.95KNN-0.05LS ceramics.

Chapter VII discusses about the synthesis & characterizations of modified KNN-LS compositions (synthesized by conventional process and showing better piezoelectric properties) namely: (i) 0.95[$K_{0.5}Na_{0.5}NbO_3$]-0.05[$LiSbO_3$]

(ii) $0.95[(K_{0.5}Na_{0.5})_{0.94}Ag_{0.06}NbO_3]$-$0.05LiSbO_3$ (iii) $0.95[(K_{0.5}Na_{0.5})Nb_{0.98}Ta_{0.02}O_3]$-$0.05LiSbO_3$ (iv) $0.95[(K_{0.5}Na_{0.5})Nb_{0.94}V_{0.06}O_3]$-$0.05LiSbO_3$ synthesized by microwave process.

Chapter VIII presents the conclusions of the present work and recommendations for future work in this field.

This work has resulted in the following publications:

List of Research Publications/Accepted/Communicated papers

[1] **P. Palei**, P. Kumar and S. Sonia, Temperature dependent electrical properties of $0.95[(K\ 0.5Na\ 0.5)_{(1-x)}Ag_xNbO_3]$-$0.05LiSbO_3$ceramics, J. Electroceram., (2012) 1 (In Press).

[2] **P. Palei** and P. Kumar, Effect of silver content on the phase transition and electrical properties of $0.95[(K_{0.5}Na_{0.5})NbO_3]$-$0.05LiSbO_3$ ceramics, Solid State Sci., 14, (2012) 1338.

[3] **P. Palei** and P. Kumar, Structural and Electrical Properties of Microwave Processed Ag modified KNN-LS Ceramics, J. Microwave. Power. EE., 46, (2012) 76.

[4] **P. Palei**, P. Kumar, Dielectric, Ferroelectric and Piezoelectric Properties of (1-x)$[K_{0.5}Na_{0.5}NbO_3]$-x$[LiSbO_3]$ Ceramics, J. Phys. Chem. Sol., 73, (2012) 827.

[5] **P. Palei** and P. Kumar, Role of Sintering temperature on the Phase stability and electrical properties of $0.94[(K_{0.5}Na_{0.5})NbO_3]$-$0.06LiSbO_3$ Ceramics, Jpn. J. Appl. Phys., 51, (2012) 011503.

[6] **Palei** and P. Kumar, Impedance spectroscopy and ac conductivity studies of ferroelectric $K_{0.5}Na_{0.5})NbO_3$ Ceramics, J. Adv. Dielectr., 1 (2011) 351.

[7] **P. Palei**, M. Pattanaik, P. Kumar, Effect of oxygen environment on the dielectric and

Ferroelectric properties of KNN ceramics, Ceram. Int., 38, **(**2011) 851-854.

[8] P. Kumar, **P. Palei**, Dielectric and Ferroelectric properties of Ag modified lead free 0.94[KNN]- 0.06[LS] ceramics, Integr. Ferroelectr., 121, (2010) 24-30.

[9] P. Kumar, **P. Palei**, Effect of Sintering Temperature on Ferroelectric Properties of $0.94(K_{0.5}Na_{0.5})NbO_3$-$0.06LNbO_3$ System, Ceram. Int., 36, (2010)1725-1729.

[10]P. Kumar, **P. Palei,** Synthesis and Characterization of Lead Free $(Na_{0.5}K_{0.5})NbO_3$ ceramics, AIP Proceedings, 1063, (2008) 217-221.

[11] **P. Palei** and P. Kumar, Tantalum modified 0.95KNN-0.05LS Ceramics with improved Piezoelectric Properties and Thermal Stability (Communicated).

[12] **P. Palei** and P. Kumar, Dielectric and Piezoelectric Properties of Microwave Processed $0.95[(K_{0.5}Na_{0.5})NbO_3]$- $0.05LiSbO_3$ Ceramics (communicated).

CONTENTS

Dedication *i*

Declaration *ii*

Certificate *iii*

Acknowledgement *iv*

Abstract *v*

List of Publications *ix*

Contents *xi*

List of Figures *xvii*

List of Tables *xxv*

List of Symbols and Abbreviations *xxvii*

CHAPTER- 1 Introduction and Literature Survey

1.1 Introduction 1

1.2 Symmetry of Materials 2

1.3 Piezoelectricity 5

1.4 Ferroelectricity 7

1.5 Phase Transition 10

1.6 Lead & Lead Free Piezoelectric Ceramics 12

1.7 $K_{1-x}Na_xNbO_3$/KNN Based Materials 16

1.8 Various Methods to Improve Piezoelectric Properties 19

1.8.1 Developing Solid Solutions Near MPB 19

1.8.2 Optimization of Poling Temperature 21

1.8.3 Microwave Processing 21

1.9 Objectives of This Work 24

References 25

CHAPTER -2 Synthesis Routes and Investigated Parameters

2.1 Introduction 29

2.2 Synthesis Process 29

2.2.1 Solid State Reaction Route 30

2.2.2 Microwave processing 31
2.3 Thermal Analysis 33
2.4 X-Ray Diffraction 34
2.5 Scanning Electron Microscopy (SEM) 37
2.6 Dielectric Polarization 38
2.6.1 Dipolar Polarization 38
2.6.2 Ionic Polarization 39
2.6.3 Electronic Polarization 40
2.6.4 Interfacial Polarization 41
2.7 Dielectric Properties 41
2.7.1 Dielectric Constant (ε_r) 41
2.7.2 Dielectric Loss (tanδ) 42
2.8 Diffuse Phase Transition 43
2.9 Ferroelectric Properties 44
2.10 Poling 46
2.11 Strain vs. Electric Field Behavior 47
2.12 Piezoelectric Parameters 48
2.12.1 Piezoelectric Charge Coefficients 48
2.12.2 Electromechanical Coupling Coefficient 49
References 52

CHAPTER-3 Experimental Details

3.1 Introduction 55
3.2 Conventional Processing 55
3.3 Microwave Processing 58
3.4 Investigated Parameters 61
3.4.1 Phase Evolution and Crystal Structural Study 61
3.4.2 Densification Study 62
3.4.3 Grain Morphology Study 63
3.5 Electroding of the Sample 63
3.6 Poling 63

3.7 Electrical Properties 64
3.8 Dielectric Measurements 65
3.9 Polarization vs. Electric Field (P-E) Measurements 65
3.10 Piezoelectric Constant (d_{33}) Measurements 67
3.11 Resonance and Anti-resonance Frequency Measurement 68
3.12 Strain vs. Electric Field Measurements 68
References 71

CHAPTER-4 Structural, Dielectric, Ferroelectric and Piezoelectric Properties of (1-*x*)[$K_{0.5}Na_{0.5}NbO_3$]-*x*[$LiSbO_3$] Ceramics

4.1. Introduction 72
4.2. Optimization of Calcination and Sintering Temperatures 73
4.2.1. Thermal Analysis 73
4.2.2 Single Perovskite Phase Formation 74
4.2.3 Sintering and density study 76
4.3 Morphology Study 77
4.4 Structural Study 78
4.5 Dielectric Properties 82
4.5.1 Temperature Dependence of Dielectric Constant (ε_r) and Dielectric Loss (tanδ) 82
4.6 Diffusivity Study 87
4.7 Poling Temperature Effect on Piezoelectric and Electromechanical Properties 89
4.8 Temperature Dependence of Electromechanical Properties 91
4.9 Strain vs. Electric Field Behavior 94
4.10 Ferroelectric Properties 95
4.11 Chapter Summary 97
References 98

CHAPTER-5 Structural and Microstructural Study of Ag, Ta and Modified

0.95[($K_{0.5}Na_{0.5}$)NbO_3] -0.05[$LiSbO_3$] Ceramics

5.1 Introduction 100

5.2 XRD Analysis 101

5.2.1 Ag Modified 0.95KNN-0.05LS Ceramics 101

5.2.2 Ta Modified 0.95KNN-0.05LS Ceramics 105

5.2.3 V Modified 0.95KNN-0.05LS Ceramics 108

5.3 Sintering and Densification Behavior 111

5.3.1 Ag Modified 0.95KNN-0.05LS Ceramics 111

5.3.2 Ta Modified 0.95KNN-0.05LS Ceramics 112

5.3.3 V Modified 0.95KNN-0.05LS Ceramics 113

5.4 Morphology Study 114

5.4.1 Ag Modified 0.95KNN-0.05LS Ceramics 114

5.4.2 Ta Modified 0.95KNN-0.05LS Ceramics 115

5.4.3 V Modified 0.95KNN-0.05LS Ceramics 116

References 118

CHAPTER-6 Dielectric, Ferroelectric and Piezoelectric Properties of Ag, Ta and V Modified 0.95[($K_{0.5}Na_{0.5}$)NbO_3] –0.05[$LiSbO_3$] Ceramics

6.1 Introduction 119

6.2 Dielectric Properties 120

6.2.1 Temperature Dependent Dielectric Constant (ε_r) and Dielectric Loss (tanδ) 120

6.2.1.1 0.95($K_{0.5}Na_{0.5}$)$_{(1-x)}Ag_xNbO_3$-0.05$LiSbO_3$(x=0, 0.02, 0.04, 0.06 and 0.08) Ceramics 120

6.2.1.2 0.95($K_{0.5}Na_{0.5}$)$Nb_{(1-x)}Ta_xO_3$-0.05$LiSbO_3$ (x=0.02, 0.04, 0.06 and 0.08) Ceramics 125

6.2.1.3 0.95($K_{0.5}Na_{0.5}$)$Nb_{(1-x)}V_xO_3$-0.05$LiSbO_3$ (x=0.02, 0.04, 0.06 and 0.08) Ceramics 129

6.3 Ferroelectric Properties 134

6.3.1 0.95($K_{0.5}Na_{0.5}$)$_{(1-x)}Ag_xNbO_3$-0.05$LiSbO_3$ / KNAN-LS (x=0, 0.02, 134

0.04, 0.06 and 0.08) Ceramics

6.3.2 $0.95(K_{0.5}Na_{0.5})Nb_{(1-x)}Ta_xO_3$-$0.05LiSbO_3$ / KNNT-LS (x=0.02, 0.04, 0.06 and 0.08) Ceramics 135

6.3.3 $0.95(K_{0.5}Na_{0.5})Nb_{(1-x)}V_xO_3$-$0.05LiSbO_3$ / KNNV-LS (x=0.02, 0.04, 0.06 and 0.08) Ceramics 135

6.4 Strain vs. Electric Field (S-E) Study 137

6.4.1 $0.95(K_{0.5}Na_{0.5})_{(1-x)}Ag_xNbO_3$-$0.05LiSbO_3$ / KNAN-LS (x=0, 0.02, 0.04, 0.06 and 0.08) Ceramics 137

6.4.2 $0.95(K_{0.5}Na_{0.5})Nb_{(1-x)}Ta_xO_3$-$0.05LiSbO_3$ / KNNT-LS (x=0.02, 0.04, 0.06 and 0.08) Ceramics 138

6.4.3 $0.95(K_{0.5}Na_{0.5})Nb_{(1-x)}V_xO_3$-$0.05LiSbO_3$ / KNNV-LS (x=0.02, 0.04, 0.06 and 0.08) Ceramics 138

6.5 Piezoelectric Properties 140

6.5.1 Poling Temperature Dependent Piezoelectric and Electromechanical Properties 140

6.5.1.1 $0.95(K_{0.5}Na_{0.5})_{(1-x)}Ag_xNbO_3$-$0.05LiSbO_3$ (x=0, 0.02, 0.04, 0.06 and 0.08) Ceramics 141

6.5.1.2 $0.95(K_{0.5}Na_{0.5})Nb_{(1-x)}Ta_xO_3$-$0.05LiSbO_3$ (x=0.02, 0.04, 0.06 and 0.08) Ceramics 142

6.5.1.3 $0.95(K_{0.5}Na_{0.5})Nb_{(1-x)}V_xO_3$-$0.05LiSbO_3$ (x=0.02, 0.04, 0.06 and 0.08) Ceramics 144

6.5.2 Temperature Dependent Piezoelectric Properties 145

References 147

CHAPTER-7 Study of Microwave Processed of KNN-LS Based Ceramics

7.1 Introduction 149

7.2 Optimization of Calcination and Sintering Time 150

7.2.1 $0.95[K_{0.5}Na_{0.5}NbO_3]$-$0.05[LiSbO_3]$ / KNN-LS Ceramics 150

7.2.2 $0.95[(K_{0.5}Na_{0.5})_{0.94}Ag_{0.06}NbO_3]$-$0.05[LiSbO_3]$ / KNA6N- LS Ceramics 150

7.2.3 $0.95[(K_{0.5}Na_{0.5})Nb_{0.98}Ta_{0.02}O_3]$-$0.05[LiSbO_3]$ / KNNT2-LS 151

Ceramics
7.2.4 $0.95[(K_{0.5}Na_{0.5})Nb_{0.98}V_{0.06}O_3]$-$0.05[LiSbO_3]$ / KNNV6-LS Ceramics 151
7.3 Sintering, Morphology and Density Study 154
7.3.1 $0.95[K_{0.5}Na_{0.5}NbO_3]$-$0.05[LiSbO_3]$ / KNN-LS Ceramics 154
7.3.2 $0.95[(K_{0.5}Na_{0.5})_{0.94}Ag_{0.06}NbO_3]$-$0.05[LiSbO_3]$ / KNA6N-LS Ceramics 156
7.3.3 $0.95[(K_{0.5}Na_{0.5})Nb_{0.98}Ta_{0.02}O_3]$-$0.05[LiSbO_3]$ / KNNT2-LS Ceramics 158
7.3.4 $0.95[(K_{0.5}Na_{0.5})Nb_{0.98}V_{0.06}O_3]$-$0.05[LiSbO_3]$ / KNNV6-LS Ceramics 160
7.4 Dielectric Study 161
7.4.1 Temperature Dependent Dielectric Constant (ε_r) 161
7.4.2 Temperature dependence Dielectric Loss ($\tan\delta$) 165
7.5 Ferroelectric Properties 169
7.6 Piezoelectric Properties 172
7.6.1 Strain-Electric Field (S-E) Loop Study 173
References 178
CHAPTER-8 Conclusions and Recommendations for Future Works
8.1 Conclusions 180
8.2 Recommendations for Future Works 183

List of Figures

		Page No.
	CHAPTER-1	
Fig.1.1	Schematic representation of the classification of Point groups.	3
Fig.1.2	(a)Directional axes for a plate and (b) for a thin disc.	6
Fig.1.3	Polarization-electric field (*P*-*E*) hysteresis loop.	8
Fig.1.4	Components of a ferroelectric hysteresis loop: (a) Dielectric,(b) Polarization Switching and (c) Leakage current.	9
Fig.1.5	Free energy (*G*) as a function of polarization (*P*) at various temperatures (*T*): (a) $T<TC$, (b) $T=TC$, and (c) $T>TC$.	11
Fig.1.5	(d) Typical variation of dielectric permittivity (ε_r) as a function of temperature for a normal ferroelectric.	11
Fig.1.6	Phase diagram of lead zirconate titanate.	12
Fig.1.7	Comparison of properties between PZT materials and lead-free materials: (a) dielectric permittivity as a function of Curie temperature; (b) piezoelectric coefficient as a function of temperature.	15
Fig.1.8	The number of publications per year on lead-free piezoceramics.	15
Fig.1.9	Phase diagram of the $KNbO_3$ - $NaNbO_3$ system.	17
Fig.1.10	Dielectric and electromechanical coupling coefficients of PZT ceramics near MPB.	20
Fig.1.11	Numbers of equivalent polar axes of ferroelectrics with different phases: (a) six [001] directions in tetragonal; (b) twelve [110] directions in orthorhombic; (c) eight [111] directions in rhombohedral structure.	21
Fig.1.12	Electromagnetic spectrum illustrating specifically the microwave range.	22
Fig.1.13	Heating patterns in conventional and microwave furnaces.	23
	CHAPTER-2	
Fig.2.1	Schematics of sintering process: (a) three grains before solid-state sintering, and (b) after sintering.	31

Fig.2.2	Historical perspective of sintering ceramics using microwave energy.	33
Fig.2.3	Bragg diffraction from a set of lattice planes with a spacing *d.*	35
Fig.2.4	Characteristic x-ray diffraction patterns for various symmetries showing the corresponding splitting with respect to the cubic (111), (200) and (220) reflections.	36
Fig.2.5	The interaction of an electron beam with a sample.	38
Fig.2.6	Schematic of the dipolar orientation process.	39
Fig.2.7	Schematic of the ionic polarization.	40
Fig.2.8	Ferroelectric P –E/ hysteresis loop.	44
Fig.2.9	Probable sequence of polarization switching in ferroelectrics.	45
Fig.2.10	Schematic illustration of the poling process.	46
Fig.2.11	Strain–electric field (S–E)/ hysteresis loop (butterfly loop) in piezoelectrics.	47
Fig.2.12	A typical impedance curve of the equivalent circuit for measuring the impedance frequencies.	50

CHAPTER-3

Fig.3.1	Conventional synthesis process flowchart.	57
Fig.3.2	Schematic diagram of microwave sintering system.	59
Fig.3.3	Microwave synthesis process flowchart.	60
Fig.3.4	Schematic of the corona discharge method.	64
Fig.3.5	Diagram of the Hioki 3532-50 LCR Hitester.	65
Fig.3.6	Schematic of the Sawyer–Tower circuit for the measurement of the polarization-electric field.	66
Fig.3.7	Schematic diagram for the d_{33} measurement.	67
Fig.3.8	A setup for the measurements of strain vs. electric filed loop (a) Fiber –optical probe tip configurations; (b) Displacement sensing mechanism of adjacent fiber-optical elements.	70

CHAPTER-4

Fig.4.1	TG and DTA curves of the raw KNN powders.	74
Fig.4.2	XRD patterns of pure KNN powders calcined at different	75

temperatures.

Fig.4.3 XRD patterns of (1-*x*) KNN-*x*LS powders calcined at 850 ^{o}C for 6 h. 75

Fig.4.4 Relative density of (1-x) KNN-xLS ceramics sintered at different temperatures. 77

Fig.4.5 SEM micrographs of (1-*x*)KNN-*x*$LiSbO_3$ ceramics sintered at optimum temperature. 78

Fig.4.6 XRD patterns of (1-*x*) KNN-*x*LS ceramics sintered at optimum temperature. 79

Fig.4.7 XRD patterns of (1-*x*)KNN-*x*$LiSbO_3$ ceramics in the 2θ range of 44.5–46.5 degrees. 81

Fig.4.8 Temperature dependence dielectric constant (ε_r) of (1-*x*)KNN-*x*$LiSbO_3$ ceramics sintered at optimum temperature for (a) *x*=0 (b) *x*=0.04 (c) *x*=0.05 and (d) *x*=0.06. 85

Fig.4.9 (a) Temperature dependence of dielectric constant (ε_r) at 1 MHz frequency of (1-*x*)KNN-*x*$LiSbO_3$ ceramics. 86

Fig.4.9 (b) Temperature dependence of the dielectric constant of (1-*x*)KNN-*x*$LiSbO_3$ceramics in a low temperature range. 86

Fig.4.10 Temperature dependence of dielectric loss (tanδ) at 1 MHz frequency of (1-*x*)KNN- *x*$LiSbO_3$ ceramics. 87

Fig.4.11 Plot of $\ln(1/\varepsilon_r - 1/\varepsilon_m)$ vs. $\ln(T-T_m)$ of (1-*x*)KNN-*x*$LiSbO_3$ ceramics at 1 MHz frequency. 88

Fig.4.12 (a) piezoelectric coefficients (d_{33}) and (b) Planar mode coupling coefficients (k_p) of (1-*x*)KNN-*x*$LiSbO_3$ ceramics as a function of poling temperature. 90

Fig.4.13 Temperature dependence of the Planar mode coupling coefficient (k_p) of (1-*x*)KNN-*x*$LiSbO_3$ ceramics. 91

Fig.4.14 Temperature dependence of the frequency constant (N_p) of (1-*x*)KNN-*x*$LiSbO_3$ ceramics. 93

Fig.4.15 Variations of $\Delta f_r / f_{r35°C}$ and $\Delta k_p/k_{p35°C}$ with temperature of (1-*x*)KNN-*x*$LiSbO_3$ ceramics. 94

Fig.4.16 Strain vs. electric field (S-E) loops of (1-*x*)KNN-*x*$LiSbO_3$ ceramics. 95

Fig.4.17 Polarization-electric field (P-E) hysteresis loops of (1-x)KNN-xLiSbO$_3$ ceramics. 96

CHAPTER-5

Fig.5.1 XRD patterns of KNAN-LS ceramics calcined at 850 ^{o}C for 6h. 103

Fig.5.2 XRD patterns of KNAN-LS ceramics sintered at 1080 ^{o}C for 4h. 103

Fig.5.3 Enlarged XRD patterns of KNAN-LS ceramics in the 2θ range of 44–47 degrees. 104

Fig.5.4 XRD patterns of KNNT-LS Ceramics calcined at 850 ^{o}C for 6h. 106

Fig.5.5 XRD patterns of KNNT-LS Ceramics sintered at 1080 ^{o}C for 4h (x=0 and 0.02), 1100 ^{o}C (x=0.04 and 0.06) and 1120^{o}C (x=0.08). 106

Fig.5.6 Enlarged XRD patterns of KNNT-LS ceramics in the 2θ range of 44–47 degrees. 107

Fig.5.7 XRD patterns of KNNV-LS Ceramics calcined at 850^{o}C for 6h. 109

Fig.5.8 XRD patterns of KNNV-LS Ceramics sintered at 1080^{o}C (x=0), 1050^{o}C (x=0.02), 1030 (x=0.04), 1010 (x=0.06) and 990^{o}C (x=0.08) for 4h. 109

Fig.5.9 Enlarged XRD patterns of KNNV-LS ceramics in the 2θ range of 44.5–46.5 degrees. 110

Fig.5.10 Relative density (RD) of KNAN-LS ceramics as a function of sintering temperature. 112

Fig.5.11 Relative density (RD) of KNAN-LS ceramics as a function of sintering temperature. 113

Fig.5.12 Relative density (RD) of KNNV-LS ceramics as a function of sintering temperature. 114

Fig.5.13 SEM micrographs of KNAN-LS ceramics sintered at 1080^{o}C for 4 h. 115

Fig.5.14 SEM micrographs of KNNT-LS ceramics sintered at 1080^{o}C (x=0 and 0.02), 1100^{o}C (x=0.04 and 0.06) and 1120^{o}C (x=0.08). 116

Fig.5.15 SEM micrographs of KNNV-LS ceramics sintered at 1080^{o}C (x=0), 1050^{o}C (x=0.02), 1030 (x=0.04), 1010 (x=0.06) and 990^{o}C (x=0.08) for 4h. 117

CHAPTER-6

Fig.6.1	Temperature dependent ε_r at various frequencies of KNAN-LS ceramics with (a) x=0 (b) x=0.02 (c) x=0.04(d) x=0.06 and (e) x=0.08 sintered at 1080^{o}C.	123
Fig.6.2	(a) Temperature dependent ε_r at 10 kHz frequency of KNAN-LS ceramics with (a) x=0 (b) x=0.02 (c) x=0.04 (d) x=0.06 and (e) x=0.08 sintered at 1080^{o}C.	124
Fig. 6.2	(b) Temperature dependence of dielectric loss (tanδ) at 10 kHz frequency of KNAN-LS ceramics with (a) x=0 (b) x=0.02 (c) x=0.04(d) x=0.06 and (e) x=0.08 sintered at 1080^{o}C.	124
Fig.6.3	Temperature dependent ε_r of KNNT-LS ceramics sintered at (a) x=0 (1080^{o}C) (b) x=0.02 (1080^{o}C) (c) x=0.04 (1100^{o}C) (d) x=0.06 (1100^{o}C) and (e) x=0.08 (1120^{o}C).	128
Fig.6.4	(a)Temperature dependence of dielectric constant (ε_r) at 10 kHz frequency of KNNT-LS ceramics sintered at x=0 (1080^{o}C), x=0.02 (1080^{o}C), x=0.04 (1100^{o}C), x=0.06 (1100^{o}C) and x=0.08 (1120^{o}C).	128
Fig. 6.4	(b) Temperature dependence of dielectric loss (tanδ) at 10 kHz frequency of KNNT-LS ceramics sintered at 1080^{o}C (x=0 and 0.02),1100^{o}C (x=0.04 and 0.06) and 1120^{o}C (x=0.08).	129
Fig.6.5	Temperature dependent ε_r of KNNV-LS ceramics sintered at (a) x=0.02 (1050^{o}C) (b) x=0.04 (1030^{o}C) (c) x=0.06 (1010^{o}C) and (d) x=0.08 (990^{o}C).	132
Fig. 6.6	(a) Temperature dependence of dielectric constant (ε_r) at 10 kHz frequency of KNNV-LS ceramics sintered at 1050^{o}C (x=0.02), 1030^{o}C (x=0.04), 1010^{o}C (x=0.06) and 990^{o}C (x=0.08).	133
Fig. 6.6	(b) Temperature dependence of dielectric loss (tanδ) at 10 kHz frequency of KNNV-LS ceramics sintered at 1050^{o}C (x=0.02), 1030^{o}C (x=0.04), 1010^{o}C (x=0.06) and 990^{o}C (x=0.08).	133
Fig. 6.7	P-E Hysteresis loops of KNAN-LS ceramics sintered at 1080^{o}C for 4h.	136
Fig. 6.8	P-E Hysteresis loops of KNNT-LS ceramics sintered at 1080^{o}C (x=0 and 0.02), 1100^{o}C (x=0.04 and 0.06) and 1120^{o}C (x=0.08).	136

Fig. 6.9 P-E Hysteresis loops of KNNV-LS ceramics sintered at 1050^{o}C (x=0.02), 1030^{o}C (x=0.04), 1010^{o}C (x=0.06) and 990^{o}C (x=0.08). 137

Fig.6.10 (S−E) loops of KNAN-LS ceramics sintered at 1080^{o}C. 139

Fig.6.11 (S−E) loops of KNNT-LS ceramics sintered at sintered at 1080^{o}C (x=0 and 0.02), 1100^{o}C (x=0.04 and 0.06) and 1120^{o}C (x=0.08). 139

Fig.6.12 (S−E) loops of KNNV-LS ceramics sintered at 1080^{o}C (x=0), 1050^{o}C (x=0.02), 1030^{o}C (x=0.04), 1010^{o}C (x=0.06) and 990^{o}C (x=0.08). 140

Fig.6.13 k_p and d_{33} piezoelectric coefficients as a function of poling temperature of KNAN-LS ceramics sintered at 1080^{o}C. 142

Fig.6.14 k_p and d_{33} piezoelectric coefficients as a function of poling temperature of KNNT-LS ceramics sintered at 1080^{o}C (x=0 and 0.02), 1100^{o}C (x=0.04 and 0.06) and1120^{o}C (x=0.08). 143

Fig.6.15 k_p and d_{33} piezoelectric coefficients as a function of poling temperature of KNNV-LS ceramics sintered at 1080^{o}C (x=0), 1050^{o}C (x=0.02), 1030^{o}C (x=0.04), 1010^{o}C (x=0.06) and 990^{o}C (x=0.08). 145

Fig.6.16 Temperature dependent k_p coefficients of KNN-LS, KNAN-LS (x=0.06), KNNT-LS (x=0.02) and KNNV-LS (x=0.06) ceramics. 146

CHAPTER-7

Fig. 7.1 XRD patterns of MW processed KNN-LS ceramics calcined at 850 ^{o}C for 20, 40 and 60mins. 152

Fig. 7.2 XRD patterns of MW processed KNA6N-LS ceramics calcined at 850 ^{o}C for 20, 40 and 60 mins. 152

Fig. 7.3 XRD patterns of MW processed KNNT2-LS ceramics calcined at 850 ^{o}C for 20, 40 and 60 mins. 153

Fig. 7.4 XRD patterns of MW processed KNNV6-LS ceramics calcined at 850^{o}C for 20, 40 and 60 mins. 153

Fig. 7.5 SEM micrographs of MW processed KNN-LS ceramics. 154

Fig. 7.6 Relative density (RD) of KNN-LS ceramics as a function of sintering time. 155

Fig. 7.7 SEM micrographs of MW processed KNA6N-LS Ceramics. 156

Fig. 7.8	Relative density (RD) of KNA6N-LS Ceramics as a function.	157
Fig. 7.9	SEM micrographs of MW processed KNNT2-LS Ceramics.	158
Fig.7.10	Relative density (RD) of KNNT2-LS Ceramics as a function of sintering time.	159
Fig.7.11	SEM micrographs of MW processed KNNV6-LS Ceramics.	160
Fig.7.12	Relative density (RD) of KNNV6-LS Ceramics as a function of sintering time.	161
Fig.7.13	Temperature variation of ε_r for KNN-LS ceramics sintered at 1080^{o}C for 20 mins.	163
Fig.7.14	Temperature variation of ε_r for KNA6N-LS ceramics sintered at 1080^{o}C for 20 mins.	164
Fig.7.15	Temperature variation of ε_r for KNNT2-LS ceramics sinetered at 1080^{o}C for 30 mins.	164
Fig.7.16	Temperature variation of ε_r for KNNV6-LS ceramics sintered at 1010^{o}C for 20 mins.	165
Fig.7.17	Temperature dependence of dielectric loss (tanδ) of the microwave processed KNN-LS ceramics at various frequencies.	166
Fig.7.18	Temperature dependence of dielectric loss (tanδ) of the microwave processed KNA6N-LS ceramics at various frequencies.	167
Fig.7.19	Temperature dependence of dielectric loss (tanδ) of the microwave processed KNNT2-LS ceramics at various frequencies.	167
Fig.7.20	Temperature dependence of dielectric loss (tanδ) of the microwave processed KNNV6-LS ceramics at various frequencies.	168
Fig.7.21	(a) PE-Hysteresis loop of KNN-LS ceramics sintered at 1080^{o}C for 20 mins.	170
Fig.7.21	(b) PE-Hysteresis loop of KNA6N-LS ceramics sintered at 1080^{o}C for 20 mins.	170
Fig.7.21	(c) PE-Hysteresis loop of KNNT2-LS ceramics sintered at 1080^{o}C for 30 mins.	171
Fig.7.21	(d) PE-Hysteresis loop of KNNV6-LS ceramics sintered at 1010^{o}C for 20 mins.	171

Fig.7.22 S-E hysteresis loops of (a) KNN-LS ceramics sintered at 1080^{o}C for 20 mins (b) KNA6N-LS ceramics sintered at 1080^{o}C for 20 mins (c) KNNT2-LS ceramics sintered at 1080^{o}C for 30 mins and (d) KNNV6-LS ceramics sintered at 1010^{o}C for 20 mins. 176

List of Tables

		Page No.
Table-2.1	Sample geometries for measurement of material Properties.	51
Table-4.1	Structure and unit cell parameters of (1-*x*)KNN-*x*$LiSbO_3$ Ceramics.	81
Table-4.2	Electrical and physical properties of (1-*x*)($Na_{0.5}K_{0.5}$)NbO_3–*x*$LISbO_3$ ceramics with *x* = 0-0.06.	96
Table-5.1	Structure and unit cell parameters of KNAN-LS ceramics sintered at 1080^oC for 4h.	104
Table-5.2	Structure and unit cell parameters of KNNT-LS ceramics sintered at 1080^oC for 4h (*x*=0 and 0.02), 1100^oC (*x*=0.04 and 0.06) and 1120^oC (*x*=0.08).	107
Table-5.3	Structure and unit cell parameters of KNNV-LS ceramics sintered at sintered at 1080^oC (*x*=0), 1050^oC (*x*=0.02), 1030 ^oC (*x*=0.04), 1010 ^oC (*x*=0.06) and 990^oC (*x*=0.08) for 4h.	110
Table-6.1	ε_r ,tanδ, T_c and T_{O-T} of KNAN-LS ceramics at 10 kHz frequency sintered at 1080^oC.	125
Table-6.2	ε_r ,tanδ, and Tc at 10 kHz frequency of KNNT-LS ceramics sintered at 1080^oC (*x*=0 and 0.02), 1100^oC (*x*=0.04 and 0.06) and 1120^oC (*x*=0.08).	129
Table-6.3	ε_r ,tanδ, and Tc of KNNV-LS ceramics at 10 kHz frequency sintered at 1050^oC (*x*=0.02), 1030^oC (*x*=0.04), 1010^oC (*x*=0.06) and 990^oC (*x*=0.08).	134
Table-6.4	k_p, d_{33} and P_r values of KNAN-LS ceramics sintered at 1080^oC.	142
Table-6.5	k_p,d_{33} and P_r values of KNNT-LS ceramics sintered at 1080^oC (*x*=0 and 0.02), 1100^oC (*x*=0.04 and 0.06) and 1120^oC (*x*=0.08).	144
Table-6.6	k_p,d_{33} and P_r values of KNNV-LS ceramics sintered at 1080^oC (*x*=0), 1050^oC (*x*=0.02), 1030^oC (*x*=0.04), 1010^oC (*x*=0.06) and 990^oC (*x*=0.08).	145

Table-7.1	ε_r , tanδ and T_c of Conventional and microwave processed ceramics.	168
Table-7.2	Comparison between ferroelectric Properties of microwave and conventional processed KNN-LS, KNA6N-LS, KNNT2-LS and KNNV6-LS ceramics.	172
Table-7.3	Comparison between the various properties of microwave and conventionally processed KNN-LS, KNAN-LS, KNNT-LS and KNNV-LS ceramics.	173
Table-7.4	Remnant strain and max. strain of microwave and conventionally processed Ceramics.	177

LIST OF SYMBOLS AND ABBREVIATIONS

PZT……..	$Pb(Zr_{0.52}Ti_{0.48})O_3$
KNN…….	$K_{0.5}Na_{0.5}NbO_3$
KNN-LS……...	$(1-x)[K_{0.5}Na_{0.5}NbO_3]- x[LiSbO_3]$
KNAN-LS……	$0.95[(K_{0.5}Na_{0.5})_{(1-x)}Ag_xNbO_3]- x[LiSbO_3]$
KNNT-LS…….	$0.95[(K_{0.5}Na_{0.5})Nb_{(1-x)}Ta_xO_3]- x[LiSbO_3]$
KNNV-LS……	$0.95[(K_{0.5}Na_{0.5})Nb_{(1-x)}V_xO_3]- x[LiSbO_3]$
d_{33}.....	Piezoelectric coefficient
E_C.....	Coercive field
ε_r……	Dielectric Constant
RT……..	Room temperature
f_a…….	Anti-resonance frequency
Fr……	Resonance frequency
Kp……...	Electromechanical coupling factor
MPB……...	Morphotropic phase boundary
Pr……	Remnant polarization
PMN-PT…….	$Pb(Mg_{1/3}Nb_{2/3})O_3$-$PbTiO_3$
SEM……...	Scanning electron microscope
tanδ……	Dielectric loss

T_{O-T}…….	Orthorhombic to tetragonal phase transition
PPT…….	Polymorphic phase transition temperature
T_c……	Curie temperature
T_p……	Poling temperature
N_p……...	Frequency Constant
XRD……...	X-ray diffraction
TGA……...	Thermogravimetric analysis
DTA……...	Differential thermal analysis
DFT……	Diffuse phase transition
a, b , c…….	Unit cell parameter
γ……..	Diffusivity
CSSR……..	Conventional solid state reaction
CP……	Conventional processing
MW…….	Microwave

CHAPTER-1

Introduction & Literature Survey

1.1 Introduction

A ceramic is an inorganic, nonmetallic solid prepared by heating and subsequent cooling. The word ceramic is derived from the Greek word “keramos” which means to burn. The earliest ceramics were pottery objects made from clay and hardened in fire. Ceramic materials may have a crystalline structure, with long range ordering on an atomic scale. Ceramics have traditionally been admired and used for their mechanical, thermal and chemical stability but their unique electrical and optical properties have become of increasing importance in many electronic applications. These materials are called as electroceramics and used primarily for its electrical properties. Historically, developments in various subclasses of electroceramics have paralleled the growth of new technologies. These examples include: piezoelectrics- sonar, radar, actuators and sensors; ferroelectrics- high dielectric constant capacitors, non-volatile memories; and pyroelectrics- IR detectors. Ferroelectric ceramics were discovered in the 1940's in polycrystalline barium titanate ($BaTiO_3$) ceramics, since then, there has been a continuous succession of new materials and technology developments that have led to a significant number of industrial and commercial applications [1]. A huge leap in the research on ferroelectric materials came in the 1950's, leading to the widespread use of barium titanate ($BaTiO_3$) based ceramics in capacitor applications and piezoelectric transducer devices. Since then, many other ferroelectric ceramics including lead titanate ($PbTiO_3$), lead zirconate titanate (PZT), lead lanthanum zirconate titanate (PLZT), and relaxor ferroelectrics like lead magnesium niobate (PMN) have been developed and

utilized for a variety of applications. With the development of ceramic processing and thin film technology, many new applications have also emerged. The biggest use of ferroelectric ceramics have been in the areas such as dielectric ceramics for capacitor applications, ferroelectric thin films for non- volatile memories, piezoelectric materials for medical ultrasound imaging and actuators, and electro-optic materials for data storage and displays [2].

1.2 Symmetry of Materials

Symmetry of the material, whether it is a crystal, a thin film, a polycrystalline or an amorphous material, affects its physical properties. According to Neumann's principle, symmetry elements of all physical properties of a material must include all symmetry elements of the point group of that material. In other words, if a physical property is subjected to a symmetry element of the material, this property should not change its value [3]. It also follows from the Neumann's principle that some properties (such as dielectric permittivity, elastic compliance and electrostriction) are present in all materials and that other properties (such as piezoelectricity and pyroelectricity) can exist only in materials with certain symmetries. Moreover, the symmetry requirements may significantly reduce the number of non-zero and independent elements of a property tensor. According to Neumann's principle, the symmetry of a crystal's internal structure is reflected in the symmetry of its external properties. The elements of symmetry that are utilized by crystallographers to define symmetry about a point in space, e.g., the central point of a unit cell, are (1) a center of symmetry, (2) axes of rotation, (3) mirror planes, and (4) combinations of these [4]. All crystals can be divided into 32 different classes or point groups utilizing these symmetry elements, as shown in Fig. 1.1. These 32 point

groups are subdivisions of seven basic crystal systems that are, in order of ascending symmetry, tri-clinic, monoclinic, orthorhombic, tetragonal, rhombohedral (trigonal), hexagonal, and cubic. Out of these 32 point groups, 21 classes are noncentrosymmetric (a necessary condition for piezoelectricity to exist).

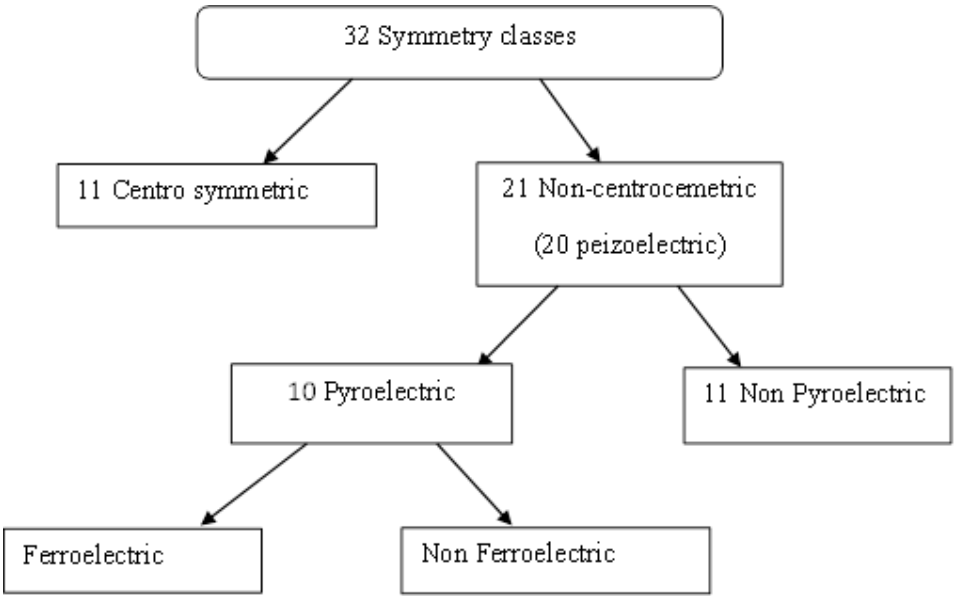

Fig.1.1 Schematic representation of the classification of point groups.

Out of these 21 noncentrosymmetric classes, 20 exhibit piezoelectric effect. One class, although lacking a center of symmetry, is not piezoelectric because of the presence of the other combined symmetry elements. A lack of a center of symmetry is all-important for the presence of piezoelectricity. When one considers that a homogeneous stress is centrosymmetric and cannot produce an unsymmetric result, such as a vector-quantity-like polarization, unless the material lacks a center of symmetry, whereby a net movement of the positive and negative ions with respect to each other (as a result of the stress) produces electric dipoles, i.e., polarization. Therefore, only 20 classes of non-

centrosymmetric crystals would exhibit piezoelectric effects. 10 of the piezoelectric point groups possess a unique polar axis and may exhibit, in the absence of an external electric field, a spontaneous polarization vector, P_S, and the pyroelectric effect along this unique axis. These 10 polar point groups are: 1, 2, m, 2mm, 4,4mm, 3, 3m, 6, and 6mm. There is a subgroup within these 10 classes that possesses spontaneous polarization which is reversible by an electric field of some magnitude less than the dielectric breakdown of the material itself, are called ferroelectrics. These materials also exhibit pyroelectric and piezoelectric effect.

Properties of a ceramic with random orientation of crystallites (or grains) are, for example, identical in all directions and may be described by introducing the symmetry axis of an infinite order [5], whose symbol is ∞. A symmetry axis of order ∞ means that material may be rotated by any angle around such an axis without changing its properties. The rotation axis of an isotropic cylinder, for example, is a ∞ axis. The point groups which contain infinity symmetry axes are called the limit groups of symmetry or Curie groups. There are seven Curie groups and all 32 crystallographic point groups are subsets of the Curie groups. Ceramic materials with a random orientation of grains possesses spherical symmetry, ∞∞m, which is centrosymmetric, and cannot exhibit a piezoelectric effect even if the symmetry of each grain belongs to one of the piezoelectric or polar point groups. If the ceramic is, however, ferroelectric, the spontaneous polarization direction in each grain may be reoriented by an external electric field in the direction of the field. Such a poled or polarized ceramic possesses symmetry of a cone, ∞m, and exhibits both piezoelectric and pyroelectric effects. The matrices of the elastic compliance, dielectric susceptibility, piezoelectric, electrostrictive and pyroelectric

coefficients of poled ferroelectric polycrystalline materials with randomly oriented grains have the same nonzero matrix elements as crystals that belong to point group 6mm.

1.3 Piezoelectricity

Since the discovery of piezoelectricity in 1880 by Jacques and Pierre Curie, the piezoelectric effect has successfully found industrial and commercial applications including sonar, transducers, medical ultrasound, actuators, and micro-positioners [1]. It is also the basis of a number of scientific techniques with atomic scale motion, such as the scanning probe microscopies, as well as more mundane uses including gas ignitors, microphones, and ink jet printers. Piezoelectricity, a property possessed by a select group of materials, describes the effect of mechanical stress on the generation of electrical charge (direct) or a deformation due to the applied electric field (converse). This inter convertible behavior was first discovered by Pierre and Jacques Curie in 1880 in certain crystals, such as quartz, zinc blends, tourmaline, and Rochelle salt. The term *piezoelectricity* has been used by scientists since 1881 to distinguish the piezoelectric phenomena from electrostriction. The piezoelectric phenomenon occurs in both the ferroelectric and the non-ferroelectric states.

The direct and converse piezoelectric effects can be described by the following equations [6]:

$$D_i = d_{ijk} X_{jk} \text{ (Direct effect)} \qquad (1.1)$$

$$S_{ij} = d_{kij} E_k \text{ (Converse effect)} \qquad (1.2)$$

where X_{ij} is the stress applied to a piezoelectric material, and D_i is the induced charge density, E_k is the electric field applied, and S_{ij} is the strain developed in the piezoelectric

material, and d_{ijk} and d_{kij} are piezoelectric coefficients with units of C/N and m/V, respectively. Both d_{ijk} and d_{kij} are third-rank tensors, however, these piezoelectric coefficients for the direct and converse effects are thermodynamically identical. Equations 1.1 and 1.2 can be simplified and may be expressed in the reduced notation form [4]:

$$D_i=d_{im}X_m \qquad (1.3)$$

$$S_m=d_{mi}E_i \qquad (1.4)$$

Where values of i=1, 2, or 3 and values of m=1, 2, 3, 4, 5, or 6, which are directional values, because all of the properties in the above equations are directional properties [1]. The values of i and m indicates about the geometries under which the properties are measured. For example, d_{31} can be measured when the induced polarization is generated in direction 3 due to a stress applied in direction 1, or when the induced strain is in direction 3 due to an electric field applied in direction 1. Whereas, d_{33} can be measured when the induced polarization is generated in direction 3 (parallel to the direction in which the ceramic element is polarized) and the stress is also applied in the same direction, or the induced mechanical strain in direction 3 when the electric field is also imposed in the same direction. The situation for the d_{31} and d_{33} measurement are shown in Fig.1.2(a) and (b) respectively.

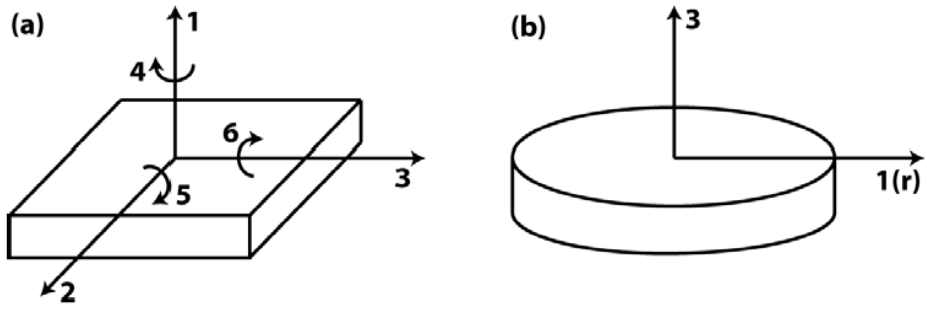

Fig. 1.2 (a) Directional axes for a plate, and (b) for a thin disc.

High piezoelectric coefficients are desirable in order to increase the charge or strain developed per force or electric field applied and will be applicable for sonar and transducer applications.

1.4 Ferroelectricity

The term *ferroelectrics* arose by analogy with ferromagnetics, mainly because they have similar characteristics: under electric fields for ferroelectric phenomena and under magnetic fields for ferromagnetic phenomena. The prefix *ferro-* derived from *ferum*, which means iron in Latin. The term is perfect for ferromagnetics, since all ferromagnetic phenomena are associated with the special type of spin arrangement of the iron atoms. But in ferroelectrics there are no iron atoms, so the prefix does not mean iron. Rather, it implies the similarity in characteristics to ferromagnetics. Like ferromagnetics, ferroelectrics exhibit a spontaneous electric polarization below the Curie temperature (T_c), a hysteresis loop, and an associated mechanical strain. However, ferroelectrics differ from ferromagnetics in their fundamental mechanisms and also in some of their applications. In a sense, ferroelectrics are the electrical analog of the ferromagnets, hence the name. The spontaneous polarization (P_s) is the so-called order parameter of the ferroelectric state. In Europe, ferroelectrics are sometimes called *Seignette electrics*. The names Seignette-electrics or Rochelle-electrics, which are also widely used, are derived from the name of the first substance found to have this property, Seignette salt or Rochelle salt. This term is somewhat misleading, because Seignette did not discover the ferroelectric phenomena. Instead, in 17^{th} century Rochelle, France, he discovered Rochelle salt (potassium-sodium tartrate–tetrahydrate, $KNaC_4H_4O_{6–4}$ H_2O), a colorless

crystalline compound with an orthorhombic structure. At that time, the material was used as a laxative. More than 200 years later, in 1921, Valasek discovered the ferroelectric phenomena in the same material [7,8]. Ferroelectrics were discovered much later than ferromagnetics. There are now more than 1,000 solid materials possessing ferroelectric properties.

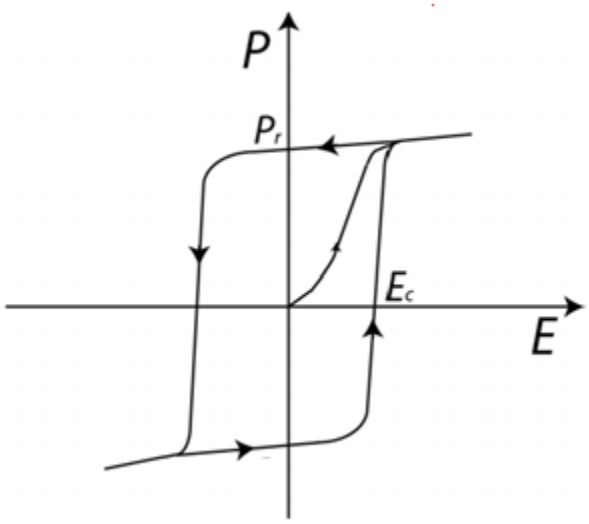

Fig. 1.3 polarization-electric field (*P*-*E*) hysteresis loop.

Ferroelectrics are defined as materials that exhibit spontaneous polarization (*Ps*) and the direction of *Ps* can be switched between two or more equilibrium symmetry equivalent states by the application of an appropriate electric field less than the breakdown strength of the material [9]. A ferroelectric crystal generally has certain regions with uniform alignment of electric dipoles, and the spontaneous polarization in such regions may be different from one another [10]. Such regions with uniform polarization are called ferroelectric domains, which form to minimize the electrostatic energy of depolarizing fields and elastic energy associated with the mechanical constraints to which the ferroelectric material is subjected as it is cooled through the paraelectric-ferroelectric phase transition. Ferroelectric materials are characterized by the development of

hysteresis loop, which displays the variation of polarization (P) as a function of applied electric field (E). As shown in Fig. 1.3, when a relatively small electric field is first applied to a ferroelectric material, it behaves like a normal dielectric and displays a linear response between polarization and electric field.

(a) Dielectric (b) Polarization Switching (c) Leakage Current

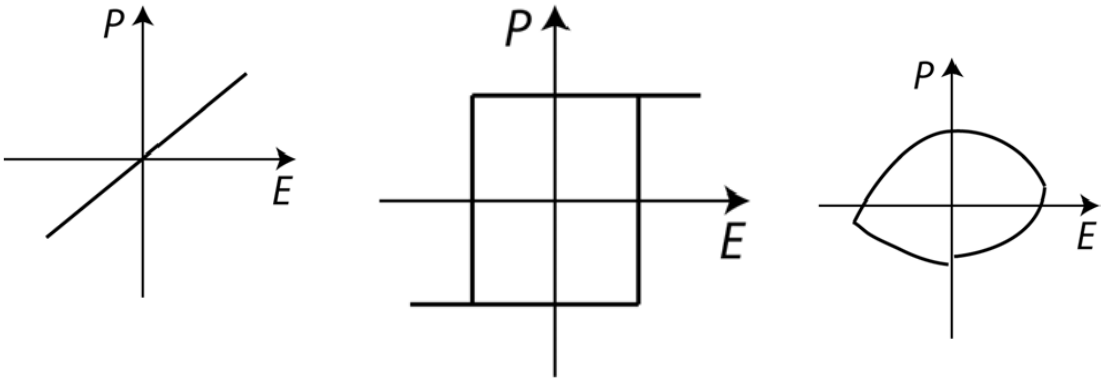

Fig. 1.4 Components of a ferroelectric hysteresis loop: (a) Dielectric, (b) Polarization Switching and (c) Leakage current (schematic).

However, as the field increases, domains begin to orient in the direction of the applied field, which results in a rapid increase in the polarization until all the domains are aligned. When the external electric field is reversed, some polarization returns to the original state, however, a large component remains in the direction of the previously applied field, exhibiting a remnant polarization (P_r) at zero electric field. As the field is reversed, the polarization can be completely reversed back to zero. The field at which it occurs is called as the coercive field (E_c). The polarization can be saturated once again in the opposite direction by increasing the field in the reverse direction. The loop can be completed by then switching the direction of the applied field. The electric polarization obtained from ferroelectric materials may be due to the result of three major

contributions: (1) a dielectric contribution, (2) a polarization (domain) switching contribution, and/or (3) a leakage current contribution. Fig. 1.4 shows the respective P-E hysteresis loops that are produced as a result of each contribution. The dielectric contribution produces a polarization that is directly proportional to the external electric field, resulting in a linear relationship (Fig. 1.4(a)), the polarization switching contribution exhibits a rectangular loop (Fig. 1.4(b)), and the leakage contribution displays an ellipse like loop (Fig. 1.4(c)). Since each of these contributions exhibits different P-E hysteresis loops, hence, the shape of the loop for different materials will vary with the amount and type of contributions present in the material.

1.5 Phase Transition

The spontaneous polarization of ferroelectric materials is exhibited over a certain temperature range specific to each material. Within this temperature range the material undergoes various structural phase transitions. The temperature at which the material changes from a ferroelectric, polar and non-centrosymmetric phase to a paraelectric, nonpolar and centrosymmetric phase, is called the Curie temperature (T_C). Since, the material is centrosymmetric and non-polar above the T_C, there are no possible polarization states available and the material doesn't exhibit spontaneous polarization or the ferroelectric effect, which is shown in Fig.1.5 (c). Below T_C, the structure becomes distorted, the symmetry of the paraelectric structure breaks and multiple polarization states becomes available and the ferroelectric phenomenon starts appearing in the material. Near the Curie point or phase transition temperature, thermodynamic properties including dielectric, elastic, optical, and thermal constants show an anomalous behavior, shown in Fig. 1.5 (d).

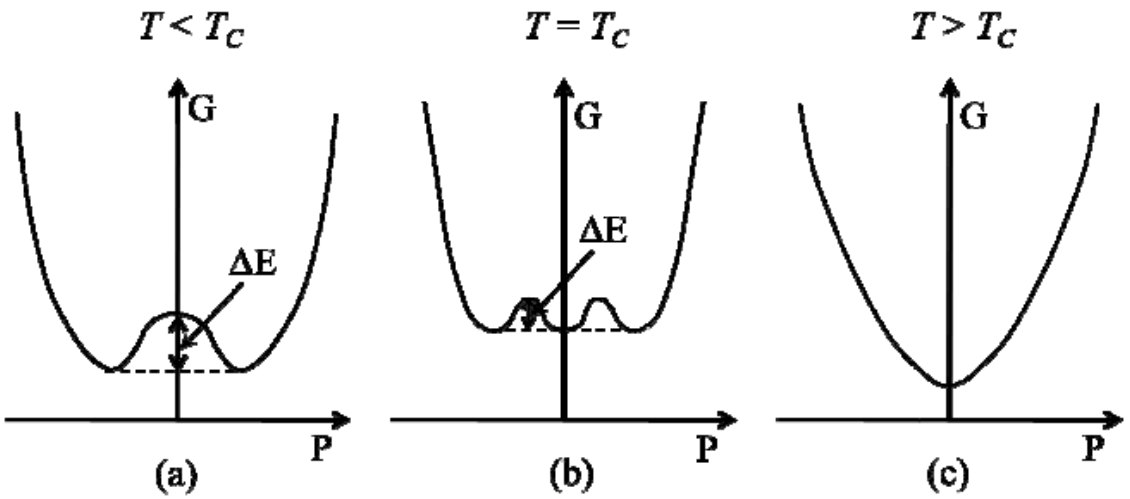

Fig. 1.5 Free energy (*G*) as a function of polarization (*P*) at various temperatures (*T*): (a) $T<T_C$, (b) $T=T_C$, and (c) $T>T_C$.

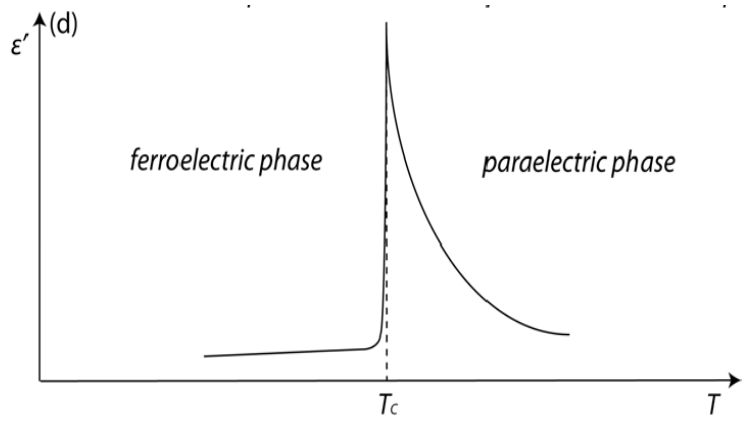

Fig.1.5 (d) Typical variation of dielectric permittivity (ε_r) as a function of temperature for a normal ferroelectric [11].

The temperature dependence of the dielectric constant (ε_r) above the Curie point ($T>T_C$) in most of the ferroelectric crystals is governed by the Curie-Weiss law:

$$\varepsilon = \varepsilon_0 + \frac{C}{T - T_o} \qquad (1.5)$$

where, ε is the permittivity of the material, ε_0 is the permittivity of the vacuum, C is the Curie constant and T_0 is the Curie-Weiss temperature. In the case of polar dielectric ceramics the value of ε, P_s and other properties are very sensitive to dopants, defects in

the crystal, porosity, grain size, sintering time and sintering temperature etc. In general the Curie-Weiss temperature T_0, is different from the Curie temperature T_C. For first order transitions, $T_0<T_C$ while for second order phase transitions, $T_0=T_C$. Some ferroelectric materials also show diffuse phase transition behavior. An additional subset of the ferroelectric phase transition called diffuse phase transition, which arises due to the compositional fluctuation in the material.

1.6 Lead & Lead Free Piezoelectric Ceramics

Among the perovskite ferroelectric materials, lead-containing compounds such as $(Pb_{0.52}Zr_{0.48})TiO_3$ (PZT) and $Pb(Mg_{1/3}Nb_{2/3})O_3–PbTiO_3$ (PMN-PT), occupy the majority of the commercial piezoelectric market because of their excellent piezoelectric and ferroelectric properties arising from the peculiar crystal chemistry of Pb^{+2} ion. The stereochemically active $6S^2$ lone pair in Pb^{2+} ion and strong structural distortion by Pb^{2+} ion displacement in these materials makes it possible to create highly polarizable and electrically active materials [12, 13].

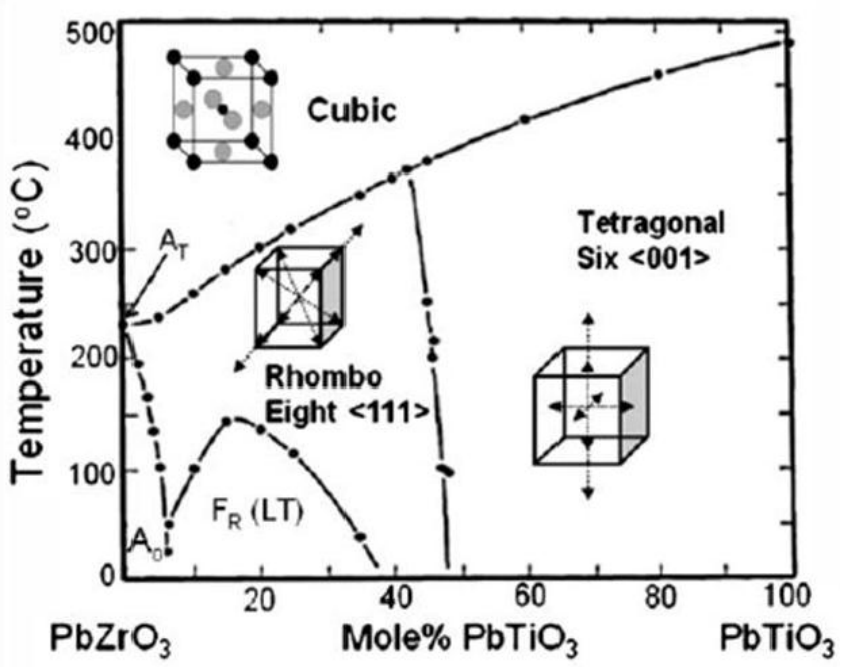

Fig. 1.6 Phase diagram of lead zirconate titanate [14].

The superior properties in these systems are obtained because of the presence of a morphotropic phase boundary (MPB) between rhombohedral, tetragonal or monoclinic phases [14]. The morphotropic phase boundary of PZT ceramics is almost vertical in the phase diagram, as shown in Fig. 1.6, which maintains the excellent piezoelectric properties across a wide temperature range. These lead-based piezoelectric materials, despite possessing excellent electromechanical properties contain a large amount of lead (> 60 wt. %) which is a toxic element. Processing of these materials is normally carried out by exposing the lead (Pb) into the open environment. There are extensive environmental issues with restoring and recycling of the lead-based materials, since lead maintains for a long time in the environment and accumulates in living tissues, damages the brain and nervous system. On the other hand, improper disposing of lead, such as disposing to open environment, could introduce it to the ecosystem and cause "acid rain". In fact, concerns about these issues have led to establish the legislation on restriction of the hazardous materials (ROHS) and end of life vehicle (EOV) by European Union (EU) [15]. Therefore, since June 2006, any products introduced to the open market may not include more than 0.1 wt.% of Pb substances. However, the presently available lead-free piezoelectric ceramics are not yet good enough to replace lead based piezoelectric materials.

A significant research on lead-free piezoelectric materials, alternatives to PZT system, began a little over ten years ago even though the base lead free materials have been known for more than half a century [16,17]. The research activities before 1990 mostly aimed at searching for the systems, whose properties are better than those of PZT. However, this was not meant for environmental protection but merely a search for the

systems with improved properties over PZT. Since 2000, the search has mostly directed to improve the already known lead-free materials to the point where they might show PZT-like properties. Till now the piezoelectric properties of lead free ceramics are far lower than the lad based ceramics. Fig.1.8 shows the number of publications per year on lead-free piezoceramics from 1950 to 2009**.** Among all the lead-free piezoelectric materials, in recent years two systems $(Bi_{1/2}Na_{1/2})TiO_3$ (BNT) and $(Na_{0.5}K_{0.5})NbO_3$ (NKN), have drawn a great deal of attention. $(Bi_{1/2}Na_{1/2})TiO_3$ possess large remnant polarization (38 $\mu C/cm^2$). But it has a high coercive field (E_c) (73 kV/cm) and a ferroelectric-to-antiferroelectric phase transition at around 200°C [18]. On the other hand, sodium potassium niobate, $K_{1-x}N_xNbO_3$/KNN, is a good candidate because it has a fairly high Curie temperature (420°C) [19].

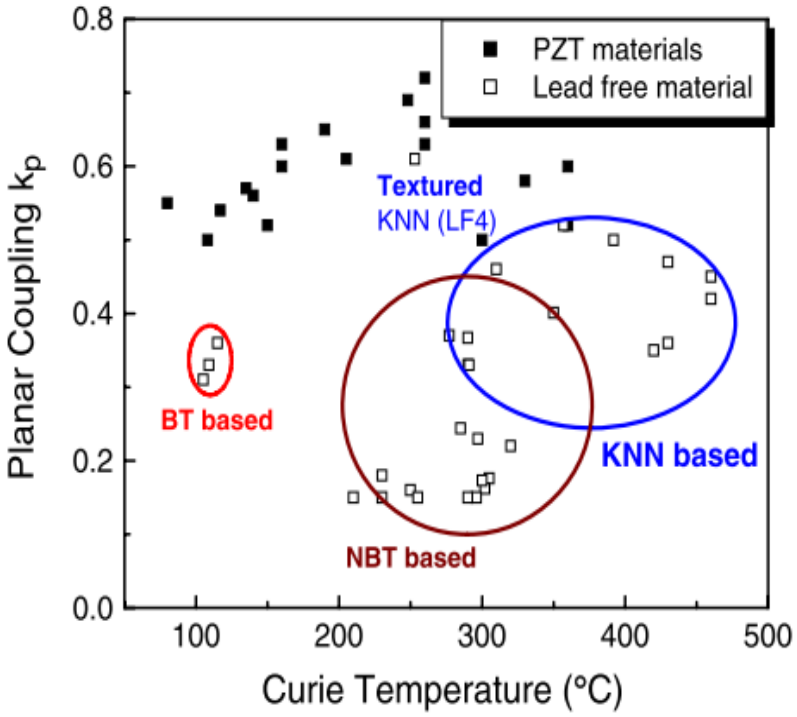

Fig.1.7 (a)

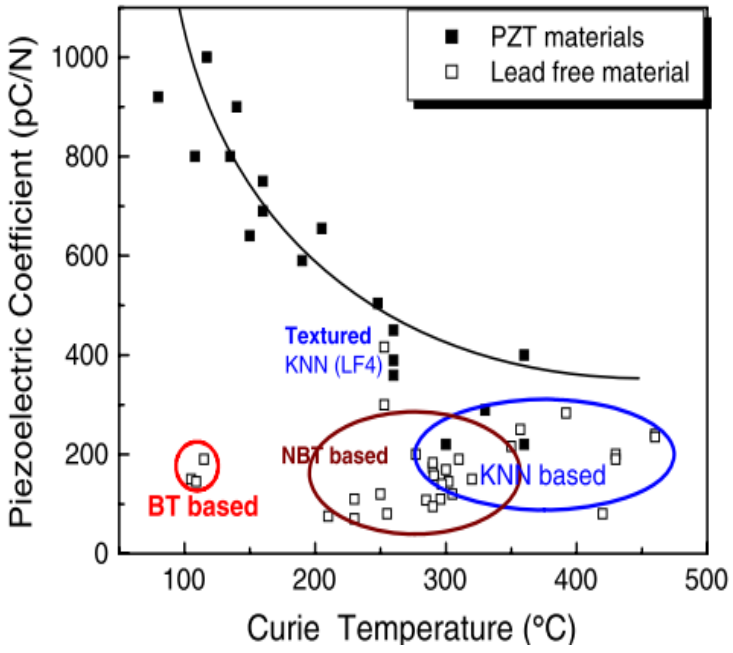

Fig.1.7 (b)

Fig.1.7 Comparison of properties between PZT materials and lead-free materials: (a) dielectric permittivity as a function of Curie temperature; (b) piezoelectric coefficient as a function of temperature [20].

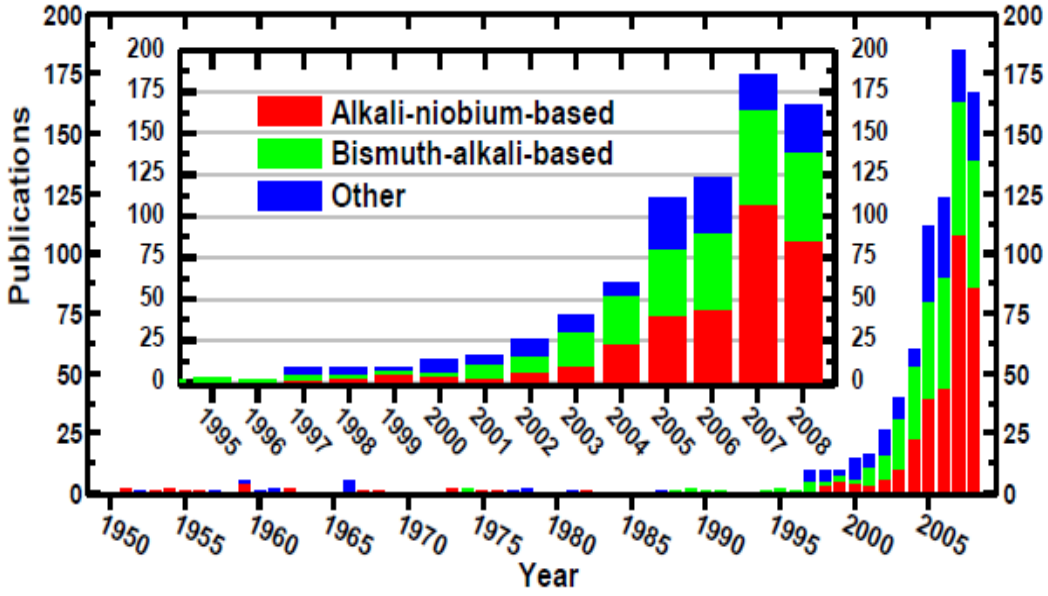

Fig 1.8 The number of publications per year on lead-free piezoceramics [21-27].

1.7 $K_{1-x}Na_xNbO_3$/KNN Based Materials

KNN is a solid solution of $KNbO_3$ (KN) and $NaNbO_3$ (NN) systems. Potassium niobate (KN) is a ferroelectric system with orthorhombic symmetry at room temperature (RT) and has the phase transitions similar to $BaTiO_3$ but with higher Tc (~ 435ºC). $NaNbO_3$ (NN) system is an orthorhombic anti-ferroelectric at room temperature with T_c ~ 355 ºC. The similarity between KNN and PZT systems is that both of these systems are composed of ferroelectric and anti-ferroelectric end-members. Fig. 1.9 shows the phase diagram of $KNbO_3$-$NaNbO_3$ system. As shown in Fig. 1.9, the substitution of K^+ in KNN system helps the stabilization of ferroelectric perovskite phase and hence reduction of formed metastable structures. The solid solution of potassium niobate and sodium niobate, $(1-x)KNbO_3–xNaNbO_3$, was found to exhibit better piezoelectric properties around the MPB at x ~ 0.5, which separates two orthorhombic ferroelectric phases [28, 29]. Therefore, $K_{0.5}Na_{0.5}NbO_3$ (KNN) has been recognized as one of the most promising host materials for new lead-free piezoelectrics. However, KNN ceramics are difficult to sinter by conventional solid state sintering technique and are subject to the problem of deliquescence. The phase stability of KNN based ceramics are limited to 1140^{o}C, hence high temperature sintering is not possible. Moreover, the piezoelectric properties of KNN ceramics is very low comparable to PZT ceramics. In order to solve these problems researchers have tried to make solid solution of KNN system with other materials. Many studies have been carried out on various KNN-based families, such as KNN−$LiTaO_3$ [30], KNN−$LiNbO_3$ [31], KNN−$LiSbO_3$ [32-34], KNN−$SrTiO_3$ [35], KNN−$BaTiO_3$ [36], KNN-$AgNbO_3$ [37]. Among all the modified KNN ceramics, KNN-LS ceramics near

MPB is of great interest. (1-x)KNN-xLiSbO$_3$/ KNN-LS is a solid solution of KNN and LiSbO$_3$ (LS) systems.

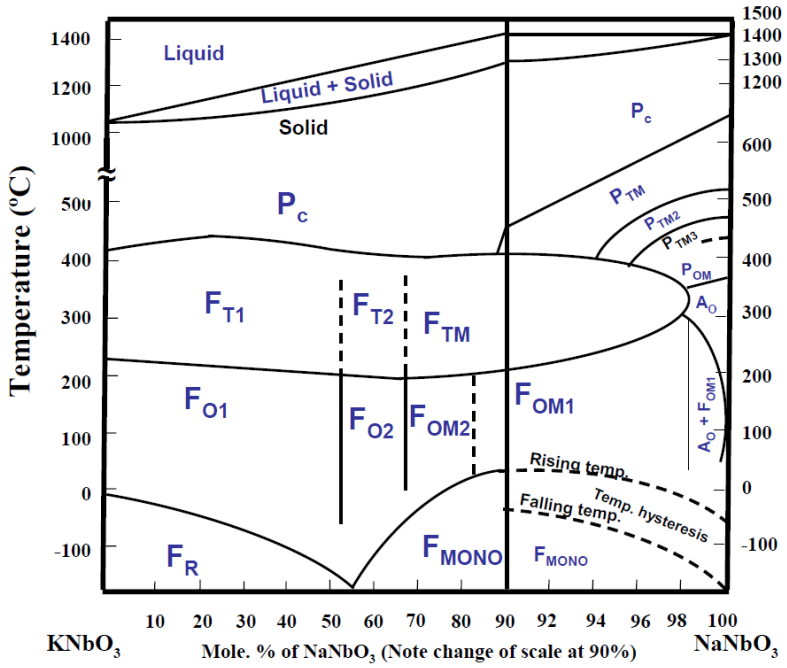

Fig. 1.9 Phase diagram of the KNbO3 - NaNbO3 system [20].

A coexistence of orthorhombic and tetragonal phase in KNN-LS ceramic was identified in the composition range for x=0.04-0.06 [33]. The enhanced dielectric and piezoelectric properties in these systems had initially been attributed to the effects of the MPB separating the orthorhombic and the tetragonal phases. It was later found that the enhanced properties in KNN-LS ceramics is due to a polymorphic phase transition [38-40]. The improved piezoelectric properties in these ceramics result from the lowering in temperature of the ferroelectric orthorhombic to tetragonal phase transition temperature (T_{O-T}) to ~ RT. But, this lowering of (T_{O-T}) gives rise to sharp temperature dependence of the piezoelectric properties (e.g., k_p), which is a problem to be addressed before these materials can be used in piezoelectric devices. It has been reported that the MPB in PZT

system is nearly vertical in the temperature-composition phase diagram [41-42] as a result the poling temperature (T_p) has no effect on different ferroelectric phases. However, the presence of MPB in KNN-based ceramics is very different from that in PZT-based ceramics. The MPB in KNN-based ceramics is an orthorhombic-tetragonal polymorphic phase transition (PPT) type [43]. The phase boundary between tetragonal and orthorhombic phases in KNN ceramics is not vertical and shows strong temperature dependent behavior. Therefore, poling of the KNN based ceramics near PPT temperature can improve the piezoelectric properties. Hence, it is necessary to examine how the poling temperature is affecting the piezoelectric properties of the KNN based ceramics. Even though KNN-LS ceramics possess excellent piezoelectric properties, still it is not comparable to PZT ceramics. Hence, further modification in this system is suggested. Lei *et al.* reported that the substitution of Ag^+ ion for $(K_{0.5}Na_{0.5})^+$ ion in KNN ceramics resulted an improvement in the piezoelectric coefficient (d_{33})~186pC/N, planar mode electromechanical coupling factor (k_p) ~42.5% and the relative density reached ~94% of the theoretical density (T.D. ~ 4.51g/cc) [37]. Xu *et al* also reported that Ag^+ ion diffuses into the KNN lattice to form a new solid solution with improved electrical properties compared to pure KNN ceramics [44]. It was also reported that the tantalum (Ta) doping in KNN based ceramics can help to improve the piezoelectric properties. Thomas *et al.* reported that the simultaneous substitution of Li and Ta shifts the T_{o-t} of the KNN based ceramics below room temperature and makes it useful for high temperature applications [45]. Recent study also confirms that substitution of Ta in place of Nb in the KNN based ceramics can significantly improve the density and piezoelectric performance of these ceramics [46-48]. Pan *et al* reported that V doping in place of Nb in pure KNN ceramics

can improve the sintering as well as electrical properties [49]. The sintering temperature was found to decrease by 200^{o}C with the substitution of small amount of V. Similar kind of effects were also observed in SBN ceramics [50]. Following these reports, in the present work we have made an attempt to study the effect of Ag, Ta and V substitution on the structural and electrical properties of 0.95KNN-0.05LS ceramics.

1.8 Various Methods to Improve Piezoelectric Properties

Till now the piezoelectric properties of lead free ceramics are lower than those of the PZT family. Various methods have been developed to further improve the piezoelectric properties of piezoelectrics.

1.8.1 Developing Solid Solutions Near MPB

Morphotropic phase boundary (MPB) of a solid solution is an intrinsic region of a phase diagram where two or more different phases coexist. In many lead-based systems, it has been shown that the solid solutions of piezoelectric materials usually exhibit better piezoelectric properties as well as dielectric properties near the MPB at the compositions. For example, the dielectric and electromechanical coupling coefficients of PZT ceramics with compositions near the MPB ($Pb(Zr_{0.52}Ti_{0.48})O_3$) are showed in Fig. 1.10. The reason that these properties show the maximum near the MPB region can be explained from a statistical point of view regarding the polar axis switching during the poling process of the materials. When a piezoelectric ceramics is poled, the different polar axes within the grains are forced to switch toward the directions that are allowed by crystallographic symmetry. Given a particular crystallographic symmetry, there are always a fixed number of equivalent polar axes along which the dipoles can switch.

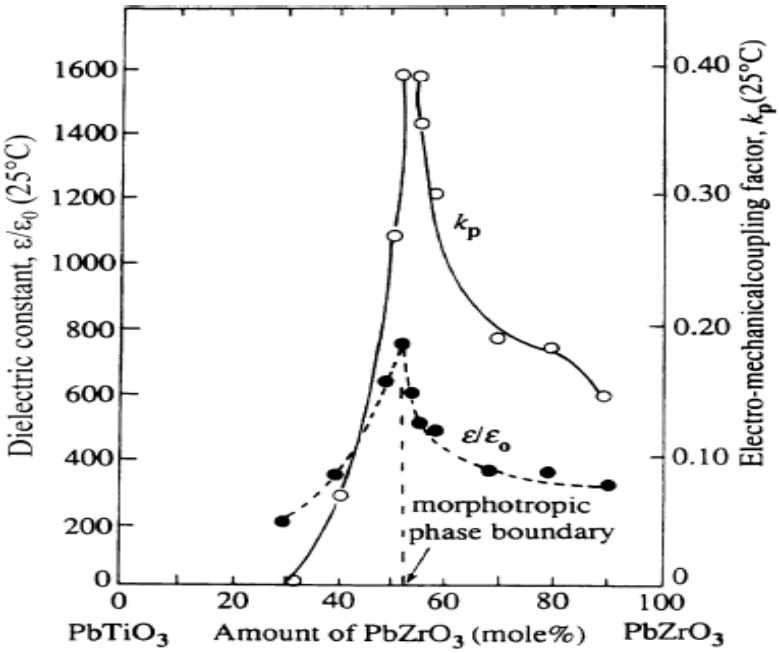

Fig. 1.10 Dielectric and electromechanical coupling coefficients of PZT ceramics near MPB [14].

The numbers of polar axes of ferroelectrics with different phases are shown in Fig.1.11. For instance, on the Zr-rich side of the MPB, the crystal symmetry of PZT is tetragonal, with 6 equivalent [001] directions of polar axes. On the Ti-rich side of the MPB, PZT is rhombohedral, with 8 equivalent [111] directions of polar axes. But at the MPB, these two different phases coexist; therefore the switching of the polar axes has 14 available directions. With a larger number of allowable polar directions, the maximum deviation of the polar axis of a grain from the average polar direction becomes smaller, so that the lowering of the net polarization in the whole polycrystalline specimen becomes less.

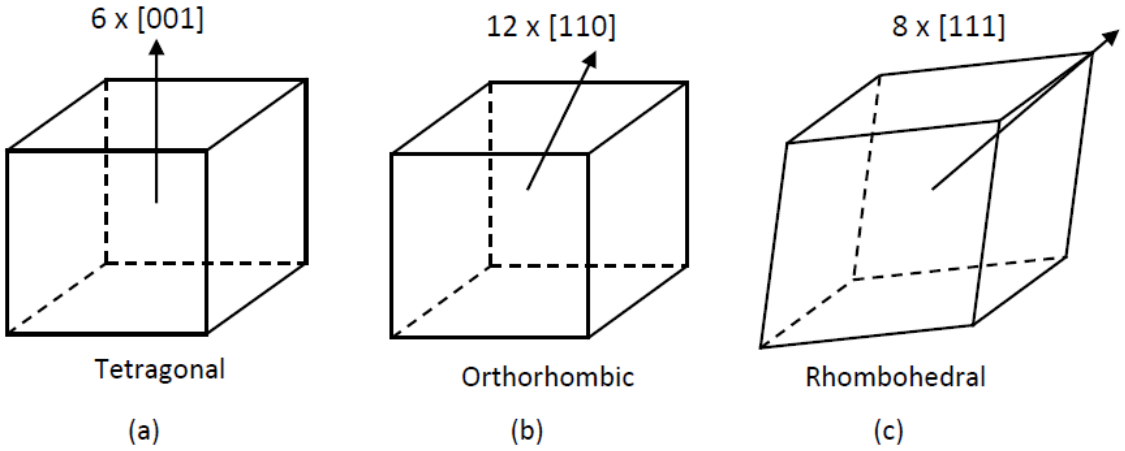

Fig. 1.11 Numbers of equivalent polar axes of ferroelectrics with different phases: (a) six [001] directions in tetragonal; (b) twelve [110] directions in orthorhombic; (c) eight [111] directions in rhombohedral structure.

1.8.2 Optimization of Poling Temperature

The MPB in KNN-based ceramics is very different from that in PZT-based ceramics. The so-called MPB in KNN based ceramics is an orthorhombic-tetragonal polymorphic phase transition (PPT). The phase boundary between tetragonal and orthorhombic phases is not vertical and shows strong temperature dependence. This suggests that the piezoelectric properties of KNN-based ceramics must be poling temperature (Tp*)* dependent.

1.8.3 Microwave Processing

Microwaves are electromagnetic waves that lie between radio and infrared frequency regions in the electromagnetic spectrum, shown in Fig.1.12. While the majority of the microwaves frequencies are dedicated for communications and radar purposes, the following frequencies are designated for industrial, scientific, and medical uses: 915 MHz, 2.45 GHz, 5.8 GHz, and 20.2-21.1 GHz [51, 52]. Home-model microwave ovens operate at a frequency of 2.45 GHz frequency due to the fact that the water molecules present in food show good microwave absorption at this frequency. The

relative availability of 915 MHz and 2.45 GHz microwave ovens resulted in their applications to processing ceramics [51].

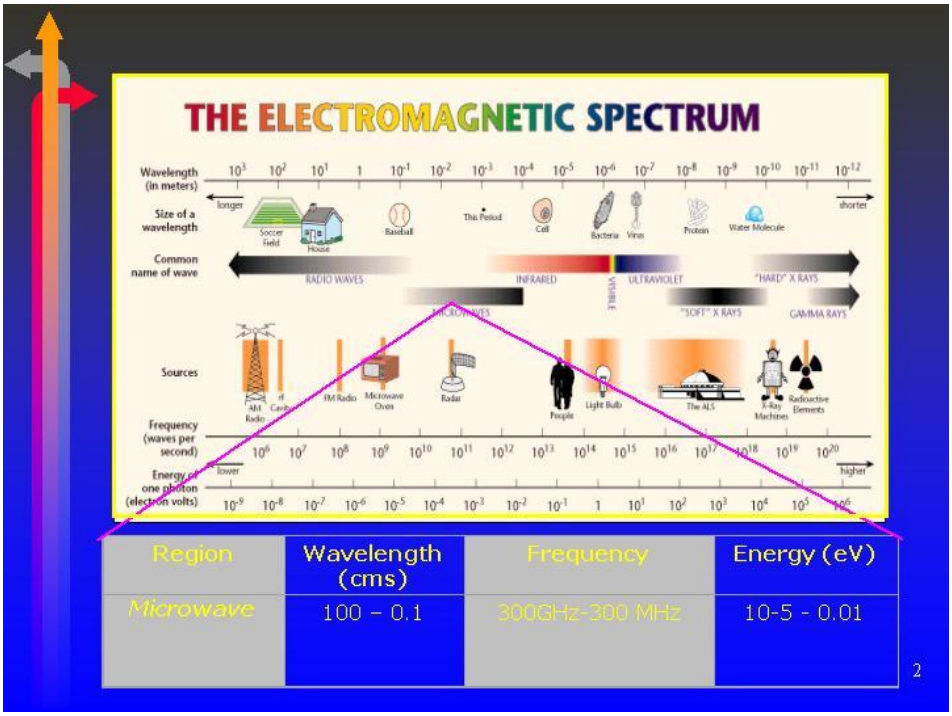

Fig.1.12 Electromagnetic spectrum illustrating specifically the microwave range.

Microwaves interact with materials in different ways. Depending on the materials Microwaves are generally reflected, transmitted, or absorbed. The ability of certain materials to convert microwaves into heat makes these materials suitable for microwave processing [53]. The main difference between a conventional and a microwave process is shown in Fig.1.13. In conventional furnaces, the heating elements supply heat to the sample; the majority of heat is concentrated along the surface of the body when compared with the interior of the sample. In a microwave furnace, the material will absorb microwave energy and then convert it into heat. The heating pattern during microwave processing is more internal in nature. It was reported that microwave processing (MWP) is superior to conventional processing (CP) due to its unique characteristics, such as rapid

heating, enhanced densification rate and improved microstructure. Microwave heating is fundamentally different from conventional heating. In the microwave process, the heat is generated internally within the material instead of originating from external sources, and hence there is an inverse heating profile. The heating is very rapid as the material is heated by energy conversion rather than by energy transfer, which occurs in conventional techniques.

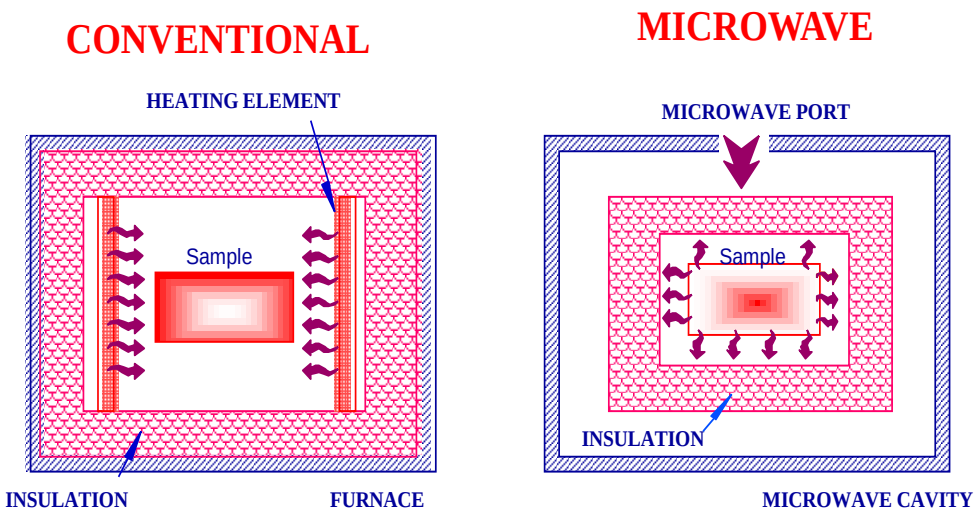

Fig. 1.13 Heating patterns in conventional and microwave furnaces.

Moreover, a major advantage of microwave calcination over conventional calcination is that not only it saves time but also the coarsening of the particles can be greatly reduced, which leads to the further increment in the diffusion rate during sintering. Reports on microwave processing of KNN based ceramics are very rare. In the present work, in order to produce highly dense KNN based ceramics, microwave processing technique has been employed.

1.9 Objectives of This Work

Although a great deal of work has been carried out in the search for lead-free piezoelectric materials based on KNN based ceramics, still it is important and

challenging to design and synthesize new lead free systems in the interest of developing new lead-free piezoelectrics with better piezoelectric and ferroelectric properties suitable for high temperature applications.

Following are the objectives of the present thesis work:

a) Synthesis of KNN-LS based ceramics near MPB in single perovskite phase by conventional solid-state reaction (CSSR) route.

b) Optimization of LS content in KNN-LS ceramics near MPB to achieve better piezoelectric properties.

c) Optimization of poling temperature to obtain better electromechanical and piezoelectric properties.

d) Optimization of sintering temperature of Ag, Ta and V doped KNN-LS system, synthesized by CSSR route.

e) Ag, Ta and V doping in MPB composition of KNN-LS system and its effect on ferroelectric and piezoelectric properties.

(e) Study of densification behavior and electrical properties of KNN-LS based ceramics (synthesized by CSSR route and showing better piezoelectric properties) processed by microwave technique.

The following series of KNN-LS based ceramics are synthesized by CSSR route:

i. $(1-x)[K_{0.5}Na_{0.5}NbO_3]-x[LiSbO_3]$ (x=0, 0.04, 0.05, 0.06)

ii. $0.95[(K_{0.5}Na_{0.5})_{1-x}Ag_xNbO_3]-0.05LiSbO_3$ (x=0, 0.02, 0.04, 0.06, 0.08)

iii. $0.95[(K_{0.5}Na_{0.5})\ Nb_{1-x}\ Ta_xO_3]-0.05LiSbO_3$ (x=0, 0.02, 0.04, 0.06, 0.08)

iv. $0.95[(K_{0.5}Na_{0.5})\ Nb_{1-x}V_xO_3]-0.05LiSbO_3$ (x=0, 0.02, 0.04, 0.06, 0.08)

References

[1] G. H. Haertling, J. Am. Ceram. Soc., 82, (1999) 797.

[2] N. Setter, J. Eur. Ceram. Soc., 21, (2001) 1279.

[3] J. F. Nye, Physical Properties of Crystals, 1985 (Oxford: Oxford University Press).

[4] D. Damjanovic, Rep. Prog. Phys., 61, (1998) 1267.

[5] Y. I. Sirotin and M. P. Shaskolskaya, Fundamentals of Crystal Physics, 1982 (Moscow: Mir).

[6] J. F. Nye, Pysical Properties of Crystals (Oxford University Press, Oxford, 1957).

[7] J. Valasek, Phys. Rev., 17, (1921)475.

[8] J. Valasek, Phys. Rev., 24, (1924) 560.

[9] M. E. Lines, and A. M. Glass, Principles and Applications of Ferroelectrics and Related Materials (Clarendon Press, Oxford, 1977)

[10] Y. Xu, Ferroelectric Materials and Their Applications (North-olland, Amsterdam, 1991).

[11] R. Blinc, and B. Zeks, Soft Modes in Ferroelectrics and Antiferroelectrics (North-Holland, Amsterdam, 1974).

[12] A. R. West, Basic Solid State Chemistry (John Wiley & Sons, New York, 1999).

[13] R. E. Cohen, Nature, 358, (1992)136.

[14] B. Jaffe, W. R. Cook, and H. Jaffe, Piezoelectric Ceramics (Academic Press, London, 1971).

[15] M. Pecht, Y. Fukuda, S. Rajagopal, IEEE Trans. Electr. Packag. Manufact., 27, (2004) 221.

[16] L. Egerton and D. M. Dillon, J. Am. Ceram. Soc., 42, (1959) 438.

[17] G. A. Smolenskii and A. I. Agranovskaya, Sov. Phys. Sol. Stat., 1, (1960) 1429.

[18] G. A. Smolenskii, V. A. Isupv, A. I. Afranovskaya and N. N. Krainik, J. Sov. Phys. Sol. Stat., 2, (1961) 2651.

[19] S. Zhang, H. J. Lee, C. Ma, and X. Tan, J. Am. Ceram. Soc., 94, (2011) 3659.

[20] T. R. Shrout and S. J. Zhang, J. Electroceram., 19, (2007) 111.

[21] J. F. Nye, Physical Properties of Crystals, Oxford Science Publications, Oxford, 1993.

[22] R. E. Newnham. In Properties of Materials: Anisotropy, Symmetry, Structure. (Oxford University Press, 2005).

[23] S. E. Park and T. R. Shrout, J. Appl. Phys., 82, (1997) 1804.

[24] S. E. Park, M. J. Pan, K. Markowski, S. Yoshikawa and L. E. Cross, J. Appl. Phys., 82, (1997) 1798.

[25] W. Pan, Q. Zhang, A. S. Bhalla, and L. E. Cross, J. Am. Ceram. Soc., 72, (1989) 7.

[26] J. E. Daniels, W. Jo, J. Rodel, V. Honkimaki, and J. L. Jones, Appl. Phys. Lett., 95, (2009) 032904.

[27] Y.J. Dai, X.W. Zhang, and K.P. Chen, Appl. Phys. Lett., 94, (2009) 042905.

[28] Z.Y. Shen, K. Wang, and J.F. Li, Appl. Phys., A 97, (2009) 911.

[29] Y. P. Guo, K. Kakimoto, and H. Ohsato, Appl. Phys. Lett., 85, (2004) 4121.

[30] Y. P. Guo, K. Kakimoto, and H. Ohsato, Mater. Lett., 59, (2005) 241.

[31] G. Z. Zang, J. F. Wang, H. C. Chen, W. B. Su, C. M. Wang, P. Qi, B. Q. Ming, J. Du, and L. M. Zheng, Appl. Phys. Lett., 88, (2006) 212908.

[32] J. Wu, Y. Wang, D. Xiao, J. Zhu, P. Yu, L. Wu and W. Wu, Jpn. J. Appl. Phys., 46, (2007) 7375.

[33] S. Zhang, R. Xia, T. R. Shrout, G. Zang, J. Wang, Sol. State Commun., 141, (2007) 675.

[34] S. Zhang, R. Xia, T. R. Shrout, Jpn. J. Appl. Phys., 46, (2007) 7375.

[35] R. Wang, R. J. Xie, K. Hanada, K. Matsusaki, H. Bando, and M. Itoh, Phys. Status Solidi (a), 202, (2005) R57.

[36] Y. Guo, K. Kakimoto, and H. Ohsato, Jpn. J. Appl. Phys., 43, (2004) 6662.

[37] Chao Lei and Zuo-Guang Ye, Appl. Phys. Lett., 93, (2008) 042901.

[38] S. J. Zhang, R. Xia, and T. R. Shrout, J. Electroceram., 19, (2007) 251.

[39] Y. J. Dai, X. W. Zhang, and G. Y. Zhou, Appl. Phys. Lett., 90, (2007) 262903.

[40] E. K. Akdogan, K. Kerman, M. Abazari, and A. Safari, Appl. Phys. Lett., 92, (2008) 112908.

[41] J. L. Jones, E. B. Slamovich, K. J. Bowman, J. Appl. Phys., 97, (2005) 034113.

[42] I. M. Reaney, D. I. Woodward, C. A. Randall, J. Am. Ceram. Soc., 94, (2011) 2242.

[43] H. Du, W. Zhou, F. Luo and D. Zhu, Appl. Phys. Lett., 91, (2007) 202907.

[44] C. Xu, D. Lin and K.W. Kwok. J. Mater. Sci: Mater. Electron., 19, (2008) 1054.

[45] T. A. Skidmore, T. P. Comyn, and S. J. Milne, Appl. Phys. Lett., 94, (2009) 222902.

[46] Y.G. Lv, C.L. Wang, J.L. Zhang, L. Wu, M.L. Zhao, J.P. Xu, Mater. Res. Bull., 44, (2009) 284.

[47] Y.F. Chang, Z.P. Yang, L. L. Wei, J. Am. Ceram. Soc., 90, (2007) 1656.

[48] D. lin, K.W. Kwok, and H.L.W. Chan, Appl. Phys. A, 91, (2008)167.

[49] H. Pan, D. Jin, W. Wu, J. Cheng, and Z. Meng, IEEE Trans. Ultrason. Ferroelectr. Freq. Control., 55, (2008) 5.

[50] Y. Wu, G. Cao, J. Mater. Sci. Lett., 19, (2000) 267.

[51] D. E. Clark, W. H. Sutton, Annual Rev. Mater. Sci., 26, (1996) 299.

[52] J. Katz, Annual Rev. Mater. Sci., 22, (1992) 153.

[53] NRC, Microwave Processing of Materials, Technical Report, 1994.

CHAPTER - 2

Synthesis Routes and Investigated Parameters

2.1 Introduction

In this chapter, the basic principles and various experimental techniques as well as the synthesis route used in this thesis work are described. Since in KNN based materials hygroscopic alkali elements are present therefore, extra care needs to be taken to obtain single perovskite phase in these materials. In the present chapter the various processes taking place during the material synthesis are presented. In order to measure the structural, microstructural and electrical properties various characterization techniques are used. These characterization techniques include: structural analysis, dielectric, piezoelectric, electromechanical, ferroelectric and thermal measurements. The concepts of these experimental methods and techniques are briefly explained, including powder x-ray diffraction (XRD), scanning electron microscopy, ferroelectric hysteresis loop measurement, strain vs. electric field loop, thermogravimetric analysis, resonance and anti-resonance frequency and piezoelectric constant measurement.

2.2 Synthesis Process

There are several methods of material synthesis such as mechanical methods, which includes solid-state reaction, ball milling etc., and the chemical methods, which includes sol-gel, wet-dry, polymer-sol-gel etc. To achieve a quality product with respect to purity, homogeneity, reactivity, particle size etc. each method finds its own advantages and disadvantages. Like the solid-state reaction method is found to be the easier, convenient and a low cost technique among other available synthesis methods by means of performance,

reliability, reproducibility and economy. Several processing techniques for electro-ceramics have been developed and some of these are discussed in the following sections.

2.2.1 Solid State Reaction Route

A solid solution is a mixture of two crystalline solids that coexist as a new crystalline solid, or crystal lattice. Usually, polycrystalline materials are prepared by the conventional solid state reaction route (CSSR). Solids usually do not react at room temperature (RT) and in order to accelerate the reaction, higher processing temperature is needed. First of all the raw materials are kept in an oven at 200 ^{o}C for 2h, in order to remove any moisture present in the materials. Then the materials are weighed according to the stoichiometry. After that, the raw materials are ball milled and then grinded to homogenize the particles [1]. Acetone is usually used as a milling medium. The phase formation temperature is decided from the thermogravimetric analysis. Here the weight loss of the sample is measured as a function of temperature. Next step is the solid state reaction between the constituents of starting materials at suitable temperature [1, 2]. This process is called calcination. Calcination causes the constituents to interact by inter diffusion between the ions. Calcination is also called as the process of phase formation. After calcination the powder is given a desired shape, and is further densified through sintering process. Sintering is a heat treatment process for making useful polycrystalline ceramics from a powder or porous material. In this process the powder is pressed into a compact, which is then heated to a temperature approximately 50-80% of the melting temperature [3]. In this way, the powder does not melt; rather the particles join to reduce the porosity of the compact by ionic diffusion as shown in Fig.2.1.

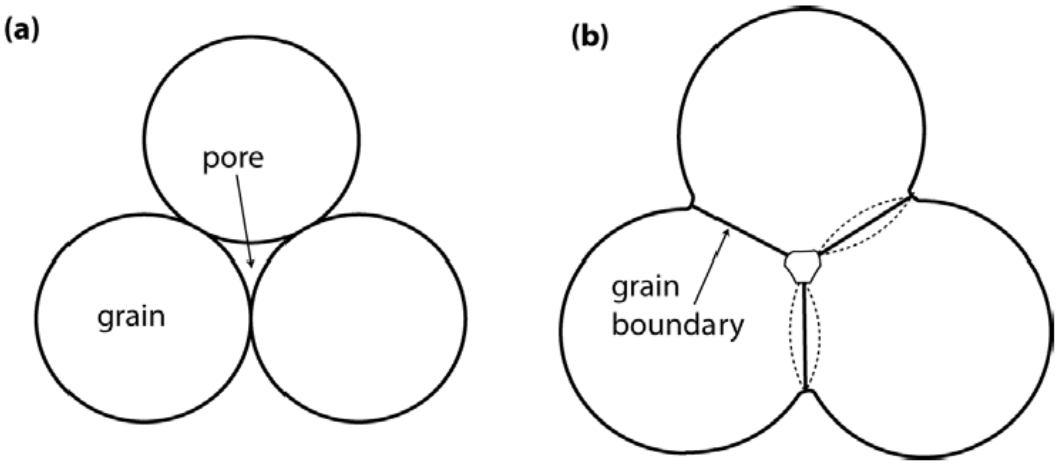

Fig. 2.1 Schematics of sintering process: (a) three grains before solid-state sintering, and (b) after sintering.

2.2.2 Microwave processing

The first reported work on sintering of ceramics using microwaves dates back to the 1960's with the patent on firing refractories by Levinson [4]. Since then, microwave technology has been successfully applied to process some of the common ceramics consisting of oxides, borides, carbides, nitrides, and a combination of these materials. Although microwave heating was conceived before 50 years ago, its use in ceramic processing is relatively new. Microwave heating is a phenomenon of electromagnetic energy dissipation inside a material [5]. Considering non-magnetic materials, the charges present in the material would respond to the electric field (that is associated with microwave) mainly by two processes (a) polarization and (b) conduction. In the microwave process, the heat is generated internally within the material instead of originating from external sources, and hence there is an inverse heating profile. The heating is very rapid as the material is heated by energy conversion rather than by energy transfer, which occurs in conventional techniques. Microwave heating is a function of the material being processed, and there is almost 100% conversion of electromagnetic energy into heat, largely within the sample itself, unlike with conventional

heating where there are significant thermal energy losses. Microwave heating has many advantages over conventional heating methods [5-8]; some of these advantages include, time and energy saving, very rapid heating rates considerably reduced processing time and temperature, fine microstructures and hence improved mechanical properties, it is environmental friendly. Due to wide availability of 2.45 GHz microwave ovens, this frequency is used by many researchers for heating different ceramics.

The absorption of microwave energy and conversion to heat occurs due to polarization and conduction and results in a rise in temperature, $\Delta T/\Delta t$, which is given by the following equation [8]:

$$\frac{\Delta T}{\Delta t} = \frac{2\pi\varepsilon_0 \varepsilon''_{eff} E^2_{rms}}{\rho c_p} \left(\frac{^oC}{s}\right) \qquad (2.1)$$

where, ε_o is the permittivity of free space (8.85×10^{-12} V m^3), ε''_{eff} is the relative effective dielectric loss due to ionic conduction and dipolar reorientation, f is the frequency, E_{rms} is the root mean square of the electric field within the material, ρ is the bulk density of dielectric material and C_p is the heat capacity of the material at constant pressure. The dissipation of microwave power is limited by the attenuation of electromagnetic waves within the material and this is quantified as penetration depth, D_p. It is defined as the distance from the surface of the material at which the power level drops to 37 % of the power at the surface. For a given microwave frequency, it can be observed from equation 1 that microwave absorption depends on the effective dielectric constant, ε''_{eff}, and the magnitude of the internal electric field, E_{rms}. Higher these values, the more the energy

(microwave) would be absorbed. However, the extent to which microwaves are converted to heat is limited by their depth of penetration. It can be observed from equation 1 that, with the increase in ε''_{eff}, the D_p will decrease i.e., at very high effective dielectric loss values, the microwave heating will focus more along the material's surface similar to that of conventional heating.

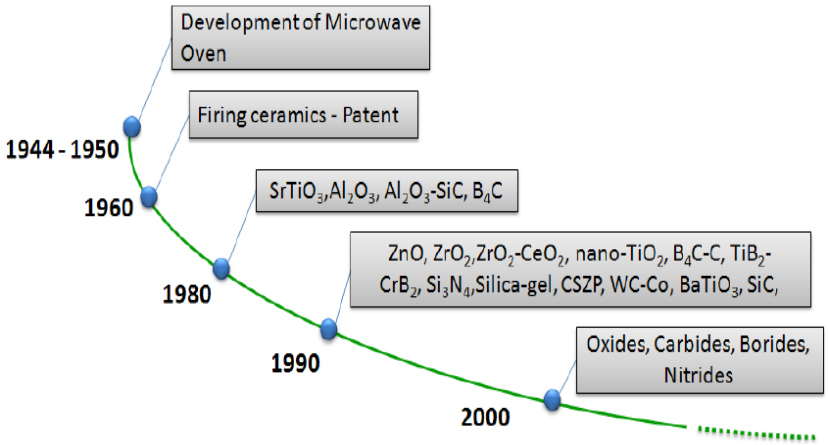

Fig. 2.2 Historical perspective of sintering of ceramics using microwave energy.

2.3 Thermal Analysis

Thermo gravimetric analysis (TGA) can be used to determine the materials thermal stability and volatile of components by monitoring the weight change at the time of heating of the specimen. The measurement is normally carried out in air or in an inert atmosphere, such as He/Ar, and the changes in weight is recorded as a function of increase of temperature of testing samples. Sometimes the measurement is performed in neon oxygen atmosphere to slow down the oxidation. Such analysis relies on a high degree of precision in three measurements: weight, temperature, and temperature change. The results from thermo gravimetric analyses are usually reported in the form of curves relating the mass lost from the sample against temperature. Form this, the temperatures at which certain chemical processes begin and

completed are graphically demonstrated. TGA is commonly employed in research to determine degradation temperatures, absorbed moisture content of materials, the level of inorganic and organic components in materials, decomposition points of explosives, and solvent residues. It is also often used to estimate the corrosion kinetics in high temperature oxidation [9, 10].

A differential thermal analysis (DTA) can be for the determination of phase diagrams, heat change measurements and decomposition in various atmospheres. DTA is a thermoanalytic technique, similar to differential scanning calorimetry (DSC). In DTA, an inert reference and the specimen under study are made to undergo identical thermal cycles, while recording any temperature difference between them [11]. This differential temperature between inert reference and the specimen is then plotted against time, or against temperature (DTA curve or thermogram). Reactions taking place in the sample, either exothermic or endothermic, can be detected relative to the inert reference. Thus, a DTA curve provides data on the transformations that have occurred, such as glass transitions, crystallization, melting and sublimation.

2.4 X-Ray Diffraction

The diffraction of X-rays was first illustrated by Max-von Laue using a crystal of copper sulphate as the diffraction grating. This discovery was immediately noticed by W. H. Bragg and W. L. Bragg, who used X-ray diffraction as a means to determine crystal structures. In this technique, an electric field is used to accelerate electrons, which are directed at a metal target [12]. The penetrating electrons eject other electrons out of their atomic orbitals, specifically from the inner most (*K*) shell. This vacancy in the *K* shell is then filled by an electron from the closest shell higher in energy (*L*) or the one above that (*M*), yielding two sharp and intense X-ray peaks, K_α and K_β, respectively [13]. The difference in energy between

the two shells is released as radiation in the form of an X-ray. Since the energies of the shells are well defined, each transition produces a monochromatic beam line. Fig. 2.3 illustrates how X-rays interact with the planes in the crystal lattice of the sample. This interaction can also be expressed by the Bragg law [13]:

$$2d_{hkl}Sin\theta = n\lambda \qquad (2.2)$$

where d_{hkl} is the interplanar spacing between the crystal planes (*hkl*), θ is the Bragg angle at which diffraction from these planes are observed, and λ is the wavelength of the X- rays.

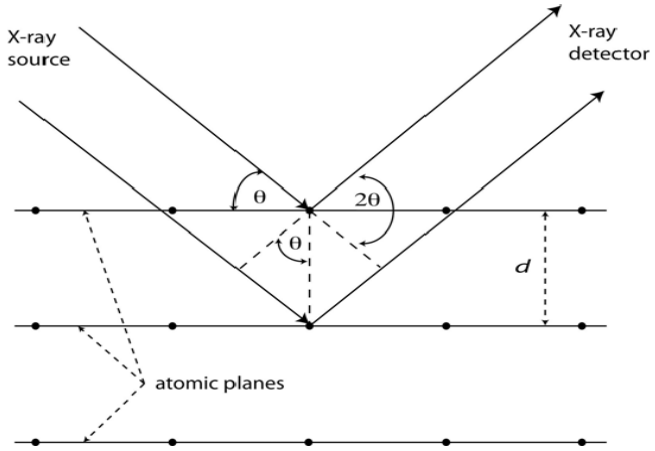

Fig. 2.3 Bragg diffraction from a set of lattice planes with a spacing *d*.

The diffracted X-rays are detected and a plot of intensity as a function of the 2θ angle is obtained. This XRD pattern provides very useful information such as the *d* spacing of the lattice planes, which is directly related to the unit cell parameters of the material, and the symmetry of the phase(s) present [14]. The K_α spectrum usually consists of two components of similar wavelength ($K_{\alpha1}$ and $K_{\alpha2}$) due to the existence of two slightly different *L* energy levels. For example, the wavelengths of the *K* radiations for a Cu target are: K_β=1.3926 Å, $K_{\alpha1}$=1.5406 Å and $K_{\alpha2}$=1.5444 Å [15]. Normally, monochromatic radiation is required in diffraction experiments, and the comparably more intense K_α radiation is usually selected.

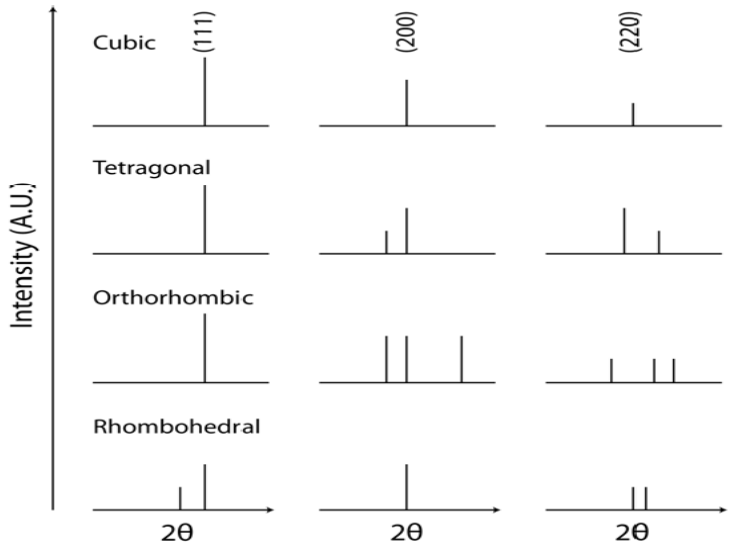

Fig. 2.4 Characteristic x-ray diffraction patterns for various symmetries showing the corresponding splitting with respect to the cubic (111), (200) and (220) reflections.

The K_α line is filtered using a thin metal foil, e.g., nickel which effectively filters the K_α line of copper. In some X-ray experiments, $K_{\alpha 1}$ and $K_{\alpha 2}$ are not resolved and a single line is observed instead of a doublet, e.g., for powder diffractometry at low angles. In this case, the average value of 1.5418 Å for K_α is used. If desired, the separate diffraction peaks can be resolved when the angle of scattering is large or the weaker $K_{\alpha 2}$ can be removed computationally. X-ray diffraction patterns can be used to monitor chemical reactions and structural properties such as phase purity and change of symmetry (phase transition). For example, if a crystal structure changes from cubic to tetragonal, the interaxial angles do not change ($\alpha, \beta, \gamma, = 90^o$), but the lengths of the unit cell are no longer equal ($a \neq b = c$) This will affect the *d*-spacings within the lattice, which in turn will result in the splitting or merging of peaks as shown in Fig. 2.4. This characteristic XRD pattern can be used to identify the symmetry and phase components of the materials.

2.5 Scanning Electron Microscopy (SEM)

A scanning electron microscope (SEM) is a type of electron microscope that images a sample by scanning it with a high-energy beam of electrons in a raster scan pattern. This technique is widely used to characterize the surface topography, morphology, compositions and crystallographic information of the samples. The fundamental principles of scanning electron microscopy (SEM) are mainly based on the accelerated electrons which carry significant amounts of kinetic energy. This energy is dissipated as a variety of signals due to the electron-sample interactions. These signals include secondary electrons (that produce SEM images), backscattered electrons (BSE), diffracted backscattered electrons (used to determine crystal structures and orientations of minerals), photons (characteristic X-rays that are used for elemental analysis and continuum X-rays), visible light (cathode luminescence), and heat. Secondary electrons and backscattered electrons are commonly used for imaging the samples. Secondary electrons are most valuable for showing morphology and topography of the samples; whereas backscattered electrons are most valuable for illustrating contrasts in composition in multiphase samples. Moreover, SEM analysis is considered to be a "non-destructive" method; hence, it is possible to analyze the same materials repeatedly [16, 17]. The schematic diagram of SEM is given in the Fig 2.5. In order to image the sample's surface, an electron beam is thermally emitted from a tungsten filament under vacuum and focused on an area (< 10 nm) and then scanned across the sample. The electrons penetrate the surface and consequently eject other electrons that are detected and used for imaging [18]. Since, electrons interacts with the material, the sample must be conducting.

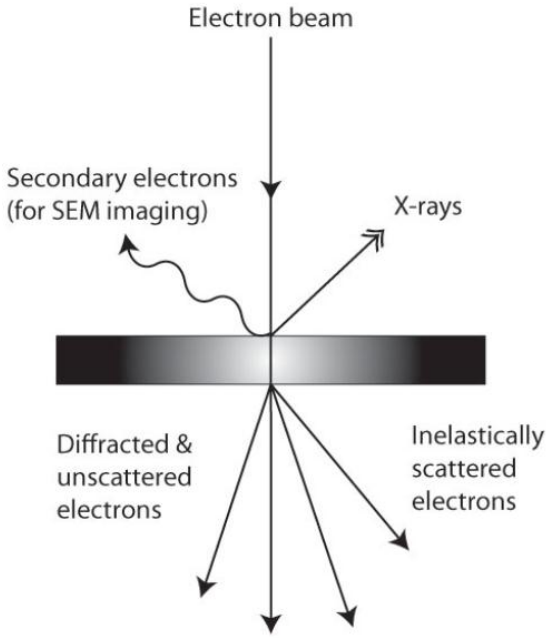

Fig. 2.5 The interaction of an electron beam with a sample.

2.6 Dielectric Polarization

The polarization in the dielectric material occurs when it is subjected to an external field and it is classified according to their origin. The various types of polarizations are [19]:

1. Dipolar polarization
2. Atomic or ionic polarization
3. Interface or space charge polarization
4. Electronic polarization

2.6.1 Dipolar Polarization (Orientational Polarization)

Dipolar polarization is a polarization that is either inherent to polar molecules (orientation polarization), or can be induced in any molecule in which the asymmetric distortion of the nuclei is possible (distortion polarization). In zero fields, the permanent dipoles will be randomly oriented and the system has no net polarization, but an

externally applied electric field will tend to align the dipoles and the material will acquire a net polarization, which is known as orientational polarization.

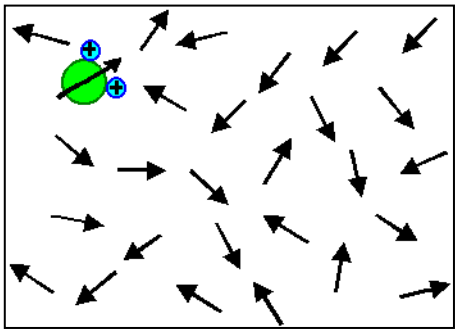

Fig.2.6 (a) Without field

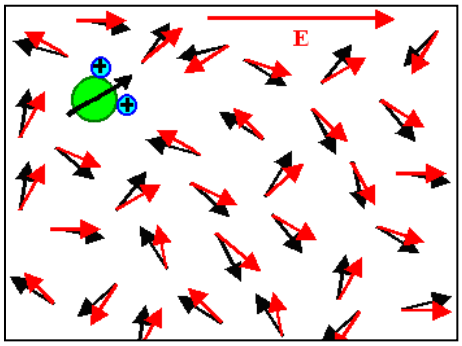

Fig.2.6 (b) With field

Fig.2.6 Schematic of the dipolar orientation process.

Dipolar polarization is frequency dependent and active in low and microwave frequency region (~ 10^{11}-10^{12} Hz) [20]. Dipolar polarization decreases with the increase in temperature. This is understandable because, higher the temperature, the greater will be the thermal energy, which increases the randomizing effect of the dipoles and acts against the orientation of the dipoles in the field direction.

2.6.2 Ionic Polarization

Ionic polarization is polarization which is caused by relative displacements between positive and negative ions in ionic crystals (for example, NaCl). If crystals or molecules do not consist of only atoms of the same kind, the distribution of charges around an atom in the crystals or molecules leans to positive or negative. As a result, when lattice vibrations or molecular vibrations induce relative displacements of the atoms, the centers of positive and negative charges might be in different locations. These center positions are affected by the symmetry of the displacements. When the centers don't correspond, polarizations arise in molecules or crystals. This polarization is called ionic polarization. Ionic polarization

causes ferroelectric transition as well as dipolar polarization. The transition, which is caused by the order of the directional orientations of permanent dipoles along a particular direction, is called order-disorder phase transition. The transition which is caused by ionic polarizations in crystals is called displacive phase transition. Since the entire ions which are heavier than electrons are displaced this mechanism is only active up to 10^{12} - 10^{13} Hz (Infra-red frequencies).This mechanism is also temperature independent. Fig.2.7 shows the situation where the distance between the ions increases by d; the symmetrical situation, where the distance decreases by d, is obvious.

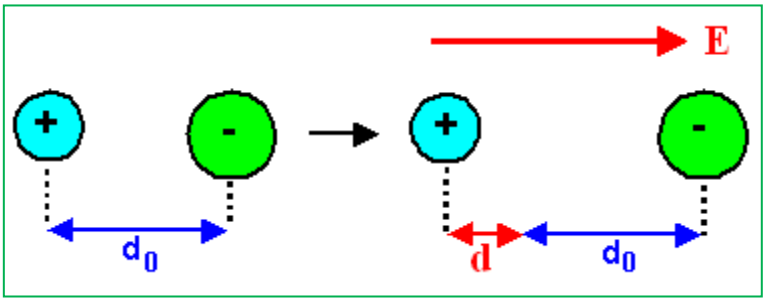

Fig.2.7 Scematic of the ionic polarization.

2.6.3 Electronic Polarization

It arises due to the relative displacement of the centers of +ve charges with respect to the centre of the –ve charges of an atom or ion when subjected to an external electric field. It is operative in all dielectrics and is temperature independent. Electronic polarization is active in the optical (visible-ultravoilet) frequency range (~ 10^{15}-10^{16} Hz). Electronic structure of an atom is independent of temperature; hence temperature has no effect on it.

2.6.4 Interfacial Polarization

In polycrystalline materials, the inter-grain boundaries are zones, where free charges (interstitial ions, vacancies, injected electrons etc.) may accumulate and cause polarization of the crystallites, which is known as interfacial polarization. The notion of interface polarization is related to separate surfaces between crystallites, which act as barriers to the motion of free charges from one crystallite to the other and is a characteristics of polycrystalline materials [21]. Interfacial polarization is prominent in low frequency (10^{-3} - 10^{3} Hz) and high temperature range. It is active in low frequency region, As the frequency is increased, the time required for the interfacial charges to be polarized is delayed. At high temperatures the increase of defect or impurities gives rise to interfacial polarization.

2.7 Dielectric Properties

Ferroelectric materials are very often dielectrics. For most applications of ferroelectric materials, the dielectric constant (ε_r) and dielectric loss ($\tan\delta$) are important practical parameters, and studies of the dielectric properties provide a great deal of information about the applicability of the ferroelectric materials in various applications.

2.7.1 Dielectric Constant (ε_r)

The relative dielectric constant (ε_r) of a material is the ratio between the charge stored on an electroded slab of material brought to a given voltage and the charge stored on a set of identical elctrocdes, separated by vacuum. It is defined as

$$\varepsilon_r = 1 + P/\varepsilon_o E \qquad (2.3)$$

where ε_r = Dielectric constant or relative permittivity of the material

E= Net electric field in the presence of dielectric material

P = Induced dipole moment / volume under an applied electric field E

ε_o= Permittivity of the free space

And, for an alternating electric field, the dielectric constant can be written as

$$\varepsilon_r = \varepsilon' - i\varepsilon'' \quad (2.4)$$

Where ε' is the real component of the dielectric constant/ relative permittivity, in phase with the applied external field E. ε'' is the imaginary component, 90^o out of phase with the applied external electric field, caused by either resistive leakage or dielectric absorption. For normal substances, the value of ε_r is low, usually under 5 for organic materials and under 20 for most inorganic solids. Ferroelectric ceramics, however generally have much higher ε_r, typically several hundred to several thousand [22].

2.7.2 Dielectric Loss (tanδ)

The charging current in an ideal dielectric leads the applied voltage by $\pi/2$ radians (90^o). However, in real dielectrics in addition to the charging current, associated with the storage of electric charge by the dipoles, a loss current must also be considered. The loss current arises from the long-range migration of charges, e.g., dc ohmic conduction and the dissipation of energy associated with the rotation or oscillation of dipoles [22]. As there is no dielectric which is a perfect insulator (is not loss free), it is generally represented by a complex dielectric constant, defined in equation 2.4. The total current in the real dielectric is a complex quantity which leads the voltage by an angle (90-δ), where δ is called the loss angle. Dielectric loss (tanδ), also known as dissipation factor, is defined as $\tan\delta = \varepsilon''/\varepsilon'$. The inverse of the loss tangent, $Q = (1/\tan\delta)$, is used as a figure of merit in high frequency piezoelectric applications.

2.8 Diffuse Phase Transition

In macroscopic homogeneous materials, the observed transition temperature is not sharply defined. The transition is smeared out over a certain temperature interval, resulting in a gradual change of physical properties in this temperature region. This phase transition is called as diffuse phase transition (DPT). Though this phenomenon is observed in several types of materials, however the most remarkable examples of DPT are found in ferroelectric materials. In the early 1950's ferroelectric diffuse phase transitions (FDPT) were first mentioned in the literature. The diffuseness of the phase transition is assumed to be due to the occurrence of fluctuations in a relatively large temperature interval around the phase transition temperature. Usually here two kinds of fluctuations are considered: (a) compositional fluctuation and (b) polarization (structural) fluctuation. From the thermodynamic point of view, it is clear that the compositional fluctuation is present in ferroelectric solids-solutions and polarization fluctuation is due to the small energy difference between high and low temperature phases around the transition temperature. This small entropy difference between ferroelectric and paraelectric phases will cause a large probability of fluctuation. According to Fritsberg, substances of less stability are expected to have a more diffuse transition [23]. For relaxor as well as other FDPT, the width of the transition region is mainly important for practical applications. Complex perovskite type ferroelectrics with distorted cation arrangements show DPT which is characterized by a broad maximum for the temperature dependence of dielectric constant (ε_r) and dielectric dispersion in the transition region. For DPT, ε_r follows modified temperature dependence Curie Weiss law [24-26].

$$\epsilon = \epsilon_0 + \frac{C}{(T-T_m)^\gamma} \qquad (2.5)$$

where, T_m is the temperature at which ε_r reaches maximum (ε_m), C is the modified Curie constant and γ is the critical exponent. The γ factor explains the diffusivity of the materials, which lies in the range $1<\gamma<2$. In case of γ equals to unity, normal Curie–Weiss law is followed and it shows the normal ferroelectric phase transition [27]. Whereas on the basis of a local compositional fluctuation model, the value of $\gamma=2$ corresponds to a completely diffused system [28]. For systems exhibiting intermediate value of diffusivity ($1\leq\gamma\leq2$) the materials are complex, hence partially disordered.

2.9 Ferroelectric Properties

The most important characteristic of ferroelectric materials is polarization reversal (or switching) by an applied external electric field. Mainly domain-wall switching in ferroelectric materials lead to the development of polarization vs. electric field (P-E) ferroelectric hysteresis loop. This hysteresis loop can be observed experimentally by using a Sawyer – Tower circuit [29].

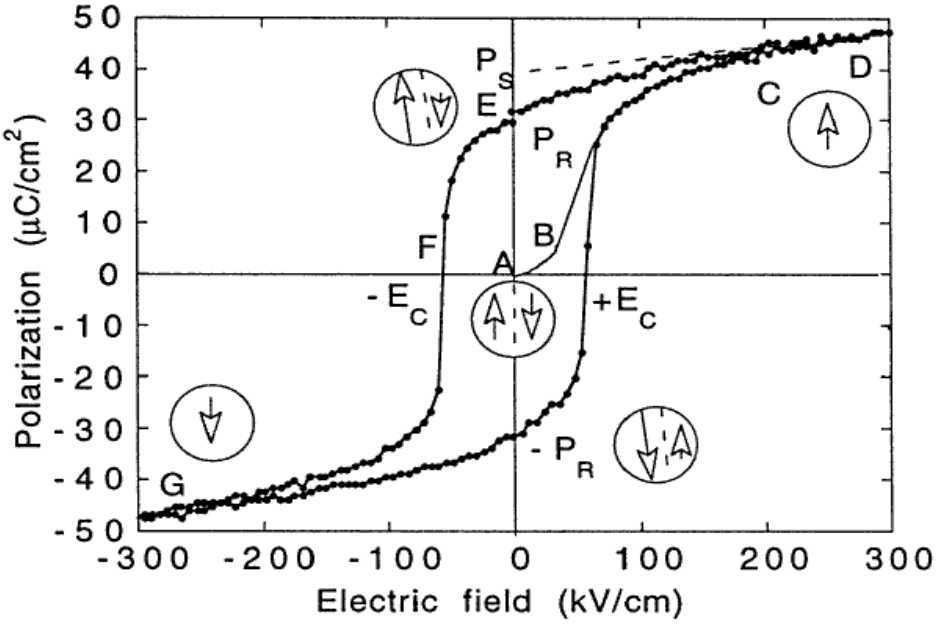

Fig. 2.8 Ferroelectric P –E/ hysteresis loop. (Circles with arrows represent the polarization state of the material at the indicated fields).

Fig. 2.8 shows P–E hysteresis loop in a ferroelectric material. At small values of the electric field, the polarization increases linearly with the field amplitude,. As the field is increased the polarization of domains with an unfavourable direction of polarization will start to switch in the direction of the field, rapidly increasing the measured charge density. An ideal hysteresis loop is symmetrical so that $+E_C = -E_C$ and $+P_R = -P_R$. The coercive field, spontaneous and remanent polarizations and shape of the loop may be affected by many factors including the thickness of the sample, the presence of charged defects, mechanical stresses, preparation conditions, and thermal treatment. The mechanism of polarization switching has been studied in detail for many bulk and thin-film ferroelectrics [30]. The polarization reversal takes place by the growth of existing antiparallel domains, by domain-wall motion, and by nucleation and growth of new antiparallel domains, which is shown in Fig. 2.9 [31].

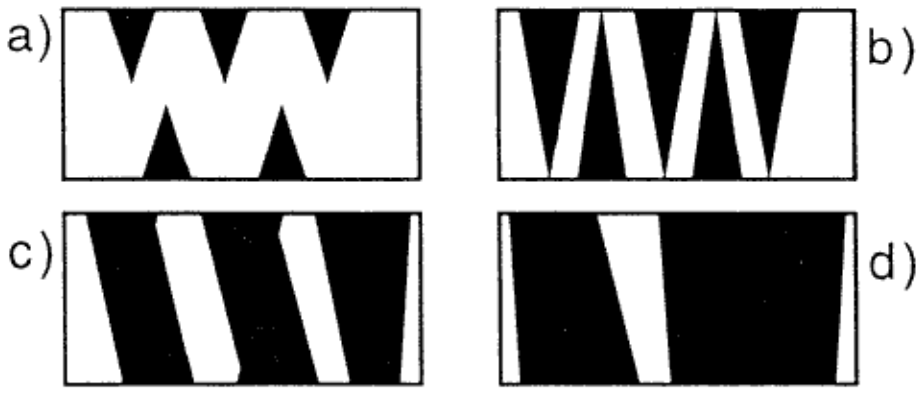

Fig.2.9 Probable sequence of polarization switching in ferroelectrics: (*a*) nucleation of oppositely oriented domains, (*b*) growth of oppositely oriented domains, (*c*) sidewise motion of domain walls and (*d*) coalescence of domains.

P-E hysteresis loop is also a function of temperature and usually area of the loop shrinks with the increase in temperature until a phase transition takes place [22]. At this point no P-E loop is observed and this temperature is called Curie temperature, T_c.

2.10 Poling

Ferroelectric crystals possess regions with uniform polarization called ferroelectric domains. Within a domain, all the electric dipoles are aligned in the same direction. There may be many domains in a crystal separated by boundaries called domain walls. Adjacent domains can have their polarization vectors in antiparallel directions, at right angles to one another etc. Adjacent domains having polarization vectors antiparallel directions and at right angles are known as having 180^o or 90^o domain walls.

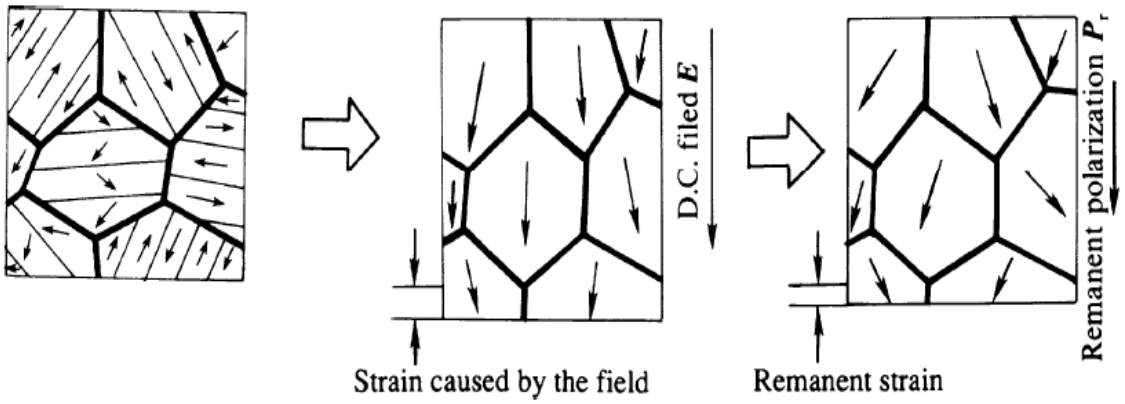

Fig. 2.10 Schematic illustration of the poling process.

A ferroelectric polycrystalline material possesses multiple ferroelectric domains. A single domain can be obtained by domain wall motion made possible by the application of a sufficiently high electric field, the process known as poling. Poling is very important for the application of polycrystalline ferroelectric ceramics. Ferroelectric ceramics do not possess any piezoelectric properties owing to the random orientations of the ferroelectric domains in the ceramics before poling. During poling, a DC electric field is applied on the ferroelectric sample to force the domains to be oriented or "poled". After poling, the electric field is removed and a

remnant polarization and remnant strain are maintained in the sample, and the sample exhibits piezoelectricity. A simple illustration of the poling process is shown in Fig. 2.10.

2.11 Strain vs. Electric Field Behavior

In addition to the polarization–electric field hysteresis loop, polarization switching by an electric field in ferroelectric materials also leads to strain–electric (S-E) field hysteresis. The strain–electric field hysteresis loop, which resembles the shape of a butterfly, arises due to three types of effects. One is the converse piezoelectric effect of the lattice, and the other two are due to switching and movement of domain walls. Ceramic samples usually contain a number of non-180^{o} domains. In addition to the pure piezoelectric response of the material within each domain [32], the movement and switching of non-180^{o} domain walls may involve a significant change in dimensions of the sample.

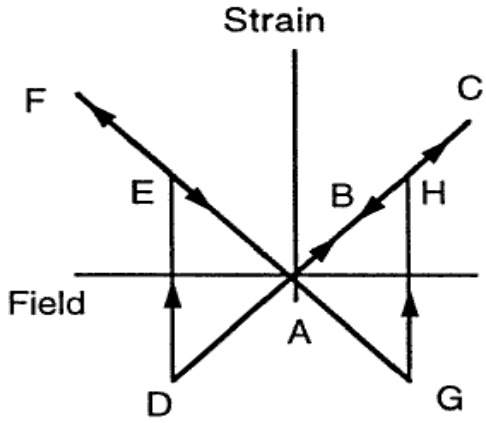

Fig. 2.11 Strain–electric field (S–E)/ hysteresis loop (butterfly loop) in piezoelectrics.

Fig. 2.11 shows the strain vs. electric field (S-E) hysteresis loop in a ferroelectric material. At zero field (point A) the strain of the crystal is taken to be zero. The electric field is then applied in the direction of the spontaneous polarization. As the field is increased, the crystal expands through the piezoelectric effect, and the strain traces the path A–B–C. The expansion continues

until the maximum field is reached (point C). At point C, the field starts to decrease, but is still parallel to P_S. The strain of the sample traces the same line but in the opposite direction (from C to A). At point A the strain is again zero. The field then changes its direction, becoming antiparallel to P_S. As the field strength increases in the negative direction, the crystal contracts with respect to point A. At point D the field is large enough to switch the direction of polarization. After switching, the polarization becomes parallel to the field, and the strain becomes positive again (point E). During further increase of the field in the negative direction, strain increases to point F, and then decreases back to point A as the field is decreased [33]. The reversal of the polarization and sudden change of the strain happens again at point G. The strain–field curve is linear, indicating that the strain is purely piezoelectric except at the switching points D and G.

2.12 Piezoelectric Parameters

The piezoelectric charge coefficients (d_{31} and d_{33}), the piezoelectric voltage coefficients (g_{31} and g_{33}) and the piezoelectric coupling factors (k_{31}, k_{33}, k_p and k_t) are the important piezoelectric parameters.

2.12.1 Piezoelectric Charge Coefficients

Piezoelectric coefficients can be measured using either the direct or converse piezoelectric effects. The piezoelectric coefficients in the direct and converse piezoelectric effects are thermodynamically identical. In order to measure the piezoelectric coefficients using the direct piezoelectric effect, a normal load is applied to a ferroelectric capacitor and the charge on the electrodes is measured. To measure the

piezoelectric coefficients using the converse piezoelectric effect, an electric field is applied and the strain in the ferroelectric material is measured.

The equations for the direct and converse piezoelectric effects are given below:

$$D = d\,T \quad \text{(Direct effect)} \qquad (2.6)$$

$$S = d\,E \quad \text{(Converse effect)} \qquad (2.7)$$

Where in equation (2.6) "d" is piezoelectric charge coefficient, 'D' is the dielectric displacement, 'T' the mechanical stress, whereas in equation (2.7) 'E' is the electric field and 'S' the mechanical strain, respectively. The piezoelectric coefficient is direction dependent i.e., tensor quantity. The longitudinal piezoelectric coefficient (d_{33}) is the value of the piezoelectric coefficient that applies to the distortion measured in the same direction as the electric field. To measure the longitudinal piezoelectric coefficient, the electrical response is parallel to the applied stress. The value measured in the direction perpendicular to an electric field is called the transverse piezoelectric coefficient (d_{31}). For the transverse piezoelectric coefficient, a stress is applied in the plane of the material and the induced charge is measured along the perpendicular direction (along which direction). High d constant is desirable for materials intended to develop motion or vibration, such as sonar or ultrasonic cleaner transducers applications [22].

2.12.2 Electromechanical Coupling Coefficient

The electromechanical coupling coefficient is defined as the ratio of the mechanical energy accumulated in response to an electrical input or vice versa. The piezoelectric coupling coefficient can be expressed as [34]:

$$K = \frac{\text{Mechanical energy converted to electrical energy}}{\text{Input mechanical energy}}$$

Or

$$K = \frac{\text{Electrical energy converted to mechanical energy}}{\text{Input electrical energy}} \qquad (2.8)$$

Under dynamic DC conditions, as opposed to static DC conditions, the behaviour of the piezoelectric materials is much more complex. It can be characterized in terms of an equivalent electrical circuit which exhibits both parallel and series resonance frequencies. To approximate these frequencies, the frequency of the minimum impedance (f_r) and maximum impedance (f_a) for the material are measured as shown in Fig. 2. 12.

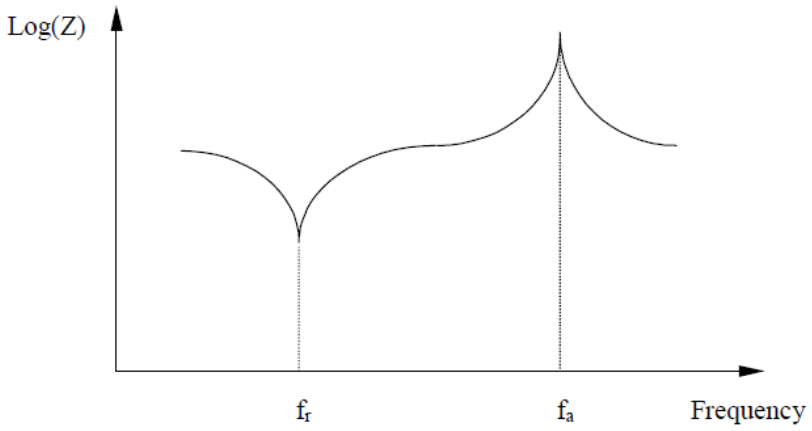

Fig. 2.12. A typical impedance curve of the equivalent circuit for measuring the impedance frequencies [35].

The f_r and f_a are called as resonance and anti-resonance frequencies. The resonance frequency is the frequency at which the sample vibrates most readily and most efficiently converts the input electrical energy to the mechanical energy [36]. Fig.2.13 shows that initially with increase in frequency the impedance decreases and reaches a minimum value at f_r, with further increase in frequency impedance increases and reaches a maximum value at f_a. K can be

determined by the dimension of the ceramic element. For a thin disc of piezoelectric ceramic, the planar mode coupling coefficients (k_p) expresses radial coupling, the coupling between the electric field parallel to the direction in which the ceramic element is polarized and mechanical effects that produce radial vibrations. The resonance measurement of a material is strongly dependent on its geometry. To assure isolation of the resonance, sample geometry must be chosen carefully [36]. Geometries suitable for measuring the different piezoelectric and elastic coefficients are presented in Table-2.1.

Table-2.1 Sample geometries for measurement of material properties.

		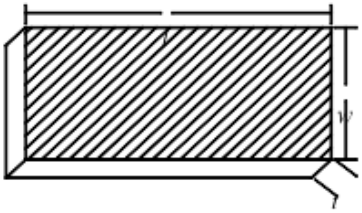	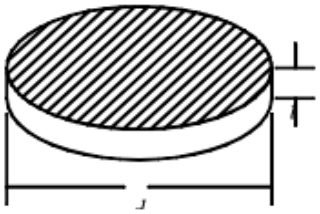
Dimensional Requirements	long, slender, length poled rod; $l > 3d$	thin, flat plate, thickness poled; $l > 3.5\ t,\ w$	thin flat disc, thickness poled $d > 10\ t$
Properties Measured	$K_3^T, k_{33}, \tan\delta, s_{33}^D,$ $s_{33}^E, d_{33}, g_{33}, Q_M$	$K_3^T, k_{31}, \tan\delta, s_{11}^D,$ $s_{11}^E, d_{31}, g_{31}, Q_M$	$K_3^T, k_p, \tan\delta, Q_M$

References

[1] A.J. Moulson & J.M. Herbert, "Electroceramics: Materials, Properties and Application", Chapman and Hall (1990).

[2] G. C. C. da Costa, A. Z. Simoes, A. Ries, C. R. Foschini, M. A. Zaghete, and J. A. Varela, Mater. Lett., 21, (2004) 414.

[3] M. N. Rahaman, Sintering of Ceramics (CRC Press, Florida, 2008).

[4] L. Levinson, Method of firing ceramic articles utilizing microwave energy, (1971).

[5] R. Roy, S. Komarnenl, and J. L. Yang, J. Am. Ceram. Soc., 68, (1985) 392.

[6] M. Venkata Ramana, S. Roopas Kiran, N. Ramamanohar Reddy, K.V. Siva Kumar, V.R.K. Murthy, B.S. Murty, Mater. Chem. Phys., 126, (2011) 295.

[7] S. Mahajan, O.P. Thakur, D.K. Bhattacharyaa, K. Sreenivas, Mater. Chem. Phys., 112, (2008) 858.

[8] D. E. Clark, and W. H. Sutton, Annual Rev. Mater. Sci., 26, (1996) 299.

[9] A D. John, The Analytical Chemistry Handbook. (McGraw Hill New York1995).

[10] A.S. Douglas; F. J. Holler; A.T. Nieman, Principles of Instrumental Analysis (Saunders college publication New York1998.)

[11] K.G. Berger, E.E. Akehurst, Int. J. Food Sci. Technol., 1, (1966) 237.

[12] M. Ladd and R. Palmer, Structure Determination by X-ray Crystallography (Kluwer Academic/Plenum Publishers, New York, 2003).

[13] L. E. Smart and E. A. Moore, Solid State Chemistry (Taylor & Francis, London 2005).

[14] A. R. West, Basic Solid State Chemistry (John Wiley & Sons, New York, 1999).

[15] B.D. Cullity, Elements of X-Ray Diffraction, **(**Addison-Wesley, 1956).

[16] E. Suzuki, J. of Microscopy., 208, (2002) 153.

[17] G. I. Goldstein, D. E. Newbury, P. Echlin, D. C. Joy, C. Fiori, E. Lifshin, Scanning electron microscopy and x-ray microanalysis.(Plenum Press ,New York 1981).

[18] C. E. Effree, N. D. Read, Ambient and Low-temperature scanning electron microscopy (Academic Press London 1991).

[19] R. V. Hippel, Dielectric materials and applications, (Cambridge Technology Press of MIT, 1995).

[20] I. Bunget and M. Popescu, Physics of Solid Dielectrics, (Elsevier, New York, 1984).

[21] L. L. Hench and J. K. West, Principles of Electronic Ceramics, (John Wiley & Sons, New York 1989).

[22] B. Jaffe, W. Cook and H. Jaffe, Piezoelectric Ceramics (Academic Press, London, 1971).

[23] G. H. Jonker, Mater. Res. Bull., 18, (1983) 301.

[24] J. Fritesberg, Proc. 4th Int. Meeting on Ferroelectricity, Leningrad (1977).

[25] J. Hao, Z. Xu, R. Chu, W. Li, G. Li, and Q. Yin, J. Alloy. Compd., 484, (2009) 233.

[26] X. G. Tang, J. Wang, X. X. Wang, and H. L. W. Chan, Solid State Commun., 131, (2004)163.

[27] L. E. Cross, Ferroelectrics, 76, (1987) 241.

[28] A. Shukla and R. N. P. Choudhary, Physica B: Condensed Matter, 405, (2010) 2508.

[29] C. B. Sawyer and C. H. Tower, Phys. Rev., 35, (1930) 269.

[30] M. E. Lines and A. M. Glass, Principles and Applications of Ferroelectrics and Related Materials (Oxford: Clarendon, 1979).

[31] V. Shur and E. Rumyantsev, J. Korean. Phys. Soc., 32, (1988) S727.

[32] D. Damjanovic, Rep. Prog. Phys., 61**,** (1998) 1267.

[33] M. E. Caspari and W. J. Merz, Phys. Rev., 80, (1950) 1082.

[34] T. Ikeda, Fundamentals of piezoelectricicty (Oxford University Press, New Work, 1990)

[35] G. H. Haertling, J. Am. Ceram. Soc. 82, (1999) 797.

[36] http://americanpiezo.com/piezo-theory/.

CHAPTER-3

Experimental Details

3.1 Introduction

This chapter describes the various steps involved in the synthesis of the compounds selected for the present work by conventional and microwave processing techniques. The details about the instruments used for the various characterizations of the samples are also given in detail.

3.2 Conventional Processing

The following series of KNN-LS based ceramics were synthesized by conventional solid state reaction route:

i. $(1-x)[K_{0.5}Na_{0.5}NbO_3]-x[LiSbO_3]$ (x=0, 0.04, 0.05, 0.06)

ii. $0.95[(K_{0.5}Na_{0.5})_{1-x}Ag_xNbO_3]-0.05LiSbO_3$ (x=0, 0.02, 0.04, 0.06, 0.08)

iii. $0.95[(K_{0.5}Na_{0.5})\ Nb_{1-x}\ Ta_xO_3]-0.05LiSbO_3$ (x=0, 0.02, 0.04, 0.06, 0.08)

iv. $0.95[(K_{0.5}Na_{0.5})\ Nb_{1-x}V_xO_3]-0.05LiSbO_3$ (x=0, 0.02, 0.04, 0.06, 0.08)

The various steps involved in conventional processing of the above mentioned ceramics are represented as a flow chart and shown in Fig.3.1. In the present work, the raw materials such as; K_2CO_3, Na_2CO_3, Li_2CO_3, Sb_2O_5, Ag_2O, Ta_2O_5 and V_2O_5 (with high purity > 99%) were used for the material preparation. The raw materials were first dried at ~ 200^oC in order to remove the moisture. Stoichiometric weights of all the powders were mixed and ball milled with acetone for 8h, using zirconia balls as the grinding media. After drying the slurry in an oven, the calcinations of the powders were carried out at 850^0C for 6h. Single perovskite phase formation was confirmed by X-ray diffraction (XRD) technique. After calcination, the powders were mixed with polyvinyl

alcohol (PVA) (which acts as a binder) to reduce the brittleness and to have better compactness amongst the granules of the powders. The green pellets of dimensions with diameter ~12 mm and thickness ~1.5 mm were made using uniaxial isostatic cold press with the help of tungsten carbide dye. The sintering of the pellets was carried out in a conventional high temperature furnace. Initially, the temperature of the pellets were raised to 600^{o}C with a very slow heating rate ~ 5^{o}C/min. and kept there for 2h to completely remove the binder. Then the pellets were sintered at a desired high temperature with a soaking time of 4h to increase the density. The sintering temperature was optimized for each composition to achieve better density in the ceramics. In order to examine the phases present in the system, XRD analysis of the sintered KNN ceramics were performed on a PW 3020 Philips diffractometer using Cu Kα (λ=0.15405 nm) radiation. The sintered microstructures were observed using a JEOL JSM-6480LV scanning electron microscope (SEM). For SEM measurement, the surface of the samples were made conducting by applying a thin layer of platinum coating. The experimental densities (d_{ex}) of the samples were measured by the Archimedes method. For electrical measurement, silver paste was applied on both sides of the sintered ceramics and fired at 500°C for 30 min for good adhesion. Dielectric constant (ε_r) and dielectric loss ($\tan\delta$) were measured as a function of temperature using a computer interfaced HIOKI 3532-50 LCR-HITESTER. The ferroelectric property was characterized by the measurement of polarization as a function of electric field using precision premier II, a standard ferroelectric testing machine (Radiant Technology). The samples for the piezoelectric property measurements were poled by corona poling unit in the temperature range from RT to above the orthorhombic to tetragonal phase transition temperature by applying a dc

electric field of 5kV/mm for 20 min. The d_{33} values of the samples were measured by Piezo meter (YE2730A d_{33} Meter, APC International Ltd.). The electromechanical coupling coefficient (k_p), mechanical quality factor (Q_m) was measured by resonance and anti-resonance method. The strain vs electric field loop behavior was studied by using precision premier II, a standard ferroelectric testing machine (Radiant Technology) with the help of MTI-2100 Fotonic Sensor.

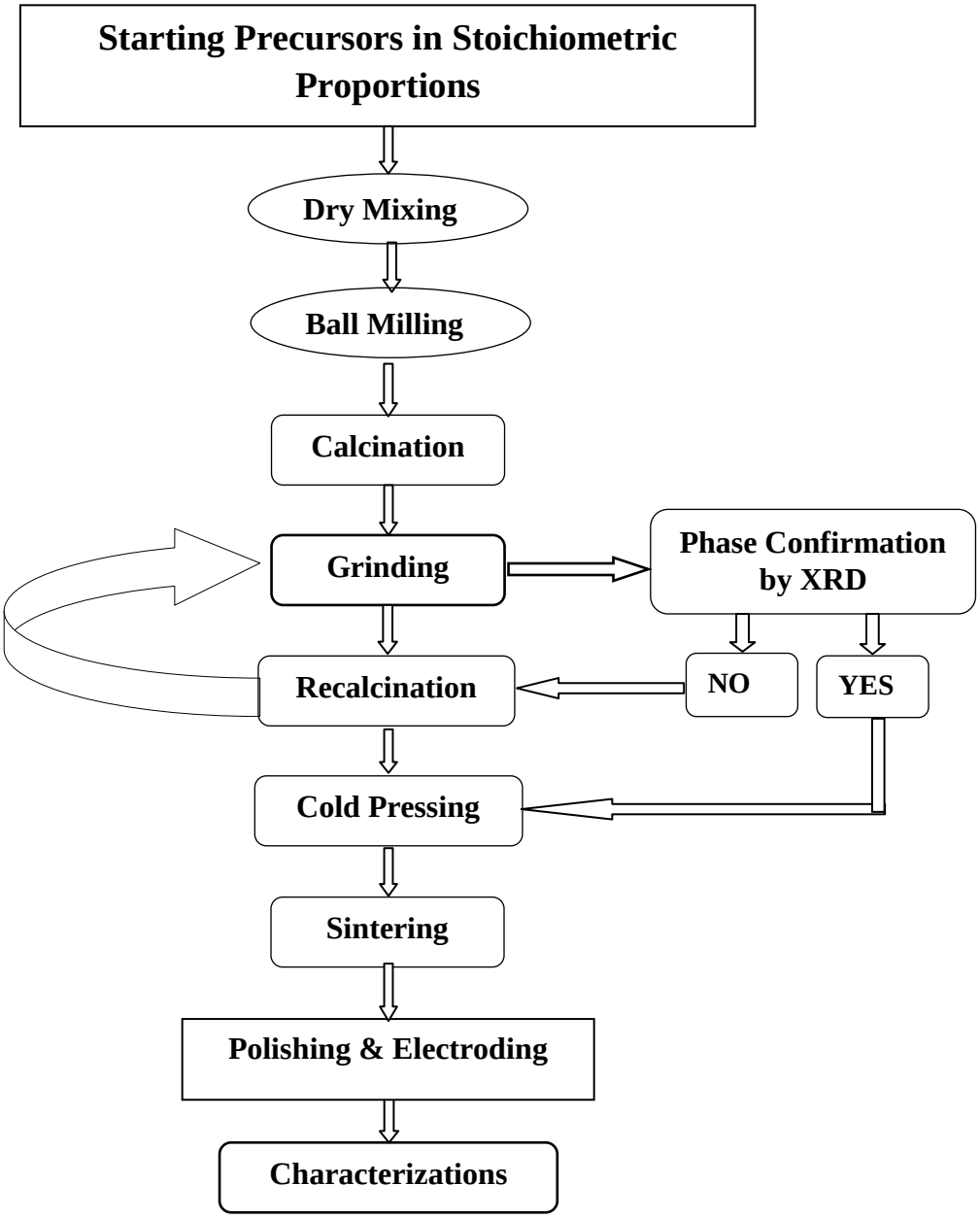

Fig. 3.1 Flowchart of the conventional synthesis process.

3.3 Microwave Processing

The following series of KNN-LS based ceramics are synthesized by microwave processing technique:

I. $0.95[K_{0.5}Na_{0.5}NbO_3]$-$0.05[LiSbO_3]$

II. $0.95[(K_{0.5}Na_{0.5})_{0.94}Ag_{0.06}NbO_3]$-$0.05LiSbO_3$

III. $0.95[(K_{0.5}Na_{0.5})Nb_{0.98}Ta_{0.02}O_3]$-$0.05LiSbO_3$

IV. $0.95[(K_{0.5}Na_{0.5})Nb_{0.94}V_{0.06}O_3]$-$0.05LiSbO_3$

The raw materials such as; K_2CO_3, Na_2CO_3, Li_2CO_3, Sb_2O_5, Ag_2O, Ta_2O_5 and V_2O_5 (with high purity > 99%) were used for the synthesis of these above compounds. The raw materials were first dried at ~ 200^oC in order to remove the moisture. Stoichiometric weights of all the powders were mixed and ball milled with acetone for 8 h, using zirconia balls as the grinding media. After drying the slurry in an oven, the calcination of the powders was carried out at 850^0C for 20 mins, 40 mins and 60mins, respectively by keeping the powders in an alumina crucible, surrounded by rectangular SiC slabs, at the centre of a microwave furnace, shown in Fig.3.2. For XRD characterizations of the calcined powders were grinded in a mortar-pestle to obtain homogeneous powders. The powder calcined at 850^0C for 60min was mixed thoroughly with 2wt% polyvinyl alcohol (PVA) and pressed into disks of diameter ~ 10 mm and thickness ~ 1.5 mm under ~60MPa pressure. The microwave sintering was carried out by placing the pellets in the centre of a 4.4 kW, 2.45-GHz multi-mode microwave cavity surrounded by rectangular SiC slabs with a heating rate of 30^oC/min.. SiC slabs were used because it absorbs the microwave and transfers to the material. The microwave furnace temperature was recorded by using a Raytek non-contact sensor (XRTG5).

Schematic diagram of microwave furnace is shown in Fig. 3.2. In order to examine the phases present in the material, the XRD analyses of the pellets were performed using PW 3020 Philips diffractometer equipped with Cu Kα (λ=0.15405 nm) radiation. The microstructures of the as sintered pellets were examined using JEOL JSM-6480LV scanning electron microscope (SEM). The various steps involved in microwave processing are represented as a flow chart and is shown in Fig.3.3.

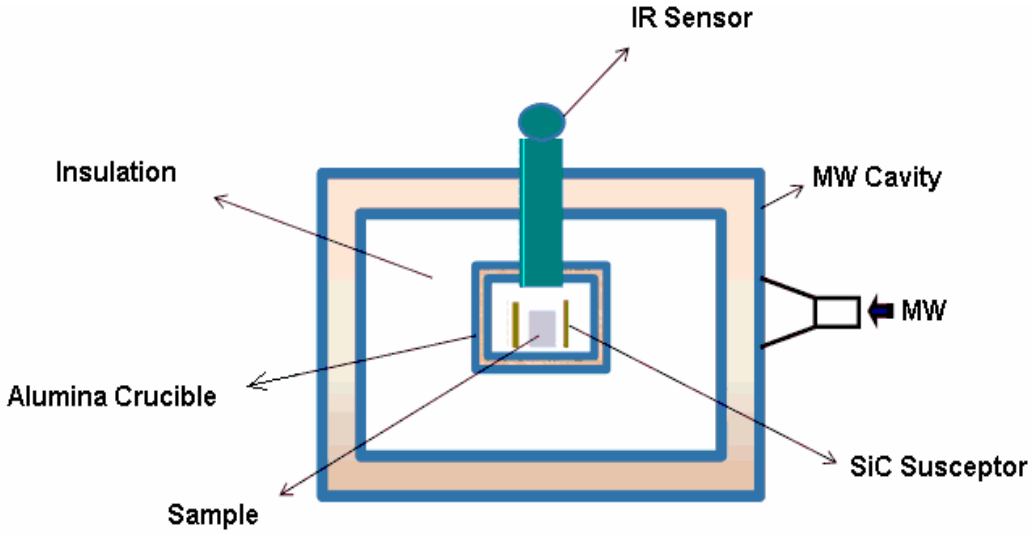

Fig.3.2 Schematic diagram of microwave sintering system.

The experimental densities (d_{ex}) of the samples were measured by the Archimedes method. For electrical measurement, silver paste was applied on both sides of the sintered ceramics and fired at 500°C for 30 min for good adhesion. Dielectric constant (ε_r) and dielectric loss ($\tan\delta$) were measured as a function of temperature using a computer interfaced HIOKI 3532-50 LCR-HITESTER. The ferroelectric property was characterized by the measurement of polarization as a function of electric field using precision premier II, a standard ferroelectric testing machine (Radiant Technology). The samples for the piezoelectric property measurements were poled by corona poling unit in the temperature range from RT to above the orthorhombic to tetragonal phase transition

temperature by applying a dc electric field of 5kV/mm for 20 min. The d_{33} values of the samples were measured by Piezo meter (YE2730A d_{33} Meter, APC International Ltd.). The electromechanical coupling coefficient (k_p) was measured by resonance and anti-resonance method. The strain vs electric field loop behavior was studied by using precision premier II, a standard ferroelectric testing machine (Radiant Technology) with the help of MTI-2100 Fotonic Sensor.

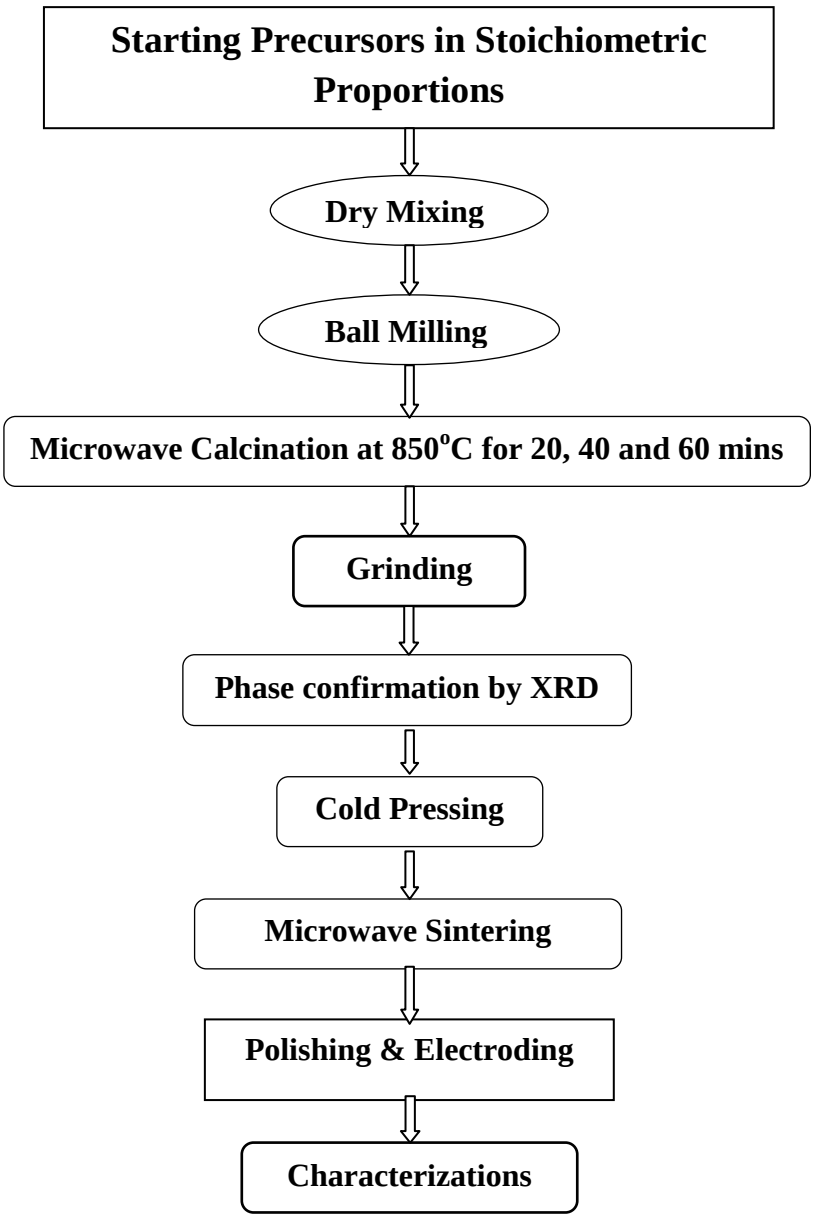

Fig.3.3 Flowchart of the microwave synthesis process.

3.4 Investigated Parameters

This section describes the details about the measurement of various structural, microstructural and electrical properties.

3.4.1 Phase Evolution and Crystal Structural Study

X-ray diffraction patterns of all the samples were collected to find out the crystal structure and the unit cell parameters of the unit cell. XRD analysis was performed on a PW 3020 Philips diffractometer using Cu Kα (λ=0.15405 nm) radiation. The diffraction data was taken in the 2θ range from 20^o to 70^o. Cu $K\alpha_2$ radiation was stripped from the collected XRD data by using standard software "X'pert high score". The 2θ values, corresponding to the peaks were noted from the diffraction patterns. The crystal structure and unit cell parameters were obtained, using a computer program package 'POWD' [1]. The XRD peaks were deconvoluted in the 2θ range from 44-47 degrees by using the Peakfit software with Gaussian approximations [2]. The fraction of the tetragonal phase (f_T) and orthorhombic phase (f_O) is determined from the integrated peak intensities of the two phases (I_T and I_O) using equation (3.1) & (3.2) [3].

$$f_T = I_T/(I_T + I_O) = \{I(002)_T + I(200)_T\} / \{I(002)_T + I(200)_T + I(002)_O + I(020)_O\} \quad (3.1)$$

$$f_O = I_O/(I_O + I_T) = \{I(002)_O + I(020)_O\} / \{I(002)_O + I(020)_O + I(002)_T + I(200)_T\} \quad (3.2)$$

where $I(002)_T$, $I(200)_T$, $I(002)_O$ and $I(020)_O$ are the integrated intensities of the tetragonal (002) and (200) peaks and orthorhombic (020) and (200) peaks, respectively.

3.4.2 Densification Study

The experimental densities of the sintered samples were measured using Archimedes method. First of all, the dry weights of the sintered samples were measured by a digital electronic balance. The sintered samples were then immersed in a glass beaker containing kerosene oil and kept under a vacuum for 30 mins to ensure that the liquid filled up the open pores completely. The suspended weight of the pellet was then measured in kerosene. Then the soaked weight was measured by blotting the pellet with a wet paper towel. The experimental densities (d_{ex}) were calculated by using the following relation:

$$d_{ex} = W_{dry} / (W_{soaked}-W_{suspended}) \text{ g/cc.} \quad (3.3)$$

Where d_{ex} is the density of the sample. Here, W_{dry} and W_{soaked} are the dry and soaked weight of the material in air and in kerosene oil, respectively.

Relative densities (RD) of different sintered samples were calculated from the d_{ex} and X-ray density (d_x). Since, the macroscopic samples usually contains minute cracks and pores, hence d_{ex} is always less than and cannot exceed the d_x. X-ray density (d_x) was calculated using the following formula [4]:

$$d_X = \left(\frac{Z \times M}{N \times V} \right) \quad (3.4)$$

Where,

Z = No. of formula units per unit cell

M = Molecular weight (gm)

N = Avogadro's number

V = Unit cell volume $(Å)^3$

Relative density (RD) of the samples were calculated using the following relation:

$$RD = (d_{ex}/ d_x) \times 100 \qquad (3.5)$$

3.4.3 Grain Morphology Study

In the present work, the topographical and morphological study was carried out by using JEOL JSM-6480LV Scanning Electron Microscope. It was used to determine the average grain size and to observe surface morphology of the samples. The average (Avg.) grain size of the samples was calculated by diagonal intercept method with the help of the "Image J" software. The avg. grain size was measured by drawing lines of known length diagonally on the micrograph. The number of grains intersected by the lines were counted. Then the avg. grain sizes were calculated by dividing the length of the line by the no. of grain coming under that line.

3.5 Electroding of the Samples

The sintered pellets were polished to achieve a thickness of ~1mm and cleaned with acetone. Sufficient care was taken to keep the faces of the pellets parallel. Then thin layer of silver paste was applied on both side of the samples and fired in an oven at 500°C for 30 min to ensure good adhesion. The pellets now act as dielectric medium between the two parallel metallic plates. Now, the samples are ready for electrical measurements.

3.6 Poling

The schematic diagram of the corona discharge method is shown in Fig. 3.4. With this method, the bottom and top electrodes are metallic plate, whereas the forming metallic electrode is usually made of a metallic wire (e.g., brass wire), with one end polished to a sharp point so that voltage of only a few kV between the two electrodes is

sufficient to create a field near the point electrode, exceeding the breakdown strength of the air in a region of a few millimeters around the point electrode.

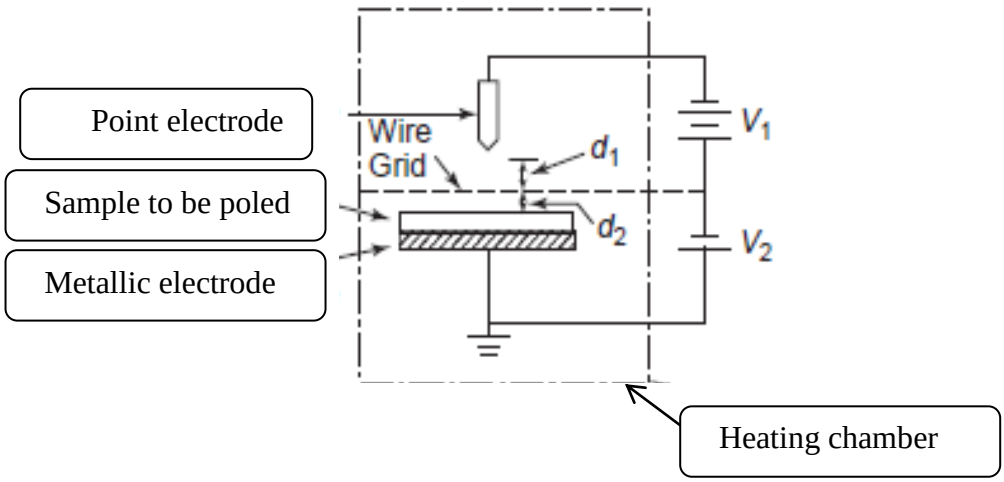

Fig. 3.4 Schematic of the corona poling method [5].

This unit consists of a sharp pointed corona needle made of brass wire of ~ 2mm diameter. The sample was placed on the metallic base plate and a high voltage (~5 kV) was applied between the corona point and the base plate. This voltage was chosen to be slightly higher than the voltage at which corona discharge starts. A bias voltage (~1.5 kV) was applied between the grid and the metallic plate to accelerate the ions. The samples were subjected to corona discharge for 20 minutes at a constant temperature. After that slowly, the temperature was decreased while the field was still active. Finally, the field was removed. During this process, the samples get polarized.

3.7 Electrical Properties

This section describes the details of various electrical properties used to study different properties of KNN-LS and modified KNN-LS ceramics.

3.8. Dielectric Measurements

In the present work, the dielectric measurements of the samples were carried out by using a computer interfaced Hioki 3532-50 LCR Hitester. The diagram of the dielectric measurement instrument is shown in Fig.3.5. The interfacing of the instrument was done by using Lab view software. The dielectric constant and dielectric loss was measured as a function of temperature at four different frequencies. The data were recorded with a heating rate of 2^{o}C/min and at an interval of 2^{o}C. The dielectric constant (ε_r) was calculated by using the following relation [6];

$$\varepsilon_r = (C \times t) / (\varepsilon_0 \times A) \qquad (3.6)$$

Where C is the measured capacitance, t is the thickness of the sample, A is the surface area of the sample and ε_0 is the permittivity of the free space (~ 8.854×10^{-12} F/m) [5].

Fig. 3.5 Diagram of the Hioki 3532-50 LCR Hitester.

3.9 Polarization vs. Electric Field (P-E) Measurements

Ferroelectric hysteresis (P-E) loops at RT for all the KNN-LS based samples were recorded using precision premier II, a standard ferroelectric testing machine (Radiant Technology). A typical ferroelectric measurement is based on the principle of Sawyer-

Tower circuit [7], which is shown in Fig.3.6. In this circuit, a step voltage (V) is applied across the pair of electrodes on the surfaces of a sample capacitor (C_s, with thickness d). This is the origin of the quantity plotted on the horizontal x-axis, which is proportional to the electric field (E=V/d) across the sample. The sample is then connected in series with a parallel RC circuit, which compensates for any phase shift due to conductivity or dielectric loss in the sample. The voltage (V_r) across the reference capacitor (C_r) is measured, and because the two capacitors are connected in series, the charge on the reference capacitor must be the same as the charge over the sample capacitor. Once the charge on the sample is known, the polarization can be determined using relation given below.

$$P = Q/A \qquad (3.7)$$

Where Q is the charge developed on the electrodes of the ferroelectric capacitor and A is the area of the electrodes.

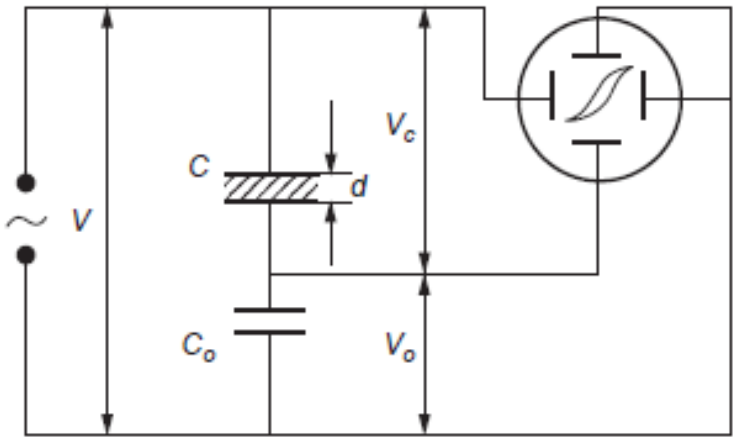

Fig.3.6 Schematic of the Sawyer–Tower circuit for the measurement of the polarization-electric field [5].

3.10 Piezoelectric Constant (d_{33}) Measurements

The piezoelectric coefficient (d_{33}) of the samples was measured by a quasi-static method using a Piezo meter (YE2730A d_{33} Meter, APC International Ltd.). The piezoelectric coefficient is defined by the following equation:

$$d_{33} = \left(\frac{D_s}{T_s} \right)_E \tag{3.8}$$

where D_s is the charge density (C/m^2) and T_s is the mechanical stress (N/m^2) at constant electric field (E). Figure 3.7 shows a schematic diagram for the d_{33} measurement using the Piezo-Meter.

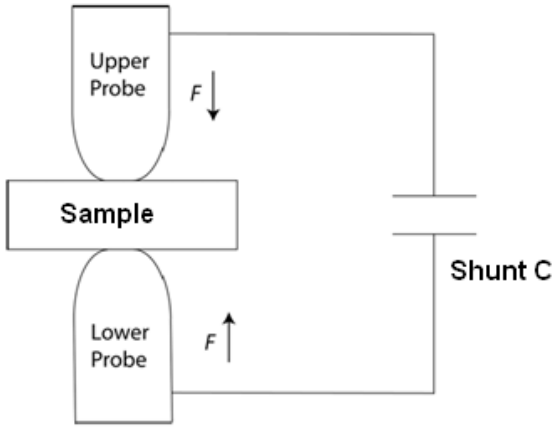

Fig. 3.7 Schematic diagram for the d_{33} measurement.

When a force (F) was applied on an area (A) of a poled sample by the upper and lower probes, a piezoelectric charge (Q) was produced due to the piezoelectric effect on the contact area (A). Hence, piezoelectric charge coefficient (d_{33}) was measured by measuring the charge developed on the surface of the sample. Equation 3.9 can be simplified as follows:

$$d_{33} = \left(\frac{Ds}{Ts} \right)_E = \frac{(Q/A)}{(F/A)} = \frac{Q}{F} = \frac{CV}{F} \tag{3.9}$$

Where C is the shunt capacitance and V is the potential difference across the shunt capacitor. The Piezo-Meter measures this potential difference, calculates the d_{33} (in pC/N) of the sample and displays the value digitally. Average d_{33} values are taken after taking measurements from various areas across a ceramic sample.

3.11 Resonance and Anti-resonance Frequency Measurement

Resonance (f_r) and anti-resonance (f_a) frequencies are used to evaluate the electromechanical coupling coefficients (k_p), mechanical quality factor (Q_m) and frequency constant (N_p). In the present work the f_r and f_a are measured by using Hioki 3532-50 LCR Hitester. In the frequency vs impedance graph, the point where impedance is minimum is called resonance frequency and the point where impedance is maximum is called anti-resonance frequency. Resonance and anti-resonance frequencies are related to each other by the equation of the form [8-9];

$$k_p^2 = 2.51\frac{(f_a - f_r)}{f_r} \qquad (3.10)$$

Where k_p is the planar mode coupling factor and it measures the efficiency of a piezoelectric material.

The mechanical quality factor is determined by the following relation [10]:

$$Q_m = \frac{1}{2\pi f_r RC}\left\{\frac{f_a^{\,2}}{f_a^{\,2} - f_r^{\,2}}\right\} \qquad (3.11)$$

Where R is the resonance impedance and C is the capacitance at 1 kHz.

3.12 Strain vs. Electric Field Measurements

Strain in a material can be induced both by bipolar and unipolar electric fields. Generally, strain versus bipolar electric field (S-E) behavior for a piezoelectric material is

a butterfly shaped loop. The strain vs. electric field loop behavior was studied by using precision premier II, a standard ferroelectric testing machine (Radiant Technology) with the help of MTI-2100 Fotonic Sensor, as shown in Fig. 3.8. It is a dual-channel, fiber-optic measurement system that performs non-contact displacement and vibration measurements. The MTI-2100 Fotonic Sensors utilize adjacent pairs of light-transmitting and light receiving fibers. Light-transmitting fibers and light receiving fibers are bundled together. The displacement is based on the interaction between the field of illumination of the transmitting fibers and the field of view of the receiving fibers. The platelet sample with electrode on both sides is connected into an external voltage source. The distance between the sample and the photonic probe is controlled by a screw device.

At contact, or zero gap, most of the light exiting the transmitting fibers is reflected directly back into the same fiber, providing very little light to the receiving fiber, which produces a zero output signal. An increase in the probe to the target distance increases [Fig. 3.8(b)], the amount of light being captured by the receiving fiber also increases. This process will continue until the entire face of the receiving fibers is illuminated with the reflected light. This point is called the "optical peak" and corresponds to maximum voltage output of the electrical signal. Further increase in distance will cause the diverging filed of reflected light to exceed the field of view of the receiving fiber, thus causing a reversal in the output-versus-distance signal relationship. Therefore the point at "optical peak" is set as a maximum point. Before the measurement starts, the distance between the sample and the Fotonic probe is first reduced by screwing backwards to get away from the optical peak to the point that gives rise to minimum intensity of received light, then the electrical signal is applied. Any displacement of the sample in response to

the electric field will then be compared with the optical peak and gives the relationship of displacement versus electric field.

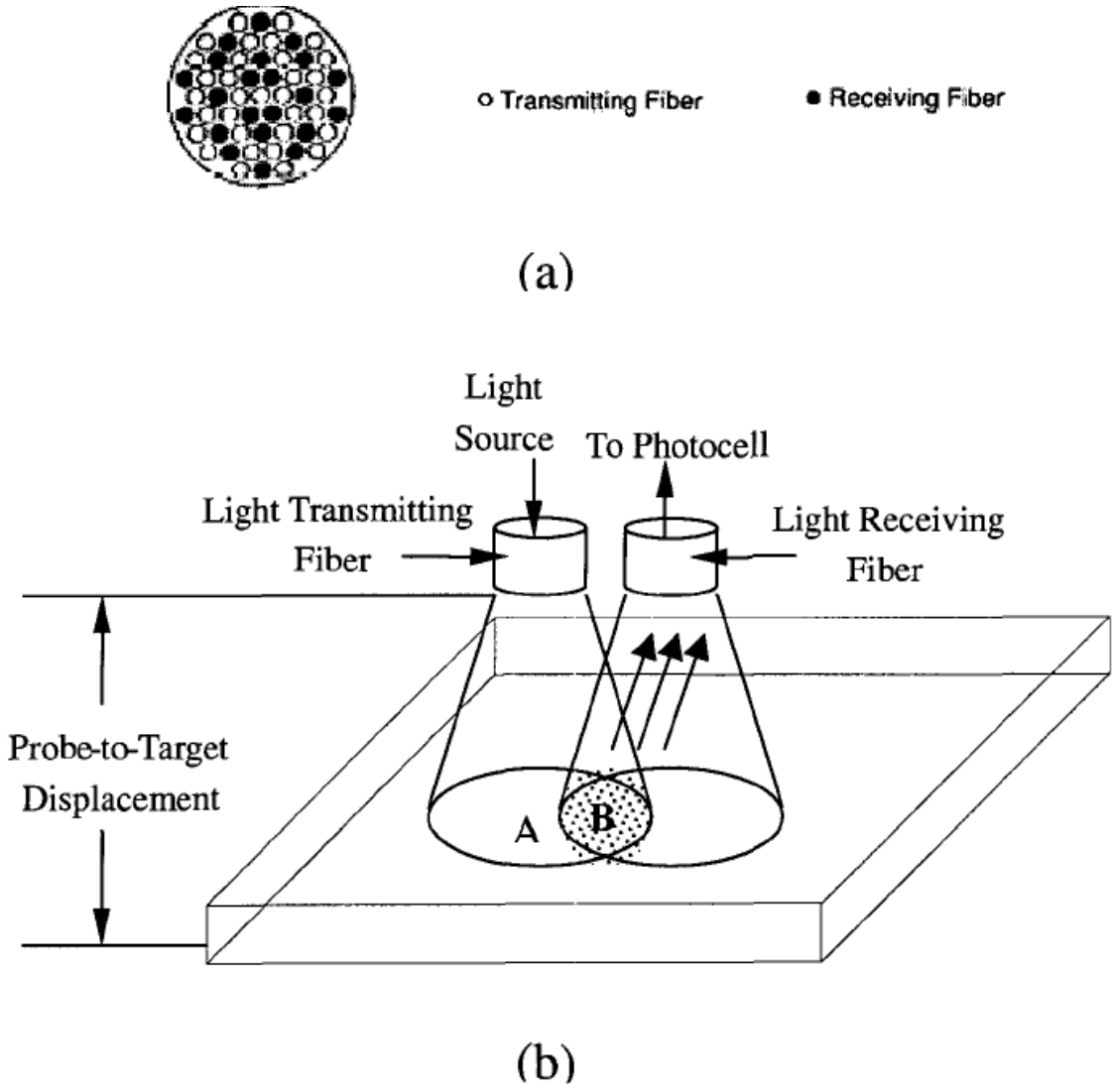

Fig. 3.8 A setup for the measurements of strain vs. electric filed loop. (a) Fiber – optical probe tip configurations; (b) Displacement sensing mechanism of adjacent fiber-optical elements.

References

[1] S. K. S. Parashar, R. N. P. Choudhary, and B. S. Murty, J.Appl. Phys., 98, (2005) 104305.

[2] C. Lei, and Z.G. Ye, J. Phys. Condens. Matter., 20, (2008) 232201.

[3] W. Ge, J. Li, D. Viehland, Y. Chang, and G. L. Messing, Phys. Rev. B, 83, (2011) 224110.

[4] S. Singh, O.P. Thakur, C. Prakash, and K.K. Raina, Mater. Lett., 61, (2007) 1082.

[5] K. C. Kao, Dielectric phenomena in Solids, (Elsevier Academic Press, London 1990).

[6] E. Barsoukov, and J. R. Macdonald, Impedance Spectroscopy: Theory, Experiment, and Applications (Wiley-Interscience, Hoboken, 2005).

[7] C. B. Sawyer and C. H. Tower, Phys. Rev. 35, (1930) 269.

[8] T. F. Hueter, D. P. Neuhaus, and J. Kolb, J. Acous. Soc. Am. 26, (1954) 696.

[9] Y. T. Chen, S. C. Lin, S. Y. Cheng, J. Alloy. Compd., 449, (2008) 101.

[10] M. Matsubara, T.Yamaguchi, K. Kikuta, S. Hirano, Jpn. J. Appl. Phys., 44, (2005) 6136.

CHAPTER-4

Structural, Dielectric, Ferroelectric and Piezoelectric Properties of (1-x)[$K_{0.5}Na_{0.5}NbO_3$]-x[$LiSbO_3$] Ceramics

4.1. Introduction

(1-*x*)$K_{0.5}Na_{0.5}NbO_3$-*x*$LiSbO_3$/KNN-LS is a solid solution of KNN and $LiSbO_3$ (LS) systems. A coexistence of orthorhombic and tetragonal phase in KNN-LS ceramics have been identified in the composition range for *x*=0.04-0.06 [1]. It has been reported that the so called MPB in $Pb(Zr_{1-x}Ti_x)O_3$ (PZT) ceramic is nearly vertical in the temperature-composition phase diagram of PZT ceramics [2-4]. It is nearly temperature independent, i.e., the poling temperature (T_p) has no effect on different ferroelectric phases. However, the presence of MPB in KNN-based ceramics is very different from that in PZT-based ceramics. The MPB in KNN-based ceramics is an orthorhombic-tetragonal polymorphic phase transition (PPT) [3]. The phase boundary between tetragonal and orthorhombic phases in KNN based ceramics is not vertical and shows strong temperature dependent behavior. Therefore, poling of the KNN based ceramics near PPT can improve the piezoelectric properties. Though there are few reports on the KNN-LS system but the effect of LS content and on the ferroelectric and piezoelectric properties of this system near MPB has not been studied simultaneously yet. Therefore, in the present chapter, the effect of poling temperature and $LiSbO_3$ content on the structural and electrical properties of (1-*x*)KNN-*x*$LiSbO_3$ (*x*=0, 0.04, 0.05 and 0.06) ceramics within the MPB region have been investigated in detail.

4.2. Optimization of Calcination and Sintering Temperatures

It is very important to develop single perovskite phase in the synthesized ferroelectric ceramics. Since, the presence of secondary phase in the ferroelectric ceramics always increases the conductivity and decreases the piezoelectric properties, which is undesirable for practical applications. Therefore, to ensure the single perovskite phase formation the calcinations temperature of the parent $K_{0.5}Na_{0.5}NbO_3$ ceramics have been optimized. It is well known that a dense ceramic body is necessary to achieve maximum dielectric and piezoelectric properties. Therefore, in the present section, the optimization of the sintering process is discussed in detail.

4.2.1. Thermal Analysis

Fig.4.1 shows the thermogravimetric and differential thermal analysis (TG/DTA) results of the uncalcined $K_{0.5}Na_{0.5}NbO_3$ (KNN) powder. The TG curve shows that the overall weight loss of the powder was ~14% from RT to 900 ^{0}C. Four endothermic peaks are observed from the DTA curve at ~94, 208, 465 and 640 ^{0}C, respectively. Sodium and potassium carbonates are hygroscopic in nature and they absorb water from the environment. Therefore, the appearance of peaks at ~ 94 and 208 ^{0}C correspond to the removal of physically and chemically absorbed water present in the KNN powder [5]. The powder mixture of KNN composition undergoes the decomposition of carbonate groups between 400 ^{0}C to 700 ^{0}C. Among the carbonates, Na_2CO_3 is the less stable and starts losing CO_2 at lower temperatures (~ 400 ^{0}C) [6]. Therefore, weight loss observed just above 400 ^{0}C could be associated with the decomposition of Na_2CO_3. The CO_2 loss originated from the Na_2CO_3 decomposition was also previously identified by mass spectrometry measurements which indicated the decomposition of this compound occurs at ~ 400 ^{0}C [7]. At

temperatures above ~ 650 °C, the weight loss produced by decomposition of carbonates has been completed and no further weight losses are observed, indicating that the final composition of the samples correspond to the nominal one. These facts are indicative that the calcination should be performed at temperatures over 650 °C. Therefore, TG/DTA study indicates that single perovskite phase can be obtained at ~ 800 ^{0}C.

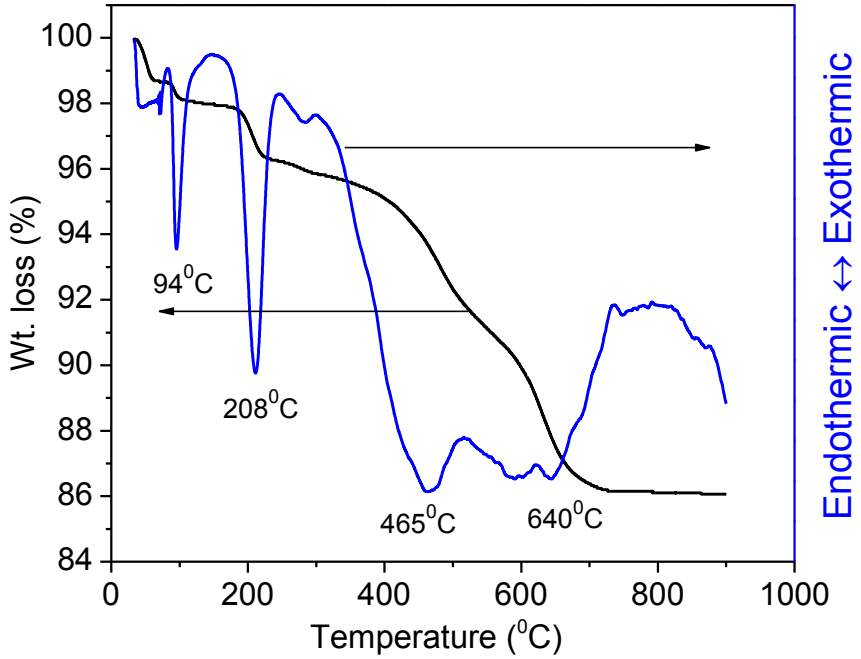

Fig.4.1 TG/DTA curves of the raw KNN powders.

4.2.2 Single Perovskite Phase Formation

Fig.4.2 shows the XRD patterns of the KNN powders calcined at 750 and 850 ^{o}C for 6 h. The formation of single perovskite phase has been confirmed at 850 ^{o}C, whereas at 750 ^{o}C small amount of secondary phase along with the perovskite phase is detected. The appearance of secondary phase peaks at 750^{o}C confirms the presence of unreacted phases in the ceramics. This suggests that single perovskite phase in KNN ceramics is developing at 850^{o}C calcination temperature. The XRD patterns of (1-*x*)KNN-*x*LS powders (x=0-0.06) calcined at 850 ^{o}C for 6 h are shown in Fig.4.3. Single perovskite

phase has been obtained in all the KNN-LS ceramics, which suggests that Li^{+} and Sb^{+5} have completely diffused into the A and B- sites of KNN-LS ceramics and formed a homogeneous solid solution.

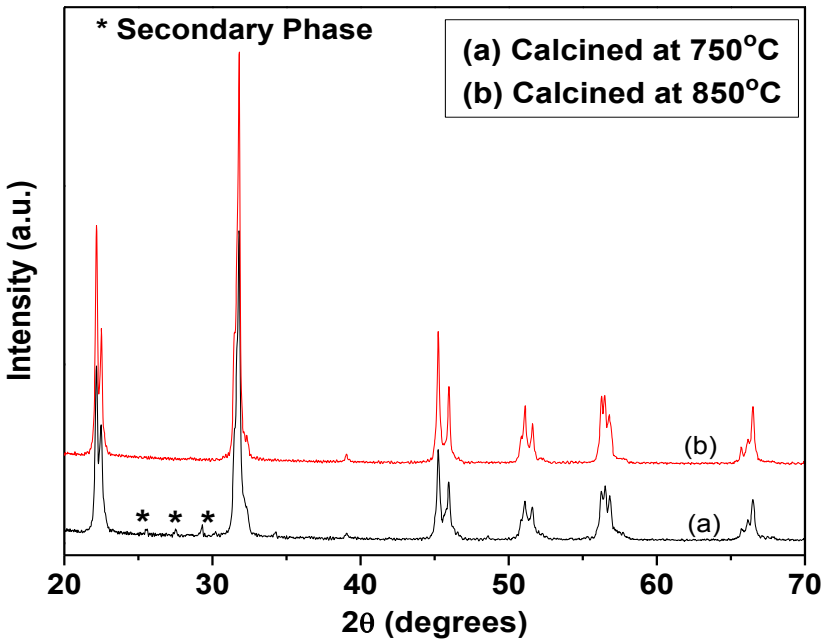

Fig.4. 2 XRD patterns of pure KNN powders calcined at different temperatures.

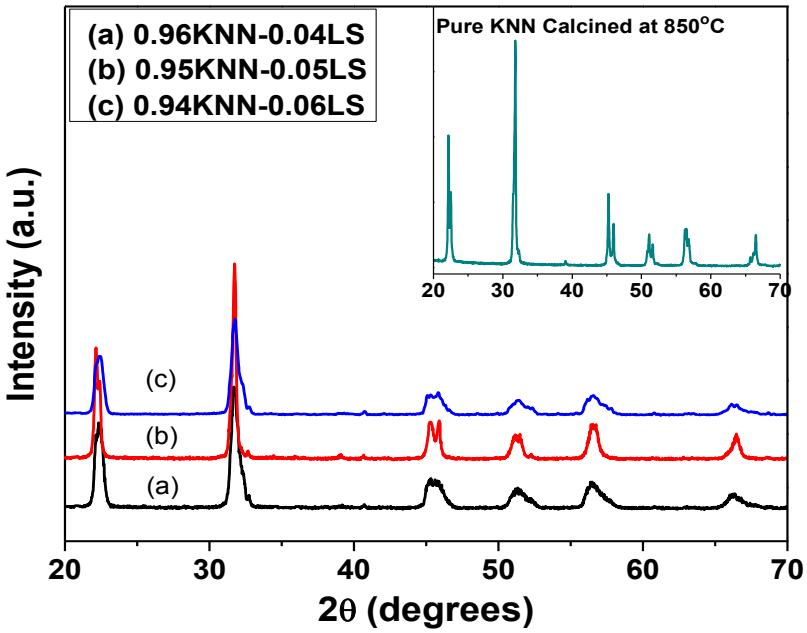

Fig. 4.3 XRD patterns of (1-*x*) KNN-*x*LS powders calcined at 850 ^{o}C for 6h.

4.2.3 Sintering and Density Study

The variation of relative density (RD) as a function of sintering temperature is shown in Fig.4.4. The sintering of all the (1-*x*)KNN-*x*LS ceramics have been carried out in the temperature range from 1060-1140 ^{o}C for 4 h. The optimum sintering temperature is found to decrease with the increase in LS content in (1-*x*)KNN-*x*LS ceramics. For pure KNN ceramics the optimum sintering temperature is found to be 1120 ^{o}C, whereas with the increase of LS content in KNN-LS ceramics it decreases to 1080 ^{o}C. The lowering of sintering temperature in (1-*x*)KNN-*x*LS with x=0.04, 0.05 and 0.06 ceramics may be due to the lower melting point of Sb_2O_5 (~655^{o}C) and Li_2CO_3 (~720^{o}C), which improves the densification with the formation of liquid phase at high temperature [8]. It is known that the formation of liquid phase, which leads to rearrangement of particles providing more effective packing is critical for densification of KNN based ceramics. In KNN-LS based ceramics, at high sintering temperature, the evaporation of alkali oxides and Sb_2O_5 takes place as they are volatile in nature. Hence, the formation of liquid phase occurs across the grain boundary, which enhances the densification process. Again, both smaller and larger volume fraction of the liquid phase results in poor microstructural and electrical properties [9]. Therefore, the volume of liquid phase during this stage of sintering has to be controlled in order to achieve full densification by filling the interstices completely. In this case, with the increase in LS content in KNN-LS ceramics initially the RD (Relative Density) increases and becomes maximum at x=0.05, but with further increase in sintering temperature RD decreases which may be due to the formation of excess liquid phase in the ceramics. The RD of pure KNN ceramics is found to be ~ 91% whereas the RD of 0.95KNN-0.05LS ceramic is ~ 94.7%, which is a significant improvement. The

results suggest that LS modification in KNN ceramics enhances the sinterability and hence increases the density.

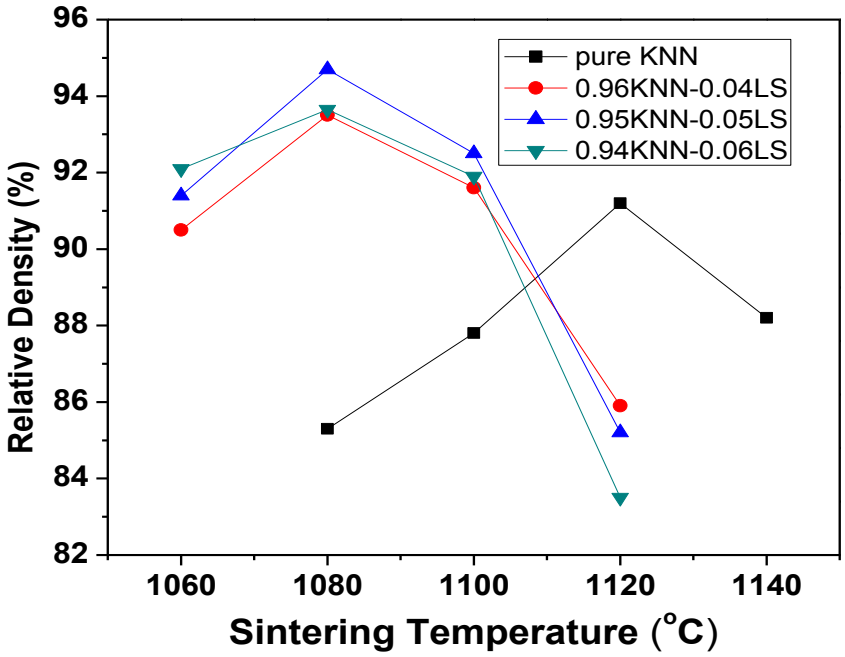

Fig.4.4 Relative density of (1-x)KNN-xLS ceramics sintered at different temperatures.

4.3 Morphology Study

Fig.4.5 shows the SEM micrographs of the (1-x)KNN-x$LiSbO_3$ (x=0, 0.04, 0.05,0.06) ceramics sintered at optimum temperature. It can be seen that with the increase in LS content the pore size decreases. Non-uniform distributions of grains are observed in all the ceramics. The average grain sizes of the ceramics are found to vary non-linearly with the increase in x content in KNN-LS ceramics. For pure KNN ceramics the average grain size is found to be ~ 2.9 µm, whereas for x=0.05 it reaches ~ 4 µm. With further increase in x content it decreases to ~ 3.4 µm. Relatively dense packing of grains are observed in 0.95KNN0.05LS ceramics in comparison to other ceramics.

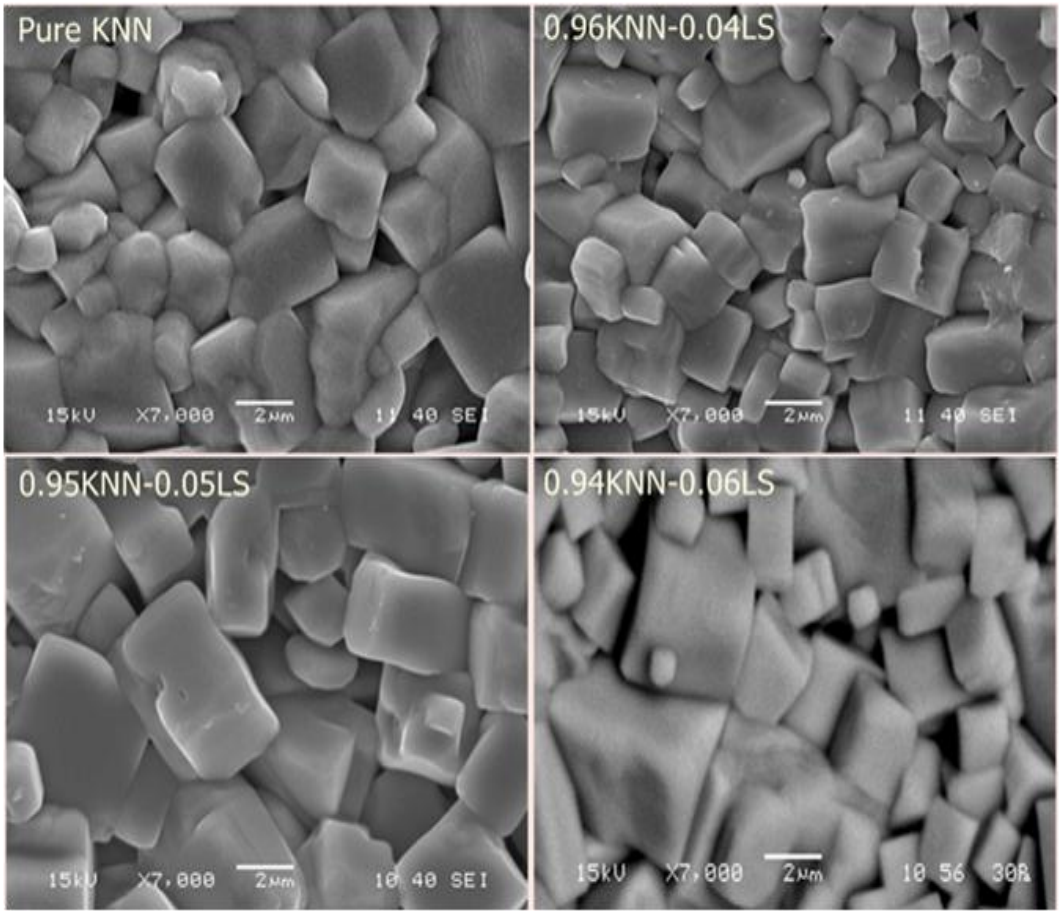

Fig.4.5 SEM micrographs of (1-*x*)KNN-*x*$LiSbO_3$ ceramics sintered at optimum temperature.

4.4 Structural Study

Fig.4.6 shows the XRD patterns of the (1-*x*)KNN-*x*LS ceramics sintered at optimum temperature. XRD peaks reveal the development of single perovskite phase without any trace of secondary phases in all the KNN-LS ceramics. This suggests that Li^{+} and Sb^{+5} ions have completely diffused into the KNN lattice to form a homogeneous solid solution. It can be seen that the ceramics with *x*=0 (KNN) and x=0.04 possess pure orthorhombic structure at RT and is confirmed by matching the XRD patterns with the JCPDS card no. 71-2171. The orthorhombic phase is characterized by (002)/(020) peak

splitting whereas, the tetragonal phase is characterized by (002)/(200) peak splitting. For *x*=0.06, the KNN-LS ceramics possesses only the tetragonal phase, which is indexed by JCPDS card no71-0945. Therefore, it can be concluded that the orthorhombic and tetragonal phases co-exist in KNN-LS ceramics for 0.04<*x*<0.06.

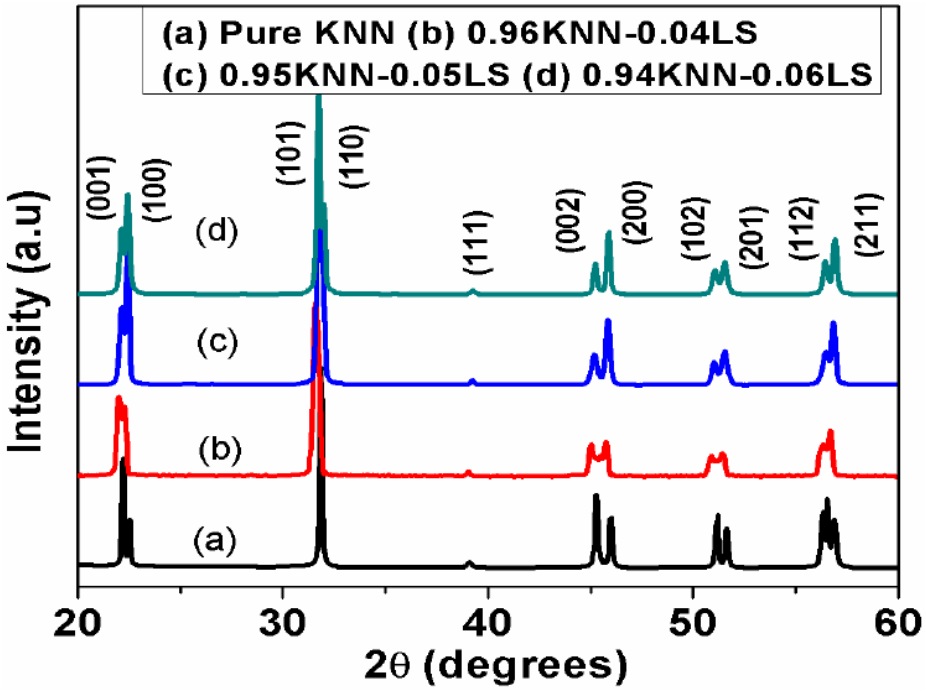

Fig.4.6 XRD patterns of (1-*x*) KNN-*x*LS ceramics sintered at optimum temperature.

In order to quantitatively investigate the effect of LS content on the crystalline phases peak de-convolution has been performed on the XRD patterns in the 2θ range of 44.5–46.5 degrees for all the KNN-LS compositions ceramics. Fig.4.7 shows the XRD patterns of KNN-LS ceramics in the 2θ range of 44.5–46.5 degrees. The XRD patterns of all the compositions in this 2θ range has been de-convoluted into four peaks, $(200)_T$, $(002)_T$, $(020)_O$ and $(002)_O$ using the Peakfit software with Gaussian approximations where the subscripts "T" and "O" denote the tetragonal and orthorhombic phases, respectively [10].

The fraction of the tetragonal (f_T) and orthorhombic phases (f_O) are determined from the integrated peak intensities of the two phases (I_T and I_O) using equation (4.1) & (4.2) [11].

$$f_T = I_T / (I_T + I_O)$$

$$= \{ I(002)_T + I(200)_T \} / \{ I(002)_T + I(200)_T + I(002)_O + I(020)_O \} \quad (4.1)$$

$$f_O = I_O / (I_O + I_T)$$

$$= \{ I(002)_O + I(020)_O \} / \{ I(002)_O + I(020)_O + I(002)_T + I(200)_T \} \quad (4.2)$$

where $I(002)_T$, $I(200)_T$, $I(002)_O$ and $I(020)_O$ are the integrated intensities of the tetragonal (002) and (200) peaks and orthorhombic (020) and (200) peaks, respectively. The calculated values of the f_T and f_O are mentioned in Fig.4.7. It is found that with the increase in x content, f_O decreases and f_T increases.

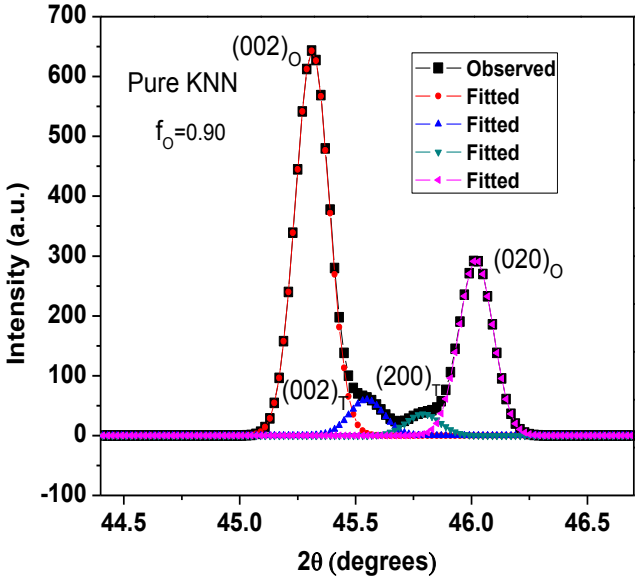

Fig.4.7 (a)

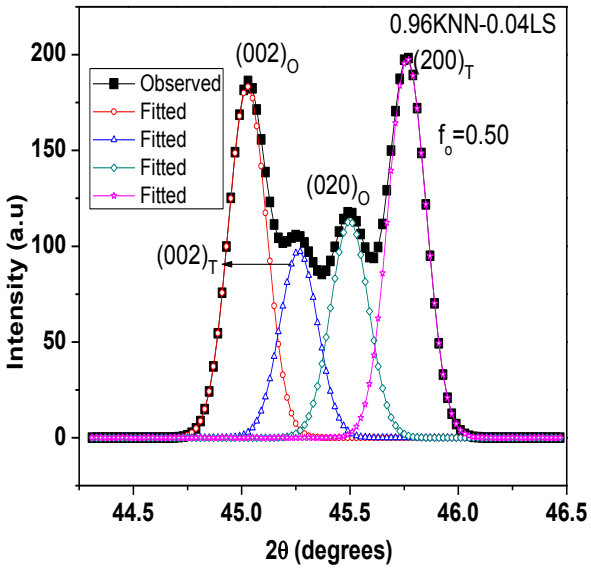

Fig.4.7 (b)

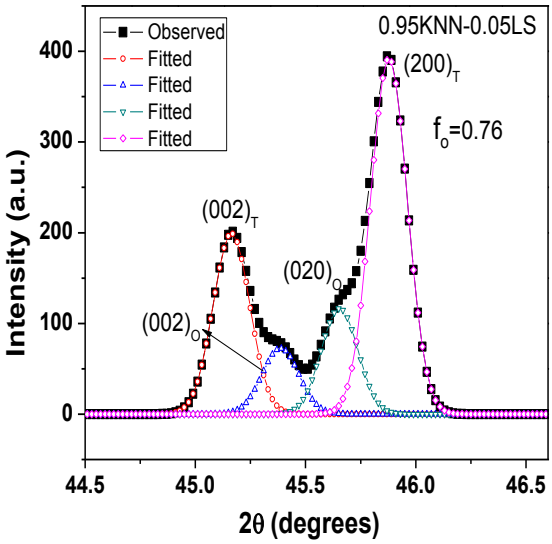

Fig.4.7 (c)

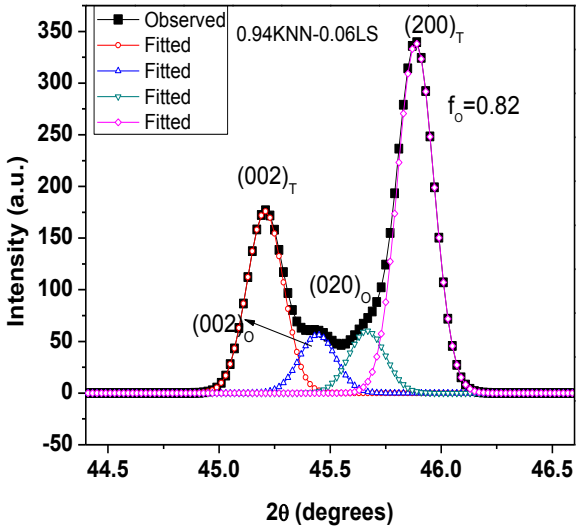

Fig.4.7 (d)

Fig.4. 7 XRD patterns of (1-*x*)KNN-*x*LiSbO$_3$ ceramics in the 2θ range of 44.5–46.5 degrees.

Table-4.1 Structure and unit cell parameters of (1-*x*)KNN-*x*LiSbO$_3$ ceramics.

Sample Name	a (Å)	b (Å)	c (Å)	Volume (Å)^3	Structure	S.D.
KNN	3.9388	4.0280	3.9953	63.39	Orthorhombic	0.0034
0.96KNN-0.04LS	3.9800	4.0156	3.9540	63.19	Orthorhombic	0.0042
0.95KNN-0.05LS	3.9638 3.9629	4.0141 3.9629	3.9657 4.0179	63.09 63.10	Orthorhombic Tetragonal	0.0023 0.0031
0.94KNN-0.06LS	3.9521	3.9521	4.0060	62.57	Tetragonal	0.0021

The structure and unit cell parameters of all the KNN-LS ceramics are listed in Table-4.1. It is found that pure KNN ceramics possess orthorhombic structure whereas the KNN-LS ceramics with x=0.06 possess tetragonal structure at room temperature (RT). Hence, with the increase in LS content the ceramic transforms from orthorhombic to tetragonal structure. The XRD patterns of (1-x)KNN-xLiSbO$_3$ ceramics with x= 0.04, 0.05 and 0.06

were refined with both tetragonal and orthorhombic structures. The unit cell volume of 0.95KNN-0.05LS ceramics is found to be nearly same for both tetragonal and orthorhombic structures, which further hints about the coexistence of both these phases at RT in this composition [12]. Again, the unit cell volume is found to decrease with the increase in LS content in KNN-LS ceramics, which may be due to the fact that the ionic radii of Li^{+} (0.68 Å) and Sb^{+5}(0.62 Å) is smaller than the ionic radii of $(Na_{0.5}K_{0.5})^{+}$ and Nb^{+5}. It is reported that vacancies are created when higher ionic radii elements are replaced by lower ionic radii elements, which in turn decreases the unit cell volume in a compound [12].

4.5 Dielectric Properties

4.5.1 Temperature Dependence of Dielectric Constant (ε_r) and Dielectric Loss (tanδ)

Fig. 4.8 (a), (b), (c) and (d) show the temperature dependence of dielectric constant (ε_r) at four different frequencies of (1-*x*)KNN-*x*$LiSbO_3$ ceramics for *x*=0, 0.04, 0.05 and 0.06, respectively. It can be seen that with the increase in x content, the Curie temperature (T_c) and the orthorhombic-tetragonal (T_{O-T}) polymorphic phase transition (PPT) of the (1-*x*)KNN-*x*$LiSbO_3$ ceramics decreases. Fig. 4.9 (a) and (b) shows the temperature dependences of the dielectric constant (ε_r) for all the compositions of (1-*x*)KNN-*x*$LiSbO_3$ ceramics at 1 MHz frequency. In order to eliminate the effect of space charge polarization contributions at high temperatures and low frequency, here the 1 MHz data are given [13]. According to previous reports, as per dielectric study, in pure KNN ceramics two phase transitions occurs above RT in the temperature dependence dielectric behavior. As shown in Fig. 4.9, in case of pure KNN ceramics i.e., for *x*=0 the

first phase transition ~ 198^{o}C is the orthorhombic-tetragonal (T_{O-T}) phase transition and the second one ~ 425^{o}C is the ferroelectric–paraelectric phase transition temperature (T_c). It is observed that both these phase transition temperatures are highly dependent on the *x* content in (1-*x*)KNN-*x*$LiSbO_3$ ceramics. In comparison to pure KNN ceramics, the substitution of LS in KNN system has significantly lowered the T_{O-T} and T_c of KNN-LS ceramics. The T_{O-T} is found to be ~198^{o}C, 115^{o}C, 43^{o}C and below RT, whereas T_c is found to be ~425^{o}C, 400.8^{o}C, 385.5^{o}C and 367^{o}C corresponding to *x*=0, 0.04, 0.05 & 0.06 in (1-*x*)KNN-*x*$LiSbO_3$ ceramics, respectively. The RT value of ε_r increases linearly with the increase in x content in (1-*x*)KNN-*x*$LiSbO_3$ceramics, which may be due to the stabilization of tetragonal structure at RT. The values of ε_r, T_{O-T} and T_c are listed in Table 4.2. Fig.4.9 (b) shows the temperature dependence of dielectric loss (tanδ) at 1MHz frequency of (1-*x*)KNN-*x*$LiSbO_3$ ceramics with *x*=0, 0.04, 0.05 and 0.06. It can be seen that with the increase in x content the value of tanδ decreases, which may be related to the increase in relative density in the samples. It is observed that higher value of tanδ is obtained with increasing temperature which may be due to the increase in the mobility of ions and imperfections in the material [14]. It can also be seen that the temperatures of peak dielectric loss and peak dielectric constant do not coincide. Kramers–Kronig relation indicates that this can be the consequence of temperature dependent relaxation near Curie temperature [15].

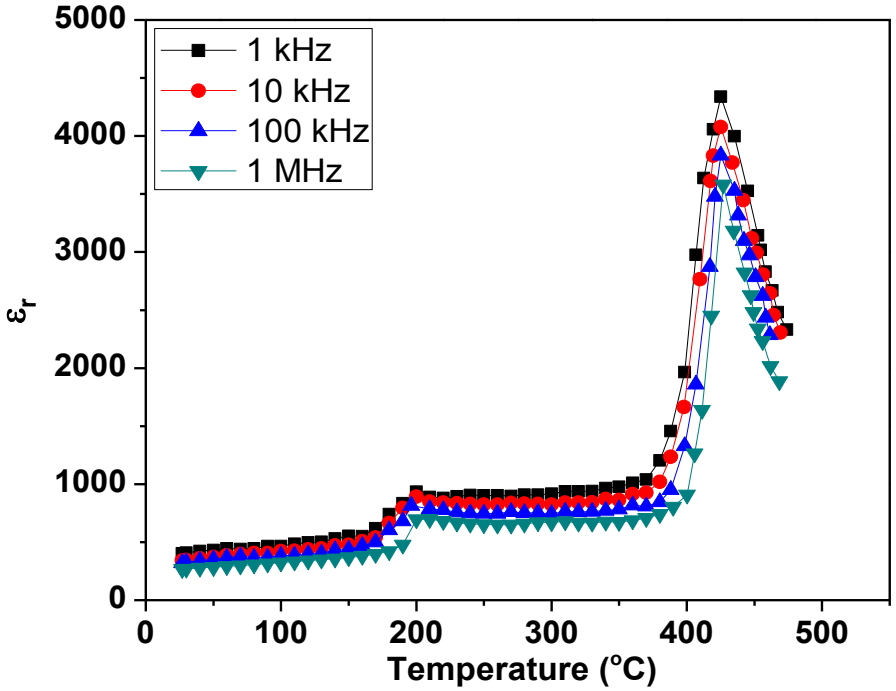

Fig.4. 8 (a)

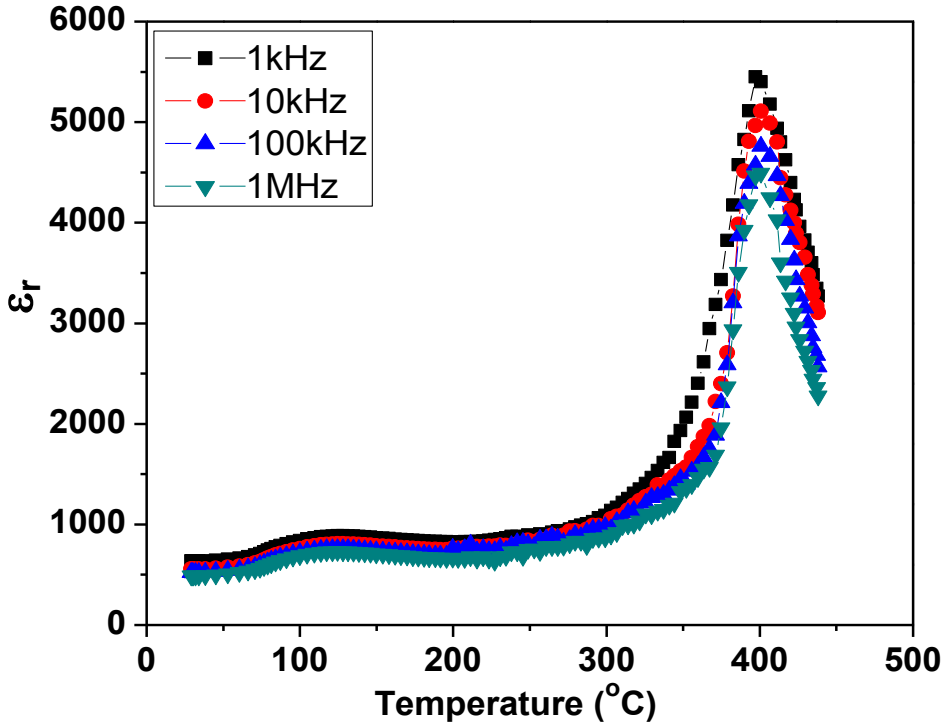

Fig.4.8 (b)

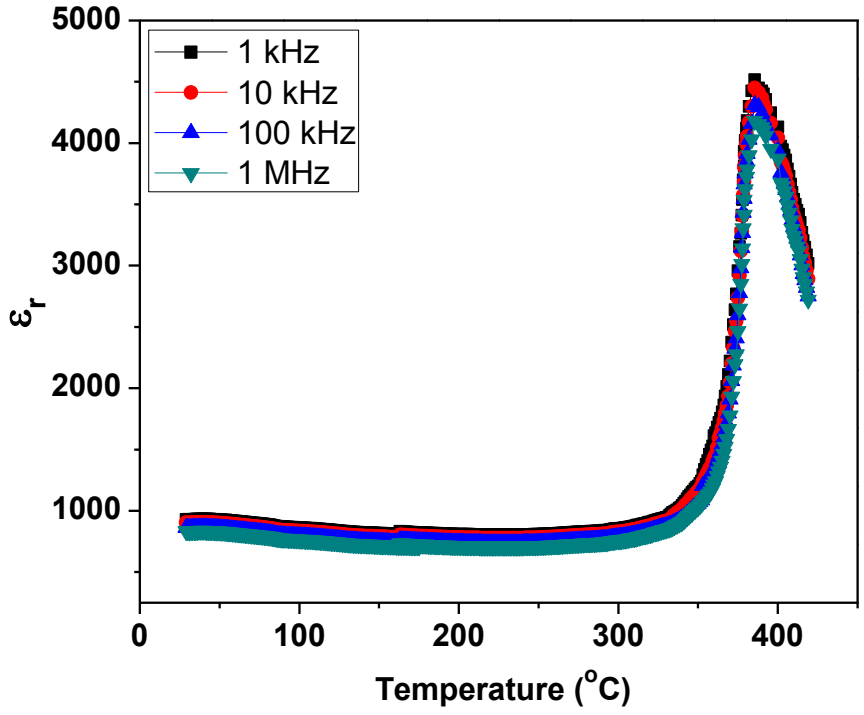

Fig.4.8 (c)

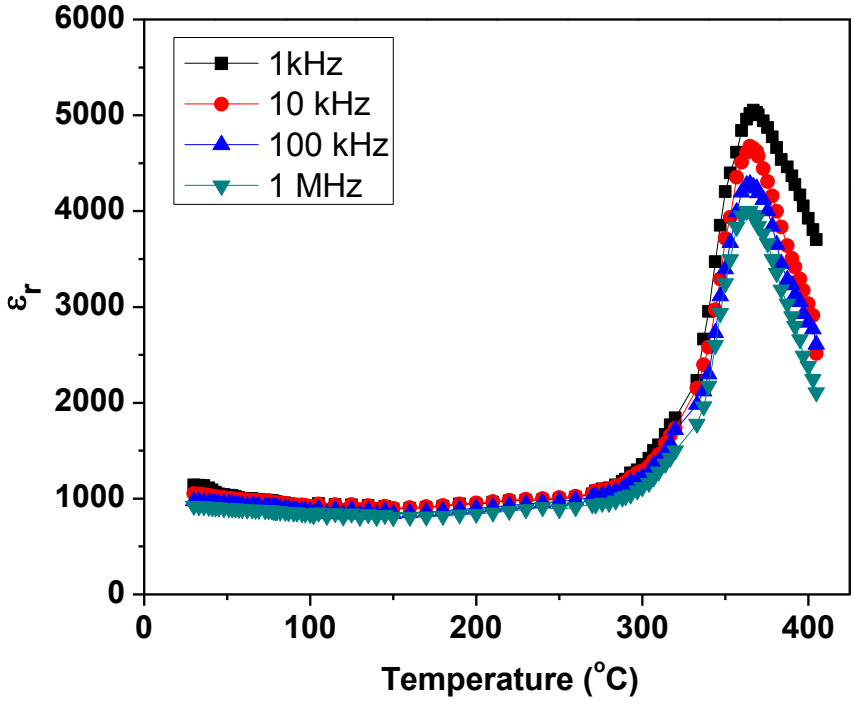

Fig. 4.8 (d)

Fig.4.8 Temperature dependence of dielectric constant (ε_r) of (1-*x*)KNN-*x*$LiSbO_3$ ceramics sintered at optimum temperature for (a) *x*=0 (b) *x*=0.04 (c) *x*=0.05 and (d) *x*=0.06.

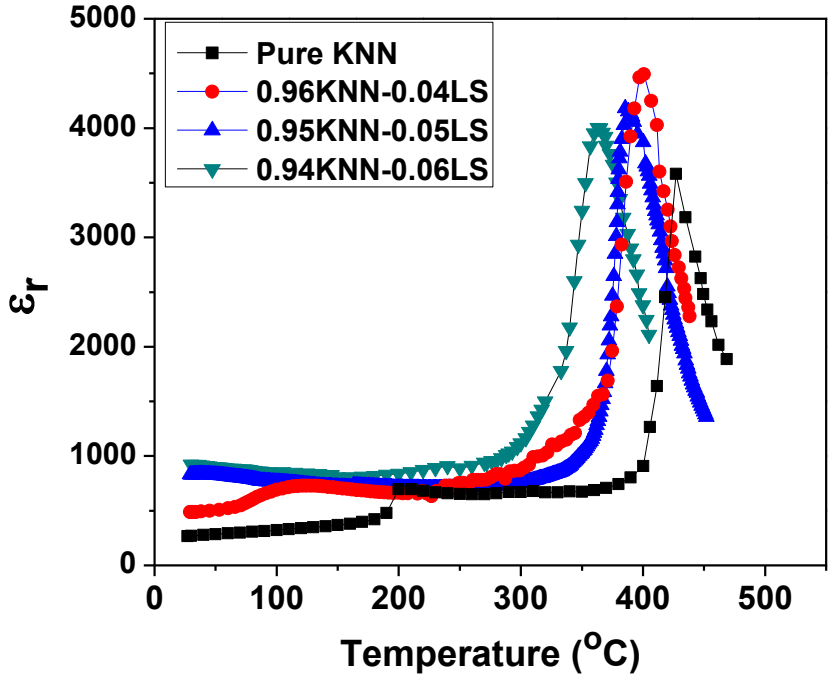

Fig.4.9 (a) Temperature dependence of dielectric constant (ε_r) at 1 MHz frequency of (1-*x*)KNN-*x*LiSbO$_3$ ceramics.

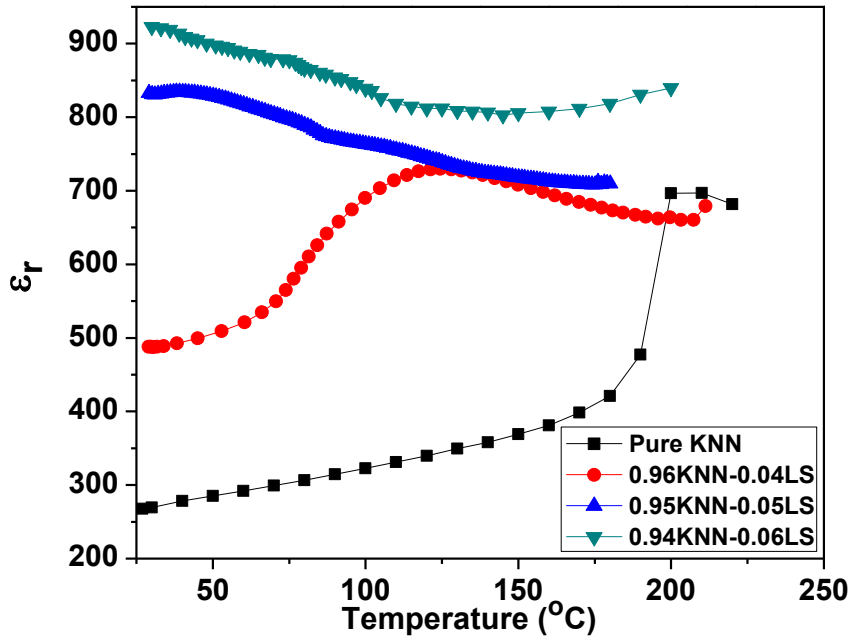

Fig.4.9 (b) Temperature dependence of the dielectric constant of (1-*x*)KNN-*x*LiSbO$_3$ceramics in a low temperature range.

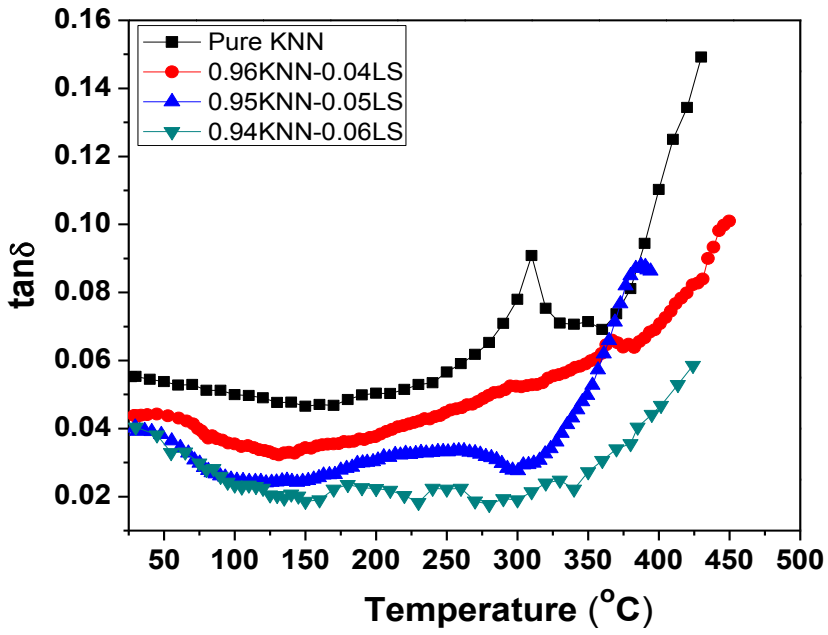

Fig.4.10 Temperature dependence of dielectric loss (tanδ) at 1 MHz frequency of (1-*x*)KNN-*x*LiSbO$_3$ ceramics.

4.6 Diffusivity Study

It can also be seen from Fig. 4.9 (a) that with the increase in x content in KNN-LS ceramics, the broadening of the peaks of ε_r at T_c increases, which indicates the increase of diffuse phase transition nature in KNN-LS ceramics. A modified Curie-Weiss law, given in relation 4.3, has been suggested to examine the diffuseness of the ferroelectric phase transition [16, 17]:

$$1/\varepsilon - 1/\varepsilon_m = (T-T_m)^{\gamma}/C \qquad (4.3)$$

Where, γ and C are constants. The parameter γ gives information about the character of the phase transition: for $\gamma = 1$, a normal Curie-Weiss law is followed, which means the transition of the system is completely ordered [18]. Whereas on the basis of a local compositional fluctuation model, the value of $\gamma=2$ corresponds to a completely diffused

system [19]. For systems exhibiting intermediate value of diffusivity ($1 \leq \gamma \leq 2$), the materials are complex, hence partially disordered.

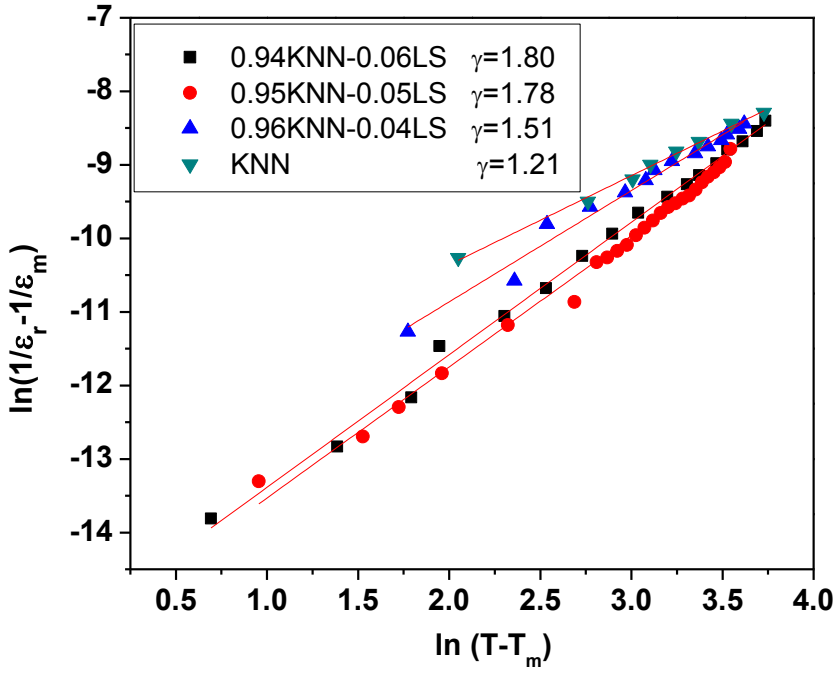

Fig.4. 11 Plot of $\ln(1/\varepsilon_r - 1/\varepsilon_m)$ vs. $\ln(T-T_m)$ (1-*x*)KNN-*x*$LiSbO_3$ ceramics at 1 MHz frequency.

The plot of $\ln(1/\varepsilon - 1/\varepsilon_m)$ vs $\ln(T-T_m)$ for all the KNN-LS ceramics are shown in Fig.4.11. The value of γ has been calculated from the slope of the curves. The value of γ increases with increase in LS content and is found to be ~1.21, 1.51,1.78 and 1.81for pure KNN, 0.96KNN-0.04LS, 0.95KNN-0.05LS and 0.94KNN-0.06LS ceramics, respectively. This confirms the increase of diffuse phase transition nature with the increase of LS content in KNN-LS system. The appearance of diffuse phase transition with the increase in LS content can be explained as follows: in perovskite-type compounds, the diffuse phase transition occurs when at least two cations occupy the same crystallographic sites: A or B in ABO_3 type perovskite structure. A cationic disorder induced by B-site substitution is always regarded as the main cause for the appearance of diffusive behavior. However,

according to previous reports, the diffusive behavior in KNN-based ceramics should attribute to a cationic disorder induced by both A-site and B-site substitutions [20]. In the solid solution of KNN-LS ceramics, K, Na and Li ions occupy A-sites of ABO_3 perovskite type structure, whereas Nb^{+5} and Sb^{+5} ions occupy B-sites, therefore the ion disorder in the perovskite unit cell can be accounted for the appearance of diffusive behavior.

4.7 Poling Temperature Effect on Piezoelectric and Electromechanical Properties

It is known that the MPB in KNN based ceramics is an orthorhombic-tetragonal polymorphic phase transition (PPT) type [3]. Unlike the MPB in PZT, the phase boundary between orthorhombic and tetragonal phases in KNN based ceramics is not vertical and shows strong temperature dependence. Hence optimization of poling temperature (T_p) is needed to achieve desired piezoelectric properties [21]. Fig.4.12 (a) and (b) show the effect of poling temperature on the values of piezoelectric coefficients (d_{33}) and electromechanical coupling coefficient (k_p). The electromechanical coupling coefficients (k_p) of the samples were calculated from the resonance (f_r) and anti-resonance (f_a) frequencies using the equation:

$$k_p = [2.51 \times \{(f_a - f_r)/f_r\}]^{1/2} \qquad (4.4)$$

Where f_r and f_a are resonant and anti-resonant frequencies (Hz) and k_p is a planar mode coupling coefficient. At f_r and f_a frequencies, the electrical impedance modulus of Z exhibits a strong variation with a minimum value at f_r and a maximum value at f_a. The planar mode electromechanical coupling coefficient (k_p) is calculated by putting the values of f_r and f_a in equation (1). It can be seen that for pure KNN ceramics with the increase of poling

temperature, there is an increasing trend for both d_{33} and k_p values. This may be due to the fact that the T_{O-T} in pure KNN ceramic occurs ~ 198^oC and the poling temperature is lower than that. As shown in Fig.4.12, the T_p has an obvious effect on the piezoelectric properties and except for pure KNN ceramics, the piezoelectric properties reach maximum values when $T_p \rightarrow T_{O-T}$. This is due to the fact that when T_p lies near orthorhombic–tetragonal PPT temperatures, non-180^o domains can switch easily and be orientated owing to the coexistence of the orthorhombic and tetragonal phases [22].

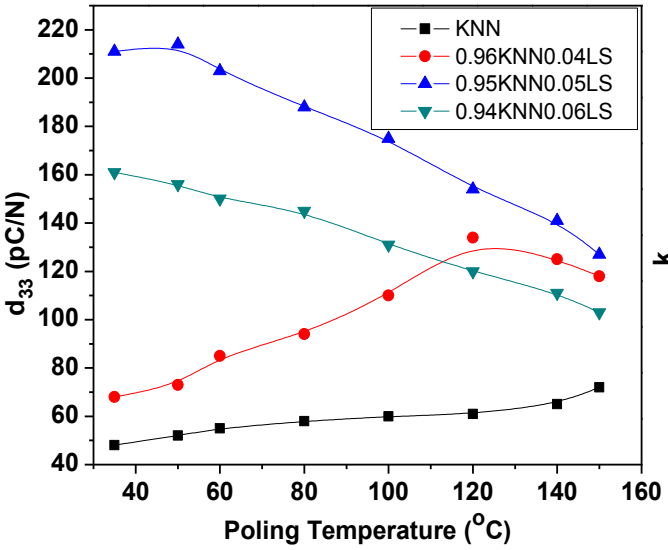

Fig.4.12 (a)

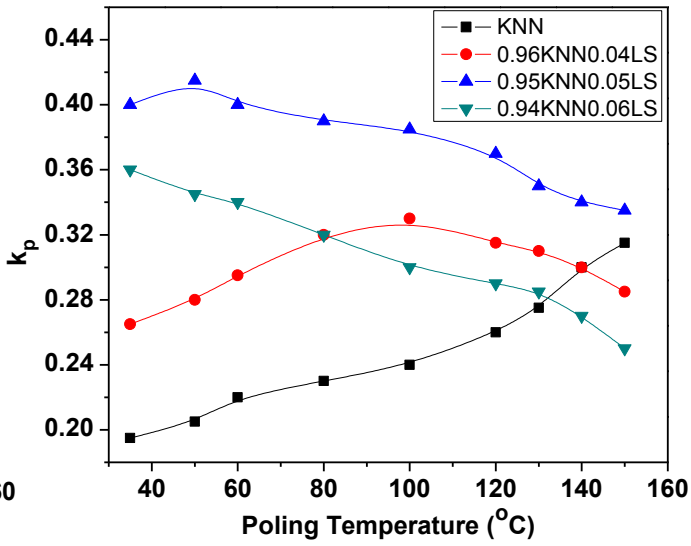

Fig.4.12 (b)

Fig.4.12 (a) piezoelectric coefficients (d_{33}) and (b) Planar mode coupling coefficients (k_p) of (1-*x*)KNN-*x*$LiSbO_3$ ceramics as a function of poling temperature.

The coexistence of the orthorhombic and tetragonal phases increases the number of polarization directions. Consequently, the higher degree of the domain alignment gives rise to highest piezoelectric properties near PPT. Maximum value of d_{33} ~ 215 pC/N and k_p ~ 0.415 at RT is obtained in case of 0.95KNN-0.05LS ceramics by choosing optimum T_p near PPT. This shows that T_p plays an important role in the enhancement of piezoelectric

properties of the KNN-based ceramics. In addition, many studies indicate that the reason for high piezoelectric properties in KNN-based ceramics such as KNN-$SrTiO_3$, KNN-$LiNbO_3$, etc., is also due to the formation of PPT at room temperature. In this study, maximum piezoelectric properties are obtained in case of 0.95KNN-0.05LS ceramics, which may be due to the presence of PPT near RT.

4.8 Temperature Dependence of Electromechanical Properties

Fig. 4.13 shows the temperature dependence of planar mode electromechanical coupling coefficients (k_p) for the (1-x)KNN-x$LiSbO_3$ ceramics. It can be seen that in all the ceramics maximum value of k_p is also obtained near PPT.

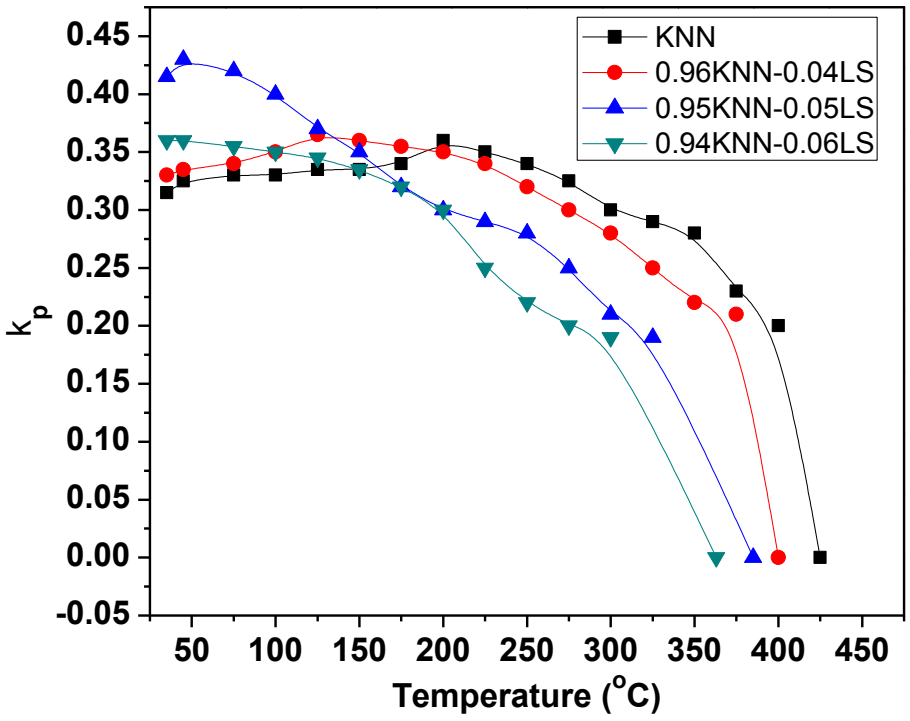

Fig.4.13 Temperature dependence of the planar mode coupling coefficient (k_p) of the (1-*x*)KNN-*x*$LiSbO_3$ ceramics.

It has been suggested that the domain structure of the KNN-based ceramics near PPT region is the coexistence of orthorhombic (O) and tetragonal (T) polarized domains. There are 12

possible spontaneous polarization (*P*s) directions for the O phase, and six possible *P*s directions for the T phase. The presence of more number of possible polarization states near PPT improves the piezoelectric properties [23]. This phenomenon has also been observed in other ceramics such as $BaTiO_3$ ceramics and $KNbO_3$ ceramics [24]. Highest value of k_p ~ 0.43 is obtained for $0.95[(K_{0.5}Na_{0.5})NbO_3]$-$0.05LiSbO_3$ ceramics at ~45^oC. For all the ceramics after PPT, the value of k_p decreases rapidly and reaches ~ 0 at the T_c which is due to the thermal depoling of the ceramics at higher temperatures.

When an unrestrained piezoelectric ceramic element is exposed to a high frequency alternating electric field, an impedance minimum, the planar or radial resonance frequency, coincides with the series resonance frequency (f_r). The relationship between the *radial mode resonance frequency constant* (N_P) and the diameter (L) of the ceramic element is expressed by [25]:

$$N_p = f_r \times L \qquad (4.5)$$

It was reported that the ceramic with high frequency constant (N_p) can be useful for high frequency applications. Fig.4.14 shows the temperature dependence of frequency constant (N_p) of (1-x)KNN-$xLiSbO_3$ ceramics. It can be seen that near PPT, the value of N_p attains a minimum value for all the (1-x)KNN-$xLiSbO_3$ ceramics except for x=0.06 and then increases with further increase in temperature. It is known that N_p is inversely proportional to elastic compliance. Elastic compliance, s, is defined as the strain produced in a piezoelectric material per unit of stress applied and is the reciprocal of the modulus of elasticity (Young's modulus, Y). Therefore, the decrease of N_p means the increase of elastic compliance. The reason behind the minimum value of N_p at PPT may

be due to the change in mechanical hardness of samples and/or the bonding strength of ionic constituents in NbO_6 octahedral at the phase transition [26]. The variations of Δf_r / $f_{r35°C}$ and $\Delta k_p/k_{p35°C}$ in the temperature range of 35°C to 300°C for the KNN-LS ceramics are shown in Fig.4.15. It is well known that Δf_r / $f_{r35°C}$ and $\Delta k_p/k_{p35°C}$ are two important performance factors of the piezoelectric ceramics. It represents the change of f_r and k_p values with increase in temperature with respect to room temperature values which determines the stability of the properties. The behavior of Δf_r /$f_{r35°C}$ is found to be exactly opposite to the behavior of $\Delta k_p/k_{p35°C}$. Similar to the behavior of N_p, the value of Δf_r /$f_{r35°C}$ decreases with the increase in temperature up to PPT except for the KNN-LS ceramics with x=0.06. Whereas the value of $\Delta k_p/k_{p35°C}$ increases with increase in temperature up to PPT except for the KNN-LS ceramics with x=0.06 and then decreases with further increase in temperature due to thermal depoling of the ceramics.

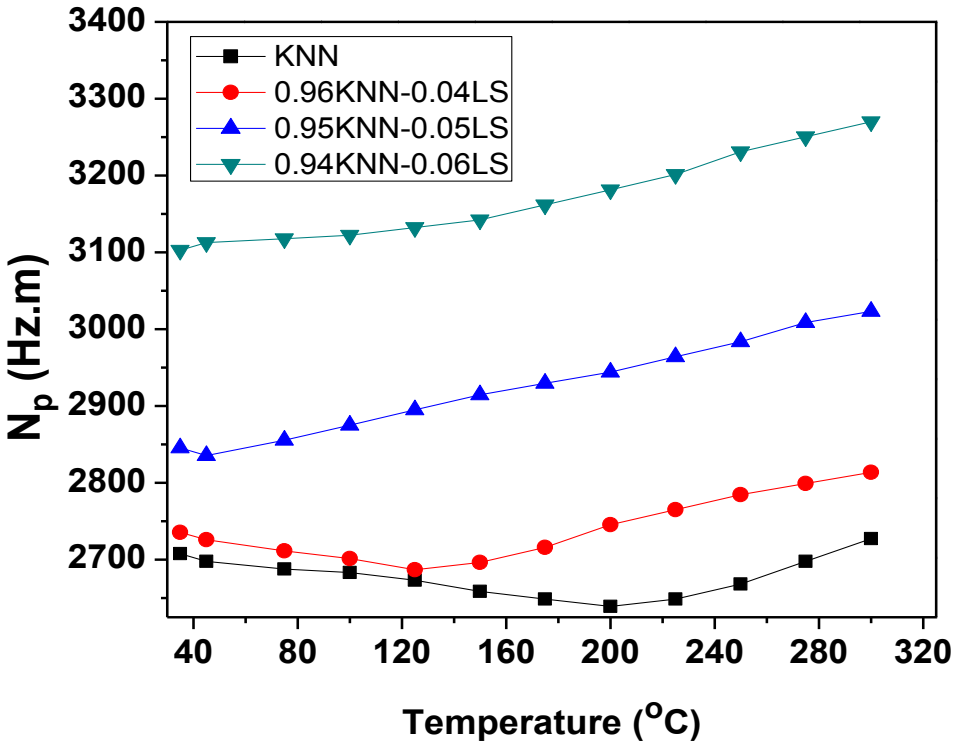

Fig.4.14 Temperature dependence of the frequency constant (N_p) of (1-*x*)KNN-*x*$LiSbO_3$ ceramics.

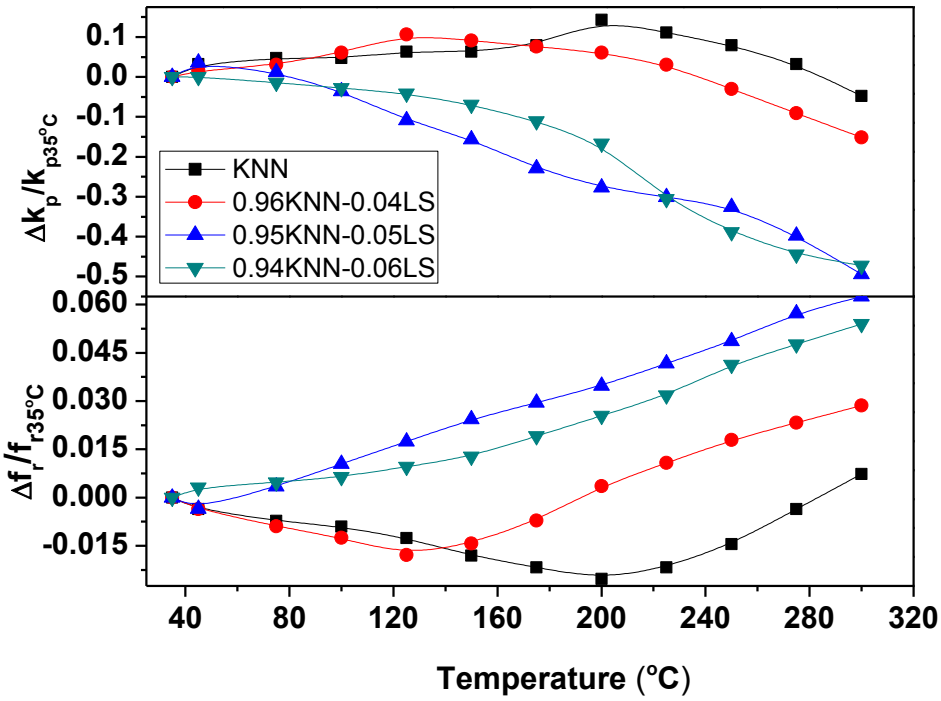

Fig.4.15 Variations of $\Delta f_r / f_{r35°C}$ and $\Delta k_p/k_{p35°C}$ with temperature of (1-*x*)KNN-*x*LiSbO$_3$ ceramics.

3.9 Strain vs. Electric Field Behavior

Fig.4.16 shows the bipolar field-induced strains of (1-x)KNN-xLS ceramics. The development of typical butterfly-shaped loops indicates the piezoelectric nature of the ceramics. The strain–electric field (S-E) hysteresis loops, which resembles the shape of a butterfly develops mainly due to three types of effects. The first one is the normal converse piezoelectric effect of the lattice, and the other two are due to the switching and movement of domain walls. Small displacements of all types of domain walls affect the polarization of the material whereas in addition to the pure piezoelectric response of the material within each domain, the movement and switching of non-180^o walls may involve a significant change in dimensions of the sample [27]. The ceramics with x=0 i.e. pure KNN ceramics possess a remnant strain ~ 0.034% whereas for x=0.04, it reaches ~ 0.052%. With further increase in *x* content, the remnant strain increases up to ~0.07% at

x=0.05 and then decreases at *x*=0.06. The maximum value of remnant strain at x=0.05 may be due to the presence of PPT close to RT which increases the non-180^{o} domain wall motion because of the reduction of the potential barrier between O and T polarization states [28].

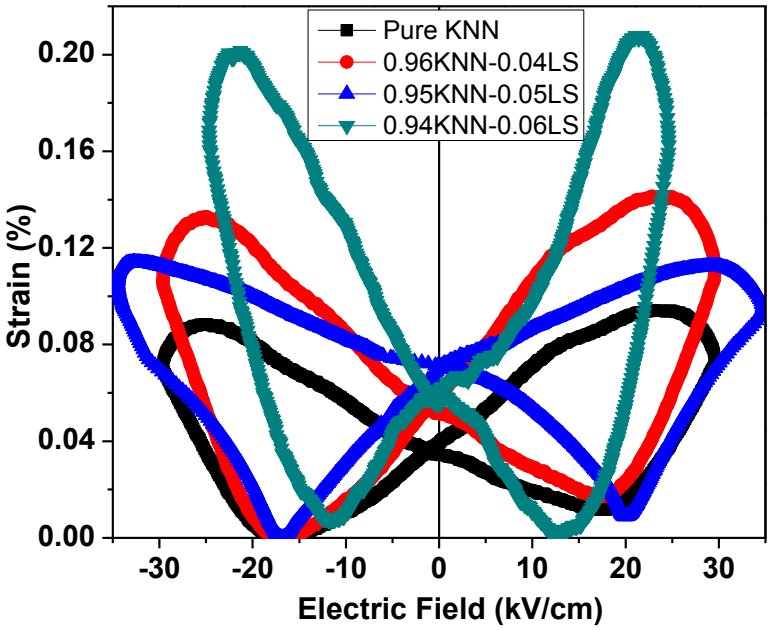

Fig.4.16 Strain vs. Electric field (S-E) loops of (1-*x*)KNN-*x*LiSbO$_3$ ceramics.

3.10 Ferroelectric Properties

In order to examine the ferroelectric nature of the KNN-LS ceramics, the polarization vs. electric field loops are measured and shown in Fig.4.17. Saturated hysteresis loops developed in all the KNN-LS ceramics. It is found that initially with the increase in *x* content up to *x*=0.05, P_r increases but with the further increase in *x* content P_r starts decreasing. The increase in P_r might be ascribed to the increase of the bulk density that diminishes the leakage current and enhances the polarization process [29, 30]. Maximum value of remnant polarization ~18.7μC/cm^2 is obtained in 0.95KNN-

0.05LS ceramics; again this may be due to the presence of PPT near RT which may be due to the presence of more number of polarization directions in the ceramics [23].

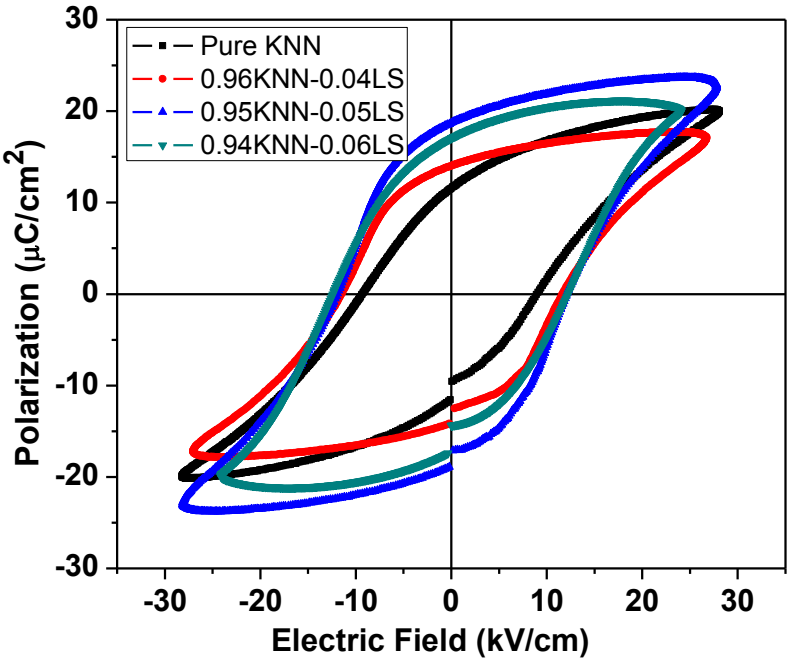

Fig.4.17 Polarization-Electric field (P-E) hysteresis loops of (1-x)KNN-xLiSbO$_3$ ceramics.

Table-4.2 Electrical and physical properties of (1-*x*)(Na$_{0.5}$K$_{0.5}$)NbO$_3$ –*x*LiSbO$_3$ ceramics with *x* = 0-0.06.

x	0	0.04	0.05	0.06
ε_r (1 MHz)	277	488	832	931
T_c (^{o}C)	425	400.8	385.5	367
T_{O-T} (^{o}C)	198	115	43	Below RT
P_r (μC/cm^2)	11.6	13.9	18.7	17.2
d_{33} (pC/N)	72	134	215	161
k_p	0.30	0.33	0.415	0.36

4.11 Chapter Summary

The effect of $LiSbO_3$ substitution in KNN ceramics near MPB region was examined in $(1-x)(Na_{0.5}K_{0.5})NbO_3$-$xLiSbO_3$ for x = 0, 0.04, 0.05 & 0.06 ceramics, synthesized by conventional solid state reaction route. The piezoelectric and ferroelectric properties with d_{33} =215pC/N, k_p =0.415 and P_r =18.7 μC/cm^2 were found to be maximum for x = 0.05. The ceramics for x = 0.05 also exhibited maximum density and the max. average grain size. The XRD study on the crystalline structure of the $(1-x)(Na_{0.5}K_{0.5})NbO_3$-$xLiSbO_3$ ceramics show that the fraction of the tetragonal phase increased and that of the orthorhombic phase decreased with the increase of x content. The Curie temperature was found to decrease with the increase of x content. The O-T phase transition temperature T_{O-T}, was located close to RT (~ 43 ^oC) for x=0.05. The maximum piezoelectric performance observed at x=0.05 was attributed to the near-room-temperature T_{O-T} , the maximum grain size and the maximum density in this composition.

References

[1] J. Wu, Y. Wang, D. Xiao, J. Zhu, P. Yu, L. Wu, and W. Wu, Jpn. J. Appl. Phys.,46, (2007) 7375.

[2] J. L. Jones, E. B. Slamovich, and K. J. Bowman, J. Appl. Phys., 97, (2005) 034113.

[3] T. R. Shrout, S. J. Zhang, J. Electroceram., 19, (2007) 111.

[4] I. M. Reaney, D. I. Woodward, and C. A. Randall, J. Am. Ceram. Soc., 94, (2011) 2242.

[5] T. Rojac, M. Kosec, P. Šegedin, B. Malič and J. Holc, Solid State Ionics, **177,** (2006) 2987.

[6] P. Patnaik, Handbook of Inorganic Chemicals, McGraw-Hill, New York, 2002.

[7] T. Hungria, M. Algueró, and A. Castro, Chem. Mater., 18, (2006) 5370.

[8] F. Rubio-Marcos, P. Ochoa, and J.F. Fernandez, J. Eur. Ceram. Soc., 27, (2007) 4125.

[9] C. W. Ahn, C. S. Park, C. H. Choi, S. Nahm, M. J. Yoo, H. G. Lee, and S. Priya, J. Am. Ceram. Soc., 92, (2009) 2033.

[10] C. Lei, and Z.G. Ye, J. Phys. Condens. Matter., 20, (2008) 232201.

[11] W. Ge, J. Li, D. Viehland, Y. Chang, and G. L. Messing, Phys. Rev. B, 83, (2011) 224110.

[12] S. Zhang, R. Xia, H. Hao, H. Liu, and T. R. Shrout, Appl. Phys. Lett., 92, (2008) 152904.

[13] H. Du, W. Zhou, F. Luo, D. Zhu, S. Qu, *et al*. J. Appl. Phys., 105, (2009) 124104.

[14] P. Kumar, S. Singh, O.P. Thakur, C. Prakash and T.C. Goel: Jpn. J. Appl. Phys., 43, (2004) 1501.

[15] M.E. Lines and A.M. Glass: Principles and Applications of Ferroelectrics and Related Materials (Clarendon Press, Oxford, 1977) 289.

[16] J. Hao, Z. Xu, R. Chu, W. Li, G. Li, and Q. Yin, J. Alloy. Compd., 484, (2009) 233.

[17] X. G. Tang, J. Wang, X. X. Wang, and H. L. W. Chan, Solid State Commun., 131, (2004)163.

[18] L. E. Cross, Ferroelectrics, 76, (1987) 241.

[19] W. Supatrra, X. L. Tan, A. Supon, and Y. Rattikorn, J. Alloys. Compd., 454, (2008) 331.

[20] Y. Guo, K. Kakimoto, and H. Ohsato, J. Phys. Chem. Sol., 65, (2004) 1831.

[21] M. I. Morozov, H. Kungl, and M. J. Hoffmann, Appl. Phys. Lett., 98, (2011) 132908.

[22] H. L. Du, W. C. Zhou, F. Luo, D. M. Zhu, S. B. Qu, and Z. B. Pei, Appl. Phys. Lett., 91, (2007) 202907.

[23] B. Jaffe, W. Cook and H. Jaffe, Academic, New York, (1971) 185.

[24] R. P. Herber, G. A. Schneider, S. Wagner, and M. J. Hoffmann, Appl. Phys. Lett., 90, (2007) 252905.

[25] J. Liu, J. Zhu, X. Li, M. Wang, X. Zhu, J. Zhu, *et al.* Mater. Lett., 65, (2011) 948.

[26] K. Higashide, K. Kakimoto, H. Ohsato, and J. Eur. Ceram. Soc., 27, (2007) 4107.

[27] D. Damjanovic, Rep. Prog. Phys., 61, (1998) 1267.

[28] Q. M. Zhang, H. Wang, N. Kim, and L. E. Cross, J. Appl. Phys., 75, (1994) 454.

[29] S.H. Park, C.W. Ahn, S. Nahm, and J.S. Song, Jpn. J. Appl. Phys., 43, (2004) L1072.

[30]Y. Guo, K. Kakimoto, and H. Ohsato, Jpn. J. Appl. Phys., 43, (2004) 6662.

CHAPTER-5

Structural and Microstructural Study of Ag, Ta and V Modified $0.95[(K_{0.5}Na_{0.5})NbO_3]$ -$0.05[LiSbO_3]$ Ceramics

5.1Introduction

The various electrical properties of a ferroelectric material depend mainly on its crystal symmetry and the quality of the microstructure. Therefore, crystal structure and microstructural study are the two important characterizations of the ferroelectric materials. In KNN based ceramics, crystal symmetry plays an important role for the enhancement of ferroelectric and piezoelectric properties [1]. In this system, when the orthorhombic to tetragonal polymorphic phase transition occurs around room temperature (RT), coexistence of both orthorhombic and tetragonal structure have been reported at RT. The presence of both these structures at RT improves the ferroelectric and piezoelectric properties [2]. The sintering of KNN based ceramics is difficult by conventional solid state reaction route (CSSR) due to the presence of the volatile alkali elements [3]. The sintering process is mainly carried out in the presence of liquid phase in KNN based ceramics [4]. However, the presence of more amount of liquid phase decreases the bulk density of the ceramics. Hence, sintering temperature has to be optimized. Grain size is also an important factor which affects the ferroelectric and piezoelectric properties [5]. In this chapter, the density, structural and microstructural properties of the Ag, Ta and V modified $0.95[(K_{0.5}Na_{0.5})NbO_3]$ -$0.05[LiSbO_3]$ ceramics are presented in detail.

5.2 XRD Analysis

X-ray diffraction experiments were performed on a PANalytical's X'Pert PRO diffractometer in a wide range of Bragg angle ($20 \leq 2\theta \leq 70^{o}$) with Cu $K_{\alpha 1}$ radiation (λ=1.5405A^{0}) at a continuous scan type having step size of 0.02 degree at room temperature. All the peaks of the XRD patterns of all the compounds were indexed in different crystal systems and unit cell configurations using 2θ values and/or inter-planer spacing (d) of each peak by a computer programme package "POWD" [6]. The best agreement between the experimental and calculated values of d (i.e. $\Sigma(d_{exp}-d_{cal}) = \Delta d$ = minimum) was chosen for the confirmation of the crystal structures.

5.2.1 Ag Modified 0.95KNN-0.05LS Ceramics

Fig.5.1 shows the XRD patterns of $0.95[(K_{0.5}Na_{0.5})_{1-x}Ag_xNbO_3]$-$0.05LiSbO_3$ (KNAN-LS) ceramics calcined at 850 ^{o}C for 6h. Single perovskite phase is developed in all the KNAN-LS ceramics without any trace of secondary phase peaks. Fig.5.2 shows the XRD patterns of KNAN-LS ceramics with *x*=0.0, 0.02, 0.04, 0.06 and 0.08 sintered at 1080^{o}C for 4h, respectively. Single perovskite phase is also identified in all the sintered KNAN-LS ceramics without any trace of secondary phase peaks. This suggests that Ag^{+} ions have completely diffused into the KNN-LS lattice to form a homogeneous solid solution. It can be seen that the ceramics with *x*=0 (pure KNN-LS) possess both orthorhombic and tetragonal structure at RT, which is already discussed in (see chapter-4). Whereas, for *x*=0.02 the ceramics possess pure orthorhombic structure which is confirmed by matching the XRD patterns with the JCPDS card no. 71-2171. For *x*=0.08, the KNAN-LS ceramics possesses the tetragonal structure only which is indexed by

JCPDS card no. 71-0945.Therefore, it can be concluded that there exists a mixed structure region between orthorhombic and tetragonal structure for $0.02<x<0.08$ in KNAN-LS ceramics [7, 8]. The transformation of crystal structure from mixed structure to pure orthorhombic structure and again to tetragonal structure may be occurring due to the distortion created in the lattice with Ag^{+} substitution on the A-site of KNAN-LS ceramics. Fig.5.3 shows the enlarged XRD patterns of the (KNAN-LS) ceramics in the 2θ range from 44^{o} to 47^{o}. The positions of the diffraction peak of the ceramics initially shift towards higher angles with the increase in *x* content up to *x*=0.04. The XRD peaks shift towards left for x=0.06 and with further increase in *x* content i.e., at *x*=0.08, it again shifts towards right. This irregularity in the shifting of the position of XRD peaks is observed due to the transformation of orthorhombic to tetragonal phases. The XRD patterns of KNAN-LS ceramics were indexed in different crystal systems and unit cell configurations. The structure and unit cell parameters are listed in Table- 5.1. The unit cell volume follows overall decreasing trend with increase in Ag content, except at *x*=0.06 where unexpected behavior is observed. The decrease of unit cell volume with the increase of *x* content can be attributed to the smaller ionic radii of Ag^{+} ions in comparison to the $(K_{0.5}Na_{0.5})^{+}$ ions and the decrease of lattice space distance because of the shifting of XRD peaks towards right [3].

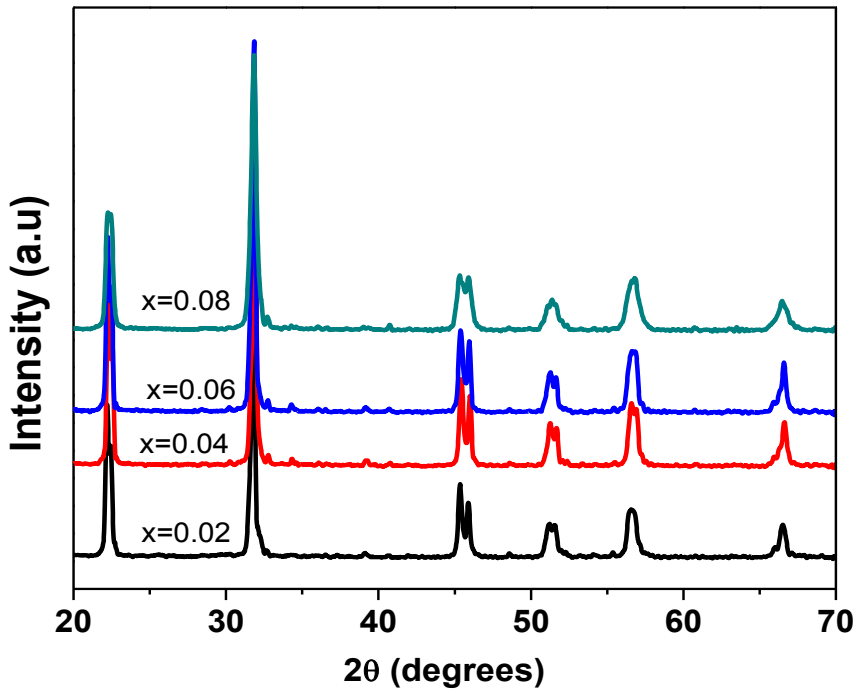

Fig.5.1 XRD patterns of KNAN-LS ceramics calcined at 850 ^{o}C for 6h.

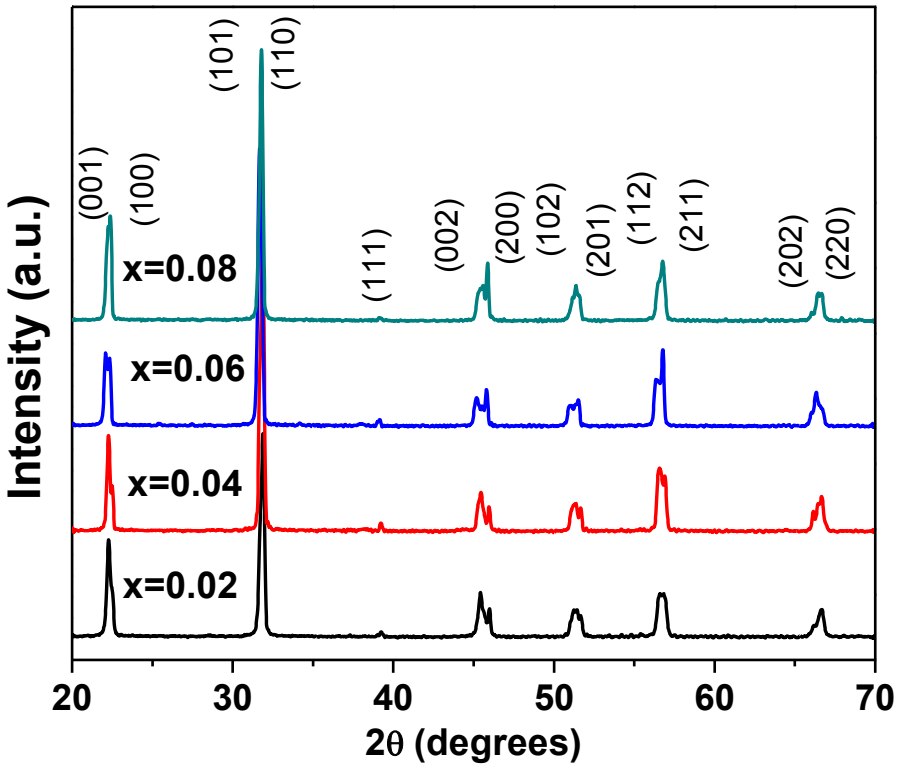

Fig.5.2 XRD patterns of KNAN-LS ceramics sintered at 1080 ^{o}C for 4h.

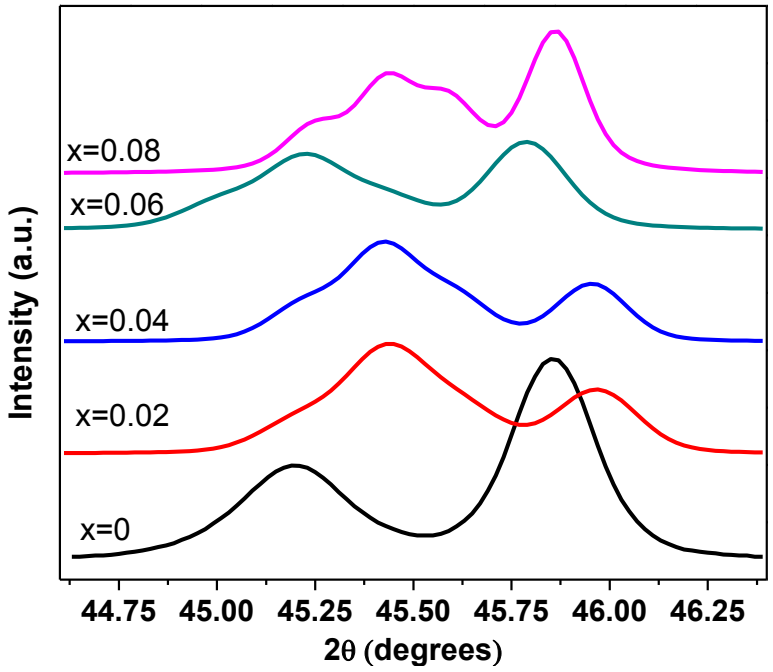

Fig.5.3 Enlarged XRD patterns of KNAN-LS ceramics in the 2θ range of 44–47 degrees.

Table 5.1 Structure and unit cell parameters of KNAN-LS ceramics sintered at 1080 ^{o}C for 4h

x	a (Å)	b (Å)	c (Å)	Vol. (Å)^3	S.D.	Structure
0	**3.9638**	**4.0141**	**3.9657**	**63.09**	**0.0023**	**Orthorhombic**
	3.9629	**3.9629**	**4.0179**	**63.10**	**0.0031**	**Tetragonal**
0.02	**3.9392**	**3.9912**	**4.0039**	**62.95**	**0.0059**	**Orthorhombic**
0.04	**3.9424**	**3.9839**	**4.0021**	**62.85**	**0.0023**	**Orthorhombic**
0.06	**3.9539**	**4.0148**	**3.9755**	**63.10**	**0.0017**	**Orthorhombic**
	3.9594	**3.9594**	**4.0183**	**62.99**	**0.0078**	**Tetragonal**
0.08	**3.9584**	**3.9584**	**4.0066**	**62.77**	**0.0075**	**Tetragonal**

5.2.2 Ta Modified 0.95KNN-0.05LS Ceramics

Fig.5.4 shows the XRD patterns of $0.95[K_{0.5}Na_{0.5}Nb_{(1-x)}Ta_xO_3]$-$0.05[LiSbO_3]$/KNNT-LS ceramics calcined at 850 ^oC for 6h. Single perovskite phase is developed in all the KNNT-LS ceramics without any trace of secondary phase peaks. Fig. 5.5 shows the XRD patterns of KNNT-LS ceramics with *x*=0-0.08 sintered at optimum temperature. Single perovskite phase is developed in all the ceramics, which suggests that Ta^{+5} ions have completely diffused into the B-site of the $0.95[K_{0.5}Na_{0.5}Nb_{(1-x)}Ta_xO_3]$-$0.05[LiSbO_3]$/(KNNT-LS) ceramics to form a homogeneous solid solution. Fig.5.6 shows the enlarged XRD patterns of the (KNNT-LS) ceramics in the 2θ range from 44^o to 47^o. It can be seen that the positions of the diffraction peak of the ceramics shift towards higher angles with the increase in *x* content. This indicates the decrease in lattice space distance (d) and unit cell volume with the increase in *x* content in KNNT-LS ceramics [9]. The XRD peaks of KNNT-LS ceramic are indexed in both tetragonal and orthorhombic crystal systems in different unit cell configurations. The indexing of XRD peaks and the determination of lattice parameters of KNNT-LS ceramics are carried out using a software package "POWD". The calculated unit cell volume and lattice parameters are given in Table 5.2. The unit cell volume of KNNT-LS ceramic with *x*=0 and *x*=0.02 are found to be nearly same for both orthorhombic and tetragonal structures, which indicates the possibility of the presence of both phases at room temperature [10]. It is found that with the increase in *x* content the unit cell volume is decreasing, which may be due to the fact that the ionic radii of Ta^{+5} is smaller than the ionic radii of Nb^{+5} [11] . It is reported that vacancies are created when higher ionic radii elements are replaced by lower ionic radii elements, which in turn decreases the unit cell volume in a compound.

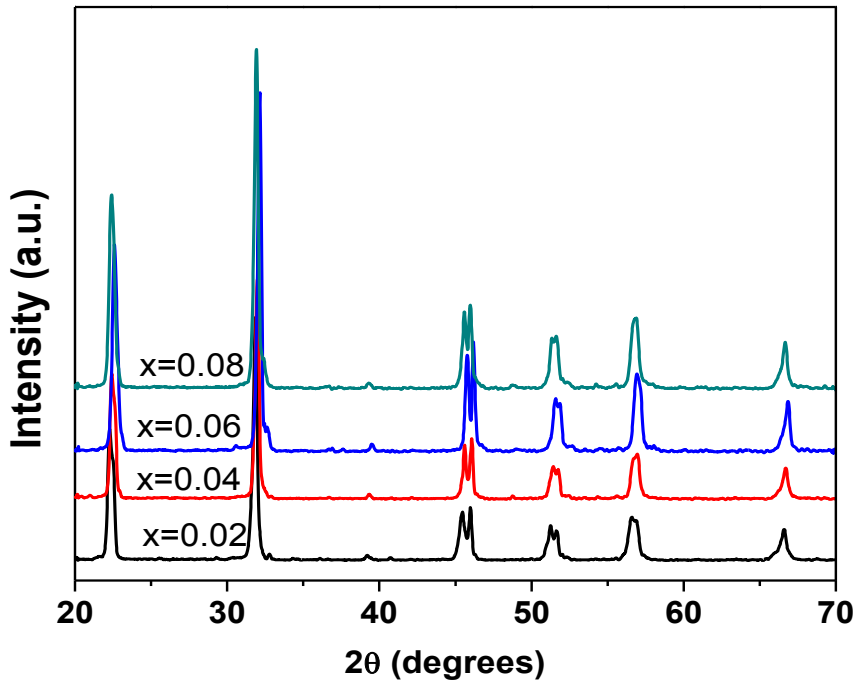

Fig.5.4 XRD patterns of KNNT-LS Ceramics calcined at 850°C for 6h.

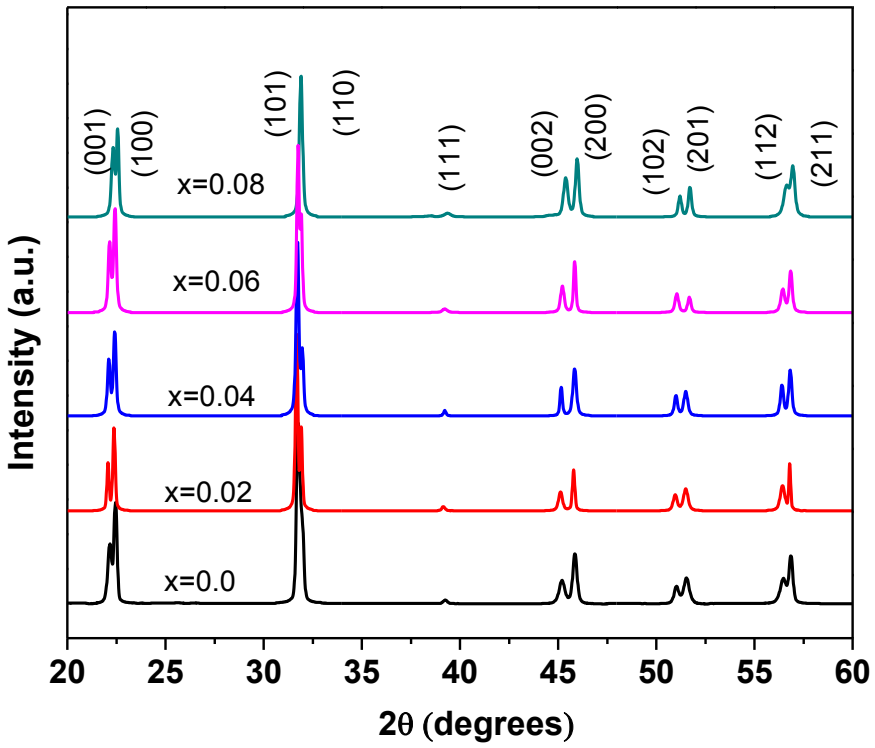

Fig.5.5 XRD patterns of KNNT-LS Ceramics sintered at 1080 °C for 4h (*x*=0 and 0.02), 1100 °C (*x*=0.04 and 0.06) and 1120°C (*x*=0.08).

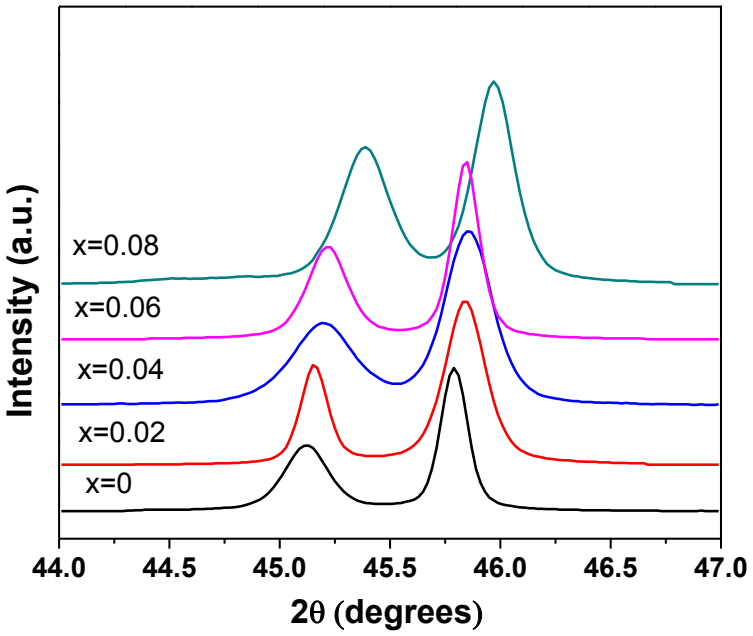

Fig.5.6 Enlarged XRD patterns of KNNT-LS ceramics in the 2θ range of 44–47 degrees.

Table 5.2 Structure and unit cell parameters of KNNT-LS ceramics sintered at 1080 ^{o}C for 4h (*x*=0 and 0.02), 1100 ^{o}C (*x*=0.04 and 0.06) and 1120^{o}C (*x*=0.08).

x	a (Å)	b (Å)	c (Å)	Vol. (Å)^3	S.D	Structure
0	**3.9638**	**4.0141**	**3.9657**	**63.09**	**0.0023**	**Orthorhombic**
	3.9629	**3.9629**	**4.0179**	**63.10**	**0.0031**	**Tetragonal**
0.02	**3.9597**	**4.0135**	**3.9631**	**62.98**	**0.0058**	**Orthorhombic**
	3.9611	**3.9611**	**4.0142**	**62.98**	**0.0065**	**Tetragonal**
0.04	**3.9582**	**3.9582**	**4.0104**	**62.83**	**0.0078**	**Tetragonal**
0.06	**3.9572**	**3.9572**	**4.0067**	**62.74**	**0.0047**	**`Tetragonal**
0.08	**3.9445**	**3.9445**	**3.9891**	**62.06**	**0.0089**	**Tetragonal**

5.2.3 V Modified 0.95KNN-0.05LS Ceramics

Fig. 5.7 shows the XRD patterns of $0.95[K_{0.5}Na_{0.5}Nb_{(1-x)}V_xO_3]$-$0.05[LiSbO_3]$/(KNNV-LS) ceramics calcined at 850^oC for 6h. Single perovskite phase is obtained in all the samples except at x=0.08. For x=0.08 perovskite phase along with secondary phases are detected, which may be due to the solubility limit of V in KNNV-LS ceramics. Fig5.8 shows the XRD patterns of KNNV-LS ceramics with x=0-0.08 sintered at optimum temperature. The XRD peaks are found to be sharp and distinct indicating good homogeneity and crystallinity of the samples. The formation of secondary phase along with the perovskite phase is also detected at x=0.08. The development of single perovskite phase in KNNV-LS ceramics for x=0-0.06 suggests that V^{+5} ions have completely diffused into the B-site of the KNNV-LS ceramics to form a homogeneous solid solution and defines the solid solution limit of V in KNNV-LS ceramics. Fig.5.9 shows the enlarged XRD patterns of the (KNNV-LS) ceramics in the 2θ range from 44.5^o to 46.5^o. It can be seen that the positions of the diffraction peak of the ceramics shift towards right with the increase in x content. This indicates the decrease in lattice space distance (d) and unit cell volume with the increase in x content. The XRD peaks of KNNV-LS ceramic are indexed in different crystal systems and unit cell configurations. The calculated unit cell volume and lattice parameters are given in Table-5.3. The crystal structure of the ceramics transforms from mixed structure for x=0 to orthorhombic structure for x=0.02, which may be due to the large distortion created by V substitution in place of Nb in KNN-LS ceramics. With further increase in x content orthorhombic structure is stabilized in KNNV-LS ceramics. The unit cell volume

decreases with the increase in *x* content in KNNV-LS ceramics, which may be due to the lower ionic radii of V^{+5} (0.54 Å) in comparison to that of Nb^{+5}(0.69 Å).

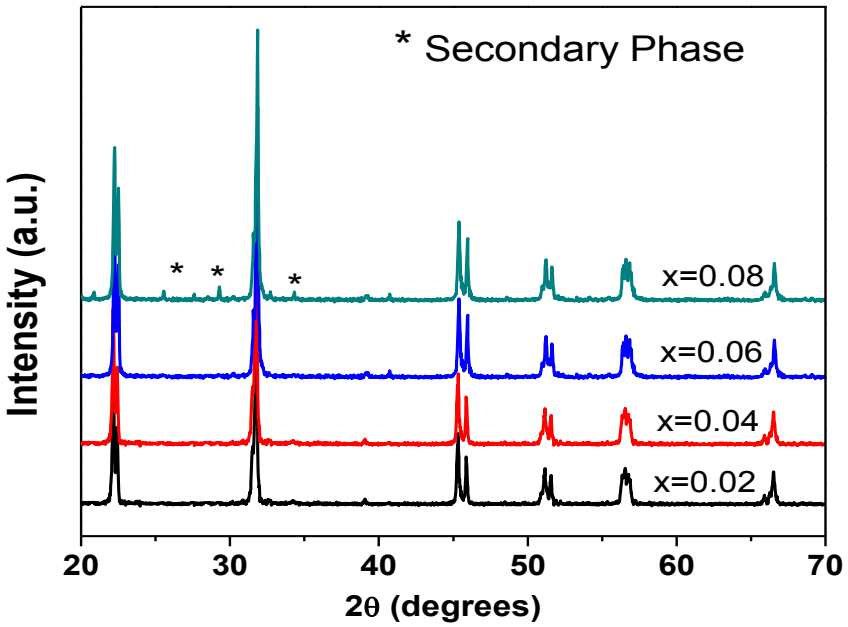

Fig.5.7 XRD patterns of KNNV-LS Ceramics calcined at 850 ^{o}C for 6h.

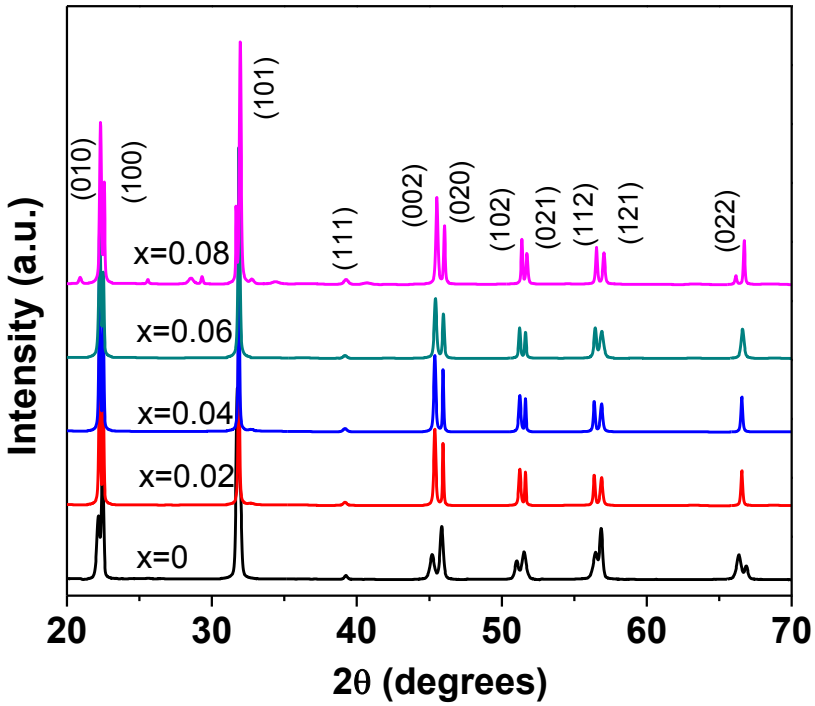

Fig.5.8 XRD patterns of KNNV-LS Ceramics sintered at 1080^{o}C (*x*=0), 1050^{o}C (*x*=0.02), 1030 (*x*=0.04), 1010 (*x*=0.06) and 990^{o}C (*x*=0.08) for 4h.

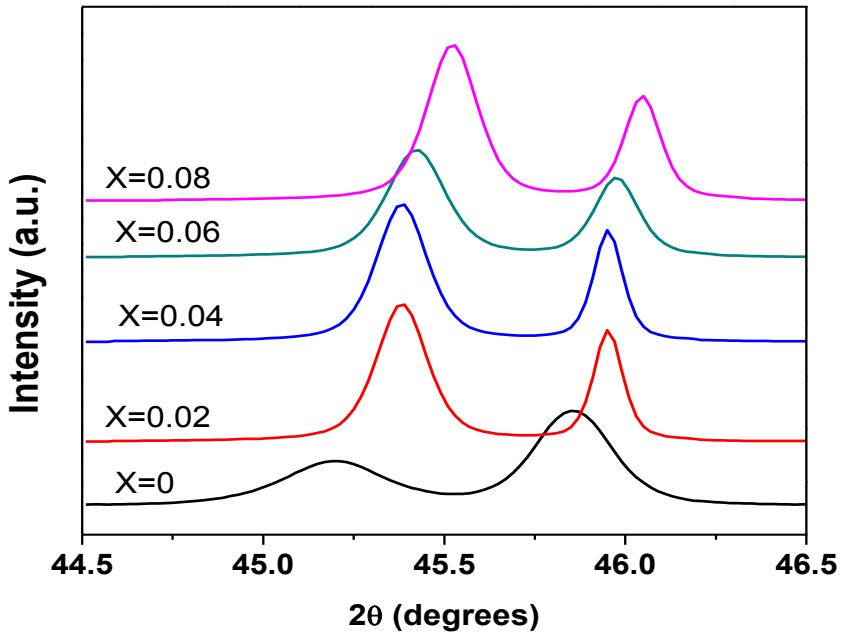

Fig.5.9 Enlarged XRD patterns of KNNV-LS ceramics in the 2θ range of 44.5–46.5 degrees.

Table 5.3 Structure and unit cell parameters of KNNV-LS ceramics sintered at sintered at 1080°C (*x*=0), 1050°C (*x*=0.02), 1030 (*x*=0.04), 1010 (*x*=0.06) and 990°C (*x*=0.08) for 4h.

x	a (Å)	b (Å)	c (Å)	Vol. (Å)^3	S.D.	Structure
0	**3.9638** **3.9629**	**4.0141** **3.9629**	**3.9657** **4.0179**	**63.09** **63.10**	**0.0023** **0.0031**	**Orthorhombic** **Tetragonal**
0.02	**3.9465**	**3.9931**	**3.9926**	**62.92**	**0.0062**	**Orthorhombic**
0.04	**3.9432**	**3.9926**	**3.9900**	**62.82**	**0.0043**	**Orthorhombic**
0.06	**3.9435**	**3.9967**	**3.9816**	**62.61**	**0.0019**	**Orthorhombic**
0.08	**3.9305**	**3.9902**	**3.9823**	**62.46**	**0.0058**	**Orthorhombic**

5.3 Sintering and Densification Behavior

The bulk density of a ferroelectric material plays an important role for the improvement of ferroelectric and piezoelectric as well as dielectric properties. Bulk density is one of the crucial parameters on which the material properties depend and hence plays an important part in devices of the system. Especially in KNN based ceramics the phase stability is limited to 1140 ^{o}C and hence higher sintering temperature is not possible [12]. The sintering process in KNN based ceramics is a crucial step to produce materials with high piezoelectric properties. It has been found that in this system a narrow sintering range exists where the materials experience considerable changes in the grain size, density, porosity, appearance of secondary phases, liquid phase and the piezoelectric and ferroelectric properties. Therefore, sintering temperature has to be optimized to obtain desired electrical properties. The bulk density is measured by Archimedes principle.

5.3.1 Ag Modified 0.95KNN-0.05LS Ceramics

Fig.5.10 shows the effect of sintering temperature on the relative density (RD) of the KNAN-LS ceramics with x=0.0-0.08. The relative density increases with the increase in sintering temperature from 1060 to 1080^{o}C, whereas with the further increase in sintering temperature, RD decreases. The results indicate that Ag substitution doesn't affect the optimum sintering temperature i.e 1080^{o}C. At 1080^{o}C sintering temperature, the RD increases initially with the increase in Ag content up to x=0.06, but with the further increase in x content RD decreases, which defines the optimum amount of Ag content in KNAN-LS ceramics. Maximum RD ~ 96.5% is obtained for the KNAN-LS ceramics with x=0.06, which is higher than the RD reported for pure KNN-LS ceramics.

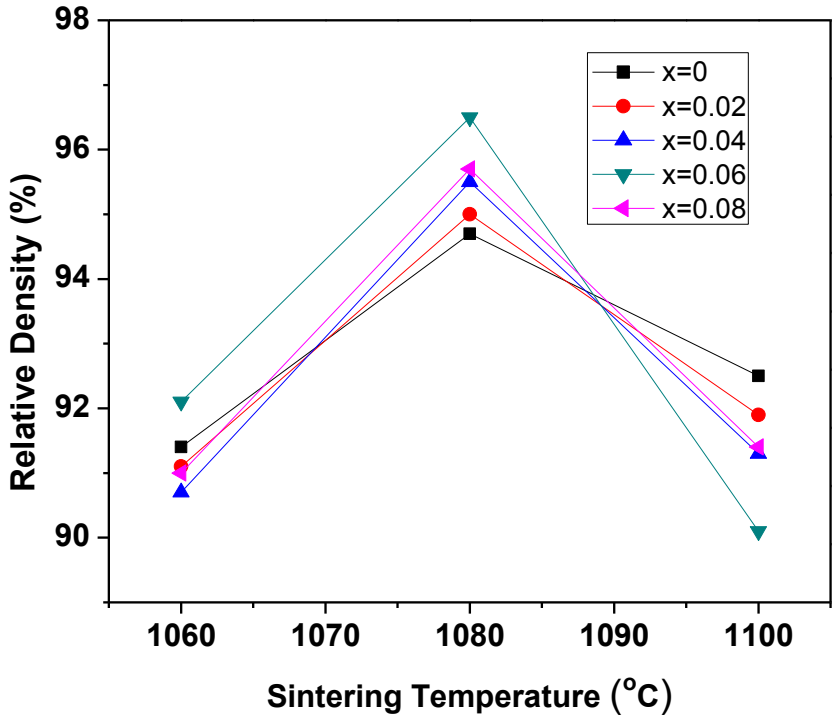

Fig.5.10 Relative density (RD) of KNAN-LS ceramics as a function of sintering temperature.

5.3.2 Ta Modified 0.95KNN-0.05LS Ceramics

Fig. 5.11 shows the relative density (RD) of KNNT-LS ceramics as a function of sintering temperature. The sintering temperature has been optimized for each composition to obtain maximum RD. The optimum sintering temperature increases with the increase in *x* content. This is due to the fact that the melting temperature of $KTaO_3$ (~1370^oC) is higher than $KNbO_3$ (1039^oC) ceramics [21], which increases the sintering temperature. The RD increases with the increase in *x* content up to 0.06, with further increase in x content the RD decreases. Maximum RD ~96.8 % is obtained for the KNNT-LS ceramics with *x*=0.06, which is higher than the RD reported for pure KNN ceramics.

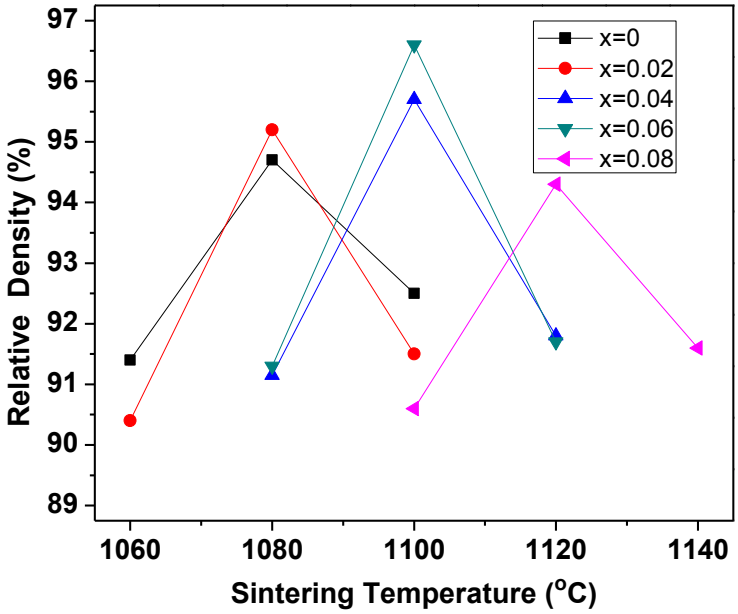

Fig. 5.11 Relative density (RD) of KNNT-LS ceramics as a function of sintering temperature.

5.3.2 V Modified 0.95KNN-0.05LS Ceramics

Fig. 5.11 shows the relative density (RD) of KNNV-LS ceramics as a function of sintering temperature. V_2O_5 is a low melting point oxide, previously which has been used in other ferroelectric systems to significantly lower the optimum sintering temperature. In this case, sintering is carried out in a temperature range from 990-1080 ^oC. It is found that with the increase in V content in KNNV-LS ceramics optimum sintering temperature decreases linearly. For x=0.02 the optimum sintering temperature reaches ~ 1050^oC and for x=0.08 it reaches ~ 990^oC. This may be due to the effect of lower melting point of V_2O_5. The value of RD is found to be maximum for KNNV-LS ceramic with x=0.06 sintered at 1010^oC for 4h. The maximum value of RD is found to be lower than the other modified ceramics in this study.

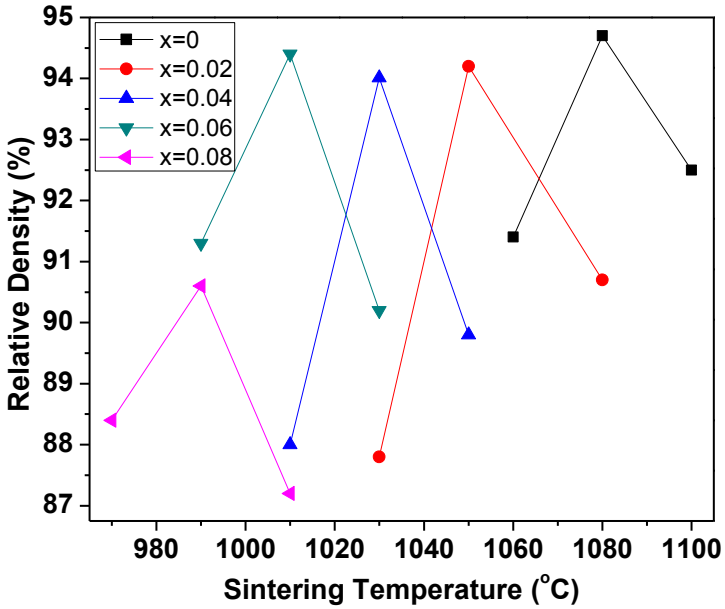

Fig. 5.12 Relative density (RD) of KNNV-LS ceramics as a function of sintering temperature.

5.4 Morphology Study

5.4.1 Ag Modified 0.95KNN-0.05LS Ceramics

Fig.5.13 shows the SEM micrographs of the KNAN-LS ceramics sintered at 1080^{o}C for 4 h. SEM micrograph shows the polycrystalline microstructure with nearly rectangular grains of different grain sizes, which are non-uniformly distributed throughout the sample surface. The grains and grain boundaries are well defined and clearly visible. For x=0 the ceramics contain few pores, but with increase in x content the pore size decreases and the dense packing of grains occurs. The packing of grains become more and more dense with the increase in x content which may be due to the lower melting point of Ag_2O. The lower melting point of Ag_2O enhances the sintering of KNAN-LS ceramics with the formation of liquid phase which is a well-known fact in KNN based ceramics as discussed in chapter-4.

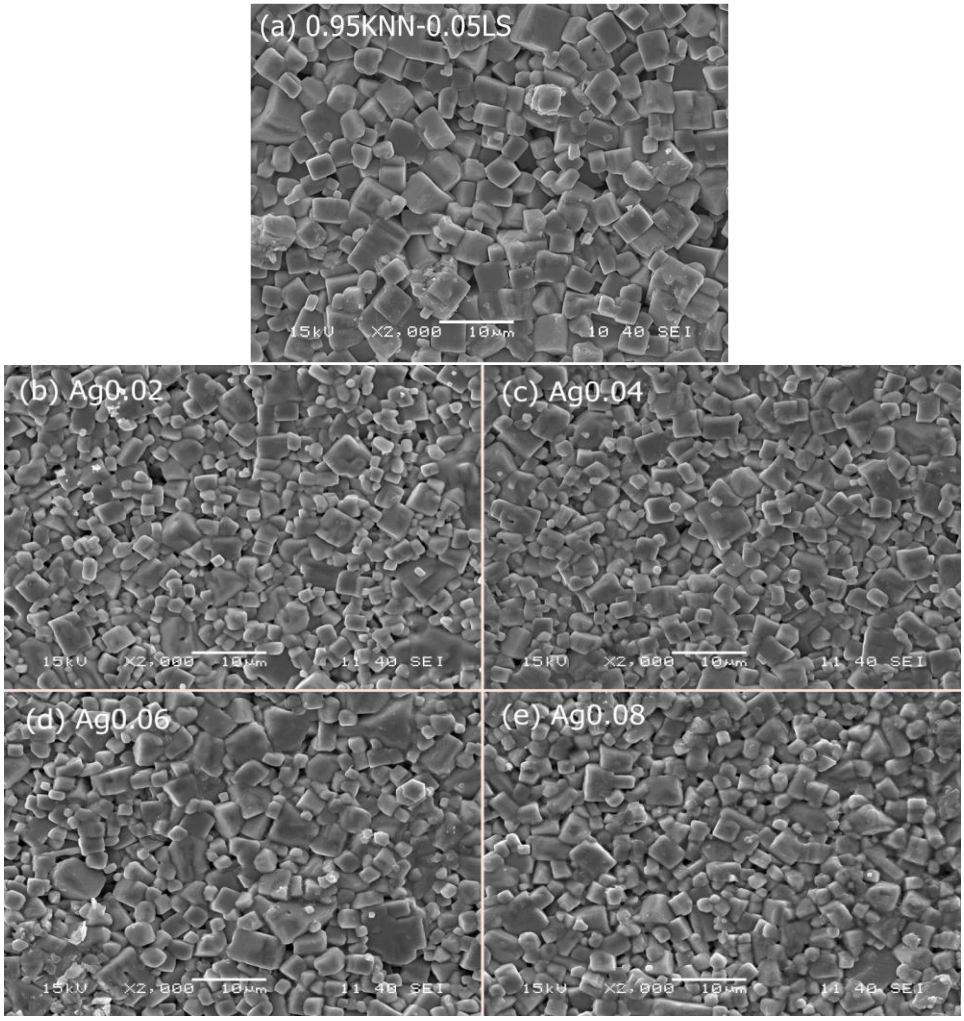

Fig. 5.13 SEM micrographs of KNAN-LS ceramics sintered at 1080^{o}C for 4 h.

5.4.2 Ta Modified 0.95KNN-0.05LS Ceramics

Fig.5.14 shows the SEM micrographs of the KNNT-LS ceramics sintered at optimum temperature. All the ceramics are found to be dense with well-defined grain boundaries. The average grain size of the ceramics decreases with the increase in Ta content. It can be seen that with increase in Ta content the sintering temperature of the ceramics also increases. The packing of grains are found to increase with increase in *x* content but the distribution of grain size become non-uniform.

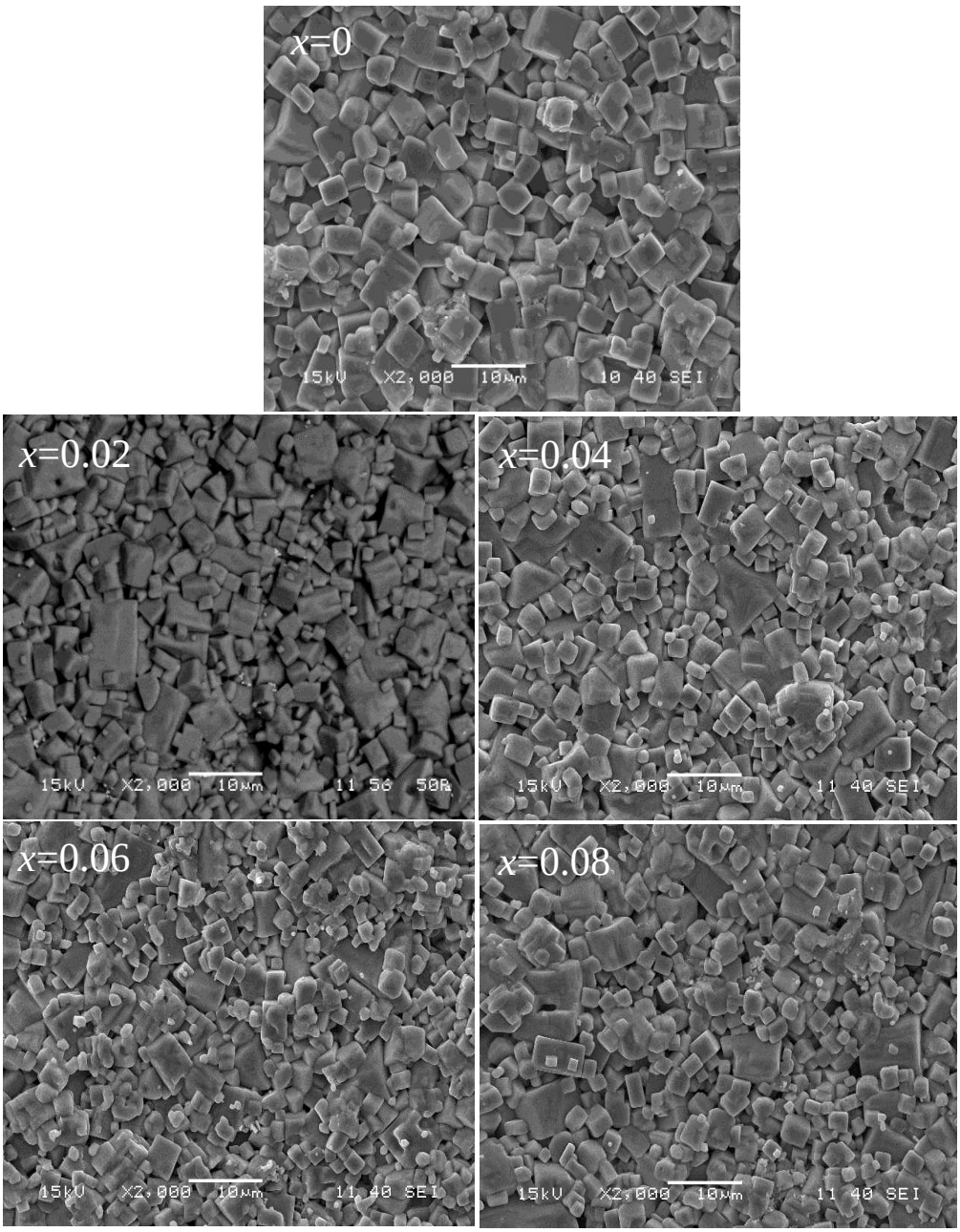

Fig. 5.14 SEM micrographs of KNNT-LS ceramics sintered at 1080^{o}C (*x*=0 and 0.02), 1100^{o}C (*x*=0.04 and 0.06) and 1120^{o}C (*x*=0.08).

5.4.3 V Modified 0.95KNN-0.05LS Ceramics

Fig.5.15 shows the SEM micrographs of the KNNV-LS ceramics sintered at optimum temperature. All the ceramics are found to possess appreciable amount of pores and the porosity is found to be maximum for the ceramics with *x*=0.08. The average grain

size of the ceramics decreases with the increase in *x* content. Well defined grain boundary is obtained for unmodified KNN-LS ceramics but for the V modified ceramics the grain boundaries are not visible clearly. The sintering here in this case is taking place in the presence of liquid phase. The decrease of RD in V modified ceramics may be due to the formation of more amount of liquid phase.

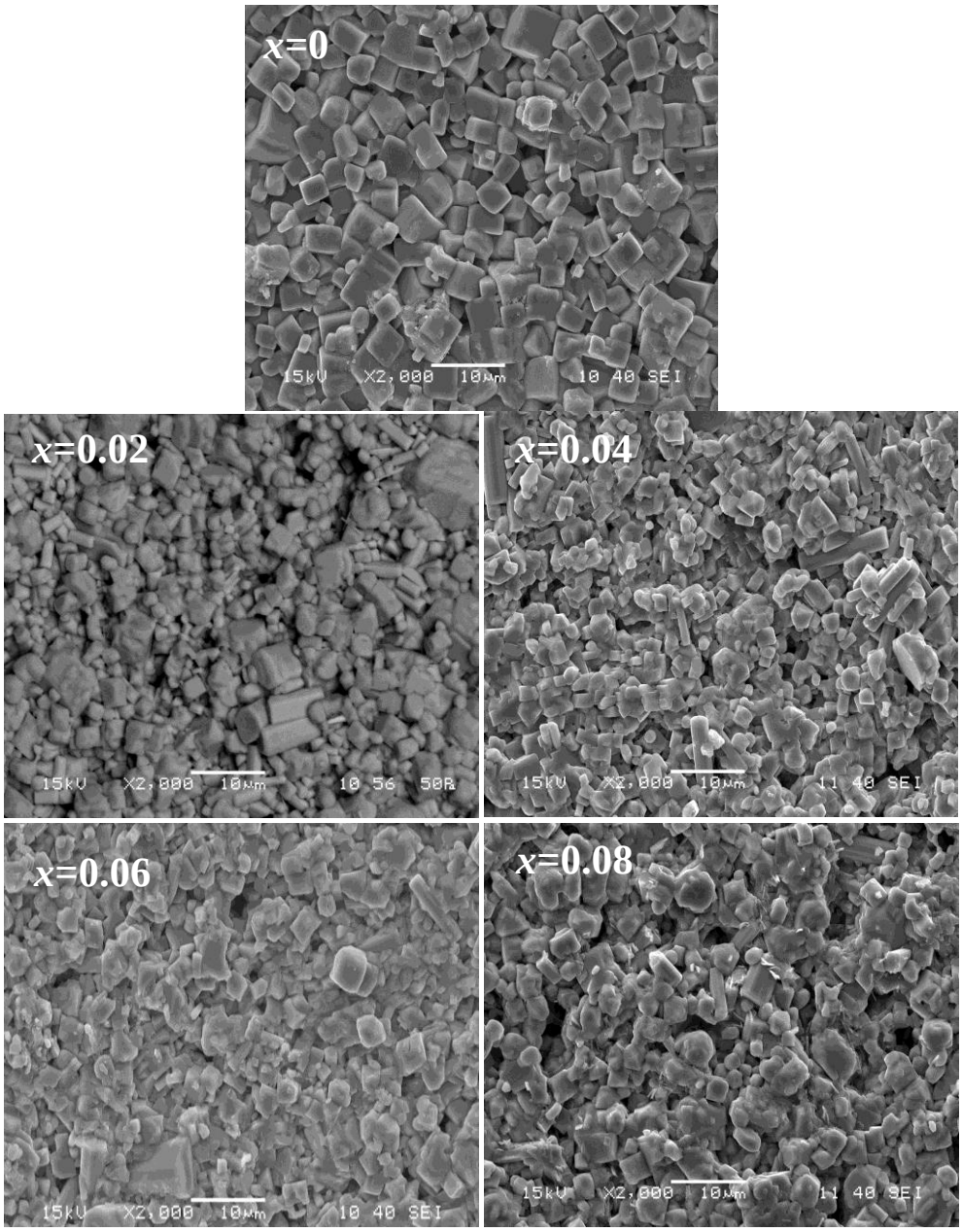

Fig.5.15 SEM micrographs of KNNV-LS ceramics sintered at 1080°C (*x*=0), 1050°C (*x*=0.02), 1030 (*x*=0.04), 1010 (*x*=0.06) and 990°C (*x*=0.08) for 4h.

References

[1] F. R. Macros, P. Marchet, T. M. Mejean, and J. F. Fernandez, Mater. Chem. Phys., 123, (2010) 91.

[2] L. Wu, J. L. Zhang, S. F. Shao, P. Zheng and C. L. Wang, J. Phys. D: Appl. Phys., 41, (2008) 035402.

[3] C. Lei, and Z. G. Ye, Appl. Phys. Lett., 93, (2008) 2956410.

[4] S. Zhang, H. J. Lee, C. Ma, and X. Tan, J. Am. Ceram. Soc., 94, (2011) 3659.

[5] C. A. Randall, N. Kim, J. P. Kucera, W. Cao and T. R. Shrout, J. Am. Ceram. Soc., 81, (1998) 677.

[6] E. Wu, POWD, an interactive powder diffraction data interpretation and indexing program, Version 2.1, School of Physical Science, Flinders University of South Australia.

[7] D. Lin K. W. Kwok, and H. W. L. Chan. Appl. Phys. Lett., 91, (2007) 143513.

[8] Y. Wang, Y. Lu, M. Wu, D. Wang, Y.g Li and Y. Wang. Int. J.Appl. Ceram.Technol., (2011) DOI: 10.1111/j.1744-7402 02650.x.

[9] S. K. S. Parashar, R. N. P. Choudhary, and B. S. Murty , J. Appl. Phys., 94, (2003) 6091.

[10] S. Zhang, R. Xia, H. Hao, H. Liu, and T. R. Shrout, Appl Phys Lett., 92, (2008) 152904.

[11] Yuan Zhou, Min Guo, Ci Zhang, and Mei Zhang, Ceram. Int., 35, (2009) 3253.

[12] X. Sun, J. Chen, R. Yu, X. Xing, L. Qiao, and G. Liu, Sci. technol. Adv. Mater., 9, (2008) 025004.

CHAPTER-6

Dielectric, Ferroelectric and Piezoelectric Properties of Ag, Ta and V Modified 0.95[($K_{0.5}Na_{0.5}$)NbO_3] -0.05[$LiSbO_3$] Ceramics

6.1 Introduction

Dielectric study of the ferroelectric materials gives information about the phase transition temperatures, dielectric constant and dielectric loss dependence on temperature and frequency. For multilayer capacitors (MLC) and high power applications high value of dielectric constant (ε_r) with low dielectric loss (tanδ) is required [1]. Whereas, study of ferroelectric and piezoelectric properties gives information about remnant polarization (P_r), coercive field (E_c), piezoelectric coefficient (d_{33}) and electromechanical coupling coefficients (k_p). High value of P_r, with low E_c, is required for non-volatile ferroelectric random access memory (NVFRAM) applications, whereas high values of d_{33} and k_p are required for transducer applications [2-3]. In pure KNN ceramics above room temperature (RT) two phase transition peaks are observed in the temperature dependent dielectric curve. The first phase transition (~200^oC) is called as the orthorhombic to tetragonal (T_{O-T}) polymorphic phase transition temperature (PPT) whereas the second one (~420^oC) is the ferroelectric to paraelectric phase transition temperature. According to previous reports, in KNN based systems the shifting of the T_{O-T} towards room temperature (RT) side enhances the dielectric as well as the ferroelectric and piezoelectric properties [4]. However, with the shifting of the T_{O-T} in KNN based systems, the piezoelectric properties become highly temperature dependent. Therefore, in KNN based systems the temperature dependent piezoelectric property needs to be studied [5]. In the present chapter, looking at the importance of the above mentioned properties the

dielectric, ferroelectric and piezoelectric properties of the Ag, Ta and V modified 0.95KNN-0.05LS ceramics are discussed in detail.

6.2 Dielectric Properties

6.2.1 Temperature Dependent Dielectric Constant (ε_r) and Dielectric Loss (tanδ)

6.2.1.1 $0.95(K_{0.5}Na_{0.5})_{(1-x)}Ag_xNbO_3$-$0.05LiSbO_3$ / KNAN-LS (*x*=0, 0.02, 0.04, 0.06 and 0.08) Ceramics

The variation of ε_r with temperature at different frequencies of KNAN-LS ceramics sintered at 1080^{o}C for 4h is shown in Fig. 6.1(a, b, c, d, e). It is found that in all the ceramics with the increase in frequency ε_r value decreases. The decrease in the value of ε_r can be explained on the basis of decrease in polarization with the increase in frequency. Polarization of a dielectric material is the sum of the contributions of dipolar, electronic, ionic and interfacial polarizations [6]**.** At low frequencies, all the polarization mechanism respond easily to the time varying electric field but as the frequency of the electric field increases different polarization contributions filters out, as a result, the net polarization of the material decreases which leads to the decrease in the value of ε_r. The temperature dependence of ε_r and tanδ at 10 kHz frequency for KNAN-LS ceramics with *x*=0, 0.02, 0.04, 0.06 and 0.08 are shown in Fig. 6.2 (a) and (b). For pure KNN-LS ceramics two phase transitions are observed at ~43^{o}C and ~385.5^{o}C, respectively. The first phase transition temperature is known as the orthorhombic-tetragonal phase transition temperature (T_{O-T}) and the second one is the Curie temperature (T_c) of the pure KNN-LS ceramics. The occurrence of T_{O-T} close to RT confirms the possibility of the simultaneous presence of orthorhombic and tetragonal structures in pure KNN-LS ceramics [4]. It is found that for the ceramics with *x*=0.02 the T_{O-T} and T_c are shifted to 120^{o}C and 380^{o}C respectively. However, with further increase in *x* content, there is a

decrement in both these phase transition temperatures are observed. It can also be seen that with the increase in *x* content from *x*=0.02 to 0.08 the value of ε_r at RT increases, which may be due to the stabilization of tetragonal structure with the shifting of T_{O-T} towards lower temperature side [7]. Maximum value of ε_r at RT is obtained when *x*=0.08, which indicates that the presence of T_{O-T} must be just below RT. This is because value of ε_r near phase transition temperature is more than the nearby temperatures [8]. The values of ε_r, tanδ, T_{O-T} and T_c are given in Table-6.1. It can be seen that with increase in temperature the value of tanδ increases in all the ceramics, which may be due to the increase of space charge polarization and mobility of charged defects in the material [9].

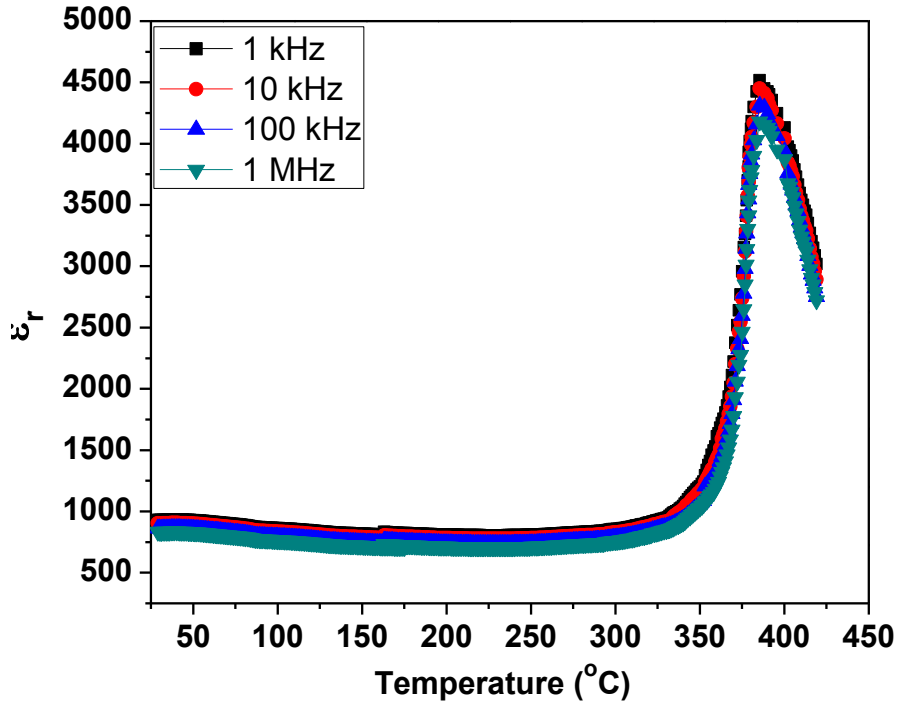

Fig.6.1 (a)

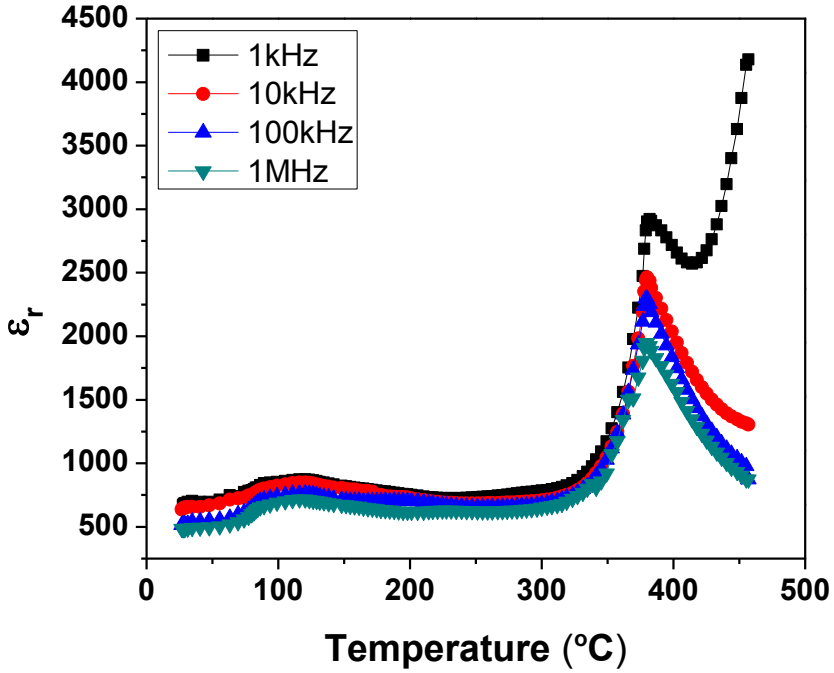

Fig.6.1 (b)

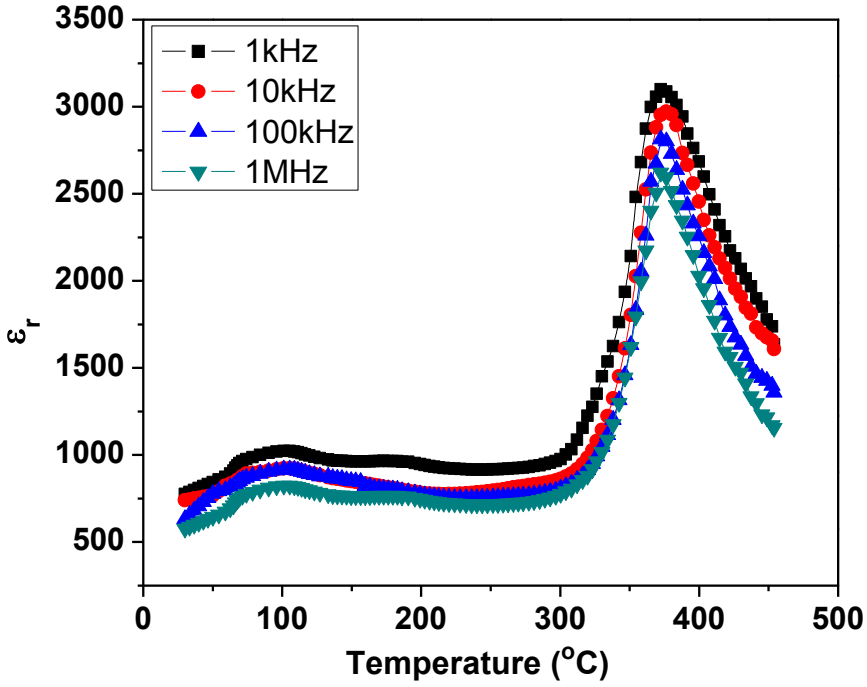

Fig.6.1 (c)

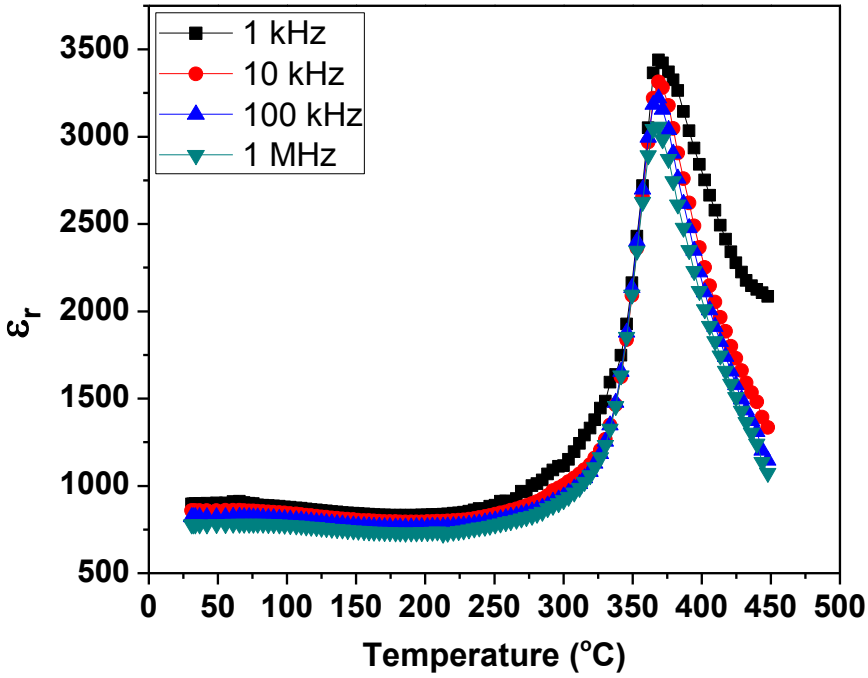

Fig.6.1 (d)

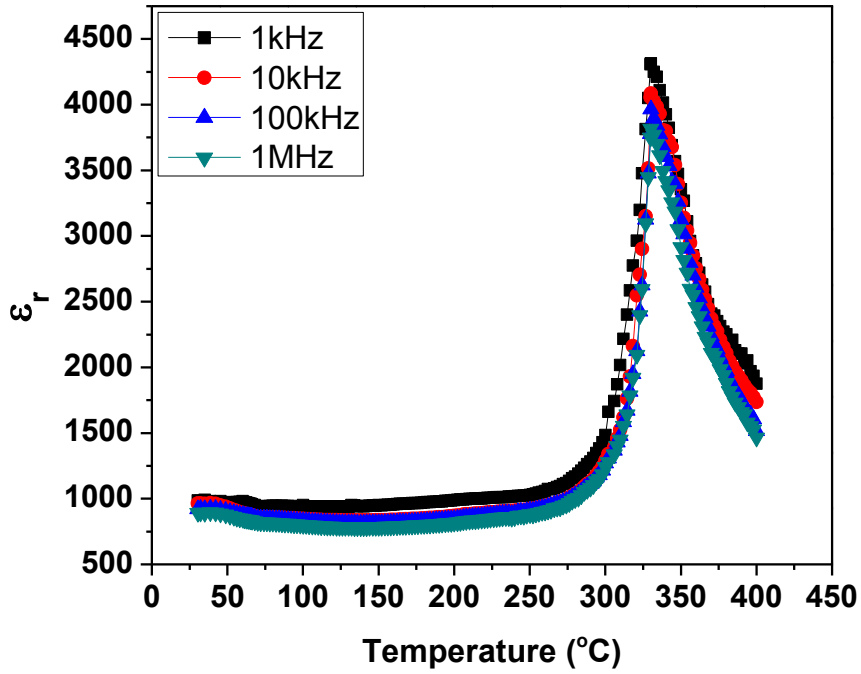

Fig.6.1 (e)

Fig.6.1 Temperature dependent ε_r at various frequencies of KNAN-LS ceramics with (a) x=0 (b) x=0.02 (c) x=0.04(d) x=0.06 and (e) x=0.08 sintered at 1080°C.

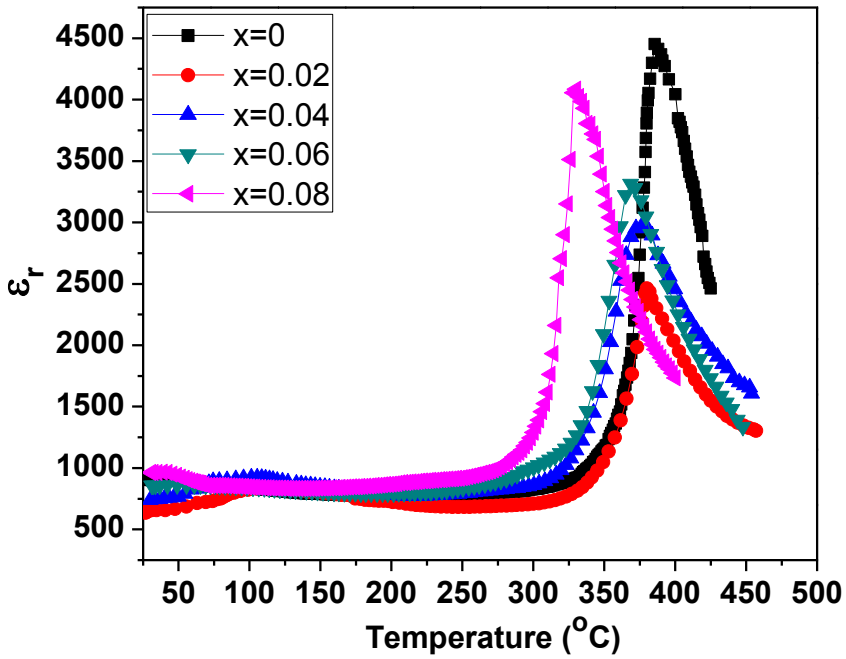

Fig.6.2 (a) Temperature dependent ε_r of KNAN-LS ceramics at 10 kHz frequency with (a) *x*=0 (b) *x*=0.02 (c) *x*=0.04(d) *x*=0.06 and (e) *x*=0.08 sintered at 1080^{o}C.

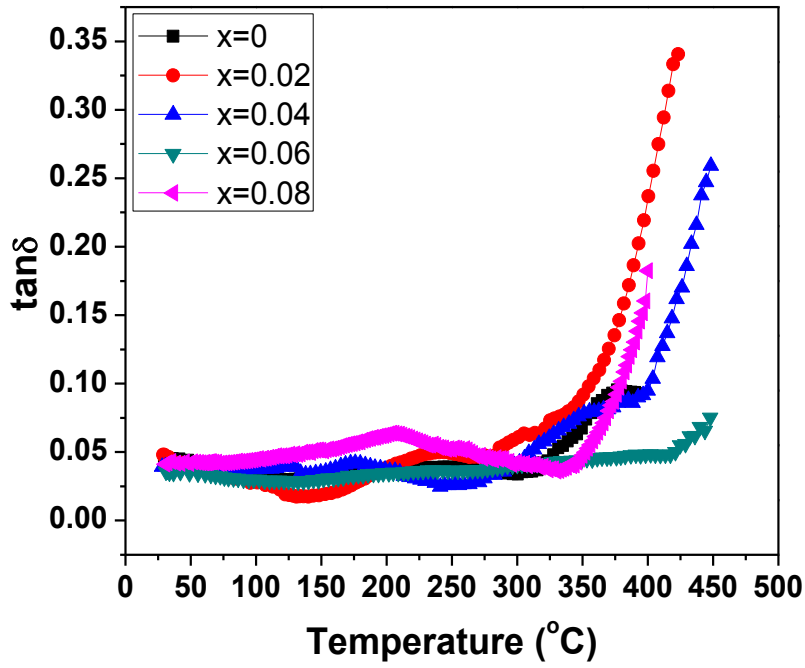

Fig. 6.2 (b) Temperature dependence of dielectric loss (tanδ) at 10 kHz frequency of KNAN-LS ceramics with (a) *x*=0 (b) *x*=0.02 (c) *x*=0.04(d) *x*=0.06 and (e) *x*=0.08 sintered at 1080^{o}C.

Table-6.1 ε_r , tanδ, Tc and T_{O-T} of KNAN-LS ceramics at 10 kHz frequency sintered at 1080^{o}C.

x	0	0.02	0.04	0.06	0.08
ε_r (10 kHz)	903	633	740	858	941
tanδ (10 kHz)	0.0465	0.048	0.039	0.035	0.041
Tc (^{o}C)	385.5	380	376	368	331
T_{O-T} (^{o}C)	43	120	101	65	Below RT

6.2.1.2 0.95($K_{0.5}Na_{0.5}$)$Nb_{(1-x)}Ta_xO_3$-0.05$LiSbO_3$ / KNNT-LS (*x*=0.02, 0.04, 0.06 and 0.08) Ceramics

The variation of ε_r with temperature at different frequencies of KNNT-LS samples sintered at optimum temperatures (ceramics with highest relative density) for 4h are shown in Fig. 6.3 (a, b, c, d). With the increase in frequency ε_r value decreases in all the ceramics, this may be due to the decrease in the net polarization in the materials at higher frequency. The temperature dependence of dielectric constant (ε_r) of the KNNT-LS ceramics at 10 kHz frequency is shown in Fig. 6.4(a). Similar to pure KNN ceramics, the KNNT-LS ceramics with *x*=0 shows two phase transitions. The first one located ~43^{o}C is the orthorhombic-tetragonal phase transition (T_{O-T}) whereas the second one located ~385.5^{o}C is called as the ferroelectric-paraelectric phase transition (T_c). However, with the increase in *x* content both these phase transition temperatures are found to decrease, which may be due to the stabilization of tetragonal phase at RT. The reason behind the decrease of T_c can be further explained in terms of the decrease of the c/a ratio in the ceramics (chapter-5). Since it is known that c/a ratio is the direct reflection of tetragonality i.e., with decrease in c/a ratio, tetragonality decreases which in turn decreases the T_c [10]. The RT value of ε_r in the KNNT-LS ceramics is found to increase

with the increase in *x* content up to x=0.06, whereas with the further increase in *x* content the value of ε_r decreases. The temperature dependence of dielectric loss (tanδ) behavior of KNNT-LS ceramics at 10 kHz frequency is shown in Fig. 6.4 (b). In low temperature region (RT to 125^{o}C) initially the values of tanδ decreases with the increase in x content; this may be due to the improvement of bulk density with the increase in x content and shifting of T_{O-T} below RT (chapter-5) [11]. Higher value of tanδ is obtained for *x*=0.08, which may be due to the increase in porosity and decrease in relative density in the ceramics. The tanδ value of KNNT-LS ceramics for *x*=0.02 remains very less in a broad temperature range, which is very important for high temperature applications [12]. The values of ε_r, tanδ and T_c of KNNT-LS ceramics are given in Table-6.2.

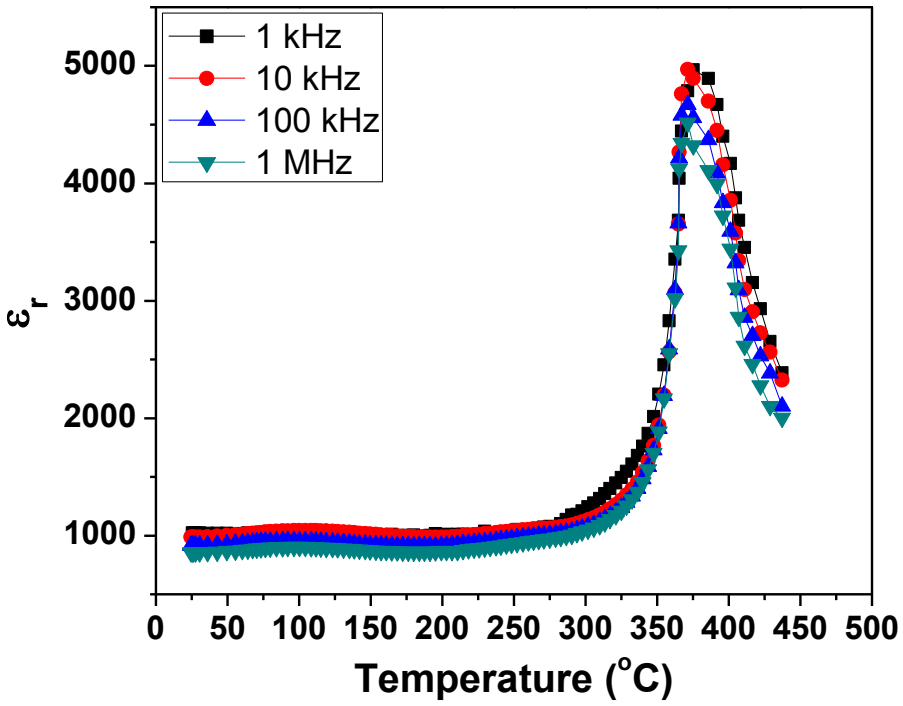

Fig. 6.3 (a)

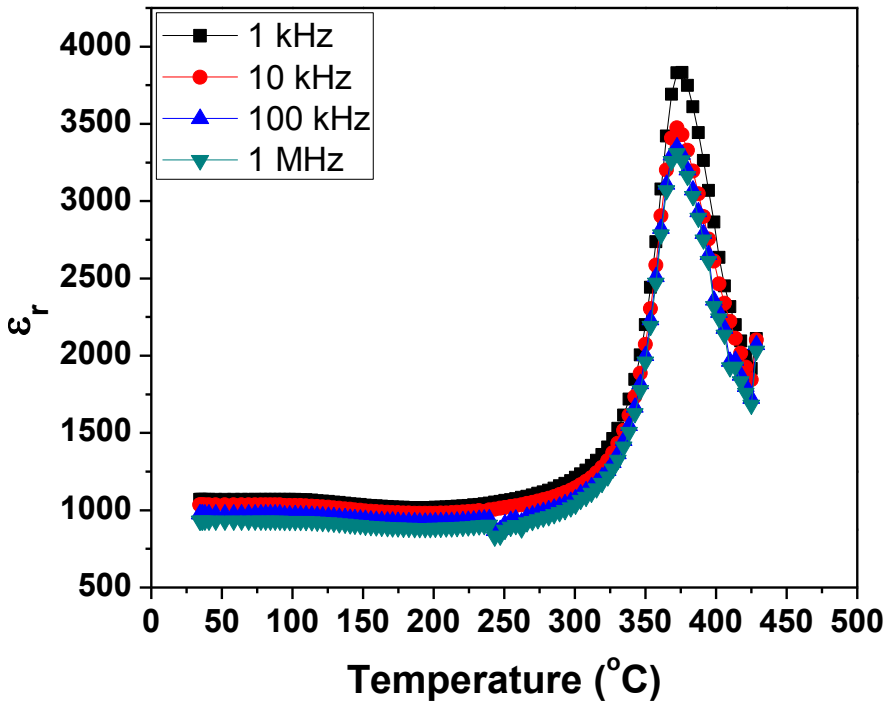

Fig. 6.3 (b)

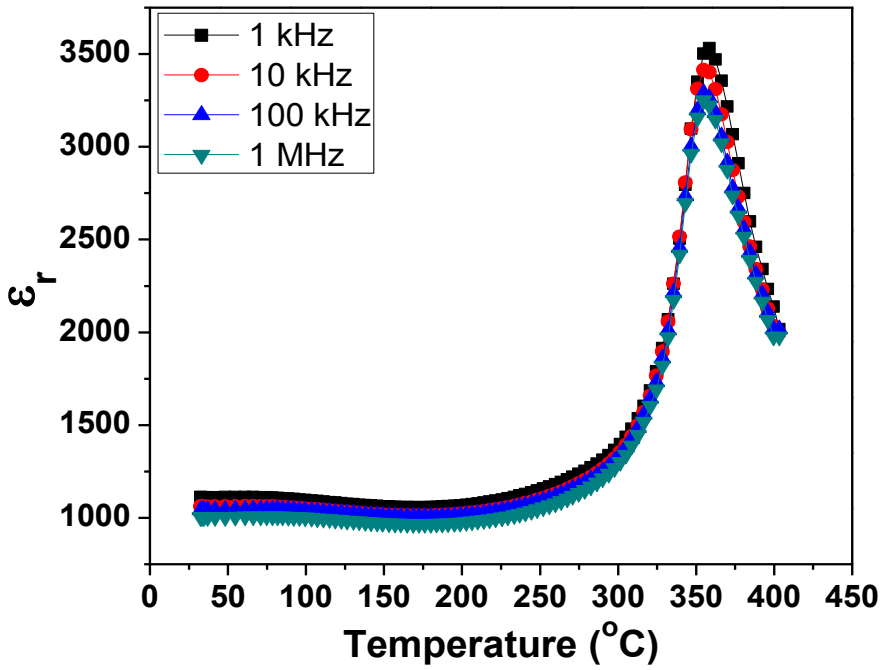

Fig. 6.3 (c)

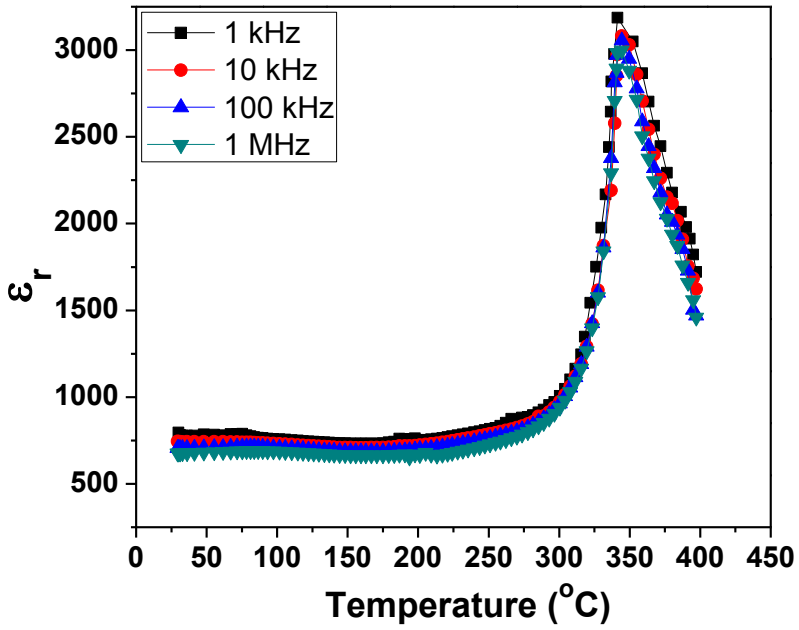

Fig. 6.3 (d)

Fig.6.3 Temperature dependent ε_r of KNNT-LS ceramics sintered at (a) *x*=0 (1080^{o}C) (b) *x*=0.02 (1080^{o}C) (c) *x*=0.04 (1100^{o}C) (d) *x*=0.06 (1100^{o}C) and (e) *x*=0.08 (1120^{o}C).

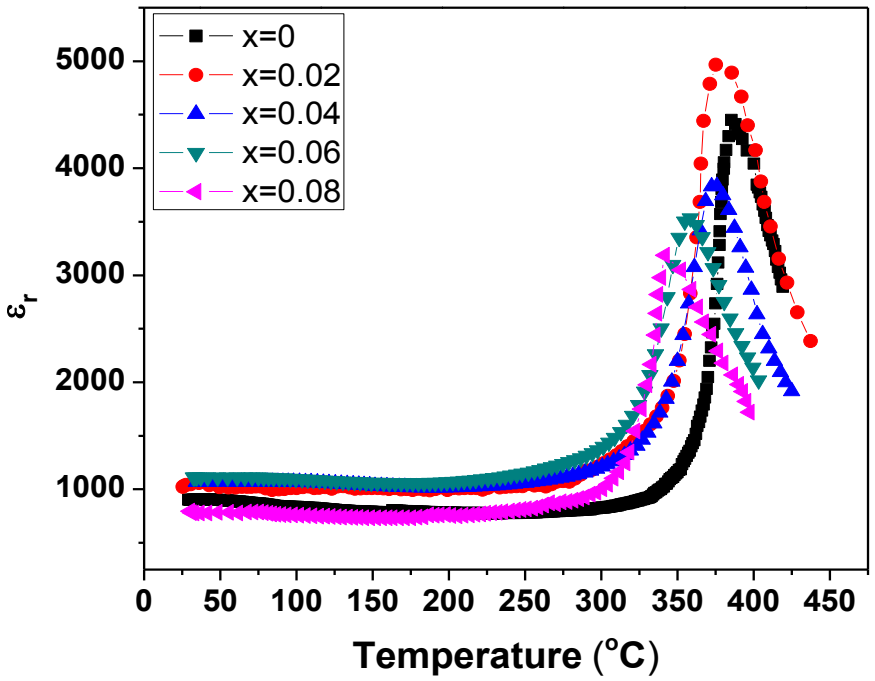

Fig. 6.4 (a) Temperature dependence of dielectric constant (ε_r) at 10 kHz frequency of KNNT-LS ceramics sintered at *x*=0 (1080^{o}C), *x*=0.02 (1080^{o}C), *x*=0.04 (1100^{o}C), *x*=0.06 (1100^{o}C) and *x*=0.08 (1120^{o}C).

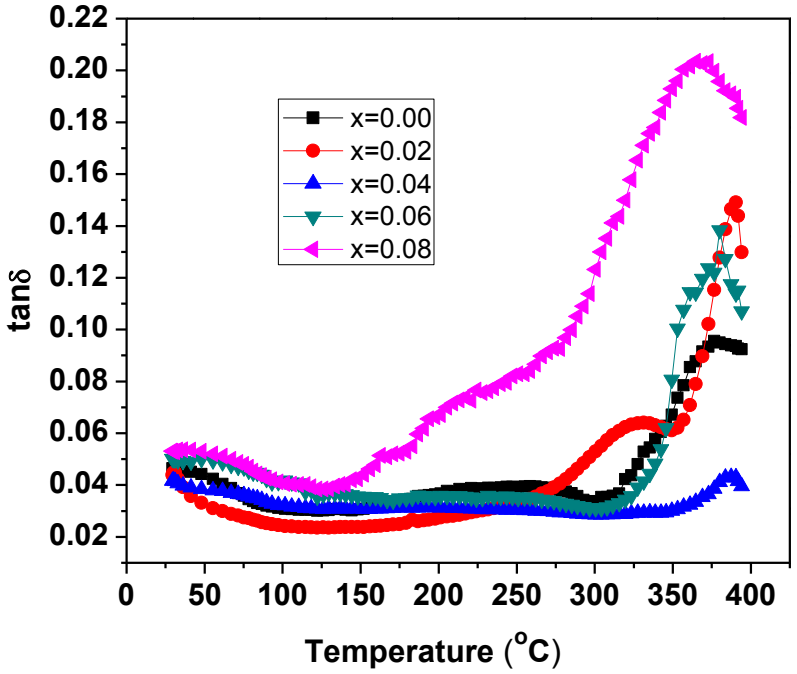

Fig. 6.4 (b) Temperature dependence of dielectric loss (tanδ) at 10 kHz frequency of KNNT-LS ceramics sintered at 1080°C (*x*=0 and 0.02), 1100°C (*x*=0.04 and 0.06) and 1120°C (*x*=0.08).

Table-6.2 ε_r ,tanδ, and Tc of KNNT-LS ceramics at 10 kHz frequency at 1080°C (*x*=0 and 0.02), 1100°C (*x*=0.04 and 0.06) and 1120°C (*x*=0.08).

x	0	0.02	0.04	0.06	0.08
ε_r (10 kHz)	903	1023	1112	1070	794
tanδ (10 kHz)	0.0465	0.038	0.0036	0.034	0.048
Tc (°C)	385.5	376	371	356	341

6.2.1.3 $0.95(K_{0.5}Na_{0.5})\ Nb_{(1-x)}V_xO_3$-$0.05LiSbO_3$ / KNNV-LS (*x*=0.02, 0.04, 0.06 and 0.08) Ceramics

The variation of ε_r as a function of temperature at different frequencies of KNNV-LS samples sintered at optimum temperatures (ceramics with highest relative density) for 4h are shown in Fig. 6.5(a, b, c, d). Decrement in the value of ε_r is observed with the increase in frequency in all the ceramics, this may be also due to the decrease in the net polarization in the materials at higher frequency. The comparison between the

temperature dependence of dielectric constant (ε_r) of the different KNNV-LS ceramics at 10 kHz is shown in Fig. 6.6(a). It is found that T_{O-T} and T_c of KNNV-LS ceramics for *x*=0.02 are found to be ~395^oC and 131^oC, respectively which is higher than the unmodified KNN-LS ceramics. The increase of T_{O-T} and T_c with the initial increase of *x* content is attributed to the large mismatch in the ionic radius of V^{+5} (~ 0.54 Pm) and Nb^{+5} (0.69Pm). This mismatch increases the distortion in the unit cell which increases the T_{O-T} and T_c [13]. However, with further increase in V content both these transition temperature decreases. Generally, when higher ionic radii atom is replaced by lower ionic radii atom, the unit cell volume decreases, which in turn decreases the T_c in the materials [14]. This suggests that beyond x=0.02, the effect of decrement of unit cell volume dominates over ionic size mismatch and hence there is decrease of T_{O-T} and T_c for higher V content. The RT value of ε_r is found to be maximum for the KNNV-LS ceramics with *x*=0.06 ceramics, which may be due to the enhanced relative bulk density in the ceramics (see chapter-5). The temperature dependence of dielectric loss (tanδ) behavior of KNNV-LS ceramics at 10 kHz frequency is shown in Fig. 6.6 (b). The tanδ values at RT increases initially with increase in *x* content and then decreases for *x*=0.06 and again increases for *x*=0.08. It can be seen that in all the KNNV-LS ceramics, the value of tanδ increases with increase in temperature, this may be due to the increase of space charge polarization and mobility of defects at higher temperatures. The values of ε_r, tanδ and T_c of KNNV-LS ceramics are given in Table-6.3.

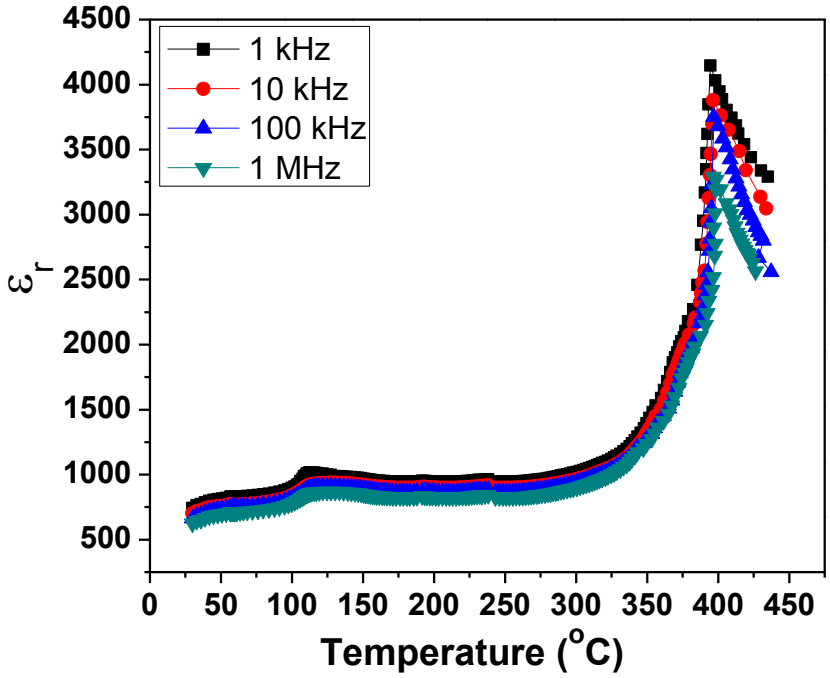

Fig.6.5 (a)

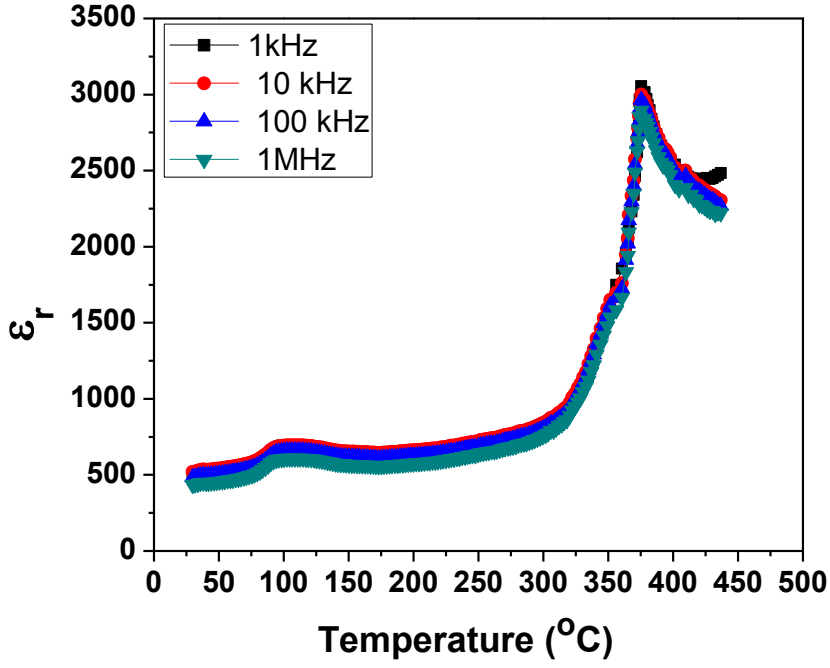

Fig.6.5 (b)

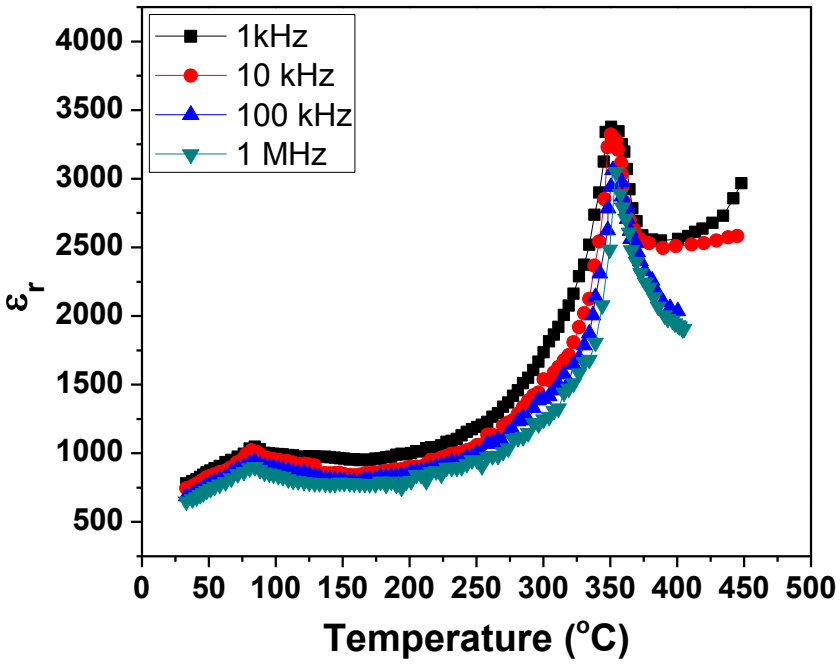

Fig.6.5 (c)

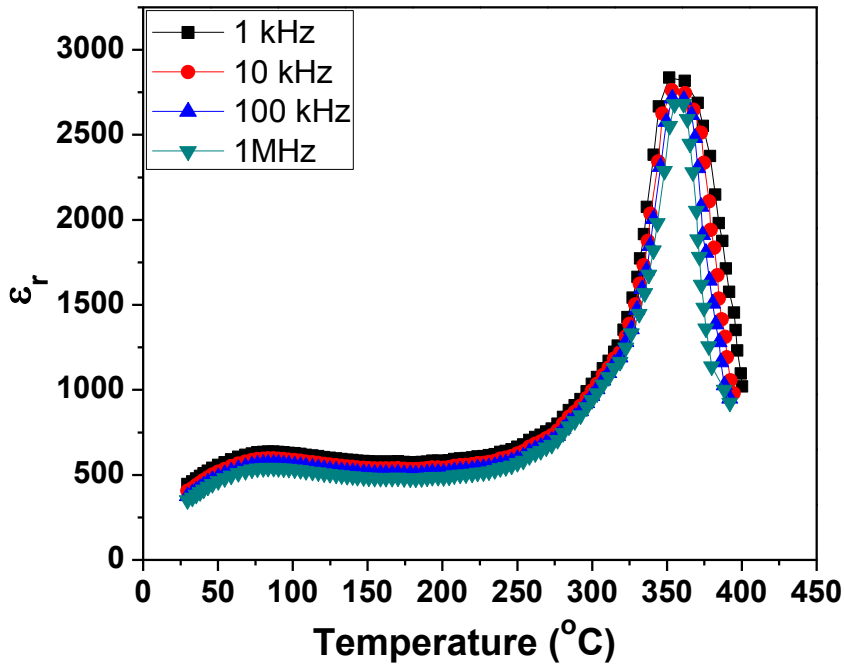

Fig.6.5 (d)

Fig.6.5 Temperature dependent ε_r of KNNV-LS ceramics sintered at (a) *x*=0.02 (1050°C) (b) *x*=0.04 (1030°C) (c) *x*=0.06 (1010°C) and (d) *x*=0.08 (990°C).

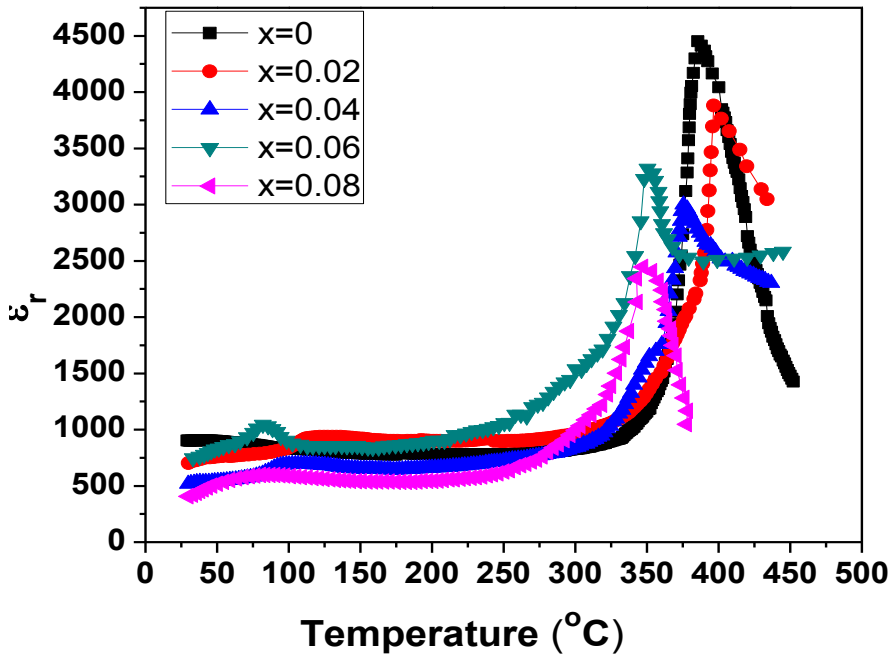

Fig. 6.6 (a) Temperature dependence of dielectric constant (ε_r) at 10 kHz frequency of KNNV-LS ceramics sintered at 1050°C (*x*=0.02), 1030°C (*x*=0.04), 1010°C (*x*=0.06) and 990°C (*x*=0.08).

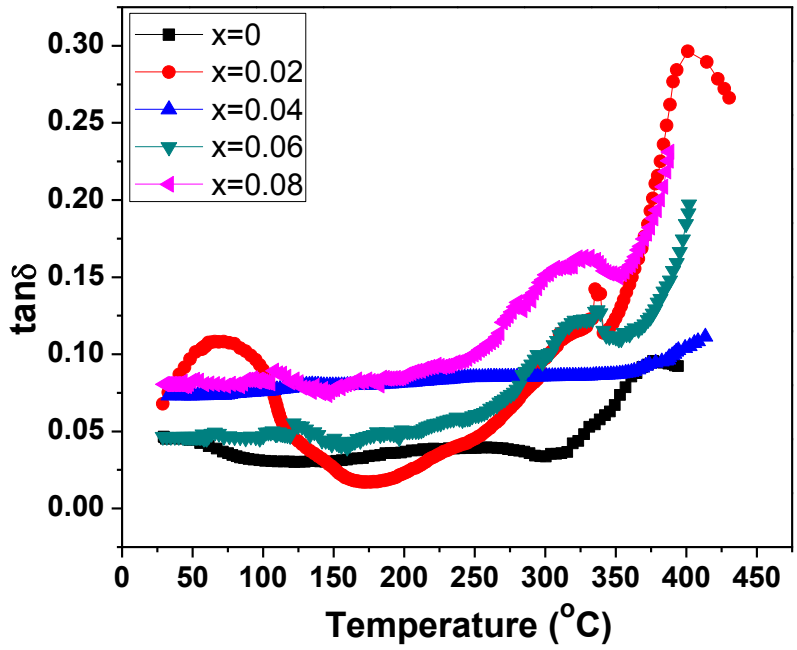

Fig. 6.6 (b) Temperature dependence of dielectric loss (tanδ) at 10 kHz frequency of KNNV-LS ceramics sintered at 1050°C (*x*=0.02), 1030°C (*x*=0.04), 1010°C (*x*=0.06) and 990°C (*x*=0.08).

Table-6.3 ε_r ,tanδ, and Tc of KNNV-LS ceramics at 10 kHz frequency sintered at 1050^{o}C (*x*=0.02), 1030^{o}C (*x*=0.04), 1010^{o}C (*x*=0.06) and 990^{o}C (*x*=0.08).

x	**0**	**0.02**	**0.04**	**0.06**	**0.08**
ε_r	903	701	519	745	406
tanδ	0.046	0.067	0.073	0.048	0.08
Tc (^{o}C)	385.5	395	378	350	343
T_{O-T} (^{o}C)	43	131	109	87	81

6.3 Ferroelectric Properties

In this section, the polarizations versus electric field (P-E) hysteresis loop study of conventionally synthesized Ag, Ta and V modified KNN-LS ceramics has been discussed.

6.3.1 $0.95(K_{0.5}Na_{0.5})_{(1-x)}Ag_xNbO_3$-$0.05LiSbO_3$ / KNAN-LS (x=0, 0.02, 0.04, 0.06 and 0.08) Ceramics

Fig. 6.7 shows the P-E hysteresis loops of the KNAN-LS ceramics sintered at 1080^{o}C for 4h, respectively. The development of saturated P-E hysteresis loops confirm the ferroelectric nature of the KNAN-LS ceramics. The values of remnant polarization, P_r, spontaneous polarization, P_s, and coercive field, E_c, of all the KNAN-LS ceramic samples are given in Table 2. The increment in the value of remnant polarization (P_r) is observed from *x* =0.02 (P_r ~ 13.7μC/cm^2) up to a maximum value (P_r ~ 21.9μC/cm^2) at *x*=0.06, and then it decreases again when *x*= 0.08. The maximum value of P_r at *x*=0.06 could be attributed to the shifting of orthorhombic to tetragonal polymorphic phase transition temperature (PPT) towards RT, higher relative bulk density and optimum

amount of Ag content in the ceramics. The presence of PPT near RT increases the number of polarization directions due to the presence of both orthorhombic and tetragonal structures, which increases the ferroelectric properties [15].

6.3.2 $0.95(K_{0.5}Na_{0.5})Nb_{(1-x)}Ta_xO_3$-$0.05LiSbO_3$ / KNNT-LS (x=0, 0.02, 0.04, 0.06 and 0.08) Ceramics

In order to examine the ferroelectric nature of the KNNT-LS ceramics, the polarization vs. electric field loops are measured and shown in Fig.6.8. Saturated hysteresis loops developed in all the KNNT-LS ceramics. Maximum value of remnant polarization ~ 24.65μC/cm^2 is obtained for KNNT-LS ceramics with x=0.02; again this may be due to the presence of PPT near RT which facilitates the easy alignment of domains. It has been suggested that the domain structure of the KNN-based ceramics near PPT region is the coexistence of orthorhombic (O) and tetragonal (T) polarized domains. There are 12 possible spontaneous polarization (Ps) directions for the *o* structures and six possible Ps in directions for the *t* structures. The presence of more number of possible polarization states near PPT improves the ferroelectric properties [16].

6.3.3 $0.95(K_{0.5}Na_{0.5})Nb_{(1-x)}V_xO_3$-$0.05LiSbO_3$ / KNNV-LS (x=0, 0.02, 0.04, 0.06 and 0.08) Ceramics

Fig.6.9 shows the P-E hysteresis loops of the KNNV-LS ceramics sintered at optimum temperatures. The development of P-E hysteresis loops again confirm the ferroelectric nature of the KNNV-LS ceramics. It is found that with the increase in V content the value of P_r decreases up to x=0.04, but for x=0.06 it increases and reaches a maximum value ~ 14.60 μC/cm^2. However with the further increases in x content P_r value decreases. The overall decrease of P_r and increase of E_c value in the KNNV-LS ceramics in comparison to the other modified KNN-LS ceramics is attributed to the low relative

bulk density due to the development of higher amount of liquid phase in the grain boundary region. The development of excess liquid phase also increases the dielectric loss i.e., conductivity in the ceramics [17].

.

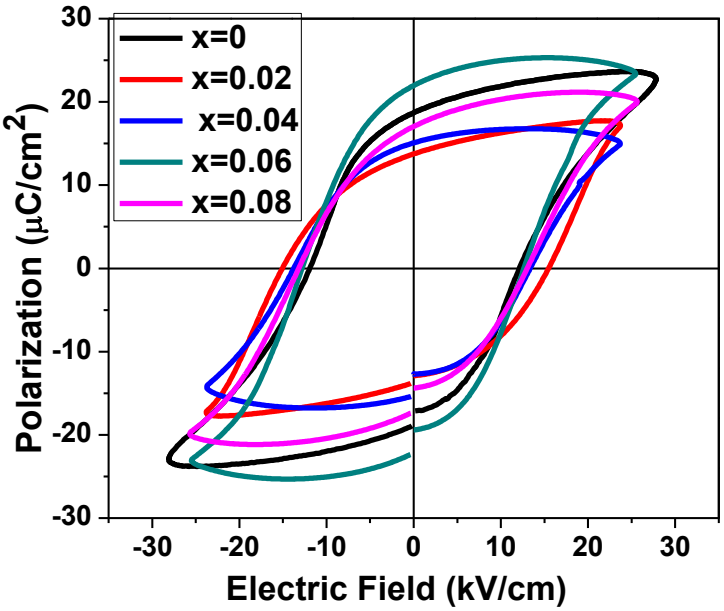

Fig. 6.7 P-E Hysteresis loops of KNAN-LS ceramics sintered at 1080°C for 4h.

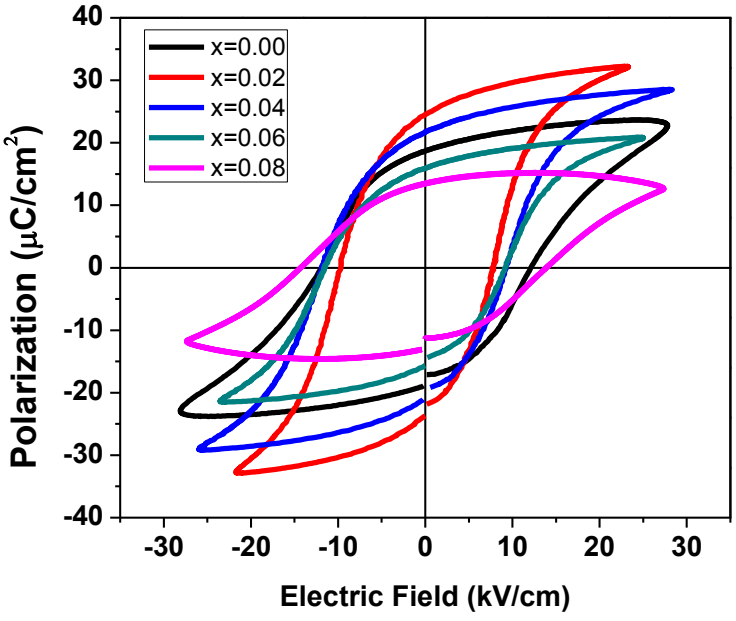

Fig. 6.8 P-E Hysteresis loops of KNNT-LS ceramics sintered at 1080°C (*x*=0 and 0.02), 1100°C (*x*=0.04 and 0.06) and 1120°C (*x*=0.08).

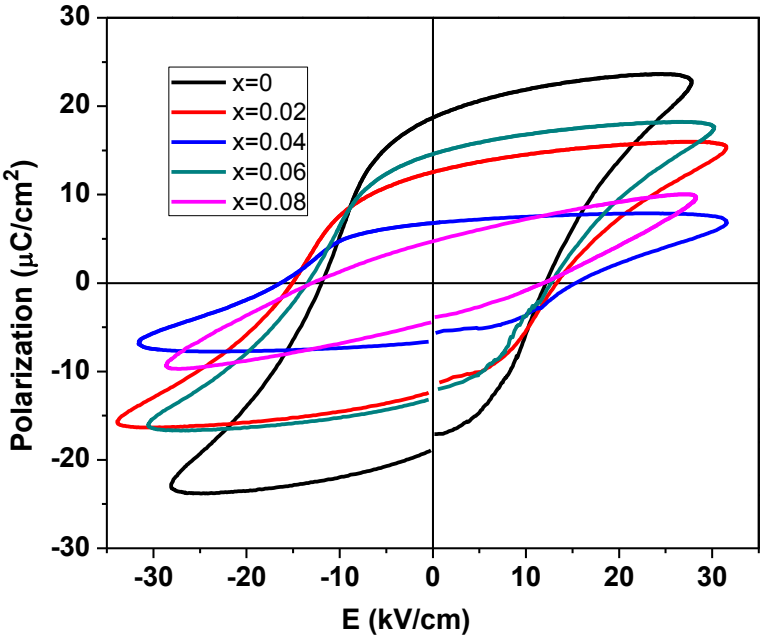

Fig. 6.9 P-E Hysteresis loops of KNNV-LS ceramics sintered at 1050°C (*x*=0.02), 1030°C (*x*=0.04), 1010°C (*x*=0.06) and 990°C (*x*=0.08).

6.4 Strain vs. Electric Field (S-E) Study

In this section, the study of strain versus electric field (S-E) loops of conventionally synthesized Ag, Ta and V modified KNN-LS ceramics have been discussed.

6.4.1 $0.95(K_{0.5}Na_{0.5})_{(1-x)}Ag_xNbO_3$-$0.05LiSbO_3$ / KNAN-LS (x=0, 0.02, 0.04, 0.06 and 0.08) Ceramics

Fig.6.10 shows the bipolar field-induced-strain (S−E) loops of KNAN-LS ceramics with *x*=0, 0.02, 0.04, 0.06 and 0.08. Typical butterfly-shaped S−E loops are observed in all the ceramics with varying remnant strain. The strain–electric field (S-E) hysteresis loops, which resembles the shape of a butterfly develops due to the three types of effects. The first one is the normal converse piezoelectric effect of the lattice, and the other two are due to the switching and movement of domain walls. Small displacements of all types of domain walls affect the polarization of the material whereas the movement and switching of non-180° walls may involve a significant change in dimensions of the

sample, in addition to the pure piezoelectric response of the material within each domain [18]. The ceramics with *x*=0 possess a remnant strain ~ 0.07% whereas for *x*=0.02 it reaches ~ 0.04%. With further increase in *x* content, the remnant strain increases up to ~0.085% at *x*=0.06. The maximum value of remnant strain at *x*=0.06 may be again due to the shifting of PPT ~ 65^{o}C which facilitates the non-180^{o} domain wall motion because of the reduction of the potential barrier between o and t polarization states [19].

6.4.2 0.95($K_{0.5}Na_{0.5}$)$Nb_{(1-x)}Ta_xO_3$-0.05$LiSbO_3$ / KNNT-LS (x=0, 0.02, 0.04, 0.06 and 0.08) Ceramics

Fig.6.11 shows the bipolar field-induced-strain (S−E) loops of KNNT-LS ceramics with *x*=0, 0.02, 0.04, 0.06 and 0.08. The ceramics with *x*=0 i.e. Pure KNN-LS ceramic possess a remnant strain ~ 0.07% whereas for *x*=0.02 it reaches ~ 0.084%. With further increase in *x* content, the remnant strain decreases. The maximum value of remnant strain at *x*=0.02 may be due to the presence of T_{o-t} close to RT which increases the non-180^{o} domain wall motion because of the reduction of the potential barrier between O and T polarization states [20]. According to Devonshire theory, a little discrepancy of the free energy exists in the mixed phases near MPB of any system. In KNN based ceramics the orthorhombic to tetragonal polymorphic phase transition plays a similar role like MPB in PZT based systems. Therefore, domain wall motion and ferroelectric phase transitions in these compositions are prone to be induced by electric field [21].

6.4.3 0.95($K_{0.5}Na_{0.5}$)$Nb_{(1-x)}V_xO_3$-0.05$LiSbO_3$ / KNNV-LS (x=0, 0.02, 0.04, 0.06 and 0.08) Ceramics

Fig.6.11shows the bipolar field-induced-strain (S−E) loops of KNNV-LS ceramics with *x*=0, 0.02, 0.04, 0.06 and 0.08. It can be seen that with increase in *x* content the remnant strain in the ceramics decreases. The ceramics with *x*=0.02 possess a remnant

strain ~ 0.035% whereas for x=0.04 it reaches ~ 0.03%. With further increase in x content, the remnant strain attains a maximum value ~ 0.046%. The maximum value of remnant strain at x=0.06 may be due to the shifting of T_{O-T} towards RT which increases the non-180^o domain wall motion because of the reduction of the potential barrier between O and T polarization states [19].

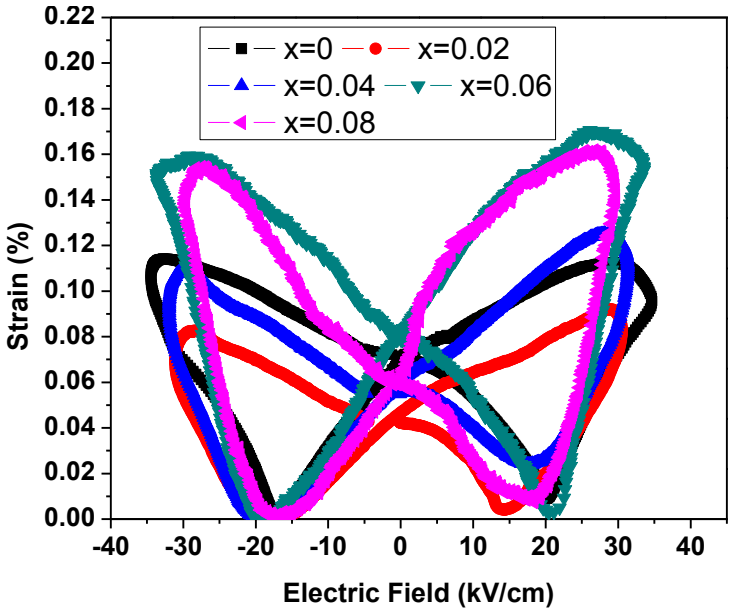

Fig.6.10 (S−E) loops of KNAN-LS ceramics sintered at 1080^{o}C.

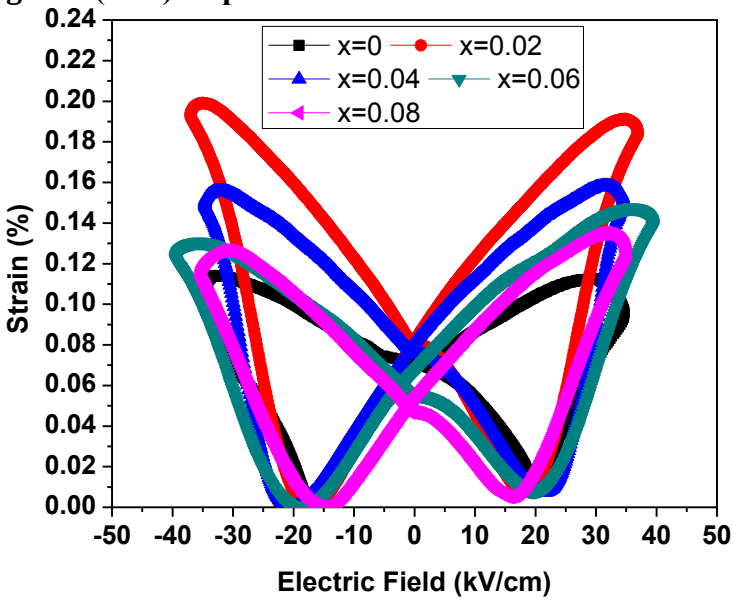

Fig.6.11 (S−E) loops of KNNT-LS ceramics sintered at sintered at 1080^{o}C (x=0 and 0.02), 1100^{o}C (x=0.04 and 0.06) and 1120^{o}C (x=0.08).

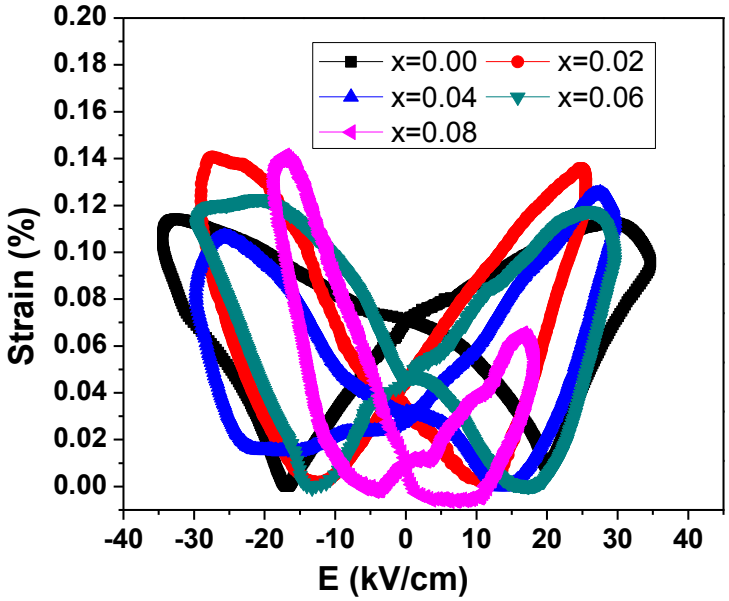

Fig.6.12 (S−E) loops of KNNV-LS ceramics sintered at 1080^{o}C (*x*=0), 1050^{o}C (*x*=0.02), 1030^{o}C (*x*=0.04), 1010^{o}C (*x*=0.06) and 990^{o}C (*x*=0.08).

6.5 Piezoelectric Properties

6.5.1 Poling Temperature Dependent Piezoelectric and Electromechanical Properties

In this section, the effect of poling temperature on the piezoelectric coefficients (d_{33}) and planar mode coupling coefficients (k_p) have been investigated. It is reported that better piezoelectric properties are obtained when the orthorhombic to tetragonal phase polymorphic phase transition temperature (PPT) lies near RT in KNN based ceramics [22]. This suggests that maximum domain alignment occurs around the PPT region because of the presence of both orthorhombic and tetragonal structures. Therefore, it is expected that the poling of these ceramics near PPT region will be very effective to achieve better piezoelectric properties.

6.5.1.1 $0.95(K_{0.5}Na_{0.5})_{(1-x)}Ag_xNbO_3$-$0.05LiSbO_3$ / KNAN-LS (*x*=0, 0.02, 0.04, 0.06 and 0.08) Ceramics

Fig. 6.13 shows the effect of poling temperature on the values of d_{33} and k_p piezoelectric coefficients of KNAN-LS ceramics. It has recently been reported that the MPB in KNN based ceramics is an orthorhombic to tetragonal polymorphic phase transition (PPT) [23]. Unlike the MPB in PZT, the phase boundary between orthorhombic and tetragonal phases in KNN based ceramics is not vertical and shows strong temperature dependence. Hence, optimization of poling temperature (T_p) in KNN based ceramics is very important to achieve the desired piezoelectric properties. When T_p lies near orthorhombic–tetragonal PPT temperatures, non-180^o domains can switch and be orientated owing to the coexistence of the orthorhombic and tetragonal phases [24]. Consequently, the higher degree of the domain alignment can be obtained, which results in large piezoelectric properties. As shown in Fig. 6.13, the T_p has an obvious effect on the piezoelectric properties of the KNAN-LS ceramics and the piezoelectric properties reach maximum values when $T_p \rightarrow T_{O-T}$. Maximum values of piezoelectric coefficients (d_{33}) ~ 227pC/N and planar mode coupling coefficients (k_p) ~ 0.425 are obtained in case of KNAN-LS (with *x*=0.06) ceramics by choosing optimum T_p near PPT. The improvement of the piezoelectric properties while poling at optimum T_p may be due to the co-existence of orthorhombic (O) and tetragonal (T) structures which increases the number of poling directions and hence better poling takes place. The values of d_{33}, Q_m and k_p of all the KNAN-LS ceramics are listed in Table-6.4. The d_{33} and k_p values of KNAN-LS ceramics (with *x*=0.06) are found to be higher than pure KNN-LS ceramics even though the PPT of pure KNN-LS occurs ~43^{o}C, which may be due to the effect of optimum amount of Ag content in KNAN-LS ceramics. The above results suggest that in

KNN based ceramics where two phase transition exists above the RT, there the T_p must be chosen near the orthorhombic to tetragonal polymorphic phase transition temperature.

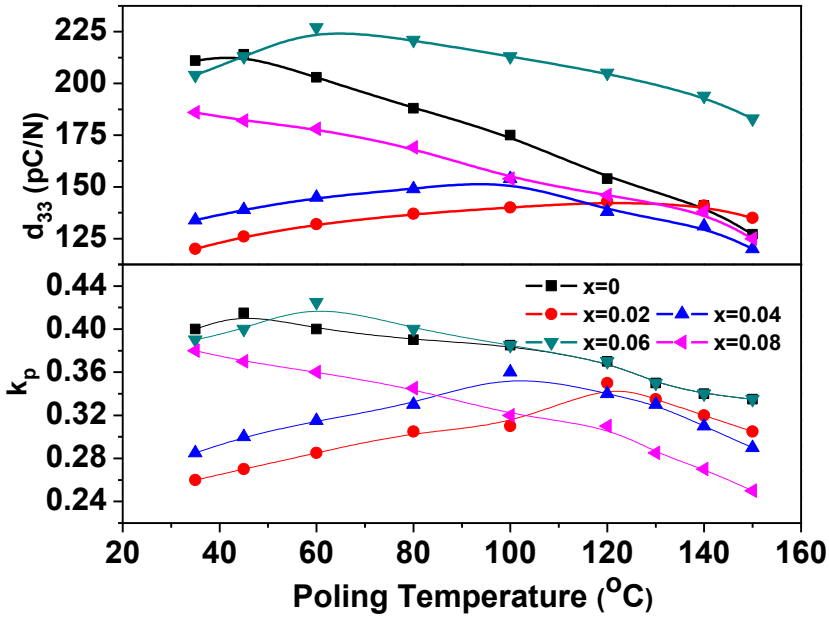

Fig.6.13 k_p and d_{33} piezoelectric coefficients as a function of poling temperature of the KNAN-LS ceramics sintered at 1080^{o}C.

Table-6.4 k_p, d_{33}, Q_m and P_r values of KNAN-LS ceramics sintered at 1080 ^{o}C.

x	**0**	**0.02**	**0.04**	**0.06**	**0.08**
k_p	0.415	0.35	0.36	0.425	0.38
d_{33} (pC/N)	215	143	157	227	186
Pr ($\mu C/cm^2$)	18.7	13.7	15.1	21.9	16.97
Q_m	71	88	112	81	69

6.5.1.2 0.95($K_{0.5}Na_{0.5}$)$Nb_{(1-x)}Ta_xO_3$-0.05$LiSbO_3$ / KNNT-LS (x=0, 0.02, 0.04, 0.06 and 0.08) Ceramics

Fig. 6.14 shows the effect of poling temperature on the values of d_{33} and k_p piezoelectric coefficients of KNNT-LS ceramics. From dielectric study (section 6.2.1.2)

it is found that with the increase in Ta content, the T_{O-T} of the KNNT-LS ceramics decreases and it lies below RT. Therefore, the optimum poling temperature (T_p) must be selected near RT.

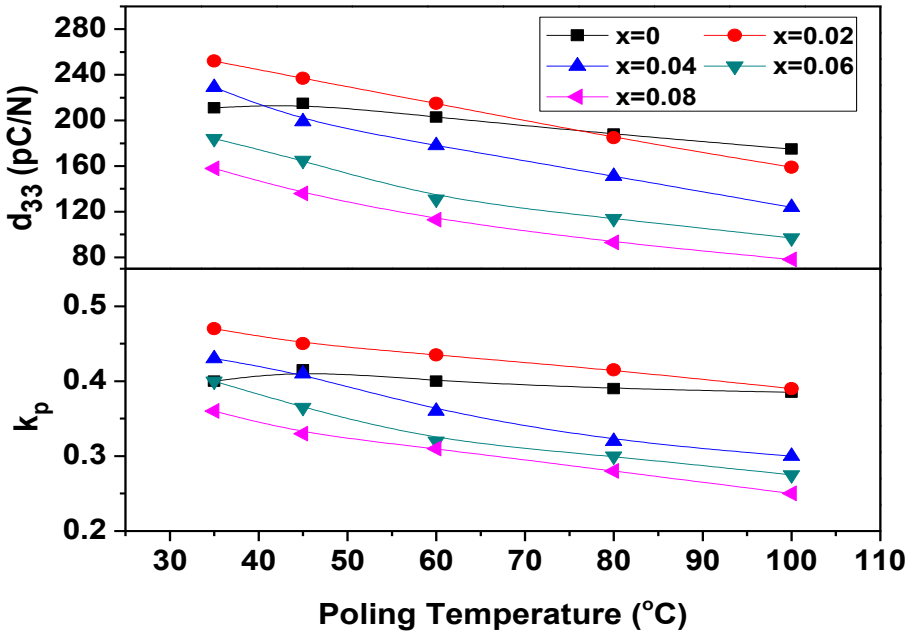

Fig.6.14 k_p and d_{33} piezoelectric coefficients as a function of poling temperature of KNNT-LS ceramics sintered at 1080°C (*x*=0 and 0.02), 1100°C (*x*=0.04 and 0.06) and 1120°C (*x*=0.08).

As shown in Fig. 6.14, maximum piezoelectric properties are obtained by poling at around ~ RT in all the ceramics except for *x*=0. Since for *x*=0, the T_{O-T} of the ceramics occurs ~ 43°C. The best properties are obtained in the compositions in which the T_{O-T} lies close to room temperature, which means that the position of T_{O-T} plays an important role in improving the piezoelectric properties, similar to MPB in PZT ceramics. Both of them are based on a two-phase coexistence zone where there are more number of spontaneous polarization states are available. The planar mode electromechanical coupling factor (k_p), piezoelectric constant (d_{33}) and remnant polarization (P_r) initially increases with increase in *x* content, reach the maxima approximately at *x* = 0.02 and then decreases with the

further increase in *x* content. The maximum value at *x*=0.02 is attributed to the presence of both the orthorhombic and tetragonal structure at RT, which is confirmed by XRD study (chapter-5). The values of d_{33}, Q_m and k_p of all the KNNT-LS ceramics are listed in Table-6.5

Table-6.5 k_p, d_{33}, Q_m and P_r values of KNNT-LS ceramics sintered at 1080^{o}C (*x*=0 and 0.02), 1100^{o}C (*x*=0.04 and 0.06) and 1120^{o}C (*x*=0.08).

x	**0**	**0.02**	**0.04**	**0.06**	**0.08**
k_p	0.415	0.47	0.43	0.4	0.36
d_{33} (pC/N)	215	252	229	184	158
Pr ($\mu C/cm^2$)	18.7	24.6	21.8	15.9	13.5
Q_m	71	98	122	134	147

6.5.1.3 0.95($K_{0.5}Na_{0.5}$)$Nb_{(1-x)}V_xO_3$-0.05$LiSbO_3$ / KNNV-LS (x=0, 0.02, 0.04, 0.06 and 0.08 Ceramics

Fig. 6.15 shows the effect of poling temperature on d_{33} and k_p values of KNNV-LS ceramics. In this case also the best piezoelectric properties are obtained by poling the ceramics near orthorhombic to tetragonal polymorphic phase transition temperature (PPT). Maximum piezoelectric properties are obtained for the KNNV-LS ceramics with *x*=0.06, this may be due to the higher relative density and low dielectric loss in the ceramics. The properties of KNNV-LS ceramics are found to be lower than the other modified ceramics. Relatively poor piezoelectric properties of KNNV-LS ceramics than the KNAN-LS and KNNT-LS ceramics may be due to the combined effect of the high dielectric loss and low relative density in the ceramics. The values of d_{33}, Q_m and k_p of all the KNNV-LS ceramics are listed in Table-6.6

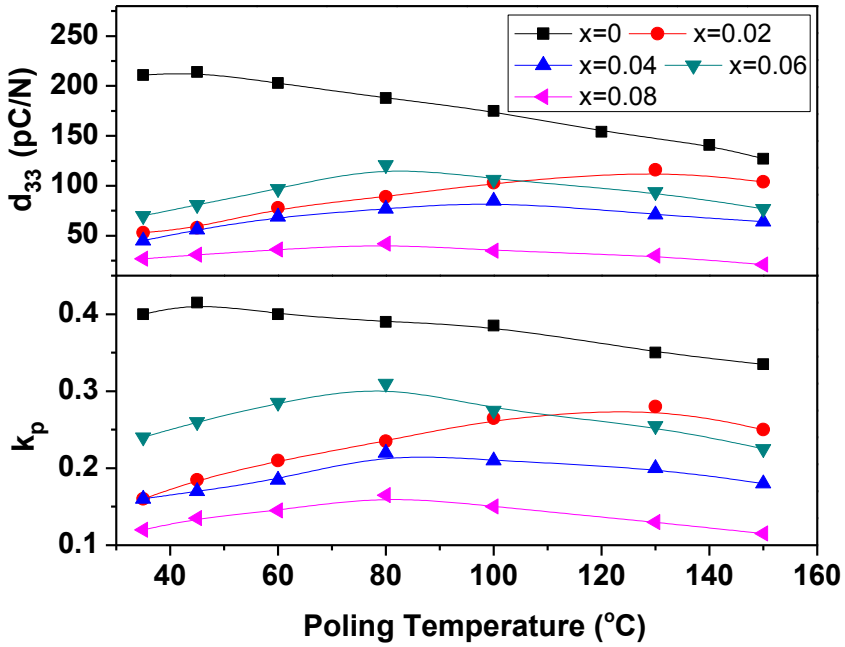

Fig.6.15 k_p and d_{33} piezoelectric coefficients as a function of poling temperature of KNNV-LS ceramics sintered at 1080°C (*x*=0), 1050°C (*x*=0.02), 1030°C (*x*=0.04), 1010°C (*x*=0.06) and 990°C (*x*=0.08).

Table-6.6 k_p, d_{33}, Q_m and P_r values of KNNV-LS ceramics sintered at 1080°C (*x*=0), 1050°C (*x*=0.02), 1030°C (*x*=0.04), 1010°C (*x*=0.06) and 990°C (*x*=0.08).

x	**0**	**0.02**	**0.04**	**0.06**	**0.08**
k_p	0.415	0.28	0.22	0.31	0.165
d_{33} (pC/N)	215	103	85	121	42
Pr ($\mu C/cm^2$)	18.7	12.6	6.8	14.6	4.7
Q_m	71	125	141	112	124

6.5.2 Temperature Dependent Piezoelectric Properties

The temperature dependent piezoelectric properties study of any piezoelectric material is important, since it provides the information about the applicability of the

material in the high temperature region [12]. Generally, the temperature range of a piezoelectric to be used in various applications is from -50^{o}C to 200^{o}C [25]. In this region the material should possess nearly temperature independent properties [25]. In the present study the temperature dependent (from RT to T_c) planar mode coupling coefficients measurement has been carried out. Fig.6.16 shows the temperature dependent planar mode coupling coefficients (k_p) Ag, Ta and V modified KNN-LS ceramics showing better piezoelectric properties. It can be seen that in case of Ta modified KNN-LS ceramics, the k_p value remains nearly unchanged up to ~ 200^{o}C, which suggests its usefulness for high temperature applications. Whereas, in Ag, and V modified KNN-LS ceramics the k_p value is highly temperature dependent.

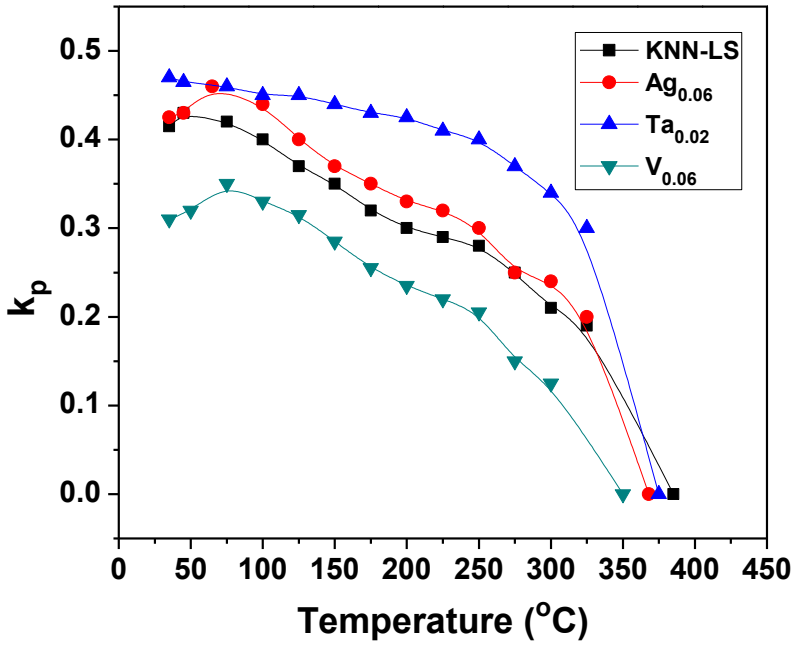

Fig. 6.16 Temperature dependent k_p coefficients of KNN-LS, KNAN-LS (*x*=0.06), KNNT-LS (*x*=0.02) and KNNV-LS (*x*=0.06) ceramics.

References

[1] K. R. Udayakumar, J. Chen, P. J. Schuele, L. E. Cross, V. Kumar, and S. B. Krupanidhi, Appl. Phys. Lett., **60**, (1992) 1187.

[2] K. Uchino, Ferroelectric Devices (Marcel Dekker, New York, 2000).

[3] N. M. Hagh, B. Jadidian, E. Ashbahian and A. Safari, IEEE Trans. Ultrason., Ferroelectr., Freq. Control, 55, (2008) 214.

[4] S. Zhang, R. Xia, H. Hao, H. Liu, and T. R. Shrout, Appl. Phys. Lett., 92, (2008) 152904.

[5] Y.Wang, J. Wu, D. Xiao, B. Zhang, W.Wu, W. Shi and J. Zhu, . J. Phys. D: Appl. Phys., 41, (2008) 245401.

[6] A. K. Singh, T.C. Goel, R.G. Mendiratta, O.P. Thakur and C. Prakash, J. Appl. Phys., 91, (2002) 6626.

[7] D. Q. Xiao , J. G. Wu , L. Wu , J. G. Zhu , P. Yu , D. M. Lin , Y. W. Liao and Y. Sun. J.Mater. Sci., 44, (2009) 5408.

[8] B. Peng, Z. Yue and L. Li, J. Appl. Phys., 109, (2011) 054107.

[9] P. Kumar, S. Singh, O.P. Thakur, C. Prakash and T.C. Goel, Jpn. J. Appl. Phys., 43, (2004) 1501.

[10] G. Yao, X. Wang, Y. Yang, and L. Li, J. Am. Ceram. Soc., 93, (2010)1697.

[11] J. Fu, R.Zuo, X. Wang and L. Li, J. Phys. D: Appl. Phys., 42, (2009) 012006.

[12] L. Wu, D. Xiao, X. Li, J. Zhu, P. Yu, Y. Sun and Y. Wang, Int. J. Appl. Ceram. Technol. 7, (2010) E39.

[13] Y. Wu and G. Cao, J. Mater. Sc. Lett., 19, (2000) 267.

[14] H. Pan, D. Jin, W. Wu, J. Cheng and Z. Meng, IEEE transactions on ultrasonics,

ferroelectrics, and frequency control, 55, 5, (2008) 994.

[15] D. A. Ochoa, J. E. García, R. Pérez, V. Gomis, A. Albareda, F. Rubio-Marcos and J. F. Fernández, J. Phys. D: Appl. Phys., 42, (2009) 025402.

[16] B. Jaffe, W. Cook and H. Jaffe. Academic, New York, (1971) 185.

[17] F. R. Marcos, P. Ochoa, and J.F. Fernandez, J. Eur. Ceram. Soc., 27, (2007) 4125.

[18] D. Damjanovic. Rep. Prog. Phys., 61, (1998) 1267.

[19] Q. M. Zhang, H. Wang, N. Kim, and L. E. Cross. J. Appl. Phys., 75, (1994) 454.

[20] Q.M. Zhang, H. Wang, N. Kim, and L. E. Cross, J. Appl. Phys., 75, (1994) 454.

[21] P. Kumar., C. Prakash, and T.C. Goel, Sci. Technol. Adv. Mater., 8, (2007)463.

[22] D. M. Lin, K. W. Kwok, K. H. Lam and H. L. W. Chan, J. Phys. D: Appl. Phys., 41, (2008) 052002.

[23] T. R. Shrout and S. J. Zhang. J.Electroceram., 19, (2007) 111.

[24] H. L. Du, W. C. Zhou, F. Luo, D. M. Zhu, S. B. Qu and Z. B. Pei, Appl. Phys. Lett., 91, (2007) 202907.

[25] S. Zhang, R. Xia, H. Hao, H. Liu and T. R. Shrout, Appl. Phys. Lett., 92, (2008) 152904.

CHAPTER-7

Microwave Processing of KNN-LS Based Ceramics

7.1 Introduction

The applications of microwave energy in remote sensing, telecommunication and food processing industries had significant impacts on our standards of living [1]. Earlier, microwaves were limited to only communications, but later it was found that this energy could also be used for heating purposes [2]. Now-a-days, the microwave oven is a common household kitchen appliance that is being used for cooking purposes. Microwave technology has proven to be useful in a number of applications and is currently used for processing of different materials as an alternative route to conventional processing techniques. Microwave (MW) processing of perovskite based ceramics has been studied since 1980 [3-6]. The unique sintering mechanism makes MWP valuable in regard to the time and energy savings as well as improving product properties for the material systems which are dielectrically lossy at microwave frequency. Moreover, the dependence of microwave absorption of materials on the dielectric properties makes it possible to synthesize and sinter these fairly lossy and highly refractory ceramics much more efficiently in a microwave field than by conventional methods. According to previous reports, the application of microwave heating for sintering of some ceramics results in low-temperature processing compared to conventional sintering methods [7, 8]. The improvements in the electrical properties like ferroelectric and piezoelectric properties are also reported by microwave processing technique [9-11]. Therefore, in the

present chapter, we have studied the effect of microwave processing on the ceramics synthesized by conventional route and showing best electrical properties.

In this chapter, all the best conventionally processed (CP) ceramics are processed by microwave technique. The single phase formation and optimum sintering conditions have been optimized by varying the sintering time. The dielectric, ferroelectric, piezoelectric and electromechanical properties are also investigated and compared with the same ceramics processed conventionally.

7.2 Optimization of Calcination Time

7.2.1 $0.95[K_{0.5}Na_{0.5}NbO_3]$-$0.05[LiSbO_3]$ / KNN-LS Ceramics

Fig. 7.1 shows the XRD patterns of KNN-LS ceramics calcined at 850 ^{o}C for 20, 40 and 60 mins in a microwave furnace. Single perovskite phase formation is confirmed at 850 ^{o}C for 60 mins whereas at other calcination times XRD peaks of secondary phases are detected. The formation of secondary phases at lower calcination time confirms the presence of unreacted phases in the compound. The formation of single perovskite phase occurs at 850^{o}C for 6h in the same compound by conventional processing (CP) technique, which shows the effectiveness of microwave processing technique. The XRD peaks in case of microwave processed ceramics are found to be sharp and distinct than the conventional one. This may be due to the increase in crystallinity and homogeneity in the ceramics [12]. The crystal structural study at RT confirms the presence of mixed structure in the ceramics.

7.2.2 $0.95[(K_{0.5}Na_{0.5})_{0.94}Ag_{0.06}NbO_3]$-$0.05[LiSbO_3]$ / KNA6N-LS Ceramics

Fig. 7.2 shows the XRD patterns of KNA6N-LS ceramics calcined at 850 ^{o}C for 20, 40 and 60 mins. The formation of single perovskite phase is confirmed at 850 ^{o}C for

60 mins whereas at other calcination times XRD peaks of secondary phases are detected. The appearance of small amount of impurity peaks ~ 25^o, 27.5^o and 28.5^o in case of 20 mins calcined samples and ~ 28.6^o for 40 mins calcined samples indicates that the decomposition of carbonates and oxides are not completed. From XRD analysis, mixed structure is obtained in the KNA6N-LS ceramics at RT. The coarsening of the particles is greatly reduced due to the rapid heating by microwave processing technique [13].

7.2.3 $0.95[(K_{0.5}Na_{0.5})Nb_{0.98}Ta_{0.02}O_3]$-$0.05[LiSbO_3]$ / KNNT2-LS Ceramics

Fig. 7.3 shows the XRD patterns of KNNT2-LS ceramics calcined at 850 ^oC for 20, 40 and 60 mins. The formation of single perovskite is developed at 850 ^oC for 60 mins whereas at other calcination times XRD peaks of secondary phases are detected. The XRD peaks are found to be sharp and distinct which may be due to the increase in crystallinity and homogeneity in the samples. The crystal structural study at RT confirms the presence of mixed structure in the ceramics.

7.2.4 $0.95[(K_{0.5}Na_{0.5})Nb_{0.98}V_{0.06}O_3]$-$0.05[LiSbO_3]$ / KNNV6-LS Ceramics

Fig. 7.4 shows the XRD patterns of KNNV6-LS ceramics calcined at 850 ^oC for 20, 40 and 60 mins. Single perovskite phase is confirmed at 850 ^oC for 60 mins whereas at other calcination times XRD peaks of secondary phases are detected. The room temperature XRD analysis confirms the presence of orthorhombic structure.

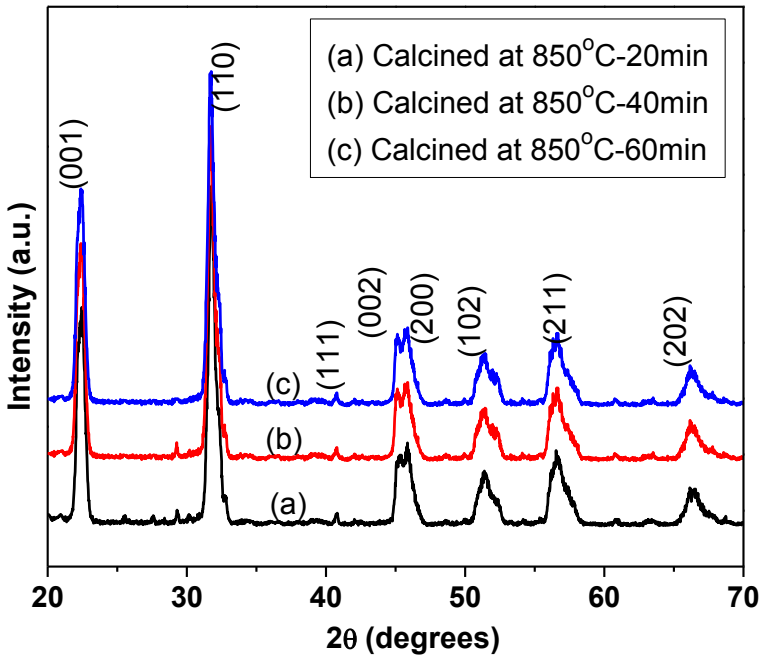

Fig. 7.1 XRD patterns of MW processed KNN-LS ceramics calcined at 850 °C for 20, 40 and 60 mins.

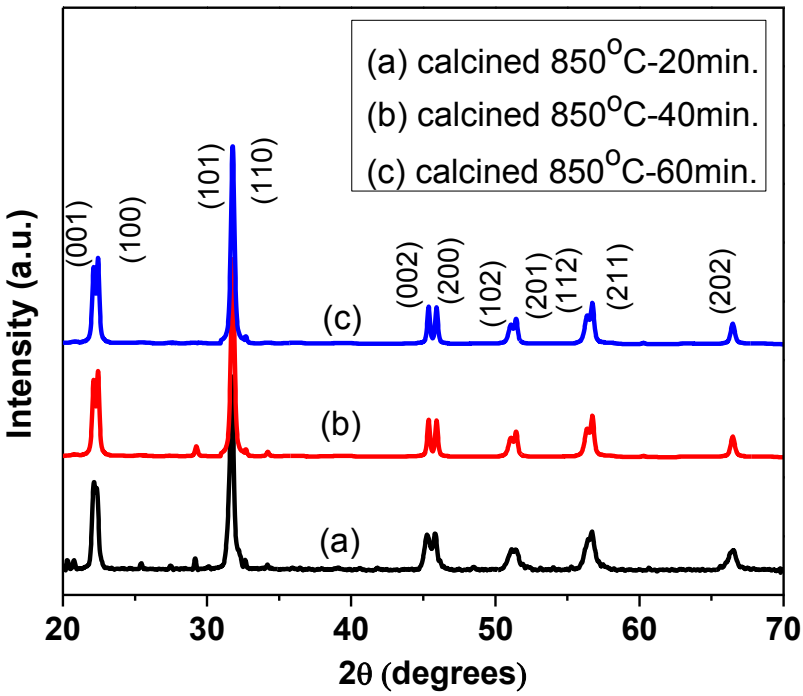

Fig. 7.2 XRD patterns of MW processed KNA6N-LS ceramics calcined at 850 °C for 20, 40 and 60 mins.

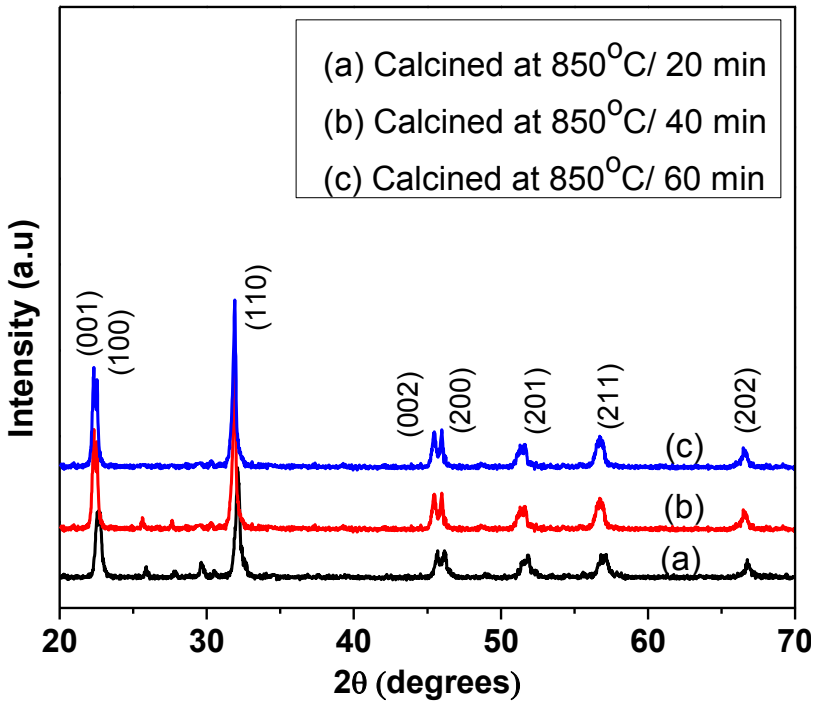

Fig. 7.3 XRD patterns of MW processed KNNT2-LS ceramics calcined at 850°C for 20, 40 and 60 mins.

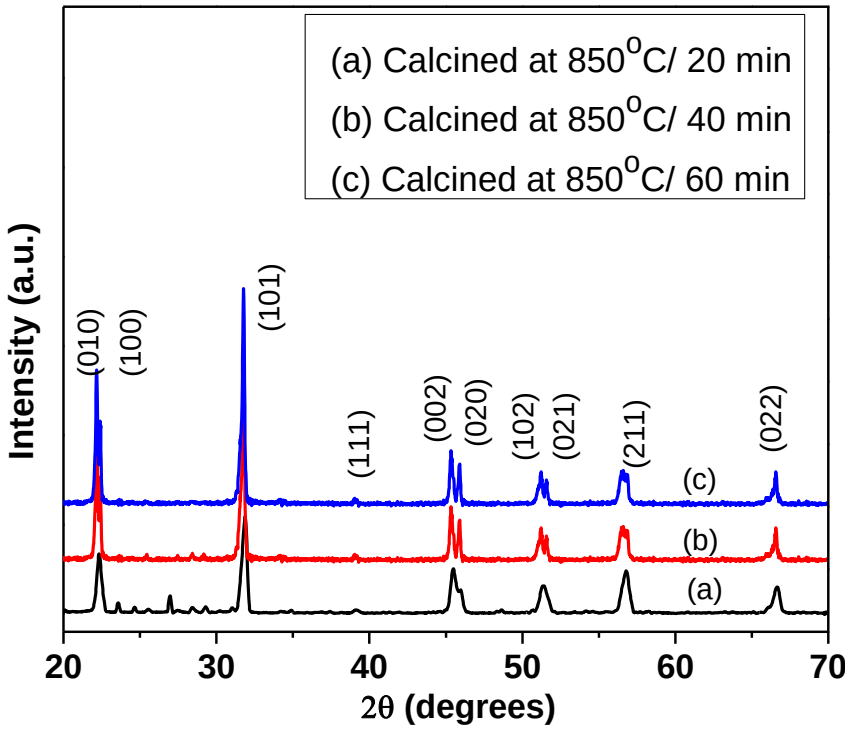

Fig. 7.4 XRD patterns of MW processed KNNV6-LS ceramics calcined at 850 °C for 20, 40 and 60 mins.

7.3 Sintering, Morphology and Density Study

7.3.1 0.95[$K_{0.5}Na_{0.5}NbO_3$]-0.05[$LiSbO_3$] / KNN-LS Ceramics

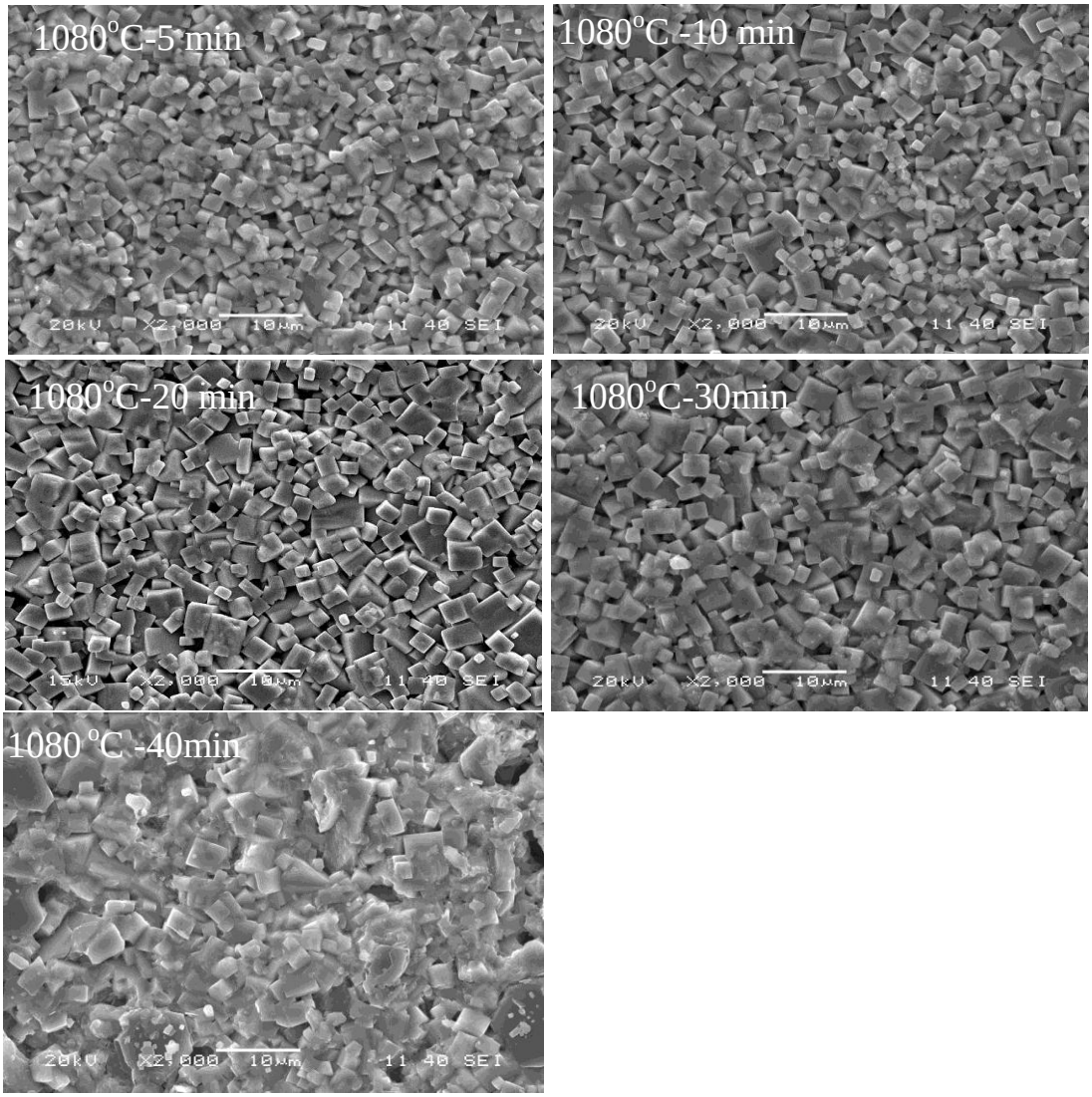

Fig. 7.5 SEM micrographs of MW processed KNN-LS ceramics.

Fig.7.5 shows the SEM micrographs of KNN-LS ceramics sintered at 1080 °C for 5, 10, 20, 30 and 40 mins, respectively. The micrographs reveal a non-uniform distribution of grains. The grain size of the KNN-LS ceramics sintered for 5 and 10 mins are found to be small in comparison to the 20 mins sintered ceramics. This result demonstrates that the grains of KNN-LS ceramics sintered at 5 and 10 mins do not grow

sufficiently, and the atomic binding force is smaller than intergranular force for these ceramics. With the increase in sintering time, the pore size significantly decreases and the average grain size increases. The microstructure of the sample sintered for 20 mins is denser and fine, the grain boundary is clear, the average grain size is about 4 μm, This indicates that the grains of the sample sintered 20 mins grow sufficiently, and the atomic binding force is greater than intergranular force [14]. However, with further increase in sintering time, the inhomogeneity of the grain size distribution increases. The microstructure of the sample sintered for 40 mins becomes more inhomogeneous and many distinct pores exist in grain boundary as can be seen in Fig. 7.5. This is because that the abnormal grain appears when the sintering time exceeds 20 mins.

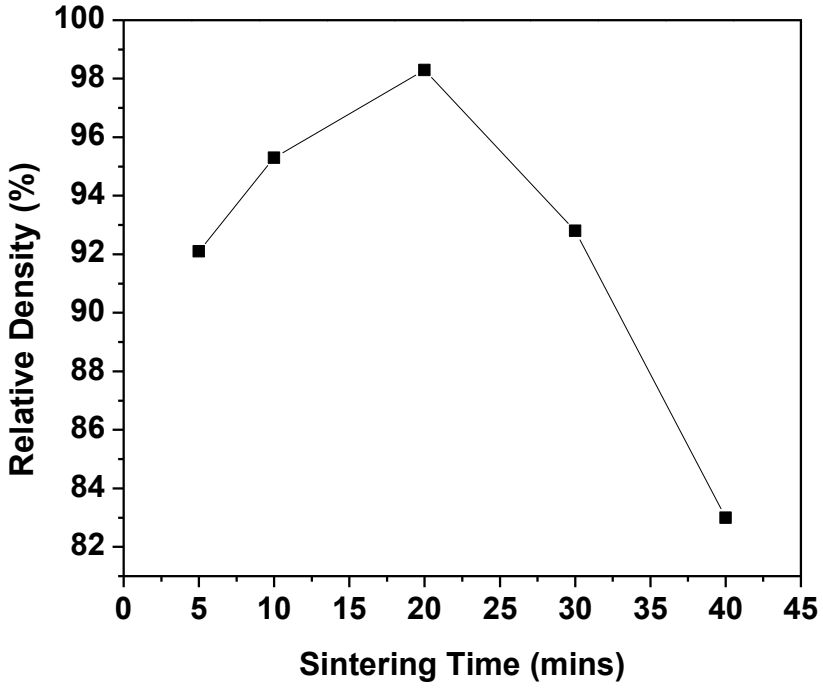

Fig. 7.6 Relative density (RD) of KNN-LS ceramics as a function of sintering time.

The relative density (RD) of the KNN-LS ceramics as a function of sintering time is shown in Fig. 7.6. RD is found to increase with the initial increase in sintering time up to 20 mins and then it decreases. The RD ~ 98.3% is obtained for the KNN-LS ceramics sintered for 20 mins, which is much higher than the same samples sintered by conventional technique. The decrease of RD at higher sintering time may be due to the melting of alkali elements, since these are volatile in nature [15].

7.3.2 $0.95[(K_{0.5}Na_{0.5})_{0.94}Ag_{0.06}NbO_3]$-$0.05[LiSbO_3]$ / KNA6N-LS Ceramics

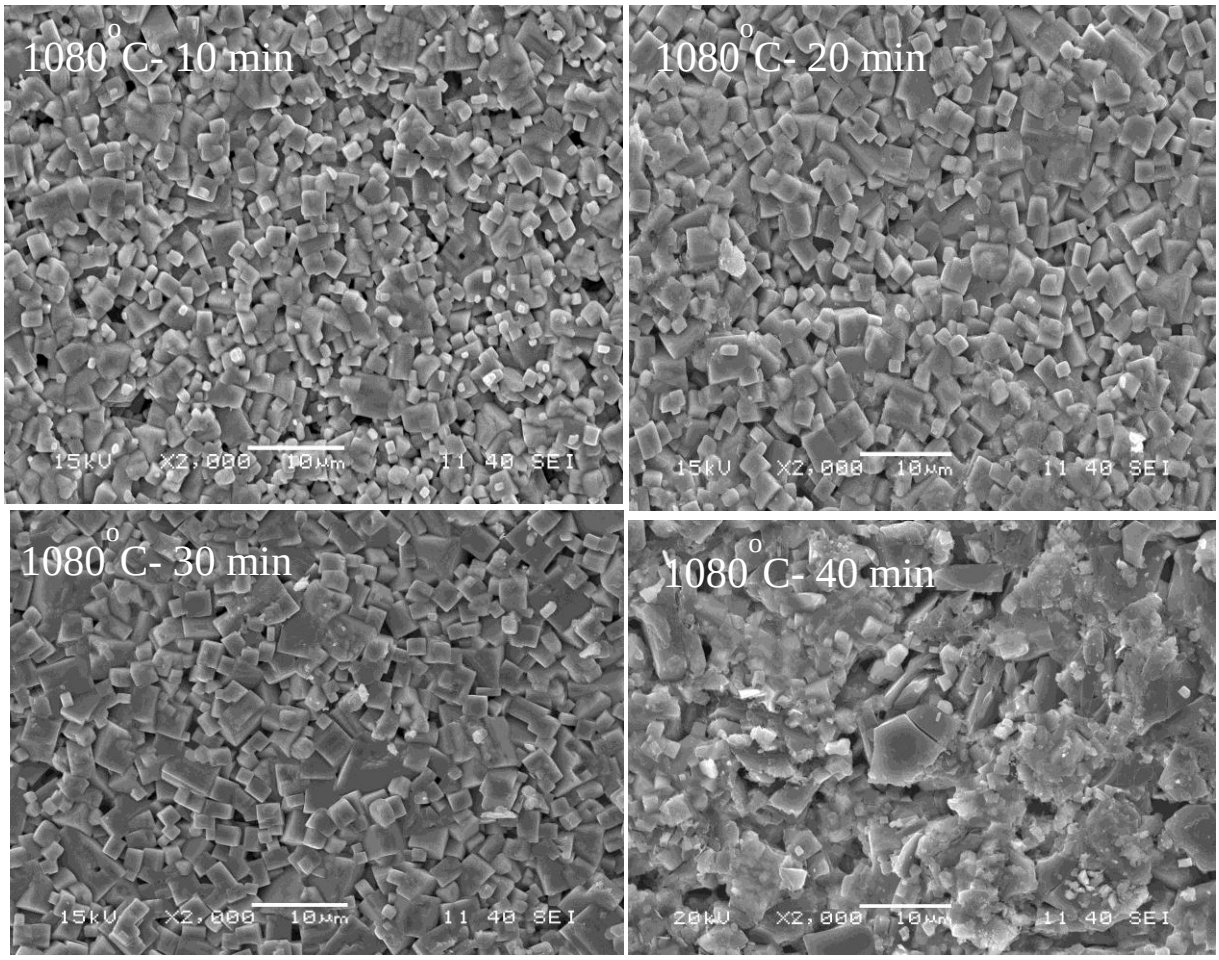

Fig. 7.7 SEM micrographs of MW processed KNA6N-LS Ceramics.

Fig.7.7 shows the SEM micrographs of the KNA6N-LS samples sintered at 1080°C for 10, 20, 30 and 40 mins, respectively. Initially, with the increase in sintering

time dense microstructure develops gradually, which indicates that the increase of sintering time is very effective in improving the density of ceramics. The ceramic sintered for 20 mins possesses denser microstructure. The density of the ceramics decreases as they are sintered over the optimum time i.e., above 20 mins. There are two reasons for the poor microstructure of the ceramic sintered over the optimum time. First, high sintering time cannot be applied in KNN based ceramics in order to avoid the volatilization of alkali elements. Second, in the present study the grain growth cannot eliminate the pores completely because the morphology of the grain is almost cubical. In the polycrystalline ceramics, it is difficult for cubic grains to be stacked orderly; therefore some pores are also preserved.

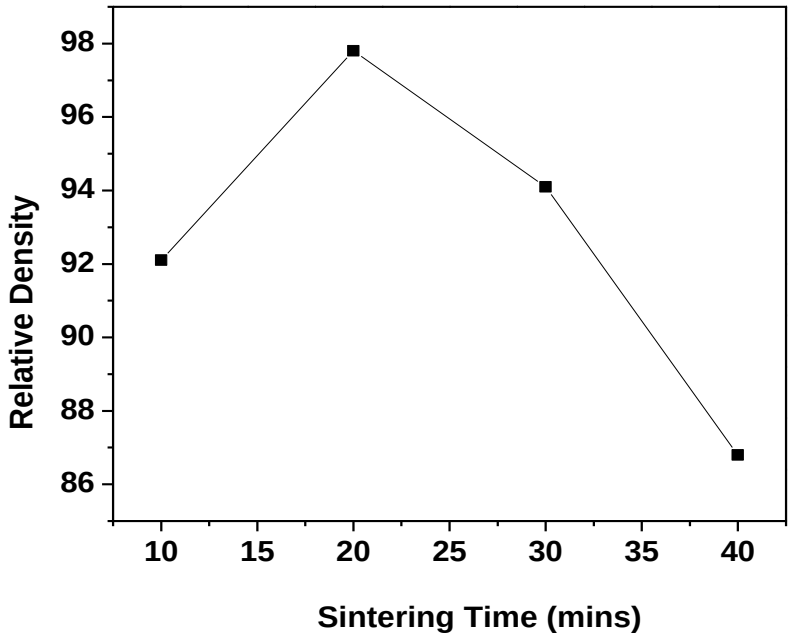

Fig. 7.8 Relative density (RD) of KNA6N-LS Ceramics as a function of sintering time.

The relative density of the KNA6N-LS ceramics as a function sintering time is shown in Fig. 7.8. RD increases with the initial increase in sintering time up to 20 mins and then it decreases. The RD of 20 mins sintered ceramics is found to be highest, which

is ~ 97.8% of the theoretical density. The decrease of RD at higher sintering time may also be due to the melting of alkali elements, since these are volatile in nature [16].

7.3.3 $0.95[(K_{0.5}Na_{0.5})Nb_{0.98}Ta_{0.02}O_3]$-$0.05[LiSbO_3]$ / KNNT2-LS Ceramics

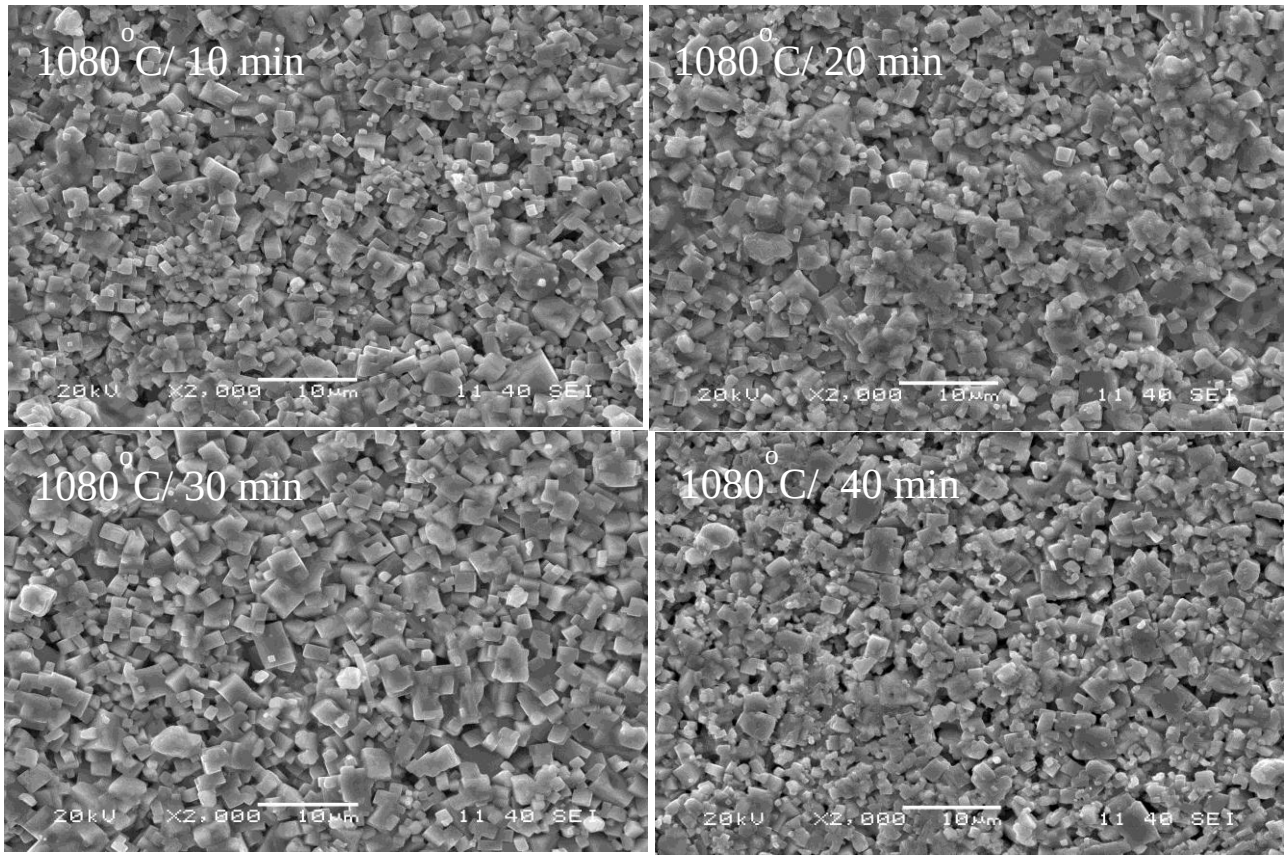

Fig. 7.9 SEM micrographs of MW processed KNNT2-LS Ceramics.

Fig.7.9 shows the SEM micrographs of the KNNT2-LS ceramics sintered at 1080^{o}C for different time intervals. It is well known that optimization of sintering process is very important to end up with a ceramic having better dielectric and ferroelectric properties [17]. Therefore, in the present case the optimum condition for sintering is defined by varying the sintering time. It is found that with the increase in sintering time up to 30 min an increment in the grain size and reduction in pore size is observed. However, with further increase in sintering time the packing of grains become poor and

pores are observed at the grain boundary. Relatively dense microstructure is obtained in case of the KNNT2-LS sample sintered for 30 mins.

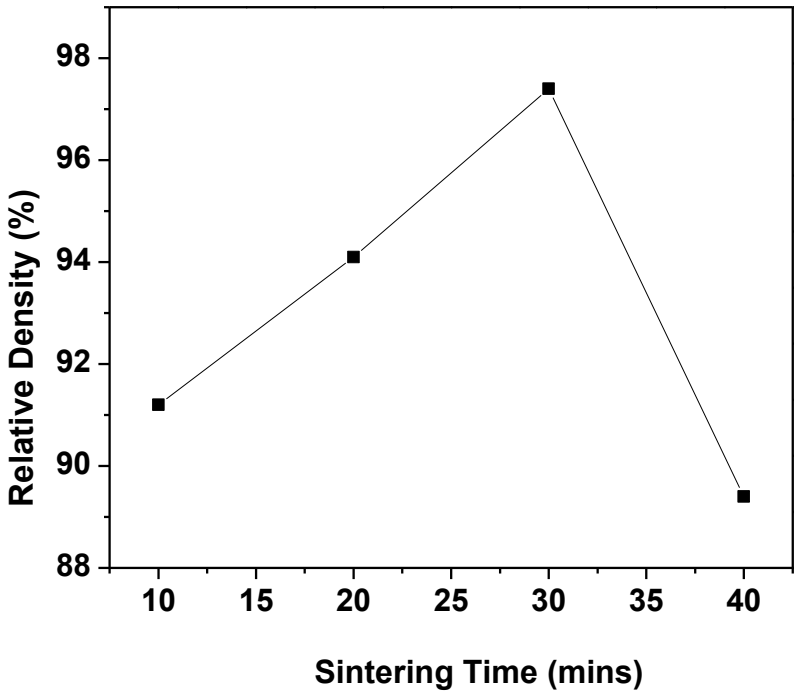

Fig. 7.10 Relative density (RD) of KNNT2-LS Ceramics as a function of sintering time.

Fig.7.10 shows the RD of KNNT2-LS ceramics as a function of sintering time. The RD of the ceramics is found to be ~ 91% for the 10 mins sintered ceramics whereas it reaches ~ 97.6% for the 30 min sintered ceramics. It can be seen that the optimum sintering time for the pure KNN-LS ceramics is 20 mins but for Ta doped ceramics it is 30 mins. The increase of optimum sintering time in case of Ta doped ceramics may be attributed to the higher melting point of $KTaO_3$ (~1370^oC) than the $KNbO_3$ (1039^oC) ceramics [18].

7.3.4 $0.95[(K_{0.5}Na_{0.5})Nb_{0.98}V_{0.06}O_3]$-$0.05[LiSbO_3]$ / KNNV6-LS Ceramics

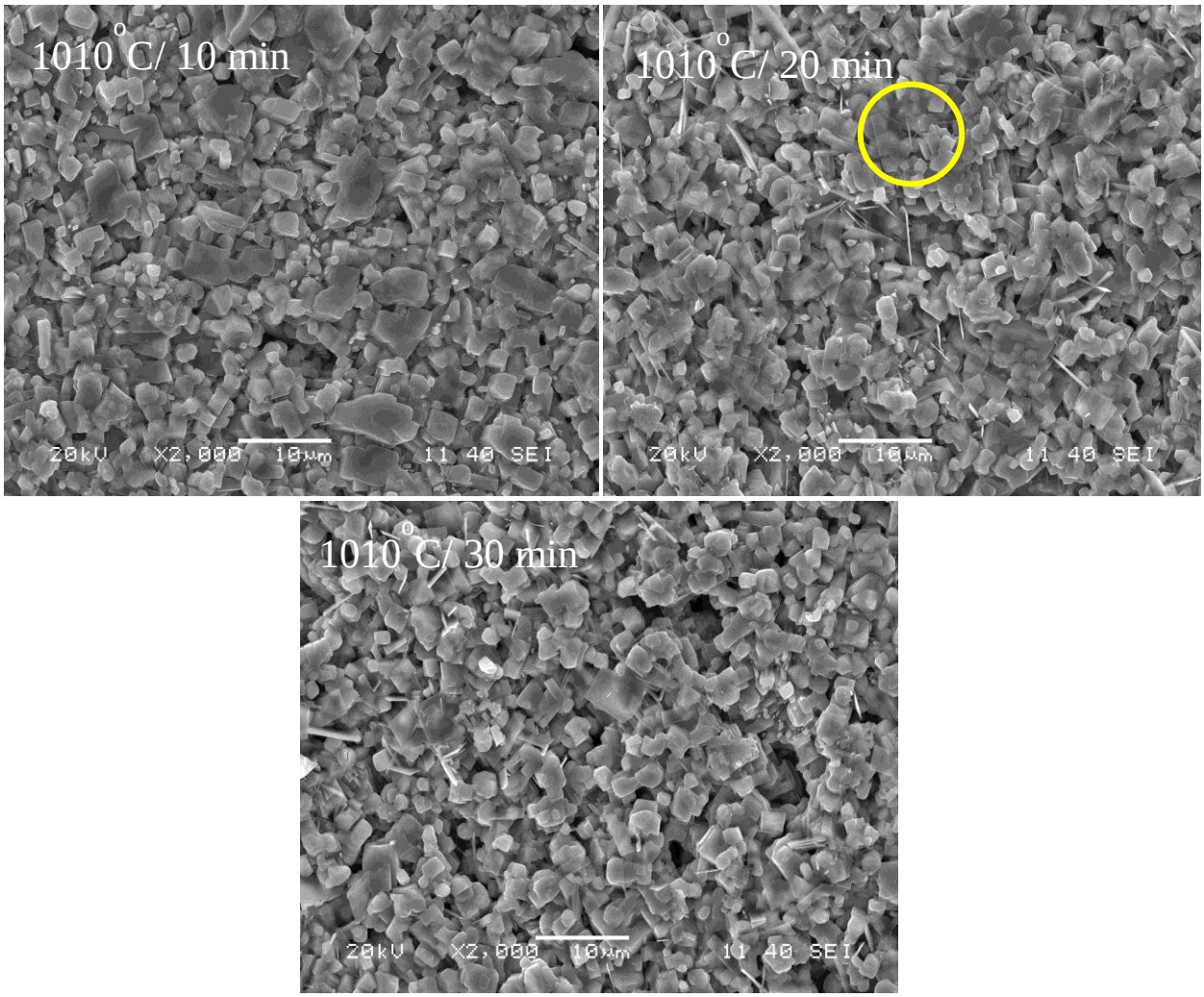

Fig. 7.11 SEM micrographs of MW processed KNNV6-LS Ceramics.

Fig.7.11 shows the SEM micrographs of KNNV6-LS ceramics sintered at 1010°C for 10, 20 and 30 mins. It can be seen that liquid phase appears across the grain boundary, which may be due to the low melting point of V_2O_5. It is distinctly observed that the grain size becomes smaller with the increase in sintering time. This is because increasing the sintering time period facilitates the liquid-phase sintering and improves the nucleation rate of the ceramics. Therefore, the grains become smaller with the increase of sintering time. It is clear from Fig.7.11 that a few pores exist in the grain boundary for the ceramics sintered for 10 mins and the pores are nearly eliminated in ceramics sintered for

20 mins. With further increase in sintering time the evaporation of alkali elements takes place and more pores appeared across the grain boundary. Fig.7.12 shows the RD of KNNV6-LS ceramics as a function of sintering time. The RD of the ceramics sintered for 10, 20 and 30 mins is found to be ~ 92.4%, 95.1% and 89.4% respectively. The RD of KNNV-LS ceramics is found to be lower than the other microwave processed ceramics, which may be due to the development of excess liquid phase in the sample (circled in Fig.7.9).

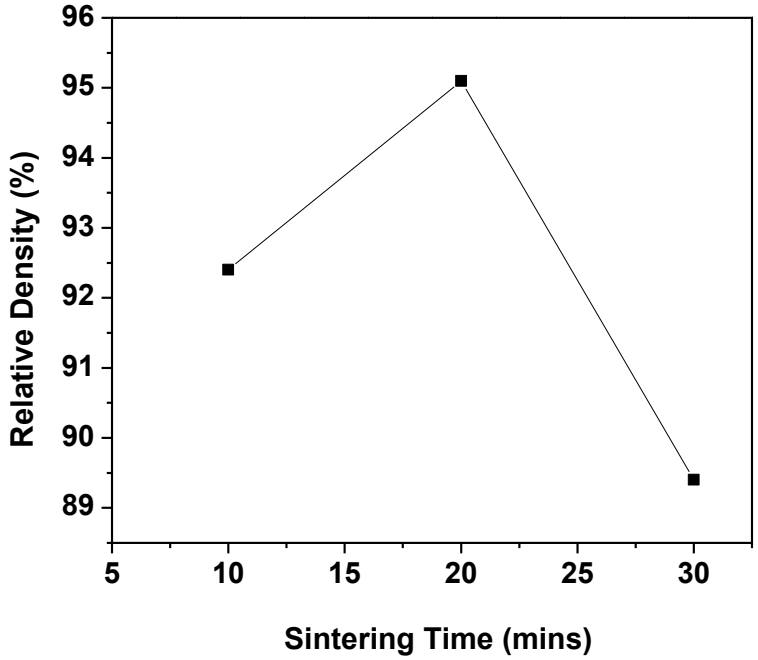

Fig. 7.12 Relative density (RD) of KNNV6-LS Ceramics as a function of sintering time.

7.4 Dielectric Study

7.4.1 Temperature Dependent Dielectric Constant (ε_r)

Fig.7.13 shows the temperature dependence dielectric constant at various frequencies of microwave processed KNN-LS ceramics sintered at 1080^{o}C for 20 mins. In pure KNN ceramics two phase transitions are observed above room temperature (RT)

in the temperature dependent dielectric constant curve behavior. The first one located ~ 200^{o}C is the orthorhombic to tetragonal (T_{O-T}) polymorphic phase transition temperature and the second one ~ 420^{o}C is called as the ferroelectric to paraelectric phase transition (Curie) temperature [19]. In the present case both these phase transition temperatures are shifted towards low temperature region with the substitution of Li and Sb in place of ($K_{0.5}Na_{0.5}$) and Nb, respectively. The T_{O-T} and T_c in microwave processed KNN-LS ceramics are observed ~ 44^{o}C and 387 ^{o}C, respectively whereas for the conventionally prepared KNN-LS ceramics T_{O-T} and T_c occurs ~ 43^{o}C and 385.5^{o}C, respectively. The value of ε_r at RT for the microwave processed KNN-LS ceramics at 10 kHz frequency is found to be ~ 960 which is higher than the conventionally prepared ceramics (~ 903). This may be due to the combined effect of better microstructure and enhanced bulk density in case of microwave processed ceramics [20]. Fig.7.14 shows the temperature dependence ε_r at various frequencies of microwave processed KNA6N-LS ceramics sintered at 1080^{o}C for 20 mins. The T_{O-T} and T_c of KNA6N-LS ceramics are found to be ~ 63^{o}C and 363^{o}C respectively, whereas in case of conventionally prepared ceramics these two phase transitions occur ~ 65 ^{o}C and 368 ^{o}C (chapter-6). The RT value of ε_r at 10 kHz frequency for microwave processed ceramic is also found to be (~980) higher than the same ceramics processed conventionally (~858). Fig.7.15 shows the temperature dependence ε_r at various frequencies of microwave processed KNNT2-LS ceramics sintered at 1080^{o}C for 30 mins. The T_{O-T} and T_c of KNNT2-LS ceramics are found to be ~ below RT and 377^{o}C, respectively, whereas in case of conventionally prepared ceramics these two phase transitions occur ~ below RT and 378^{o}C. The value of ε_r at RT for microwave processed ceramic is also found to be (~1171) higher than the conventional

one (~1023). Fig.7.16 shows the temperature dependence ε_r at various frequencies of microwave processed KNNV6-LS ceramics sintered at 1010°C for 20 mins. The T_{O-T} and T_c of KNNV6-LS ceramics are found to be ~ 82°C and 348°C, respectively, whereas in case of conventionally prepared ceramics these two phase transitions occur ~ 87°C and 350°C. The RT value of ε_r at 10 kHz frequency for microwave processed ceramic is also found to be (~905) higher than the conventional one (~745). The microwave processed ceramics are found to possess higher value of ε_r than the conventionally prepared ceramics, which shows the effectiveness of microwave processing over conventional one. The values of ε_r and T_c of conventional and microwave processed ceramics are compared in Table-7.1.

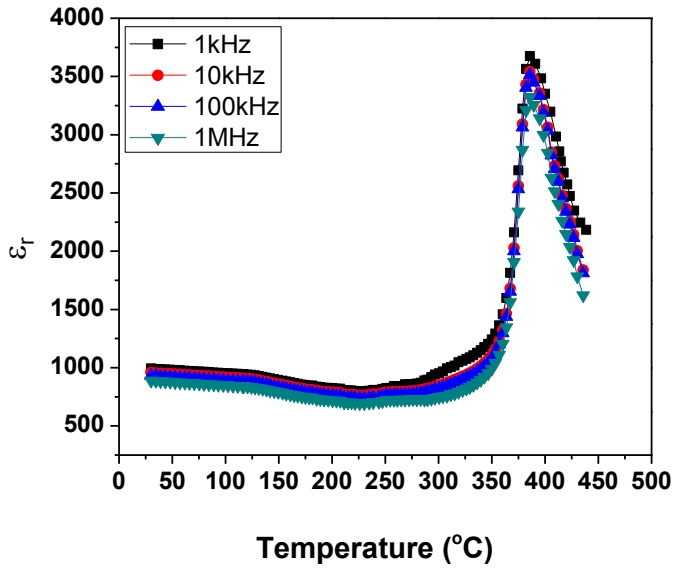

Fig.7.13 (a)

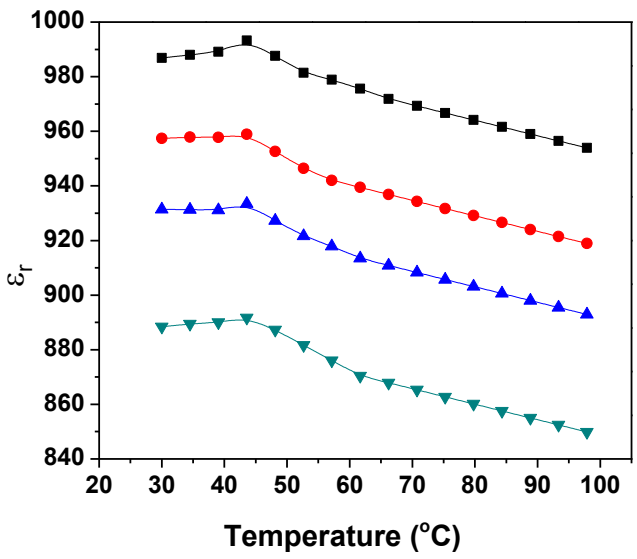

Fig.7.11 (b)

Fig. 7.13 Temperature variation of ε_r of KNN-LS ceramics sintered at 1080°C for 20 mins.

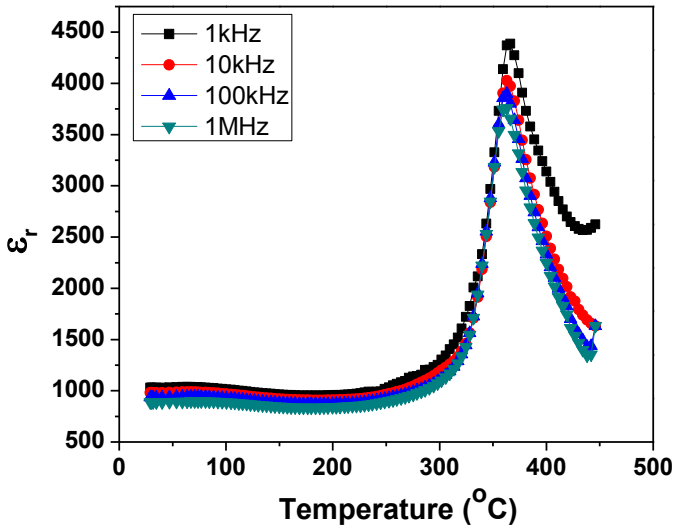

Fig.7.14 (a)

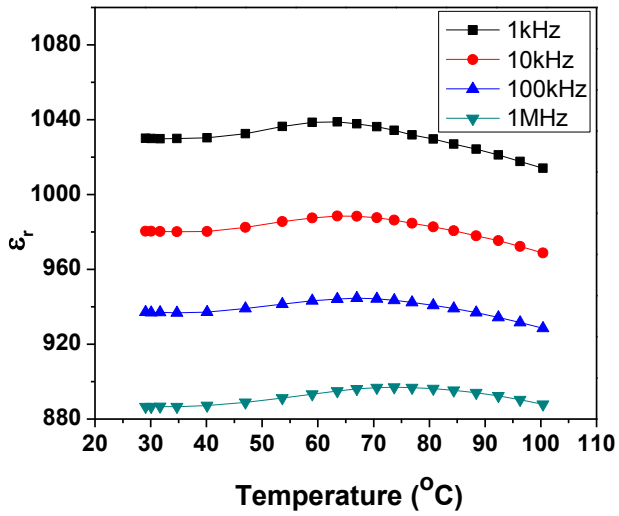

Fig.7.14 (b)

Fig.7.14 Temperature variation of ε_r of KNA6N-LS ceramics sintered at 1080^{o}C for 20 mins.

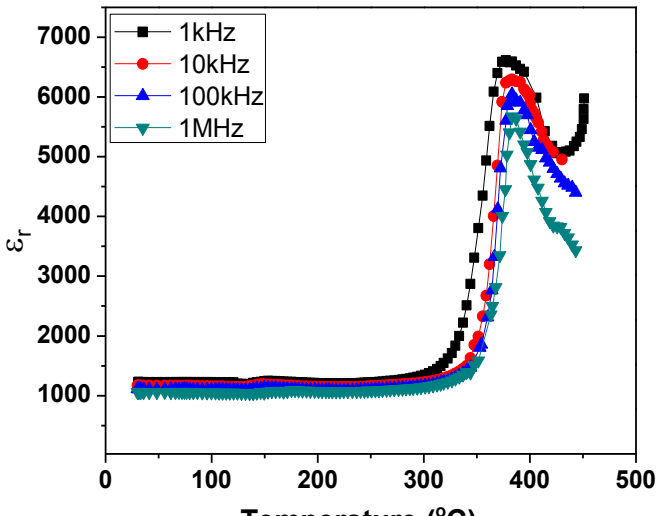

Fig.7.15 (a)

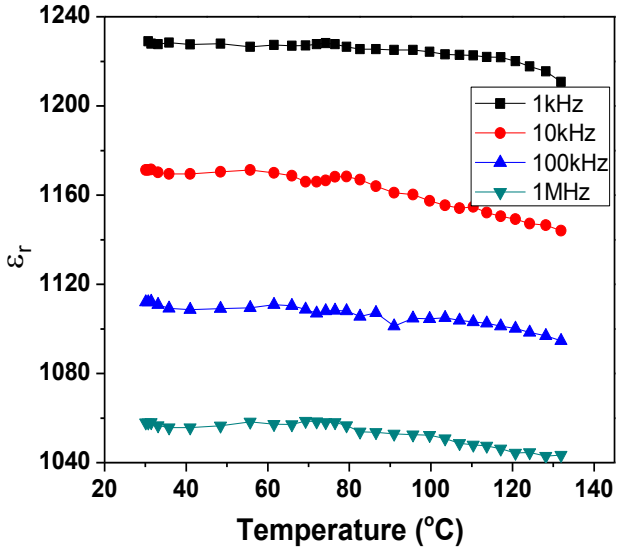

Fig.7.15 (b)

Fig.7.15 Temperature variation of ε_r of KNNT2-LS ceramics sinetered at 1080^{o}C for 30 mins.

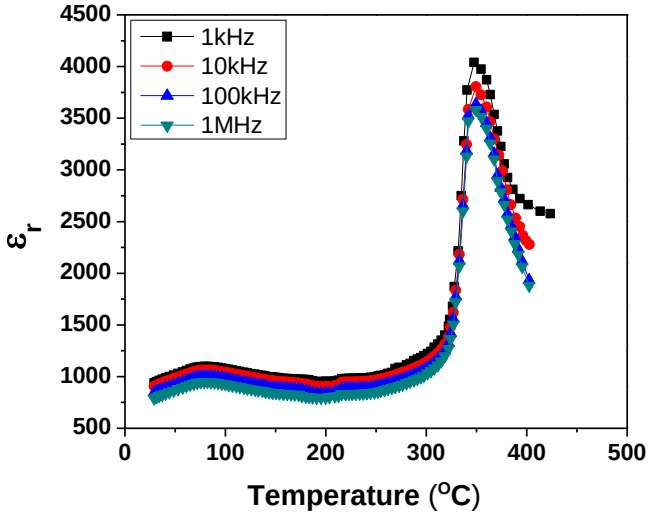

Fig.7.16 (a)

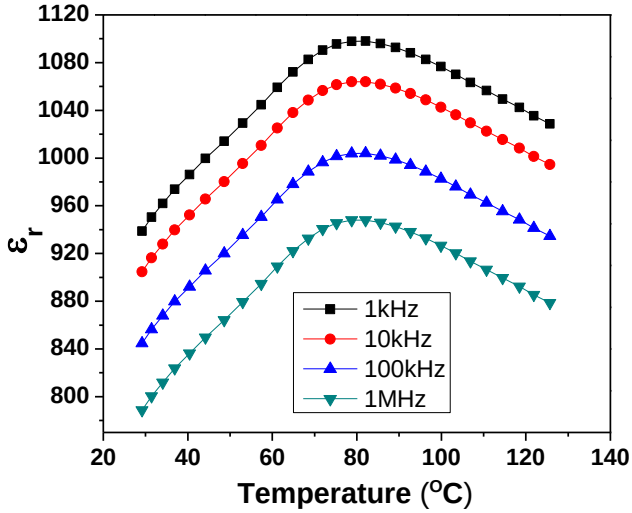

Fig.7.16 (b)

Fig.7.16 Temperature variation of ε_r of KNNV6-LS ceramics sintered at 1010^{o}C for 20 mins.

7.4.2 Temperature Dependent Dielectric Loss (tanδ)

The temperature dependence of dielectric loss (tanδ) of the microwave processed KNN-LS ceramics at various frequencies are shown in Fig.7.17. The dielectric loss of this ceramic is found to be much lower than the conventionally prepared ceramics. The RT value of tanδ at 10 kHz frequency is found to be ~ 0.031, whereas it is ~ 0.046 in the conventionally processed ceramic. The reduction of dielectric loss in MW processed ceramics may be due to the effect of microwave heating which reduces the porosity in ceramics [21]. The temperature dependence of dielectric loss (tanδ) of the microwave processed KNA6N-LS ceramics at various frequencies is shown in Fig.7.18. The value of tanδ of these ceramics at RT is also found to be lower than the conventionally prepared ceramics. The value of tanδ at 10 kHz frequency is found to be ~ 0.031 whereas the same conventionally processed ceramic possess a tanδ value ~ 0.037. This may be again due to the increase of bulk density. The temperature dependence of dielectric loss (tanδ) of the

microwave processed KNNT2-LS and KNNV6-LS ceramics at various frequencies are shown in Fig.7.19 & Fig.7.20, respectively. The RT value of tanδ at 10 kHz frequency for KNNT2-LS and KNNV6-LS ceramics are found to be ~0.028 and ~0.041, respectively. These values are lower than the conventionally prepared ceramics. Again, this is due to the development of nearly pore free microstructure with better density in the microwave processed ceramics. The values of tanδ of conventional and microwave processed ceramics are compared in Table-7.1.

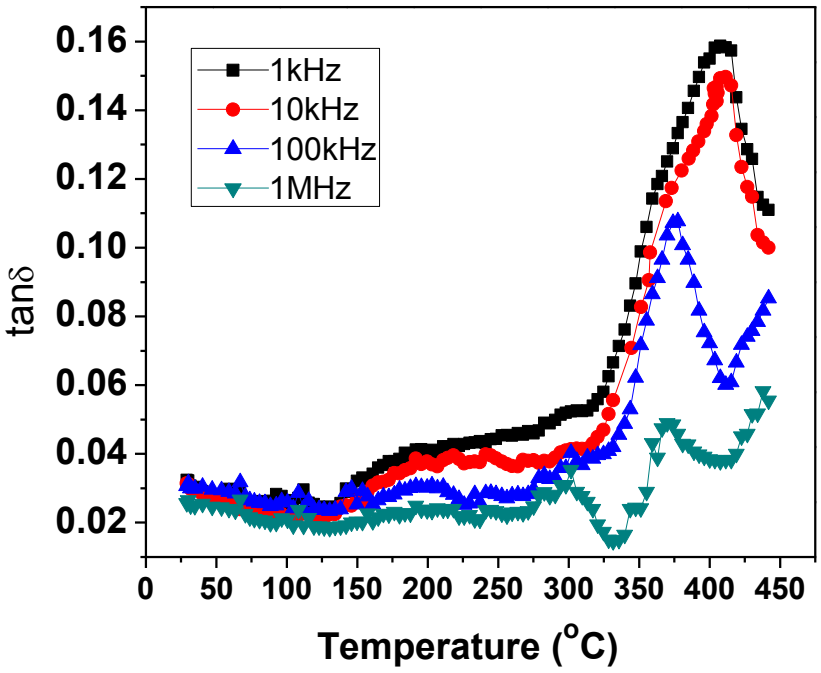

Fig.7.17 Temperature dependence of dielectric loss (tanδ) of the microwave processed KNN-LS ceramics at various frequencies.

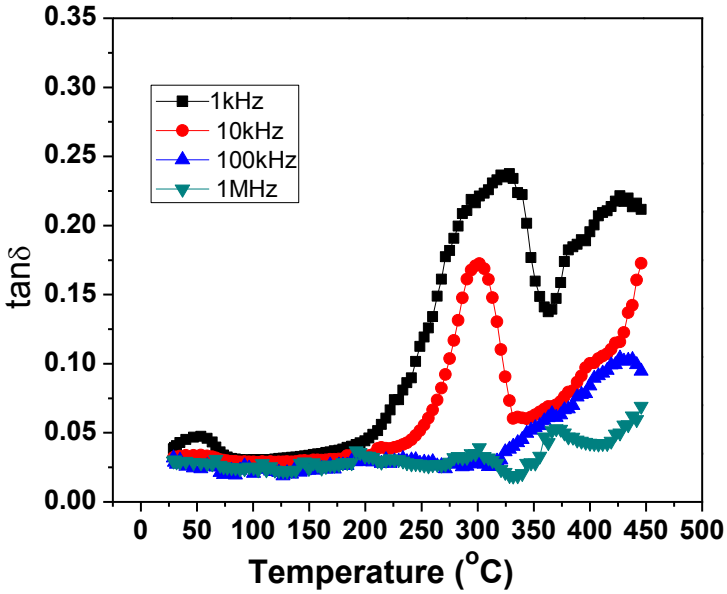

Fig.7.18 Temperature dependence of dielectric loss (tanδ) of the microwave processed KNA6N-LS ceramics at various frequencies.

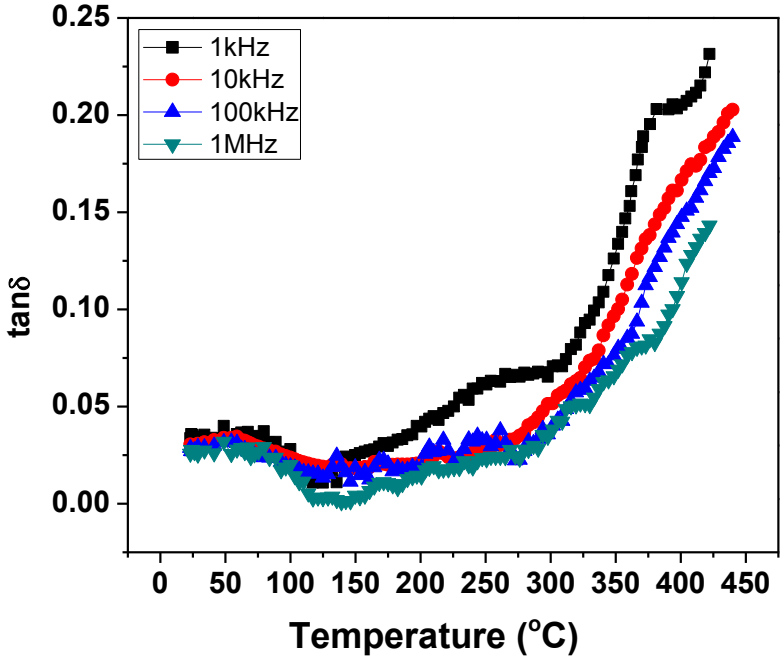

Fig.7.19 Temperature dependence of dielectric loss (tanδ) of the microwave processed KNNT2-LS ceramics at various frequencies.

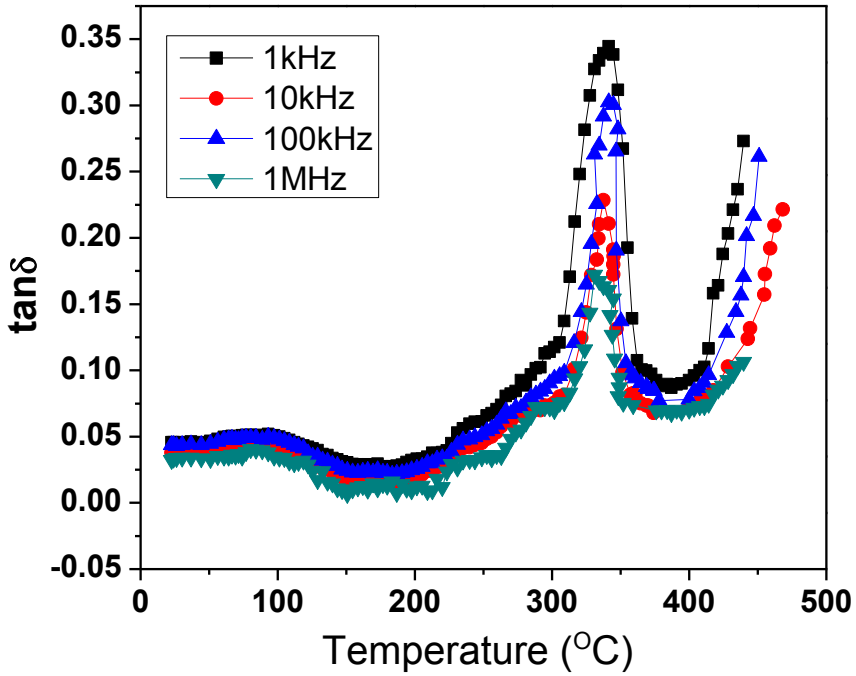

Fig.7.20 Temperature dependence of dielectric loss (tanδ) of the microwave processed KNNV6-LS ceramics at various frequencies.

Table-7.1 ε_r, tanδ and T_c of Conventional and microwave processed ceramics.

Sample	0.95KNN-0.05LS		KNNT2-LS		KNA6N-LS		KNNV6-LS	
	MWP	CP	MWP	CP	MWP	CP	MWP	CP
ε_r (10 kHz)	960±15	903±10	1171±25	1023±20	980±14	858±10	905±15	745±20
tanδ (10 kHz)	0.031 ±0.002	0.046 ±0.004	0.028 ±0.003	0.038 ±0.005	0.031 ±0.01	0.037 ±0.005	0.041 ±0.002	0.048 ±0.004
T_c (^oC)	387±02	385.5±02	377±01	376±02	363±02	368±02	348±01	350±02

7.5 Ferroelectric Properties

The polarization vs. electrical field (P-E) hysteresis loops of microwave processed KNN-LS, KNA6N-LS, KNNT2-LS and KNNV6-LS ceramics are shown in Fig.7.21 (a-d), respectively. The development of well saturated hysteresis loops in all these ceramics confirms the ferroelectric nature of these ceramics. It is found that these microwave processed ceramics possess better ferroelectric properties than their conventional counter parts. It is known that the ferroelectric properties of any material strongly depend upon its microstructural properties. In the present case the microstructural properties of microwave processed ceramics are found to be better than the conventionally processed ceramics. The detail comparisons between the ferroelectric properties are given in Table-7.2. Among all the ceramics synthesized by MW processing technique in the present work, the microwave processed KNNT2-LS ceramics possess highest value of remnant polarization ($P_r \sim 30.85\ \mu C/cm^2$) and lowest coercive field ($E_c \sim 11.3$ kV/cm). It can also be seen that the E_c values of microwave processed ceramics are found to be higher than the same ceramics processed conventionally, which is attributed to the relatively smaller grain size in the former one. It is well known that the coercive filed of a ferroelectric material depends on its grain size. If the grain size is smaller, then the number of grain boundaries will be higher which restricts the easy rotation of the domain walls and hence increases E_c [22].

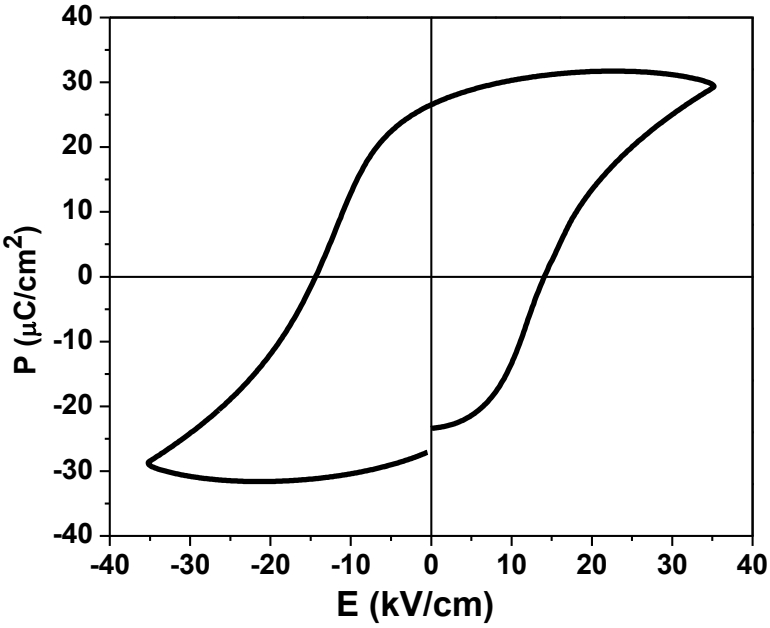

Fig.7.21 (a) PE-Hysteresis loop of KNN-LS ceramics sintered at 1080°C for 20 mins.

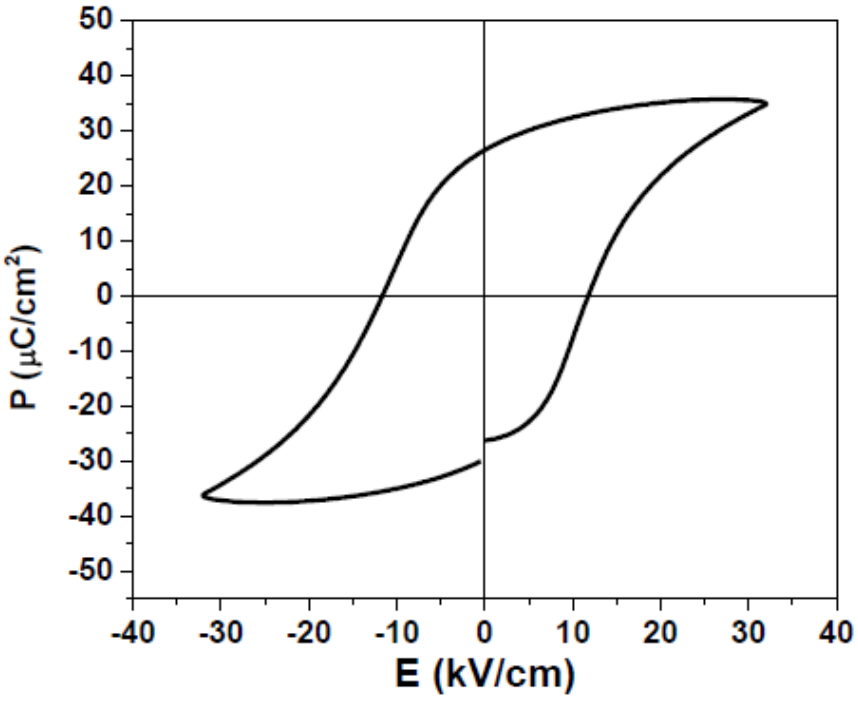

Fig.7.21 (b) PE-Hysteresis loop of KNA6N-LS ceramics sintered at 1080°C for 20 mins.

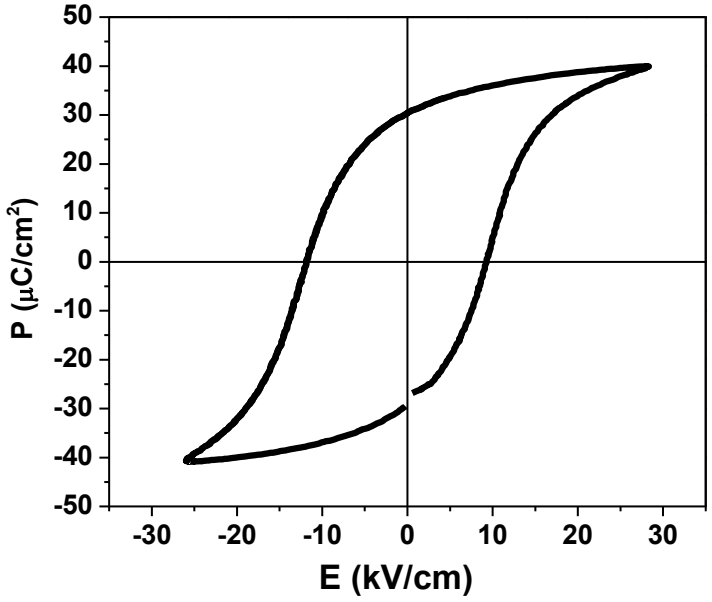

Fig.7.21 (c) PE-Hysteresis loop of KNNT2-LS ceramics sintered at 1080^{o}C for 30 mins.

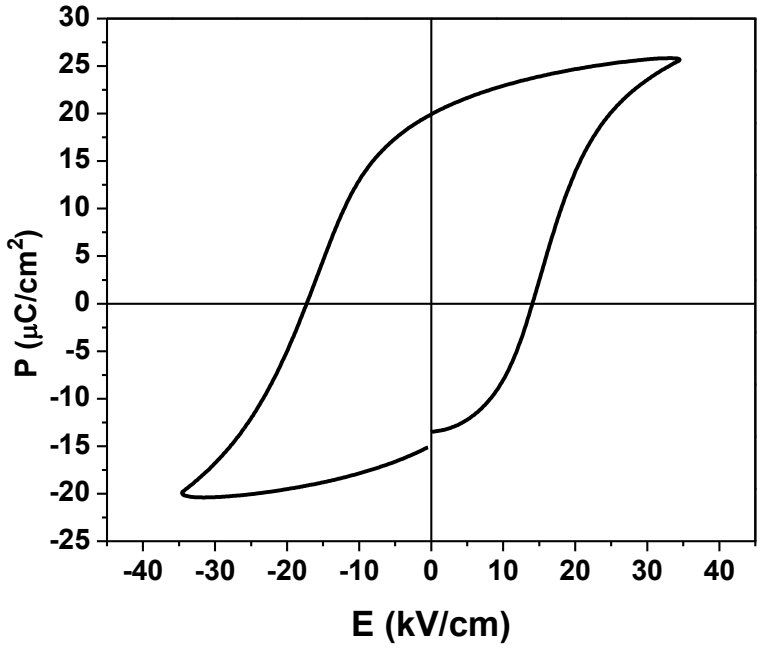

Fig.7.21 (d) PE-Hysteresis loop of KNNV6-LS ceramics sintered at 1010^{o}C for 20mins.

Table-7.2 Comparison between ferroelectric Properties of microwave and conventional processed KNN-LS, KNA6N-LS, KNNT2-LS and KNNV6-LS ceramics.

Sample Name	Remnant Polarization (P_r) μC/cm^2		Coercive Field (E_c) kV/cm	
	MWP	CP	MWP	CP
KNN-LS	26.40±0.2	18.7±0. 3	14.12±0.4	11.8±0.3
KNA6N-LS	25.75±0.2	21.9±0.4	11.55±0.3	12.65±0.2
KNNT2-LS	30.85±0.3	24.65±0.4	11.30±0.3	10.1±0.2
KNNV6-LS	19.65±0.03	14.6±0.4	17.22±0.3	13.75±0.4

7.6 Piezoelectric Properties

In the piezoelectric study, microwave processing effect on the piezoelectric coefficients (d_{33}), planar mode coupling coefficients (k_p) have been studied and discussed. Strains induced by the application of external electric field to unpoled samples have also been discussed. The comparison between the piezoelectric properties of microwave and conventionally processed samples have been made in detail.

The room temperature (RT) values of piezoelectric-coefficient (d_{33}), mechanical quality factor (Q_m) and plannar mode coupling coefficients (k_p) of all the microwave processed ceramics are given in Table-7.3. Microwave processed ceramics possess higher values of d_{33} and k_p than the conventionally processed ceramics prepared. This may be due to the relatively dense packing and uniform distribution of grains in the microwave processed ceramics. Among all the ceramics, the microwave processed KNNT2-LS ceramics possess highest piezoelectric properties i.e., d_{33} ~ 257 pC/N and k_p ~ 0.48.

Table-7.3 Comparison between the various properties of microwave and conventionally processed KNN-LS, KNAN-LS, KNNT-LS and KNNV-LS ceramics.

Sample	0.95KNN-0.05LS		KNNT2-LS		KNA6N-LS		KNNV6-LS	
	MWP	CP	MWP	CP	MWP	CP	MWP	CP
d_{33} (pC/N)	236±04	215±05	257±02	252±02	241±05	227±03	143±02	121±02
k_p	0.43 ±0.01	0.415 ±0.005	0.48 ±0.005	0.47 ±0.01	0.44 ±0.01	0.425 ±0.01	0.36 ±0.01	0.31 ±0.02
Q_m	95±05	71±02	135±03	98±04	110±05	81±03	95±04	112±05

7.6.1 Strain vs. Electric Field (S-E) Loop Study

Fig.7.22 (a-d) shows the strain-electric field hysteresis loops of the microwave processed KNN-LS, KNA6N-LS, KNNT2-LS and KNNV6-LS ceramics sintered at optimum conditions. The development of typical butterfly shaped loops in all the ceramics confirm the piezoelectric nature of these samples [23]. These (S-E) loops show remnant strain with coercive field. The remnant strain indicates that complete domain switching may not be taking place in the samples [24]. The hysteresis observed in the material is due to the net contribution of domain switching, domain wall motion transition caused by the high electric field and electric field induced phase transition [25]. The shape of the S-E loop developed in microwave (MW) processed KNN-LS ceramic is not symmetrical. Maximum (max.) strain and remnant strain developed in microwave processed KNN-LS ceramics are found to be ~ 0.20% and ~ 0.09%, respectively. These values are higher than the conventionally synthesized KNN-LS ceramics. The max. strain developed in the MWP KNA6N-LS ceramics is found to be 0.18% , whereas the remnant

strain is ~ 0.08%, which are also higher than the conventionally prepared KNA6N-LS ceramics. In KNNT2-LS ceramics, the max. strain and remnant strain are found to be ~0.25% and ~ 0.10%, which are again higher than the conventionally prepared KNNT2-LS ceramics. In case of KNNV6-LS ceramics, abnormal (S-E) loop is developed. The max. strain and remnant strain developed here are found to be ~ 0.18% and ~ 0.06%, which are also higher than the conventionally prepared KNNV62-LS ceramics. The comparison between the max. strain and remnant of microwave processed and conventional processed ceramics are given in Table-7.4. The above results confirms that the piezoelectric properties of MWP ceramics are found to be better than the conventionally prepared ceramics, which can be explained as follows; **i**n general, grain size and porosity influence the piezoelectric properties; grain boundaries and pore surfaces generate a depolarization field and inhibit domain-wall motion [26]. The porosity of MWP ceramics are less in comparison to CP ceramics. The distributions of grains are also relatively more uniform in case of MWP ceramics. Therefore, these facts facilitate the domain wall motion and enhance the remnant strain in MW processed ceramics. The depolarization effect and degree of inhibition of domain-wall motion are large for intra grain pores, which is more in case of conventionally processed ceramics. Abnormal grain growth in case of CP ceramics also leads to the formation of a duplex structure and probably is responsible for the reduction of remnant strain in conventionally processed ceramics [27].

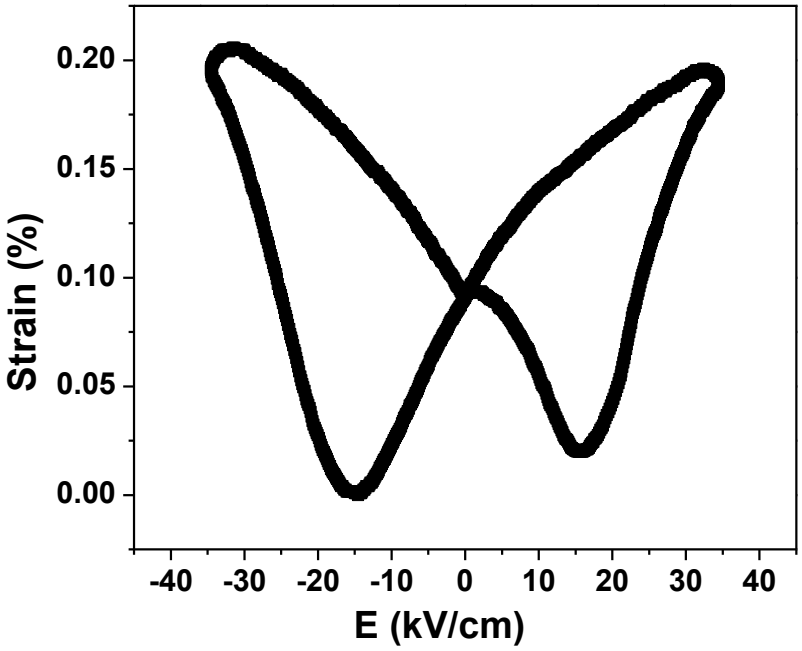

Fig.7.22 (a)

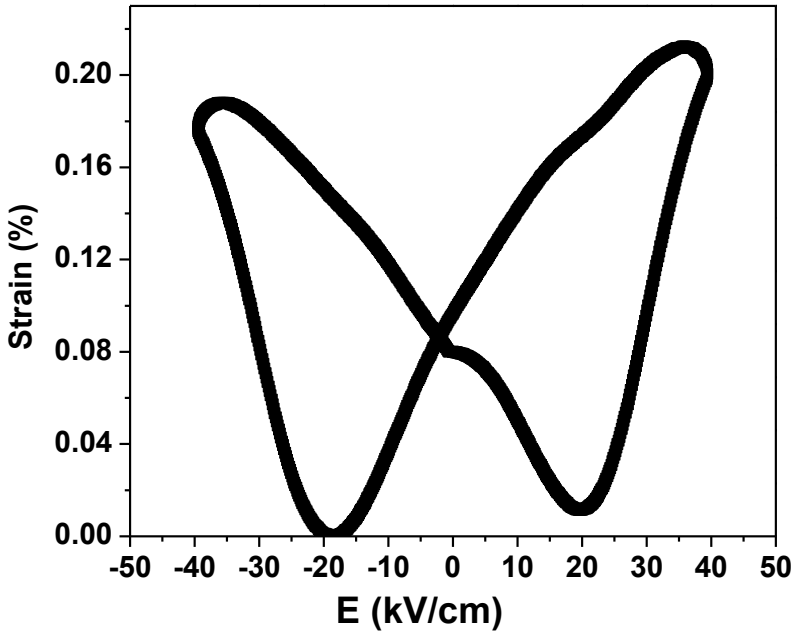

Fig.7.22 (b)

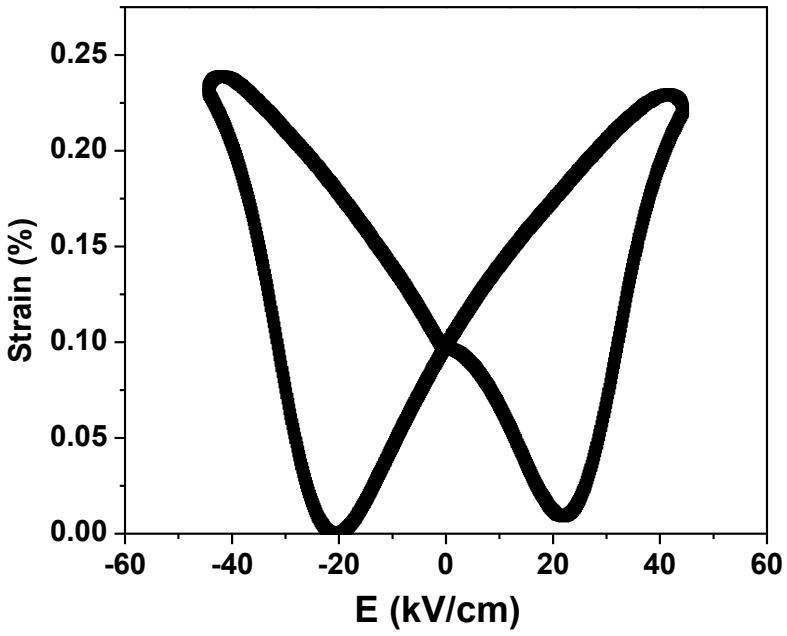

Fig.7. 22 (c)

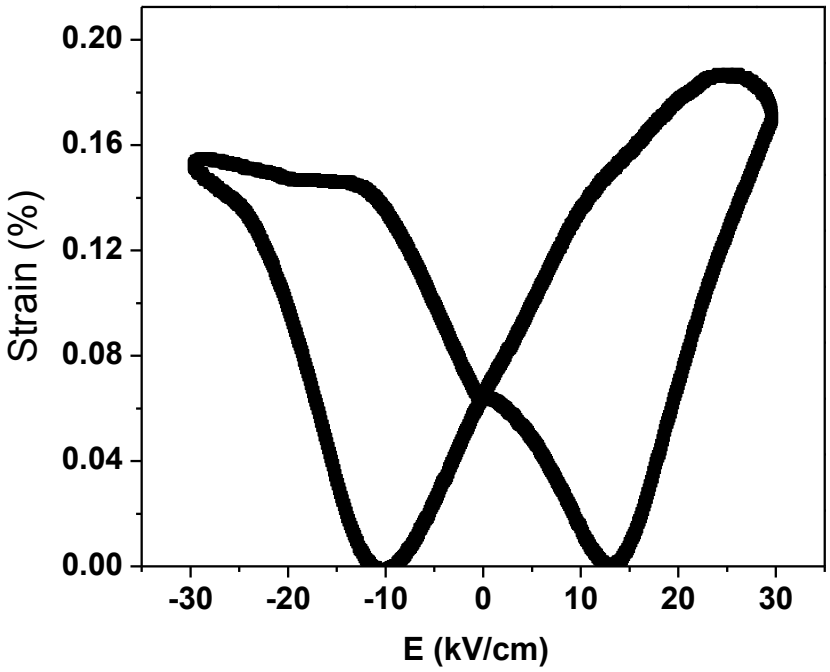

Fig.7. 22 (d)

Fig.7.22 S-E hysteresis loops of (a) KNN-LS ceramics sintered at 1080^{o}C for 20 mins (b) KNA6N-LS ceramics sintered at 1080^{o}C for 20 mins (c) KNNT2-LS ceramics sintered at 1080^{o}C for 30 mins and (d) KNNV6-LS ceramics sintered at 1010^{o}C for 20 mins.

Table-7.4 Remnant strain and max. strain of MWP and CP ceramics.

Sample	0.95KNN-0.05LS		KNNT2-LS		KNA6N-LS		KNNV6-LS	
	MWP	**CP**	**MWP**	**CP**	**MWP**	**CP**	**MWP**	**CP**
Remnant Strain (%)	0.09	0.07	0.10	0.085	0.09	0.085	0.06	0.046
Max. Strain (%)	0.20	0.11	0.25	0.20	0.20	0.16	0.18	0.11

References

[1] O. P. Gandhi, Microwave Engineering and Appliations, Pergamon Press, New York, (1981).

[2] J. M. Osepchuk, IEEE Transactions on Microwave Theory and Techniques, 32, (1984) 1200.

[3] Y. Fang, D.K. Agrawal, D.M. Roy, and R. Roy, J. Mater. Res., 9, (1994) 180.

[4] W.H. Sutton, Ceram. Bull., 68, (1989) 376.

[5] D.M.P. Mingos, D.R. Baghurst, Chem. Soc. Rev., 20, (1991) 1.

[6] K.J. Rao, B. Vaidhyanathan, M. Ganguli and P.A. Ramakrishnan, Chem. Mater., 11, (1999) 882.

[7] A. D. Reisel, S. Schops, A. Lenk and G. Schmutzler, Adv. Engg. Mater., 9, (2007) 400.

[8] B. Vaidhyanathan, D.K. Agrawal, T.R. Shrout andYi Fang, Mater. Lett., 42, (2000) 207.

[9] S. Mahajan., O.P. Thakur, D.K. Bhattacharya and K. Sreenivas, Mater. Chem. Phys., 112, (2008) 858.

[10] M. Venkata ramana, , S. Roopas kiran, N. Ramamanohar reddy, K. V. Siva kumar, V. R. K. Murthy and B. S. Murty, J. Adv. Dielectr., 1, (2011) 71.

[11] M. V. Ramanaa, S. R. Kiranc, N. R. Reddy., K.V. S. Kumar, V.R.K. Murthy and B.S. Murty, Mater. Chem. Phys., 126, (2011) 295.

[12] H. R. Rukmini, R. N. P. Choudhary and D. L. Prabhakara, Mater. Chem. Phys., 64, (2000) 171.

[13] R. R. Menezes, P. M. Souto and R. H. Kiminami, Mater. Res., 13, (2010) 345.

[14] H. Du, F. Tang, F. Luo, D. Zhu, S. Qu, Z. Pei, and W. Zhou, Mater. Res. Bull., 42, (2007) 1594.

[15] K. Kakimoto, I. Masuda, and H. Ohsato, J. Eur. Ceram. Soc. 25 (2005) 2719.

[16] R. Chen and L. Li, J. Am. Ceram. Soc., 89, (2006), 2010.

[17] S. H. Lee, S. G. Lee and Y. H. Lee, Nanoscale Res. Lett.,7, (2012)15.

[18] D. Lin, K.W. Kwok, and H.L.W. Chan, Appl. Phys. A 91, (2008) 167.

[19] Z. JingBo, D.U. HongLiang, Q. U. ShaoBo, Z. HongMei1, and X. Zhuo, Chin. Sci. Bull., 56, (2011) 2389.

[20] F. Selmi, F. Guerin, V. K. Varadana, V. V. Varadana, and S. komareni, Mater. Lett., 12, (1992) 424.

[21] T. Tao, L. Wang, and Q. Zhang, J. Alloy. Compd**.,** 486, (2009) 606.

[22] L. Egerton, and D.M. Dillion, J. Am. Ceram. Soc., 42, (1959) 438.

[23] Y. Ito, K. Nagatsuma, H. Takeudsi and S. Jyomura, J. Appl. Phys., 52, (1981) 4479.

[24] D. Damjonvic, T. R. Gururaja, and L. E. Cross, Am. Ceram. Soc. Bull., 66, (1987) 699.

[25] M. J. Haun, E. Furman, S. J. Jang, and L. E. Cross, IEEE Trans. Ultrason. Ferroelectr. Freq. Control, 36 (1989) 393.

[26] H. S. Lee, and T. Kimura, J. Am. Ceram. Soc., 81, (1998) 3228.

[27] K. Okazaki, and K. Nagata, J. Am. Ceram. Soc., 56, (1973) 82.

CHAPTER-8

Conclusions and Recommendations for Future Work

8.1 Conclusions

The major aim of the work presented in this thesis was centered around the challenging task of developing new lead-free materials for the piezoelectric applications. In the first part, the effect of LS content and poling temperature on the electrical properties of the (1-x)[$K_{0.5}Na_{0.5}NbO_3$]-x[$LiSbO_3$] (x=0, 0.04, 0.05 and 0.06)/(KNN-LS) ceramics synthesized by CSSR route within the MPB region have been investigated. The important results obtained in this part of the work are presented below:

a) Single perovskite phase formation was confirmed at 850^oC calcination temperature in all the KNN-LS ceramics. The sintering temperature was optimized to obtain dense KNN-LS ceramics. **It was found that the optimum sintering temperature decreased from 1120^oC to 1080 ^oC with modification of LS in KNN ceramics.**

b) The structural study revealed the transformation of pure orthorhombic phase to tetragonal phase with the increase in LS content. A MPB like behavior was found in between $0.06 \leq x \leq 0.04$. The RD of the ceramics was found to be maximum for x=0.05.

c) The temperature dependent dielectric study confirmed the decrease of both T_{o-t} and T_c with the increase in LS content in KNN-LS system. The diffusivity increased with the increase in LS content in KNN-LS ceramics. The presence of orthorhombic to tetragonal (T_{O-T}) polymorphic phase transition (PPT) ~ 43^oC in case of 0.95KNN-0.05LS ceramics further confirms the possibility of the presence of both orthorhombic and tetragonal phases at RT.

d) Piezoelectric and electromechanical properties were found to be strongly dependent on the poling temperature (T_p). Maximum piezoelectric, ferroelectric and electromechanical poperties i.e., d_{33} ~ 215 pc/N, P_r ~ 18.7 μC/cm^2 and k_p ~ 0.415 have been obtained in 0.95KNN-0.05LS ceramics.

Even though 0.95KNN-0.05LS ceramic showed better properties, still it is not comparable to lead based ceramics. To further improve the electrical properties of 0.9KNN-0.05LS ceramics, the effect of Ag, Ta and V on the structural and electrical properties have been studied in detail. The important results obtained in this part of the work are presented below:

a) $0.95[(K_{0.5}Na_{0.5})_{1-x}Ag_xNbO_3]$-$0.05LiSbO_3$ /(KNAN-LS) ceramics with x=0, 0.02, 0.04, 0.06 and 0.08 have been synthesized by conventional solid state reaction route (CSSR). X-ray diffraction (XRD) analysis confirmed the transformation of mixed structure to pure tetragonal structure with the increase in Ag content in KNAN-LS ceramics. The Curie temperature (T_c) of the ceramics decreased from 385.5^{o}C to 331^{o}C with the increase in silver (Ag) content from x=0 to 0.08. The KNAN-LS ceramics with x=0.06 showed better piezoelectric and ferroelectric properties (d_{33} = 227pC/N, k_p = 42.5%, T_c = 368^{o}C and P_r = 21.9 μC/cm^2).

b) $0.95[(K_{0.5}Na_{0.5})Nb_{(1-x)}Ta_xO_3]$-$0.05LiSbO_3$ (KNNT-LS) ceramics with x=0, 0.02, 0.04, 0.06 and 0.08 have been synthesized by conventional solid state reaction route (CSSR). X-ray diffraction (XRD) analysis confirmed the formation of mixed phase (tetragonal & orthorhombic) at lower concentration of Ta content in KNNT-LS ceramics. The RD as well as the sintering temperature increased with the increase in Ta content in KNNT-LS ceramics. Curie temperature (T_c) of the

ceramics decreased from 385.5^{o}C to 341^{o}C with the increase in Ta content from x=0 to 0.08 in KNNT-LS ceramics. The optimum electrical properties: piezoelectric coefficient **(**d_{33}) ~ 252 pC/N, plannar mode coupling coefficients (k_p) ~ 0.47 and remnant polarization (P_r) ~ 24.65 μC/cm^2 were obtained in the KNNT-LS ceramic with x=0.02. The excellent piezoelectric and ferroelectric properties of KNNT-LS ceramics, which are comparable to conventional PZT ceramics, indicate that these ceramics are promising candidates for lead-free piezoelectric applications.

c) Lead free 0.95[$(K_{0.5}Na_{0.5})Nb_{(1-x)}V_xO_3$]-0.05$LiSbO_3$ (KNNV-LS) ceramics with x=0, 0.02, 0.04, 0.06 and 0.08 have been synthesized by conventional solid state reaction route (CSSR). X-ray diffraction (XRD) analysis confirmed the formation of orthorhombic phase with increase in V content in KNNV-LS ceramics. The overall electrical properties were decreased in comparison to the other modified ceramics.

Finally, 0.95[$K_{0.5}Na_{0.5}NbO_3$]-0.05[$LiSbO_3$], 0.95[$(K_{0.5}Na_{0.5})_{0.94}Ag_{0.06}NbO_3$]-0.05$LiSbO_3$ / KNA6N-LS, 0.95[$(K_{0.5}Na_{0.5})Nb_{0.98}Ta_{0.02}O_3$]-0.05$LiSbO_3$/ KNNT2-LS, 0.95[$(K_{0.5}Na_{0.5})Nb_{0.94}V_{0.06}O_3$]-0.05$LiSbO_3$/KNNV6-LS ceramics were also synthesized by microwave processing technique It was found that the microwave processed ceramics exhibited better ferroelectric and piezoelectric properties, which confirmed the effectiveness of microwave processing over the conventional one. Among all the microwave processed ceramics, 0.95[$(K_{0.5}Na_{0.5})Nb_{0.98}Ta_{0.02}O_3$]-0.05$LiSbO_3$ ceramic showed maximum ferroelectric and piezoelectric properties i.e., d_{33}~ 257 pC/N, P_r ~ 30.48, k_p ~ 0.48 and remnant strain ~ 0.10% have been reported. The results in this study

indicated that the ceramic can be an effective candidate for lead free piezoelectric applications.

8.2 Recommendations for Future Work

As per present study, microwave processed $0.95[(K_{0.5}Na_{0.5})Nb_{0.98}Ta_{0.02}O_3]$-$0.05LiSbO_3$ and $0.95[(K_{0.5}Na_{0.5})_{0.94}Ag_{0.06}NbO_3]$-$0.05LiSbO_3$ ceramics exhibited better electrical properties. The following recommendations are made for the extension of present work.

(1) The processing of these ceramics can be carried out in single mode microwave furnace to study the effect of 'E' & 'H' field separately.

(2) The piezoelectric and ferroelectric properties of the KNN based ceramics are sensitive to the position of T_{O-T}, therefore temperature dependent XRD study should be carried out.

(3) In order to obtain uniform microstructure and lower the processing temperatures, these ceramics can be synthesized by combustion technique.

(4) Low temperature dielectric, ferroelectric, resonance as well as piezoelectric measurement should be carried out to identify the position of the T_{O-T} in the ceramics where it is below RT.

(5) Fatigue characterization should be done to test the stability of the piezoelectric-ferroelectric properties.

(6) For proper understanding of domains, High resolution transmission electron microscopy (HRTEM) study can be carried out.

(7) Measurement of longitudinal coupling coefficients (k_t)